REPORT 189

A MAGNETOTELLURIC SURVEY ACROSS THE EAST ALBANY–FRASER OROGEN, WESTERN AUSTRALIA

by
J Spratt, MC Dentith and CV Spaggiari

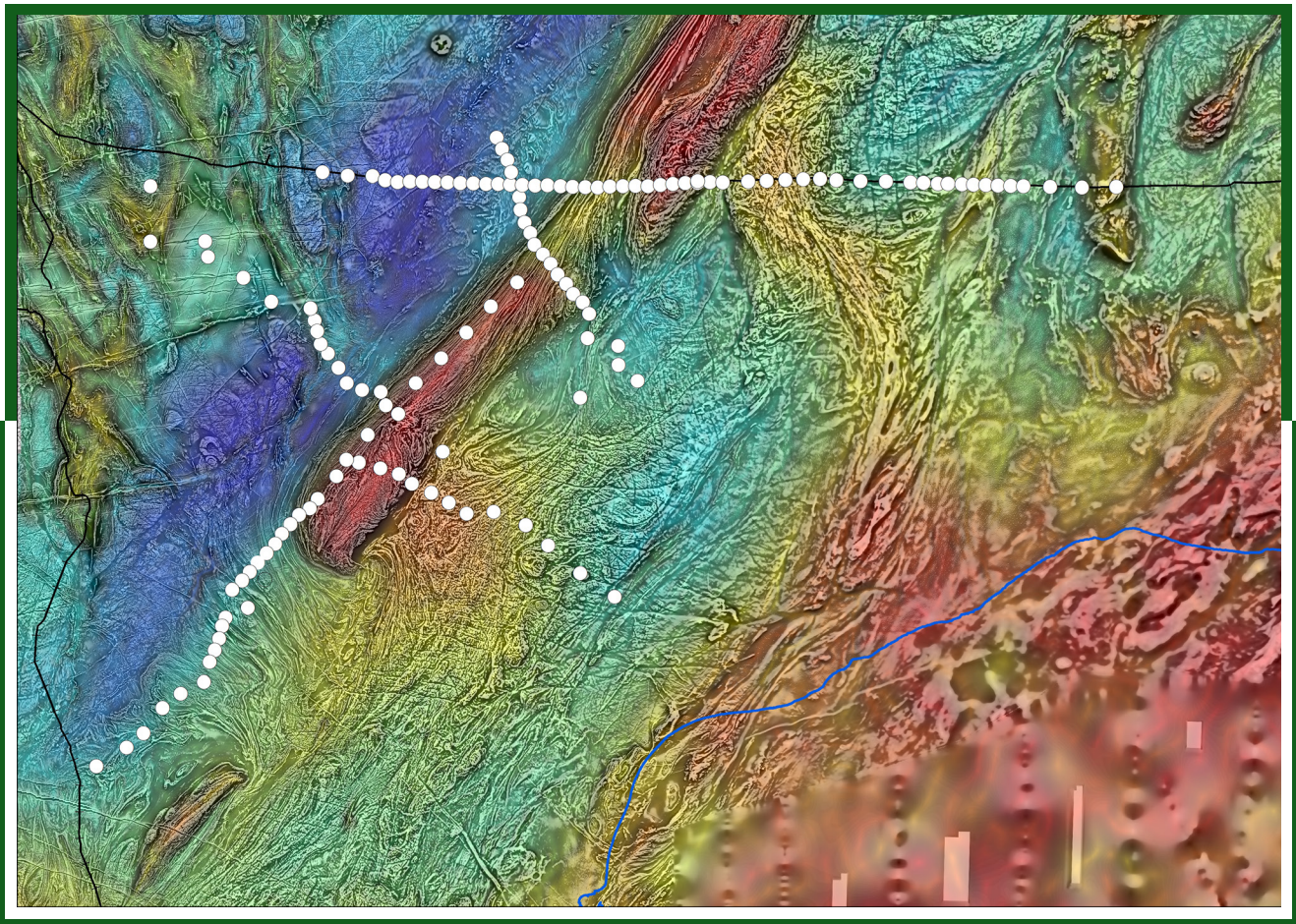

Centre for EXPLORATION TARGETING

EXPLORATION INCENTIVE SCHEME

Government of Western Australia
Department of Mines, Industry Regulation and Safety

Geological Survey of Western Australia

Government of **Western Australia**
Department of **Mines, Industry Regulation and Safety**

REPORT 189

A MAGNETOTELLURIC SURVEY ACROSS THE EAST ALBANY–FRASER OROGEN, WESTERN AUSTRALIA

by
J Spratt[1], MC Dentith[2] and CV Spaggiari

1 Independent Consultant, Wakefield, Quebec, Canada J0X3G0
2 Centre for Exploration Targeting, School of Earth Sciences, The University of Western Australia, Crawley, WA 6009, Australia

PERTH 2019

Geological Survey of Western Australia

MINISTER FOR MINES AND PETROLEUM
Hon Bill Johnston MLA

DIRECTOR GENERAL, DEPARTMENT OF MINES, INDUSTRY REGULATION AND SAFETY
David Smith

EXECUTIVE DIRECTOR, GEOLOGICAL SURVEY AND RESOURCE STRATEGY
Jeff Haworth

REFERENCE
The recommended reference for this publication is:
Spratt, J, Dentith, MC and Spaggiari, CV 2019, A magnetotelluric survey across the east Albany–Fraser Orogen, Western Australia: Geological Survey of Western Australia, Report 189, 107p.

ISBN 978-1-74168-836-8
ISSN 1834-2280

A catalogue record for this book is available from the National Library of Australia

Grid references in this publication refer to the Geocentric Datum of Australia 1994 (GDA94). Locations mentioned in the text are referenced using Map Grid Australia (MGA) coordinates, Zone 51. All locations are quoted to at least the nearest 100 m.

Published 2019 by the Geological Survey of Western Australia
This Report is published in digital format (PDF) and is available online at <www.dmp.wa.gov.au/GSWApublications>.

Further details of geological publications and maps are available from:
Information Centre
Department of Mines, Industry Regulation and Safety
100 Plain Street
EAST PERTH WESTERN AUSTRALIA 6004
Telephone: +61 8 9222 3459 Facsimile: +61 8 9222 3444
www.dmp.wa.gov.au/GSWApublications

Cover photograph: Magnetotelluric station locations plotted on a drape image of gravity (colour) and reduced to pole, first vertical derivative aeromagnetic data (greyscale). Warm colours represent a strong gravity response, cool colours low response. Railway lines are shown in black and the coastline in blue

Contents

Appendices

Figures

Tables

A magnetotelluric survey across the east Albany–Fraser Orogen, Western Australia

by

J Spratt[1], MC Dentith[2] and CV Spaggiari

Abstract

Magnetotelluric soundings at 163 locations across the east Albany–Fraser Orogen have provided 2D and 3D conductivity models of the crust and uppermost lithospheric mantle beneath four regional transects. Dimensionality and geoelectric strike analysis on these data reveal complex and variable strike directions both laterally and with depth, highlighting the need for 3D modelling. In general, the models reveal a resistive upper crust that is crosscut by several near-vertical, low resistivity zones. In some instances, low resistivity zones can be correlated with the locations of major shear zones or tectonic unit boundaries. A conductive zone in the lower crust below the Northern Foreland and the Biranup Zone coincides with a nonreflective lower crustal zone observed in seismic reflection data, and with a region of thicker crust determined from passive seismic data. This, and other regions of conductivity variation in the deep crust and mantle, are oblique to surface geological strike, suggesting detachment between the upper and lower crust.

KEYWORDS: 3D modelling, Albany–Fraser Orogen, crustal structure, magnetotelluric surveys

Introduction

The Albany–Fraser Orogen is located along the southern and southeastern margins of the Yilgarn Craton in southern Western Australia (Fig. 1). The east Albany–Fraser Orogen contains the world-class Tropicana orogenic gold deposit (Doyle et al., 2015; Blenkinsop and Doyle, 2014) and also the Nova–Bollinger mafic-hosted Ni–Cu deposit (Bennett et al., 2014; Maier et al., 2016). Both of these deposits are spatially associated with major crustal-scale structures, which is typical for these deposit types (McCuaig et al., 2010). To aid understanding of the deep subsurface structure beneath the east Albany–Fraser Orogen, the Geological Survey of Western Australia (GSWA), through the Exploration Incentive Scheme (EIS), commissioned a magnetotelluric (MT) survey along four main profiles (Fig. 1). The profile locations were chosen to complement the three active seismic lines that were acquired at a similar time (Spaggiari et al., 2014a), allowing sufficient distance from the Southern Ocean so as to not affect MT data acquisition. The principal goal of this survey was to map the electrical resistivity structure of the crust and upper lithospheric mantle beneath the survey area to investigate the nature of the transition between the Archean granite–greenstone terranes of the Yilgarn Craton and the reworked Archean, dominantly gneissic and granitic rocks of the east Albany–Fraser Orogen. This Report describes the data processing, analysis, modelling and interpretation of these data.

The MT method is a deep-penetrating, natural-source, electromagnetic technique used to image the electrical conductivity structure of the Earth's crust and upper mantle. It has been shown to be a useful tool in mapping the boundary between Archean and Proterozoic terranes, and defining deep structure beneath regions of Proterozoic orogenesis such as the Grenville Orogen (Kurtz et al., 1993; Adetunji et al., 2014), the India–Asia continental-collision zone (Nelson et al., 1996; Spratt et al., 2005; Unsworth et al., 2005) and the Mesoproterozoic Musgrave Province (Selway et al., 2011; Aitken et al., 2013). The MT method has been successfully applied to: mapping ancient orogenic sutures in the Trans-Hudson Orogen (Jones et al., 1993, 2005) and Iapetus Suture (Banks et al., 1996); delineating major terrane boundaries such as the Wopmay Orogen and the Slave Craton (Spratt et al., 2009); identifying major lithospheric structures, such as the Great Slave Lake shear zone (Wu et al., 2002) and faults beneath the Melville Peninsula of the Rae Craton (Spratt et al., 2013).

Analysis and modelling of MT data acquired across the east Albany–Fraser Orogen reveal significant differences in resistivity at all crustal levels, and in the upper lithospheric mantle, that provide key information on the crustal architecture of the region and tectonic evolution. Some of these features coincide with deep crustal shear zones, tectonic unit boundaries, and regions of voluminous magmatic activity.

1 Independent Consultant, Wakefield, Quebec, J0X3G0 Canada

2 Centre for Exploration Targeting, School of Earth Sciences, The University of Western Australia, Stirling Highway, Crawley WA 6009

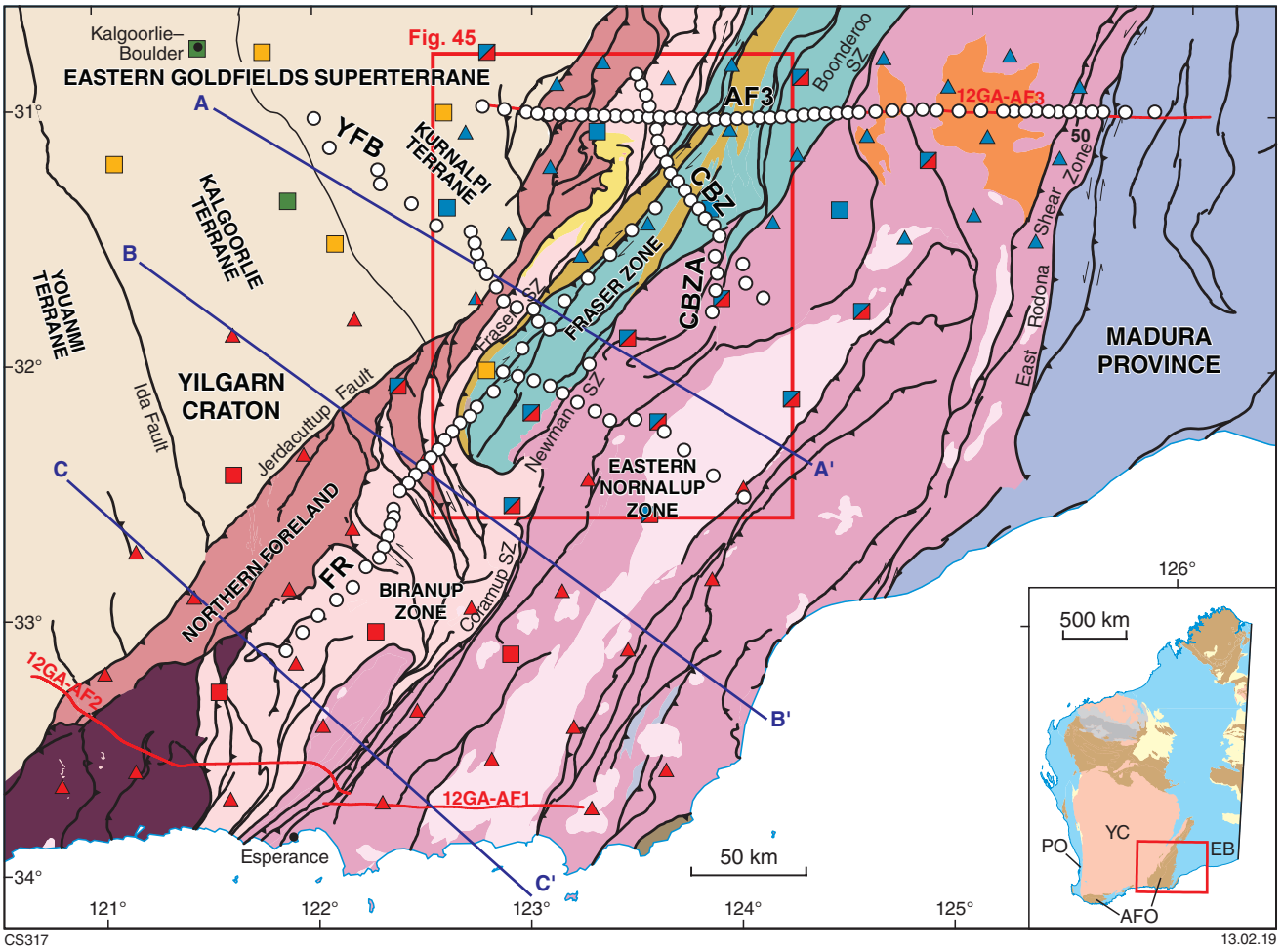

Figure 1. **Simplified pre-Mesozoic bedrock map of the east Albany–Fraser Orogen (modified from Spaggiari, 2016) showing the location of the MT survey lines, the ALFREX array and other seismic stations, locations of receiver functions stacked profiles, and three active seismic lines shot during 2012 with their respective names (modified from Sippl et al., 2017a). Inset shows a geological map of Western Australia, with Archean basement shown in pink, Proterozoic orogens in brown, and Proterozoic and younger basins in yellow and blue, respectively. Abbreviations: AFO, Albany–Fraser Orogen; EB, Eucla Basin; PO, Pinjarra Orogen; YC, Yilgarn Craton**

Regional setting

The Albany–Fraser Orogen (AFO) is defined as a region of extensive reworking of Archean Yilgarn Craton crust during Paleoproterozoic and Mesoproterozoic tectonic events (Kirkland et al., 2011; Spaggiari et al., 2014b, 2015). The AFO lies along the southern and southeastern margin of the Yilgarn Craton (Fig. 1), which together form the southern part of the West Australian Craton. Paleoproterozoic tectonism from at least c. 1815 Ma was dominated by extension in a continental rift setting that produced voluminous, dominantly felsic magmatism and an extensive siliciclastic basin system, the Barren Basin (Spaggiari et al., 2015). This rift evolved into an ocean–continent transition by c. 1500 Ma, with the craton edge in a passive margin setting (Spaggiari et al., 2015). A change to convergence is indicated by the presence of an oceanic arc (the Loongana Arc) in the adjacent Madura Province. This oceanic arc collided with the craton margin before c. 1330 Ma, triggering Stage I of the Albany–Fraser Orogeny (Spaggiari et al., 2015; Smithies et al., 2015). Two distinct tectono-thermal stages define the Albany–Fraser Orogeny (Clark et al., 2000; Bodorkos and Clark, 2004a; Spaggiari et al., 2014b, 2015; Smithies et al., 2015). Stage I, between c. 1330 and 1260 Ma, is interpreted to have resulted from the accretionary event producing voluminous felsic and mafic magmatism, high-temperature metamorphism, and large-scale folding, thrusts and shear zones. In contrast, Stage II, between 1225 and 1140 Ma, is interpreted as an intracratonic event that resulted in voluminous A-type felsic and mafic magmatism, generally high-temperature metamorphism, deformation and reactivation of major structures.

The Albany–Fraser Orogen is truncated by the Darling Fault and the Mesoproterozoic to Neoproterozoic Pinjarra Orogen to the west. To the south, the orogen is interpreted to be continuous into the Wilkes Land region of eastern Antarctica (Fitzsimons, 2003, and references therein; Aitken et al., 2016; Morrissey et al., 2017). To the east, the Albany–Fraser Orogen is separated from the adjacent Madura Province by the Rodona Shear Zone, which represents the suture between modified Archean Yilgarn crust and exotic (oceanic and oceanic-arc type) basement rocks under cover (Spaggiari et al., 2015; Spaggiari and Smithies, 2015). Granite–greenstone sequences of the Yilgarn Craton are interpreted to extend a significant distance to the southeast beneath the Albany–Fraser Orogen, truncated by major southeast-dipping thrusts such as the Jerdacuttup Fault and Cundeelee Shear Zone (Figs 1–3; Spaggiari et al., 2014a). Seismic reflection data show that several thrust faults lie inboard of these major structures, consistent with interpretations of a gradational boundary between unmodified craton and the Northern Foreland of the Albany–Fraser Orogen (Spaggiari et al., 2009 and references therein, 2014a,b).

The Yilgarn Craton is subdivided into seven terranes (Cassidy et al., 2006; Pawley et al., 2012) bounded by large-scale, dominantly northwesterly trending fault systems. Within the MT survey area, the east Albany–Fraser Orogen intersects the Neoarchean (2970–2630 Ma) Eastern Goldfields Superterrane, which is separated from the Youanmi Terrane to the west by the north-northwesterly trending Ida Fault (Fig. 1; Cassidy et al., 2006; Pawley et al., 2012; Wyche et al., 2012). The Eastern Goldfields Superterrane is divided into four, fault- or shear zone-bounded tectono-stratigraphic terranes, which from southwest to northeast are the Kalgoorlie, Kurnalpi, Burtville and Yamarna Terranes (Cassidy et al., 2006; Pawley et al., 2012; Wyche et al., 2012). These terranes host variable occurrences of highly mineralized (orogenic gold, komatiite-associated Ni–Cu), elongate belts of Neoarchean deformed and metamorphosed, volcanic and intrusive felsic, mafic and ultramafic rocks, and sedimentary rocks (Kositcin et al., 2008; Pawley et al., 2012; Wyche et al., 2012; GSWA, 2017).

The Albany–Fraser Orogen is divided into the Northern Foreland, the component adjacent to the Yilgarn Craton itself, and dominantly crystalline basement gneisses of the Kepa Kurl Booya Province which is further subdivided into the Biranup, Nornalup and Fraser Zones, and the Tropicana Zone, which lies to the north of the study area (Fig. 1; Spaggiari et al., 2009, 2014b). The Biranup Zone is dominated by deformed orthogneisses with ages between c. 1810 and 1625 Ma, and includes Archean granitic rocks with geochemical and isotopic characteristics of Yilgarn Craton heritage (Kirkland et al., 2011; Spaggiari et al., 2014a,b; Smithies et al., 2015). The Biranup and eastern Nornalup Zones comprise similar basement lithologies, but in the southern part of the east Albany–Fraser Orogen are separated by a major shear zone network that includes the Coramup Shear Zone (Bodorkos and Clark., 2004b; Spaggiari et al., 2014a). The eastern Nornalup Zone has been extensively intruded by granitic rocks and gabbros of the 1330–1280 Ma Recherche Supersuite and the 1200–1140 Ma Esperance Supersuite (Smithies et al., 2015). To the northeast, the major shear zone boundary between the Biranup and eastern Nornalup Zones widens and hosts the Fraser Zone, an approximately 450 km-long, northeasterly trending belt of dominantly high-density, metagabbroic, granulite-facies rocks (Fig. 2; Smithies et al., 2013; Maier et al., 2016; Spaggiari, 2016). The Fraser Zone is bounded to the west and south by the Fraser Shear Zone, and to the east by the Boonderoo and Newman Shear Zones. Metagabbros interlayered with granitic and sedimentary gneisses of the Fraser Zone are dated between c. 1310 and 1280 Ma, and were exhumed from mid-crustal depths during Stage I of the Albany–Fraser Orogeny (Clark et al., 2014; Kirkland et al., 2014; Spaggiari et al., 2015; Maier et al., 2016). The northeastern part of the eastern Nornalup Zone is covered by Cretaceous shale and siltstone of the Madura Formation and Eocene limestone successions of the Eucla Basin (Lowry, 1970).

Geophysical background

Strong contrasts in density and magnetism within the Albany–Fraser Orogen have facilitated geological mapping using sparse outcrop and drillcore information, and potential field datasets (Spaggiari, 2016). High-resolution, small-scale geophysical surveys related to mineral exploration have also aided geological mapping and interpretation in the study area. These are available through the Department of Mining, Industry Regulation and Safety (DMIRS) website at

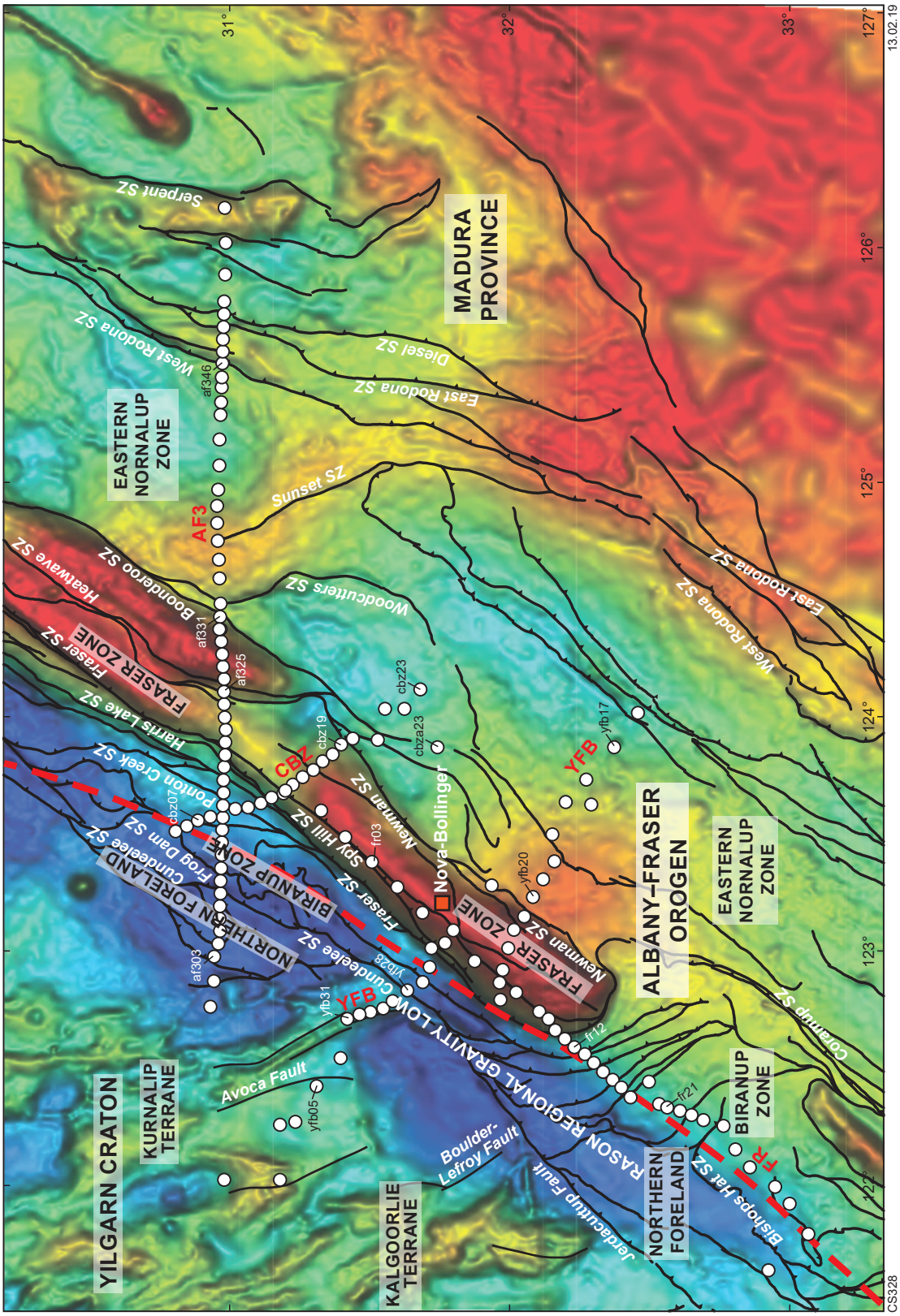

Figure 2. **Bouguer gravity image showing the locations of the MT survey lines and selected MT stations, the Fraser Zone, the Rason Regional Gravity Low, and major structures. The red dashed line shows the approximate axis of the zone of thickened crust, derived from passive seismic data and receiver function analysis (Sippl et al., 2017a)**

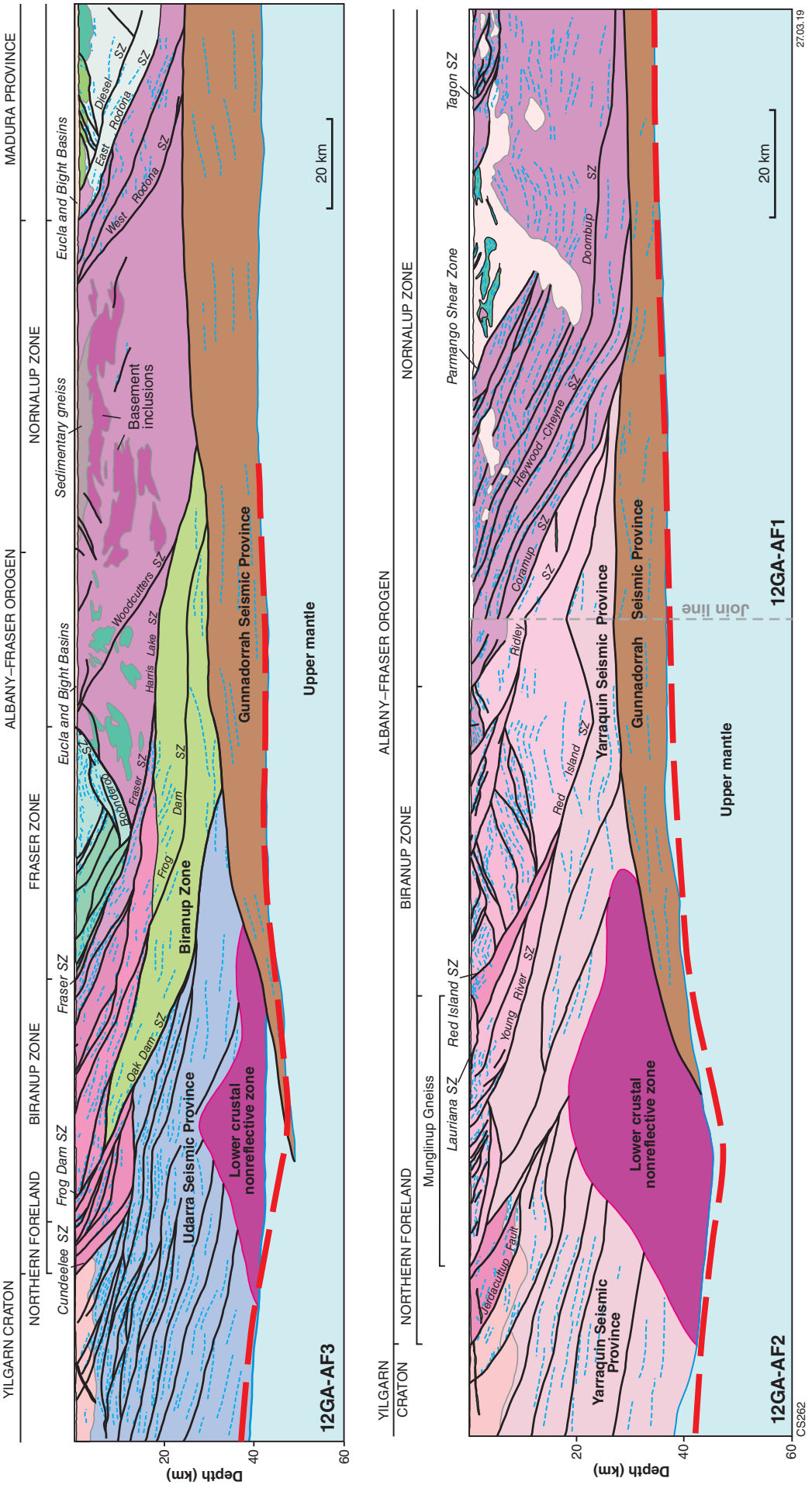

Figure 3. **Interpreted active seismic profiles (from Spaggiari et al., 2014a). The red dashed line shows the Moho depth values obtained from single receiver function traces shown in Figure 4a (after Sippl et al., 2017a). Note the join between 12GA-AF2 and 12GA-AF1, which is situated at a bend on the seismic profile (Fig. 1) resulting in distorted geometries of the shear zones**

<www.dmp.wa.gov.au/geophysics>. However, the most significant datasets regarding the MT work are two deep seismic reflection profiles at the northern end of, and to the south of, the MT survey area (Fig. 1; Spaggiari et al., 2014a). In addition, the ALbany–FRaser EXperiment (ALFREX) passive seismic array covered the same area as the MT survey, as well as farther to the south and east (Figs 1, 2; Sippl et al., 2017a,b).

Seismic reflection profile 12GA-AF3, which follows part of the east–west Trans-Australian Railway, coincides with the AF3 MT transect (Figs 1, 2). The interpretation of the seismic dataset in conjunction with potential field data shows that the structural architecture is dominated by numerous, moderately southeasterly dipping faults and shear zones in the region to the west of the Fraser Zone (Fig. 3; Spaggiari et al., 2014a). The Fraser Zone itself is interpreted as V-shaped, extending to a depth of about 12–15 km (Spaggiari et al., 2014a; Brisbout, 2015). In seismic profile 12GA-AF3, the Fraser Zone is bounded by the southeast-dipping Fraser Shear Zone to the west, and by the apparently west-dipping Boonderoo Shear Zone to the east, although it is unclear whether this contact is primarily a lithological one, or is the shear zone itself. To the east of the Fraser Zone within the eastern Nornalup Zone, far fewer structures are evident. This likely coincides with the voluminous Mesoproterozoic intrusions of the Recherche and Esperance Supersuites, which are largely confined to this zone (Spaggiari, 2016; Sippl et al., 2017a), and which likely have less variation in rock acoustic properties than the lithologies to the west.

Several 'seismic provinces' are interpreted in the middle to lower crust. These are regions of different seismic character that cannot be correlated with surface or upper-crustal geology (Korsch et al., 2014). A notable feature is a nonreflective zone in the lower crust, predominantly beneath the surface expression of the Northern Foreland, but extending beneath the Biranup Zone (Fig. 3). The Udarra and Yarraquin Seismic Provinces occur predominantly to the west of and also above this feature, and are interpreted as middle to lower crust of the Yilgarn Craton (Korsch et al., 2014; Spaggiari et al., 2014a). To the east of the nonreflective zone, beneath the western margin of the Fraser Zone in seismic profile 12GA-AF3, the Moho appears to be offset by a west-dipping shear zone. To the east of the nonreflective zones in both seismic profiles 12GA-AF3 and 12GA-AF2, the lowermost crust is assigned to the approximately 5–10 km-thick Gunnadorrah Seismic Province (Fig. 3)

The passive seismic recordings of the ALFREX array have been used to produce a surface wave velocity volume using ambient noise recordings (Sippl et al., 2017b). Major structures between the Yilgarn Craton and Northern Foreland of the Albany–Fraser Orogen do not coincide with a velocity boundary. The most obvious variation in velocity is associated with the Fraser Zone, which, as expected, coincides with a high velocity zone. The Fraser Zone appears to be an upper-crustal feature, consistent with the seismic reflection profile and potential field data forward modelling (Brisbout, 2015).

Modelling of receiver functions derived from the passive seismic ALFREX array defines a linear zone of crust about 5–10 km thicker than elsewhere (Figs 1, 4, 5; Sippl et al., 2017a). The trend of this zone of thicker crust is the same as the dominant trend of the east Albany–Fraser Orogen, and also coincides with the nonreflective lower crust beneath the Northern Foreland and Biranup Zone (Figs 2–4). It also occurs beneath the southwestern part of the Fraser Zone, and beyond its termination to the southwest, where it appears the Moho may be faulted (Fig. 5; Sippl et al., 2017a). The zone of thicker crust is a likely explanation for a distinct linear gravity low (the Rason Regional Gravity Low of Fraser and Pettifer [1980]) observed on the northwestern side of the Fraser Zone (Fig. 2). This result is also consistent with marine-source seismic refraction data that imaged a deep crustal root (to about 60 km depth) beneath the southern margin of the Yilgarn Craton and the central to west Albany–Fraser Orogen (Tassell and Goncharov, 2006).

Magnetotellurics theory and background

Magnetotellurics (MT) is a geophysical method that involves measuring and relating natural time-varying electric and magnetic fields in order to resolve the electrical conductivity structure of the subsurface of the Earth (Cagniard, 1953; Wait, 1962). The relationship between these horizontal and mutually perpendicular fields recorded at each station provides amplitude (apparent resistivity) and phase lags as a function of frequency (or period, the inverse of frequency), commonly referred to as MT response curves (Fig. 6). With increasing depth, there is an exponential decrease in the amplitudes of the electromagnetic fields, the so-called skin-depth phenomenon. As the depth of penetration (or skin depth) of these fields is directly related to frequency (the lower the frequency, the greater the depth) and the resistivity of the material (the greater the resistivity, the greater the depth), estimates of resistivity vs depth can be made beneath each site. For this reason, during the description of the processing and interpretation of the MT data (see below), period can be thought of as a proxy for depth. However, since the conductivity of the Earth varies from location to location, the conversion factor from period to depth will also vary. To image the deep mantle lithosphere, long periods must be sampled and this requires recording times of tens of hours.

Prior to 2D modelling, MT data are typically analysed to determine the regional geoelectric strike direction, as well as the degree of dimensionality, in order to generate an accurate representation of a 2D Earth. Where the Earth is 1D, the conductivity structure is layered and independent of the geoelectric strike direction. Within a 2D Earth (in which conductivity structure varies laterally so that the response curves are different across and perpendicular to geological or, more correctly, geoelectrical strike), apparent resistivities and phases need to be calculated in both directions (or modes). The transverse-electric (TE) mode describes current flowing parallel to geoelectric strike and is predominantly sensitive to current concentration and flow patterns. The transverse-magnetic (TM) mode describes current flow perpendicular to strike and is more sensitive to charges induced on lateral boundaries.

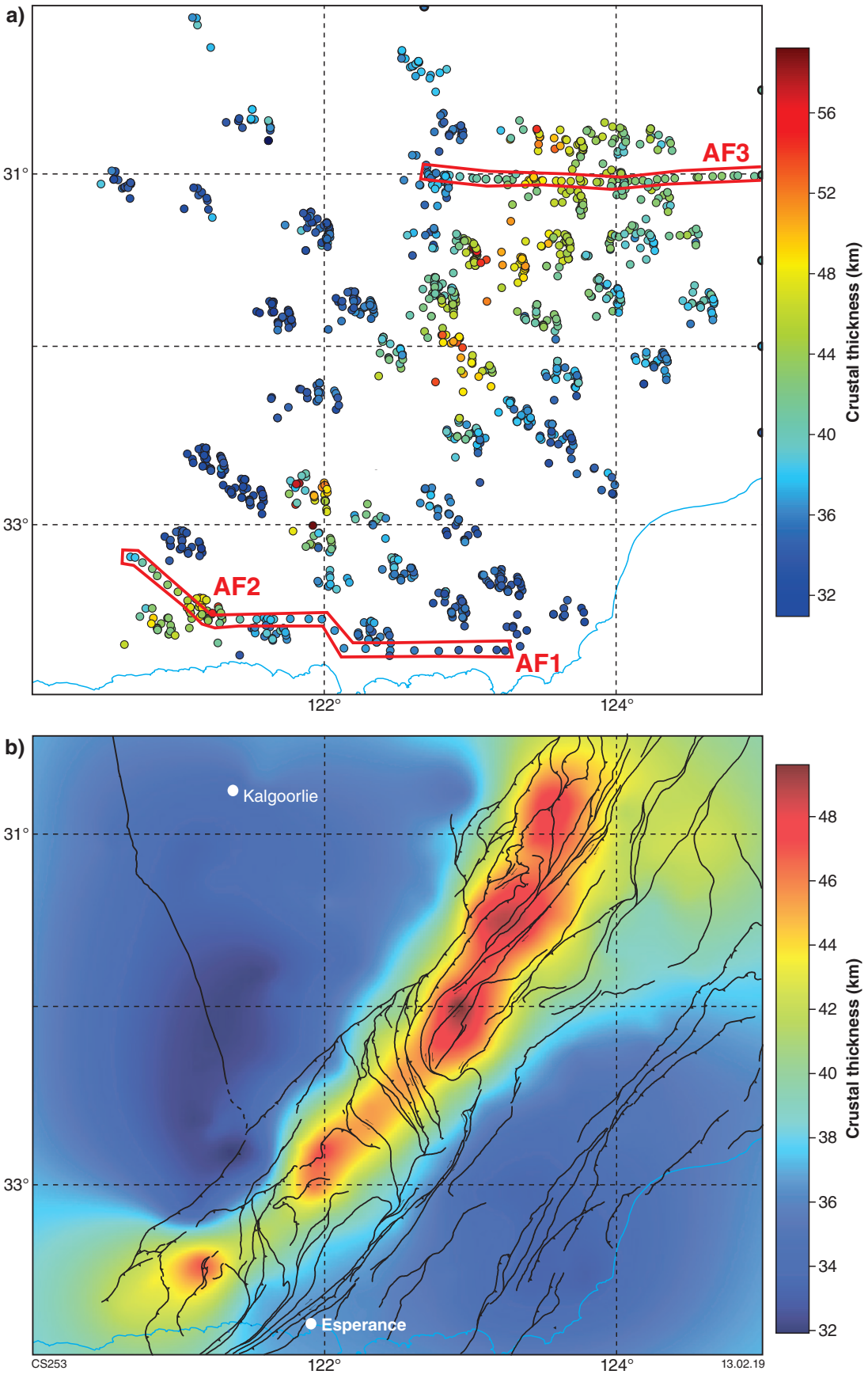

Figure 4. **Crustal thickness maps after Sippl et al. (2017a): a) Moho depth values obtained from individual receiver function traces, assuming a bulk crustal V_P/V_S ratio of 1.73. Each depth value is plotted at its Moho piercing point location. Moho picks from the active seismic profiles 12GA-AF1, 12GA-AF2 and 12GA-AF3 were also included; b) crustal thickness map obtained by interpolating all the point measurements shown in a). The traces of shear zones, faults and tectonic unit boundaries (from Fig. 1) are shown for reference**

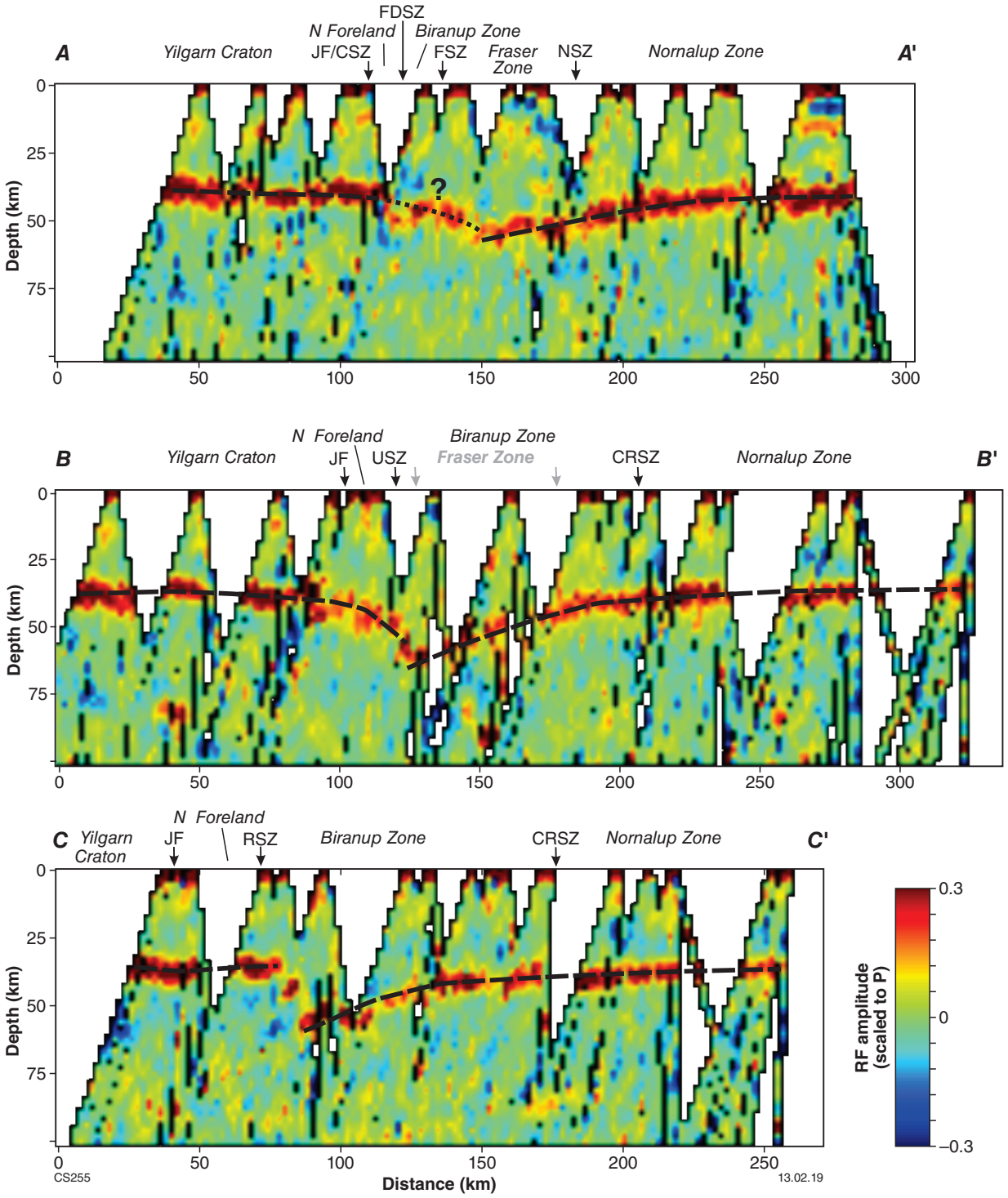

Figure 5. **Three profiles obtained from common conversion point stacking of receiver functions with locations shown in Figure 1 (after Sippl et al., 2017a). The Moho is identified as the most prominent phase of positive receiver function amplitudes, which imply an upward velocity decrease, denoted in shades of red and highlighted by a dashed line or, where uncertain, by a dotted line. Black arrows show approximate location of major faults or shear zones. Grey arrows or text denote features that are projected onto the profile. Abbreviations: CRSZ, Coramup Shear Zone; CSZ, Cundeelee Shear Zone; FDSZ, Frog Dam Shear Zone; FSZ, Fraser Shear Zone; JF, Jerdacuttup Fault; NSZ, Newman Shear Zone; RSZ, Red Island Shear Zone; USZ, unnamed shear zone**

Modelling MT data is computationally expensive, especially in 3D, and the conductivity models are necessarily simplifications of a complex reality. Modelling in 2D allows more detailed models to be created and many more possible models to be tested, which allows for reliability testing of specific features in the resulting conductivity models. When it is necessary to model the observed responses using a 3D model, practicalities dictate that the resolution is lower and there is much less opportunity for testing specific features. As demonstrated below, the data from the Albany–Fraser MT survey are complex and indicative of 3D variations in subsurface conductivity.

Even when modelled in 3D, MT solutions are, by nature, non-unique; however, the highest resolution is observed when imaging the top of a low resistivity layer. One limitation of the method is that it is sensitive to the product of conductivity and thickness (conductance), but cannot resolve the two factors independently, i.e. apparent broad regions of enhanced conductivity may in fact be caused by quite thin zones of high conductivity. Also to be considered is that continuous networks of conductive material, of whatever type, over the very large areas where enhanced conductivity is observed, are difficult to explain geologically, as is their continuity over geological time scales.

Causes of electrical conductivity variation

The MT method is sensitive to contrasts in the resistivity of different materials and can therefore distinguish between some lithological units and can image structural and compositional features at depth. Typical Archean granulite-facies rocks, for example, commonly have high electrical resistivity values >1000 Ω.m (e.g. Wu et al., 2002), whereas sedimentary rocks are less resistive, with values in the range 10–1000 Ω.m. Conductivity variations in major crustal layers have been derived from MT surveys and laboratory measurements of various rock types and constituents (Fig. 7). Note the general three-layer classification of very resistive upper crust, less resistive lower crust and resistive mantle.

Within the crust, factors that can considerably reduce typical resistivity values include changes in mineralogy, or the presence of saline fluids (Haak and Hutton, 1986; Jones, 1992; Evans, 2012). Regardless of the type of conducting material, it is important to recognize that interconnectivity of the conducting elements is a key control on the 'bulk' conductivity of a material. If this occurs, only small amounts of the conductive component of the material are required.

At mantle depths, the electrical characteristics reflect the electrical properties of olivine. Similar to crustal responses, a major problem in understanding electrical responses from the mantle is that laboratory measurements on olivine suggest the observed resistivity of the mantle should be much higher than that derived from MT measurements. The bulk conductivity of the mantle lithosphere is predominantly attributed to its temperature and composition. Typical values of 1000–10 000 Ω-m are observed in MT studies around the world (Eaton et al., 2009), with the resistivity of dry olivine decreasing with increasing temperature, approximately one order of magnitude for every 200–300°C (Constable, 2006). The most commonly proposed causes for anomalously enhanced conductivity in the subcontinental upper mantle include the presence of interconnected conducting phases such as graphite, sulfides or thin carbon films (Duba and Shankland, 1982; Ducea and Park, 2000; Poe et al., 2010), fluids (either brine or partial melt; Glover et al., 2000), a reduction in grain size (ten Grotenhuis et al., 2004), ambient temperature variations (Ledo and Jones, 2005), oxygen fugacity (Constable, 2006), increased iron content (Jones et al., 2009), and bonded water through hydration (Karato, 1990, 2006; Jones et al., 2012).

MT data acquisition and analysis

Data acquisition

Broadband MT (BBMT) data were collected by personnel from Moombarriga Geoscience over four deployments during the period 24 April 2012 to 12 April 2013. The MT data were acquired at 5–10 km station spacing along roads and station tracks providing information along four regional profiles: AF3, CBZ (with the addition of a short section, CBZA), YFB, and FR (Fig. 1). Time-series data were recorded for an average of 40 hours at each site in an effort to resolve apparent resistivity and phase to a period of 1000 s. Station locations and acquisition times for all 137 MT sites are provided in Table 1. In addition, time-domain electromagnetic soundings were made at each MT station.

Data were recorded using two different instrument types: Phoenix Ltd MTU-5A data recorders with MTC-50 or MTC-80 magnetic induction coils, and Metronix ADU07e data recorders with MSF06 induction coils. Two (horizontal) components of the electric field (Ex and Ey) and three components of the magnetic field variation (Hx, Hy, and Hz) were measured at each site except at sites where the vertical (Hz) component was omitted because of difficult drilling conditions. Electric dipoles and horizontal coils were installed in magnetic north–south and east–west azimuths and the electric dipoles at all sites were approximately 100 m in length. The electric field was measured using non-polarizing ($Pb/PbCl_2$ solution) electrodes. These consist of a container with a porous base filled with an electrolyte solution, which provides electrical contact with the ground. At the start of the survey, all induction coils were calibrated to calculate the response of each coil to a known signal over a range of frequencies. The calibration files were then used for processing to correct for small differences between the coil responses.

Electromagnetic soundings of the near surface at each station were made using a Zonge ZT20 transmitter and SmarTEM24 receiver with a three-component RVR. A 100 m-sided square transmitter loop (Tx area = 10 000 m^2) was used with sides oriented north–south and east–west. The receiver coil had an effective area of 10 000 m^2.

Table 1. Locations and recording times of MT Stations

Site	*Latitude*	*Longitude*	*Start recording time*	*End recording time*	*Duration (hours)*	*Instrument*
af301A	-30.9911100	122.7697800	5/5/2012 4:30	7/5/2012 0:14	43.7	Phoenix
af302A	-31.0036000	122.8748333	5/5/2012 3:45	7/5/2012 1:14	45.5	Phoenix
af303A	-31.0044400	122.9781833	5/5/2012 2:30	6/5/2012 12:33	34.1	Phoenix
af304A	-31.0200330	123.0313167	7/5/2012 5:40	8/5/2012 4:41	23.0	Phoenix
af305A	-31.0258170	123.0834500	4/5/2012 3:30	6/5/2012 1:38	46.1	Phoenix
af306A	-31.0240830	123.1357000	6/5/2012 3:24	8/5/2012 4:05	48.7	Phoenix
af307A	-31.0252780	123.1878000	3/5/2012 9:45	5/5/2012 1:00	39.3	Phoenix
af308A	-31.0266830	123.2401333	6/5/2012 2:31	8/5/2012 3:23	48.9	Phoenix
af309A	-31.0266000	123.2923500	3/5/2012 8:00	5/5/2012 0:26	40.4	Phoenix
af310A	-31.0290670	123.3456694	25/5/2012 6:10	26/5/2012 2:49	20.6	Metronix
af311A	-31.0306500	123.4003833	3/5/2012 6:45	4/5/2012 21:25	38.7	Phoenix
af312A	-31.0321690	123.4531667	25/5/2012 6:10	26/5/2012 2:10	20.0	Metronix
af313A	-31.0322670	123.5050167	4/5/2012 8:50	5/5/2012 6:05	21.3	Phoenix
af314A	-31.0341330	123.5554167	26/4/2012 2:20	27/4/2012 23:16	44.9	Phoenix
af315A	-30.9896170	123.5588167	2/5/2012 7:30	3/5/2012 23:35	40.1	Phoenix
af316A	-31.0354170	123.6060833	24/4/2012 10:10	26/4/2012 0:45	38.6	Phoenix
af317A	-31.0368170	123.6587833	25/4/2012 2:00	26/4/2012 23:20	45.3	Phoenix
af318A	-31.0357170	123.7104833	2/5/2012 5:45	3/5/2012 2:44	21.0	Phoenix
af319A	-31.0389670	123.7658833	24/4/2012 9:15	26/4/2012 0:13	39.0	Phoenix
af320A	-31.0414000	123.8159333	25/4/2012 5:00	27/4/2012 2:33	45.6	Phoenix
af321A	-31.0422830	123.8684333	27/4/2012 5:30	28/4/2012 23:47	42.3	Phoenix
af322A	-31.0430670	123.9205667	26/4/2012 4:45	27/4/2012 20:51	40.1	Phoenix
af323A	-31.0392830	123.9718000	1/5/2012 4:30	2/5/2012 21:48	41.3	Phoenix
af324A	-31.0370500	124.0263833	27/4/2012 7:30	29/4/2012 0:18	40.8	Phoenix
af325A	-31.0352330	124.0786000	1/5/2012 3:00	2/5/2012 3:58	25.0	Phoenix
af326A	-31.0363500	124.1317667	28/4/2012 2:30	29/4/2012 23:41	45.2	Phoenix
af327A	-31.0309830	124.1829333	30/4/2012 2:00	2/5/2012 0:31	46.5	Phoenix
af328A	-31.0273830	124.2353333	29/4/2012 4:00	1/5/2012 0:57	45.0	Phoenix
af329A	-31.0237170	124.2873333	29/4/2012 3:15	1/5/2012 0:13	45.0	Phoenix
af330A	-31.0211830	124.3387000	2/5/2012 2:00	3/5/2012 0:23	22.4	Phoenix
af331A	-31.0189000	124.3907667	26/8/2012 8:15	27/8/2012 8:32	24.3	Phoenix
af332A	-31.0191000	124.4441833	26/8/2012 6:45	28/8/2012 4:38	45.9	Phoenix
af333A	-31.0164170	819.5878711	26/8/2012 4:30	28/8/2012 5:04	48.6	Phoenix
af334A	-31.0146780	124.5496111	25/8/2012 10:00	27/8/2012 5:27	43.5	Metronix
af335A	-31.0114890	124.6273222	25/8/2012 10:00	27/8/2012 4:36	42.6	Metronix
af336A	-31.0068670	124.7057111	21/8/2012 7:00	23/8/2012 0:24	41.4	Metronix
af337A	-31.0033500	124.7797833	31/8/2012 3:45	2/9/2012 2:03	46.3	Phoenix
af338A	-31.0016670	124.8505667	16/8/2012 9:15	19/8/2012 0:43	63.5	Phoenix
af339A	-31.0049000	124.9181833	17/8/2012 9:45	19/8/2012 1:09	39.4	Phoenix
af340A	-31.0073500	125.0192500	24/8/2012 9:55	25/8/2012 23:55	38.0	Phoenix
af341A	-31.0068670	125.1263833	31/8/2012 2:30	2/9/2012 1:17	46.8	Phoenix
af342A	-31.0082830	125.2288000	18/8/2012 9:30	21/8/2012 6:07	68.6	Phoenix
af343A	-31.0087280	125.2821833	18/8/2012 8:15	20/8/2012 23:21	63.1	Phoenix
af344A	-31.0102500	125.3427333	18/8/2012 7:30	21/8/2012 7:09	71.7	Phoenix
af345A	-31.0102000	125.3855500	21/8/2012 9:00	23/8/2012 21:59	61.0	Phoenix
af346A	-31.0111000	125.4437667	24/8/2012 8:00	26/8/2012 0:58	41.0	Phoenix
af347A	-31.0110670	125.4921333	24/8/2012 7:00	26/8/2012 4:08	45.1	Phoenix

Table 1. continued

Site	Latitude	Longitude	Start recording time	End recording time	Duration (hours)	Instrument
af348A	-31.0113890	125.5432111	23/8/2012 10:30	25/8/2012 4:02	41.5	Metronix
af349A	-31.0126000	125.5942833	22/8/2012 4:00	24/8/2012 3:03	47.1	Phoenix
af350A	-31.0130280	125.6474861	25/8/2012 10:00	27/8/2012 2:01	40.0	Metronix
af351A	-31.0124500	125.6997167	22/8/2012 6:30	24/8/2012 3:10	44.7	Phoenix
af352A	-31.0134330	125.8118833	19/8/2012 7:00	22/8/2012 4:23	69.4	Phoenix
af353A	-31.0120330	125.9447000	24/8/2012 3:15	26/8/2012 2:28	47.2	Phoenix
af354A	-31.0062500	126.0888667	24/8/2012 2:30	26/8/2012 1:52	47.4	Phoenix
cbz05A	-30.8651670	123.4975000	3/9/2012 3:00	4/9/2012 23:47	44.8	Phoenix
cbz06A	-30.9058000	123.5194667	3/9/2012 4:45	5/9/2012 0:19	43.6	Phoenix
cbz07A	-30.9454000	123.5423667	3/9/2012 6:30	5/9/2012 0:47	42.3	Phoenix
cbz08A	-31.0786830	123.5919333	28/8/2012 3:00	30/8/2012 8:08	53.1	Phoenix
cbz09A	-31.1246170	123.5981167	28/8/2012 4:45	30/8/2012 7:16	50.5	Phoenix
cbz10A	-31.1706170	123.6160167	29/8/2012 1:45	31/8/2012 5:56	52.2	Phoenix
cbz11A	-31.2081830	123.6400500	1/9/2012 11:00	2/9/2012 23:37	36.6	Phoenix
cbz12A	-31.2509719	123.6575277	29/8/2012 4:45	31/8/2012 6:39	49.9	Phoenix
cbz13A	-31.2842219	123.6939722	29/8/2012 6:10	31/8/2012 21:59	63.8	Phoenix
cbz14A	-31.3189724	123.7259780	30/8/2012 10:00	1/9/2012 0:54	38.9	Metronix
cbz15A	-31.3575371	123.7552033	30/8/2012 10:00	1/9/2012 1:51	39.8	Metronix
cbz16A	-31.3903445	123.7917988	30/8/2012 10:00	1/9/2012 2:28	40.5	Metronix
cbz17A	-31.4267774	123.8211666	31/8/2012 8:30	2/9/2012 1:33	41.1	Phoenix
cbz18A	-31.4560274	123.8628333	31/8/2012 9:30	2/9/2012 2:07	40.6	Phoenix
cbz19A	-31.4976107	123.8887777	2/9/2012 4:30	3/9/2012 9:58	29.5	Phoenix
cbz20A	-31.5864719	123.8835833	2/9/2012 6:15	4/9/2012 0:29	42.2	Phoenix
cbz21A	-31.6120011	124.0128592	10/2/2013 11:45	12/2/2013 4:22	40.6	Metronix
cbz22A	-31.6812405	124.0136764	10/2/2013 11:45	12/2/2013 3:45	40.0	Metronix
cbz23A	-31.7378258	124.0957536	10/2/2013 11:45	12/2/2013 3:01	39.3	Metronix
cbza021A	-31.6496080	123.8792030	1/9/2012 11:00	3/9/2012 2:48	39.8	Metronix
cbza022A	-31.7130630	123.8759630	1/9/2012 11:00	3/9/2012 1:50	38.8	Metronix
cbza023A	-31.8005551	123.8543888	1/9/2012 8:30	3/9/2012 0:46	40.3	Phoenix
fr01A	-31.3863563	123.5866287	11/4/2013 11:00	12/4/2013 23:26	36.4	Phoenix
fr02A	-31.4732718	123.4766110	11/4/2013 10:30	13/4/2013 0:17	37.8	Phoenix
fr03A	-31.5683266	123.3732237	12/4/2013 4:00	13/4/2013 2:15	22.3	Phoenix
fr04A	-31.6607018	123.2681660	12/4/2013 5:00	13/4/2013 3:40	22.7	Phoenix
fr05A	-31.7499383	123.1605386	11/2/2013 11:00	13/2/2013 7:58	45.0	Phoenix
fr06A	-31.9369843	122.9585546	11/2/2013 23:30	14/2/2013 1:38	50.1	Phoenix
fr07A	-32.0862377	122.8266425	15/12/2012 9:00	17/12/2012 4:18	43.3	Phoenix
fr08A	-32.1677962	122.7461617	27/1/2013 5:30	29/1/2013 3:47	46.3	Phoenix
fr09A	-32.2011405	122.7136387	29/1/2013 6:00	30/1/2013 3:29	21.5	Phoenix
fr10A	-32.2250597	122.6673304	31/1/2013 4:00	1/2/2013 22:47	42.8	Phoenix
fr11A	-32.2589153	122.6305162	29/1/2013 3:45	31/1/2013 3:55	48.2	Phoenix
fr12A	-32.2933080	122.5946828	8/2/2013 5:30	9/2/2013 12:31	31.0	Phoenix
fr13A	-32.3298652	122.5649099	28/1/2013 14:45	29/1/2013 22:46	32.0	Metronix
fr14A	-32.3625486	122.5287306	28/1/2013 14:45	29/1/2013 23:34	32.8	Metronix
fr15A	-32.3955416	122.4909768	28/1/2013 14:45	30/1/2013 1:59	35.2	Metronix
fr16A	-32.4294311	122.4569342	27/1/2013 8:30	28/1/2013 18:43	34.2	Phoenix
fr17A	-32.4607297	122.4241451	8/2/2013 4:00	10/2/2013 21:59	66.0	Phoenix
fr18A	-32.4934201	122.3822104	7/2/2013 9:45	8/2/2013 23:26	37.7	Metronix

Table 1. continued

Site	Latitude	Longitude	Start recording time	End recording time	Duration (hours)	Instrument
fr19A	-32.5589232	122.4483225	7/2/2013 9:45	8/2/2013 22:49	37.1	Metronix
fr20A	-32.5945286	122.3537965	30/1/2013 11:45	31/1/2013 16:40	28.9	Metronix
fr21A	-32.6243897	122.3379668	6/2/2013 3:40	8/2/2013 1:41	46.0	Phoenix
fr22A	-32.6697677	122.3250892	2/2/2013 3:30	3/2/2013 7:13	27.7	Phoenix
fr23A	-32.7113663	122.3061171	1/2/2013 9:45	2/2/2013 18:40	32.9	Metronix
fr24A	-32.7535922	122.2841177	1/2/2013 9:45	3/2/2013 0:20	38.6	Metronix
fr25A	-32.8251824	122.2595077	6/2/2013 3:00	7/2/2013 8:39	29.7	Phoenix
fr26A	-32.8669785	122.1593591	3/2/2013 9:45	5/2/2013 0:53	39.1	Metronix
fr27A	-32.9176287	122.0823015	3/2/2013 9:45	5/2/2013 1:38	39.9	Metronix
fr28A	-33.0077930	121.9995489	5/2/2013 9:45	7/2/2013 3:51	42.1	Metronix
fr29A	-33.0588762	121.9264040	5/2/2013 9:45	7/2/2013 3:12	41.4	Metronix
fr30A	-33.1255216	121.7967349	7/2/2013 9:45	9/2/2013 4:51	43.1	Metronix
yfb01	-31.0375361	122.0498608	Not available	Not available	Not available	Not available
yfb02	-31.2369810	122.0478758	Not available	Not available	Not available	Not available
yfb03	-31.2377283	122.2766953	Not available	Not available	Not available	Not available
yfb04	-31.2933400	122.2890011	Not available	Not available	Not available	Not available
yfb05	-31.3697560	122.4364445	Not available	Not available	Not available	Not available
yfb06	-31.4561710	122.5540868	Not available	Not available	Not available	Not available
yfb07	-31.5240860	122.7351992	Not available	Not available	Not available	Not available
yfb08	-31.6439750	122.7907563	Not available	Not available	Not available	Not available
yfb09	-31.7509750	122.8703133	Not available	Not available	Not available	Not available
yfb10	-31.7821430	123.0130876	Not available	Not available	Not available	Not available
yfb11	-31.8612440	123.0873979	Not available	Not available	Not available	Not available
yfb12	-31.9980320	123.2760047	Not available	Not available	Not available	Not available
yfb13	-32.1812280	123.3021006	Not available	Not available	Not available	Not available
yfb14	-32.2135820	123.4919886	Not available	Not available	Not available	Not available
yfb15	-32.2608620	123.6289109	Not available	Not available	Not available	Not available
yfb16	-32.3336680	123.7232439	Not available	Not available	Not available	Not available
yfb17	-32.4332230	123.8603019	Not available	Not available	Not available	Not available
yfb18	-32.5167230	124.0067721	Not available	Not available	Not available	Not available
yfb019A	-32.2211832	123.3777891	19/11/2012 9:00	21/11/2012 14:14	53.2	Metronix
yfb020A	-32.1453544	123.2273413	19/11/2012 9:00	21/11/2012 23:17	62.3	Metronix
yfb021A	-32.1139246	123.1456626	10/12/2012 9:00	11/12/2012 14:14	29.2	Metronix
yfb022A	-32.0778641	123.0896728	18/11/2012 5:00	20/11/2012 23:31	66.5	Phoenix
yfb023A	-32.0573625	123.0122896	18/11/2012 4:00	20/11/2012 22:54	66.9	Phoenix
yfb024A	-32.0373368	122.9210244	17/11/2012 10:00	19/11/2012 23:52	61.9	Phoenix
yfb025A	-32.0262956	122.8681554	17/11/2012 8:00	19/11/2012 23:10	63.2	Phoenix
yfb026A	-31.8306600	123.0352624	21/11/2012 4:00	24/11/2012 21:59	90.0	Phoenix
yfb027A	-31.7761899	122.9336698	21/11/2012 6:00	24/11/2012 9:00	75.0	Phoenix
yfb028A	-31.6955647	122.8354008	11/12/2012 9:00	13/12/2012 3:54	42.9	Phoenix
yfb029A	-31.6095754	122.7598961	11/12/2012 9:00	13/12/2012 2:34	41.6	Phoenix
yfb030A	-31.5639908	122.7460389	20/11/2012 5:00	22/11/2012 2:55	45.9	Phoenix
yfb031A	-31.4805853	122.7175996	20/11/2012 7:00	23/11/2012 21:59	87.0	Phoenix

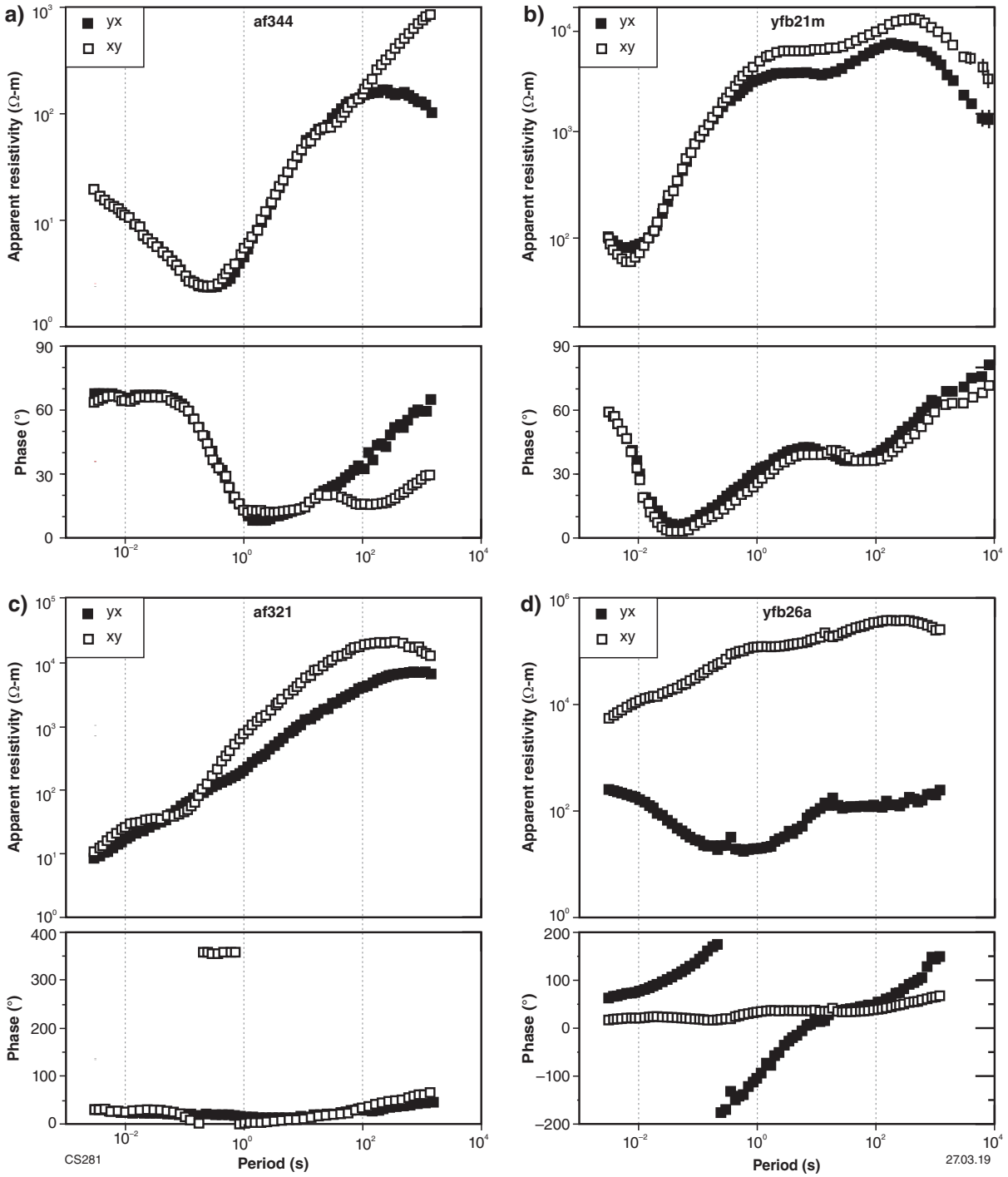

Figure 6. **Examples of MT soundings from four stations. The open squares show data measured in the north–south direction (XY response) and the closed squares show data measured in the east–west direction (the YX response): a) example of excellent broadband MT data quality at site af344; b) example of excellent merged broadband MT and long period MT data quality at site yfb21; c) example of out of phase data high frequencies at site af321; d) example where most of one curve is out of quadrant at site yfb26**

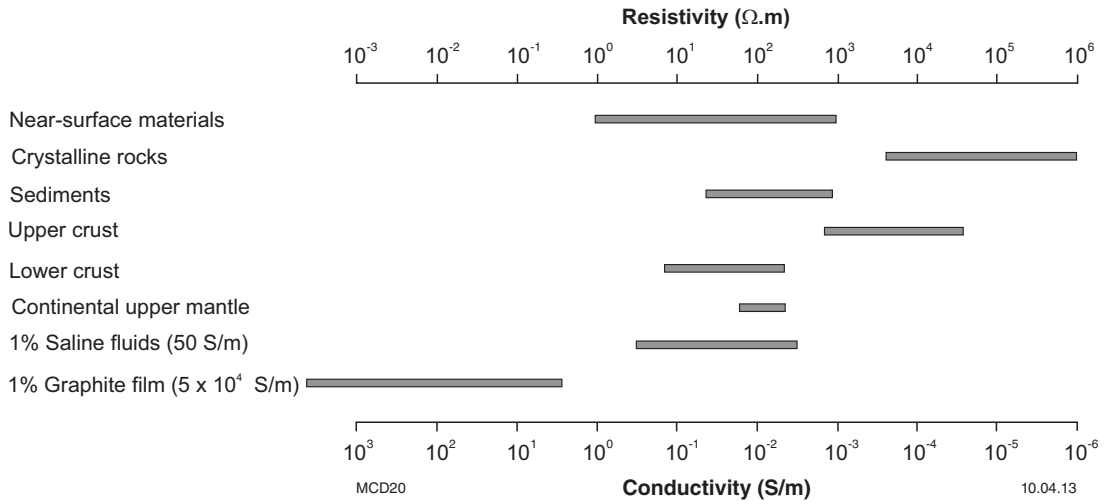

Figure 7. Resistivity ranges of selected geological entities and materials. S/m = siemens per metre. Redrawn from Jones (1999) with additions

A limited number of long-period MT (LPMT) recordings were subsequently made at selected broadband sites by personnel from The University of Western Australia and the Geological Survey of Western Australia (GSWA). Bad weather severely limited the data that could be acquired due to inaccessibility to the survey area. The data were recorded using ANSIR MT equipment. The electric field was measured with an L-shaped electrical array 40–50 m in length with non-polarizing ($Pb/PbCl_2$ solution) electrodes. The magnetic field was measured using a 3-component Bartington magnetometer. The MT data can be downloaded from the DMIRS data portal GeoVIEW.WA (Government Ground Geophysics surveys – MAGIX Registered number 70989; www.dmp.wa.gov.au/geoview).

Data processing

Variations of the electric and magnetic field components of the Earth are recorded as a function of time, i.e. these data comprise time series and are in the 'time domain', which are subsequently converted to the 'frequency domain'. This enables parameters of interest to be calculated as a function of frequency (or period), used to model electrical conductivity variations as a function of depth.

The electric and magnetic time series were checked in the field after each recording to ensure that adequate signal was being recorded, and to check that the equipment had been deployed correctly and functioned properly. Electric field measurements (E) are typically recorded in the north–south direction (Ex) and the east–west direction (Ey). Magnetic field components (H) are recorded with the same notation (Hx and Hy), plus the vertical component (Hz).

The time-series data were processed using robust remote-reference algorithms supplied by Phoenix Limited and based on the coherence-sorted cascade decimation method of Wight and Bostick (1981) and the heuristic robust approach of Jones and Jödicke (1984). Remote reference processing (Gamble et al., 1979) compares recordings from different locations to identify noise in the time series, whereas the coherence-based methods are based on statistical comparison of the various time series. A simultaneously recording station within the traverse was used as the remote reference.

MT response curves

Data in the frequency domain are typically presented as MT response curves, plotting the apparent resistivity and phase as a function of period (Fig. 6). Note that electrical resistivity (ρ) is the reciprocal of electrical conductivity (σ) and that period (s) is the reciprocal of frequency (Hz). The BBMT and, where applicable, LPMT data were merged to provide one set of response curves for each site. Excellent data quality was acquired at the majority of the 163 sites, with little scatter and small error bars over a broad period range of 0.004 – 1000 s (Fig. 6a) and up to 10 000 s where long period data were recorded (Fig. 6b). In some cases, primarily along the AF3 profile, the data recorded in one direction were out of phase (dropping below 0°) at periods between 0.1 and 10 s, an indication of current channelling or distortion at relatively shallow depths (e.g. Fig. 6c,d). Appendix 1 shows the response curves for each site acquired. Where there is a high degree of scatter with large error bars or where the phases are out-of-quadrant (either below 0° or above 90°), the data points have been removed prior to initiating data modelling.

Static corrections

MT data are prone to 'static shifts' due to heterogeneous electrical properties in the near surface at a scale smaller than the resolving capability of the MT data. The result is an upwards or downwards frequency-independent shift of the apparent resistivity curve in the TE-mode, TM-mode, or both. The amount of shift is called the static shift factor, or factors. Failure to account for this will lead to incorrect estimation of resistivities and the depths at which they occur during data modelling.

As static shift effects typically result in lowering an apparent resistivity curve, where the apparent resistivity curve of one mode was much higher than another, the lower curve was raised to match that of the other curve at

the highest frequency. This helps to reduce the effect of anisotropic shift, but does not account for the static shift cases where both curves are affected.

The time-domain electromagnetic (TEM) soundings collected at each MT site are not affected by these small-scale heterogeneities. To correct for static shift in the MT data, the TEM data are modelled to resolve the near-surface electrical resistivity assuming a 1D Earth. Forward MT data are then calculated from the resulting model. A comparison can be made between the real MT data and the forward calculated response curves from the TEM data. The measured MT response curves are then shifted to match those derived from the TEM data. An example of TEM curves, 1D models and curve matching from site af319 is shown in Figure 8.

In theory, this is a simple procedure, but in electrically resistive areas it is often quite difficult to collect high-quality data. Of the 110 TEM sites recorded, approximately 39% of the TEM collected was not usable due to the high electrical resistivity of the near surface and the resulting low-quality data that were collected. Where adequate TEM data were collected it was possible to produce forward MT from the TEM data that overlapped sufficiently in terms of period to allow correction of static shift.

Estimates of depth penetration

The depth of penetration, or 'skin depth', is defined by the solution to the wave equation for a plane wave propagating through a homogeneous half-space and is the point at which the amplitude of the fields reduces to a factor of 1/e of that at the surface (Cagniard, 1953). Over a large region, where the 2D conductivity structure is variable, electromagnetic fields at any particular period often have vastly different penetration depths from one site to the next. Additionally, it is possible for 2D structures to exist where the depth of penetration is different for the two modes of propagation (TE and TM; Jones, 2006). Penetration depths at 1000 s beneath each site have been estimated using Schmucker's C-function conversion (Schmucker, 1970) and the Niblett–Bostick depth approximation (Niblett and Sayn-Wittgenstein, 1960; Bostick, 1977; Fig. 9). At most sites these estimates infer sufficient penetration (>250 km) in at least one direction to model lithospheric mantle features. The easternmost sites along Profile AF3 and the southwestern sites along Profile FR show significant differences in the estimated penetration depths in the xy (east–west) and yx (north–south) directions, suggestive of strong contrasts and 2D and/or 3D variations in the conductivity structure.

Dimensionality and strike analysis methodology

In a 2D modelling scenario, the direction of geoelectric strike is assumed to be consistent, i.e. there must not be any localized or off-profile geoelectrical property variations, and the strike direction must be known. Frequency dependent pseudosections, induction vectors and phase tensors have been analysed to determine the dimensionality and geoelectric strike direction of the data. Sections of the data that are 1D, independent of strike, are identified, as well as sections that are influenced by three-dimensionality and cannot be represented with a 2D model. Ideally, where structure is truly 2D, a model is generated along a profile at one strike angle for all periods; however, where the subsurface structure is complex and this angle varies along the profile or with depth, the data may need to be subdivided into sections and modelled separately at different strike angles. As the primary focus of this work is to study the deeper structure, where necessary, models are generated at a strike angle that corresponds to longer periods. The data have been divided into four profiles (AF3, YFB, CBZ and FR) for strike analysis and 2D modelling (Fig. 1) and the preferred geoelectric strike direction has been determined for each of the profiles.

Pseudosections of phase and apparent resistivity responses for each of the sites along the four profiles were generated for both the TE- and TM-modes for all data points not deemed to be overly noisy and with out-of-quadrant phases removed. As apparent resistivities may be affected by static shift, the phase pseudosections are typically observed to determine areas that are 1D. The Earth can be regarded as 1D for cases where 2D models are independent of the geoelectric strike angle, at periods where the phases in the TE- and TM-modes are similar, and where induction vectors are small.

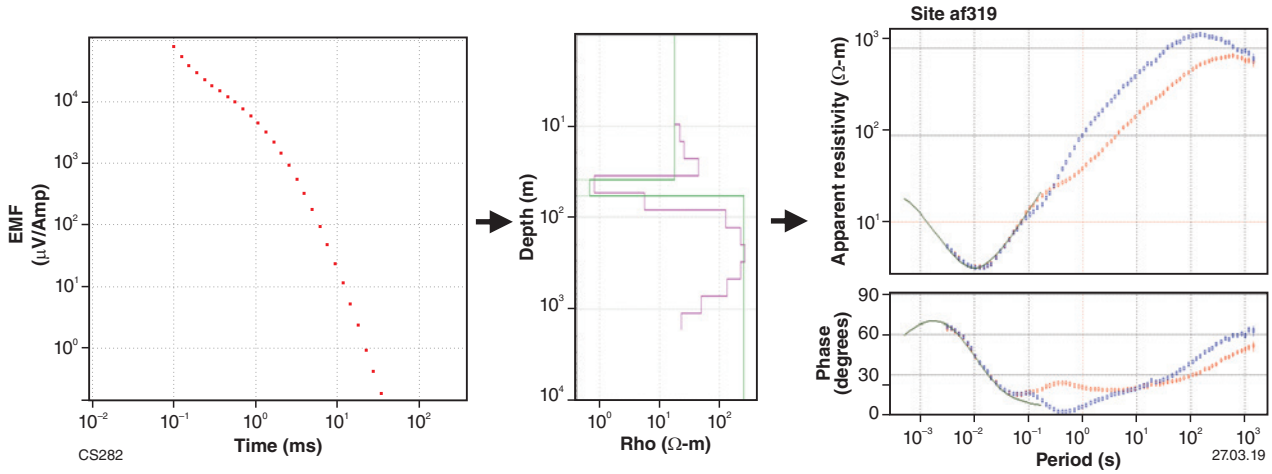

Figure 8. Examples of time-domain electromagnetic soundings, 1D models and curve matching from site af319. EMF, electromotive force

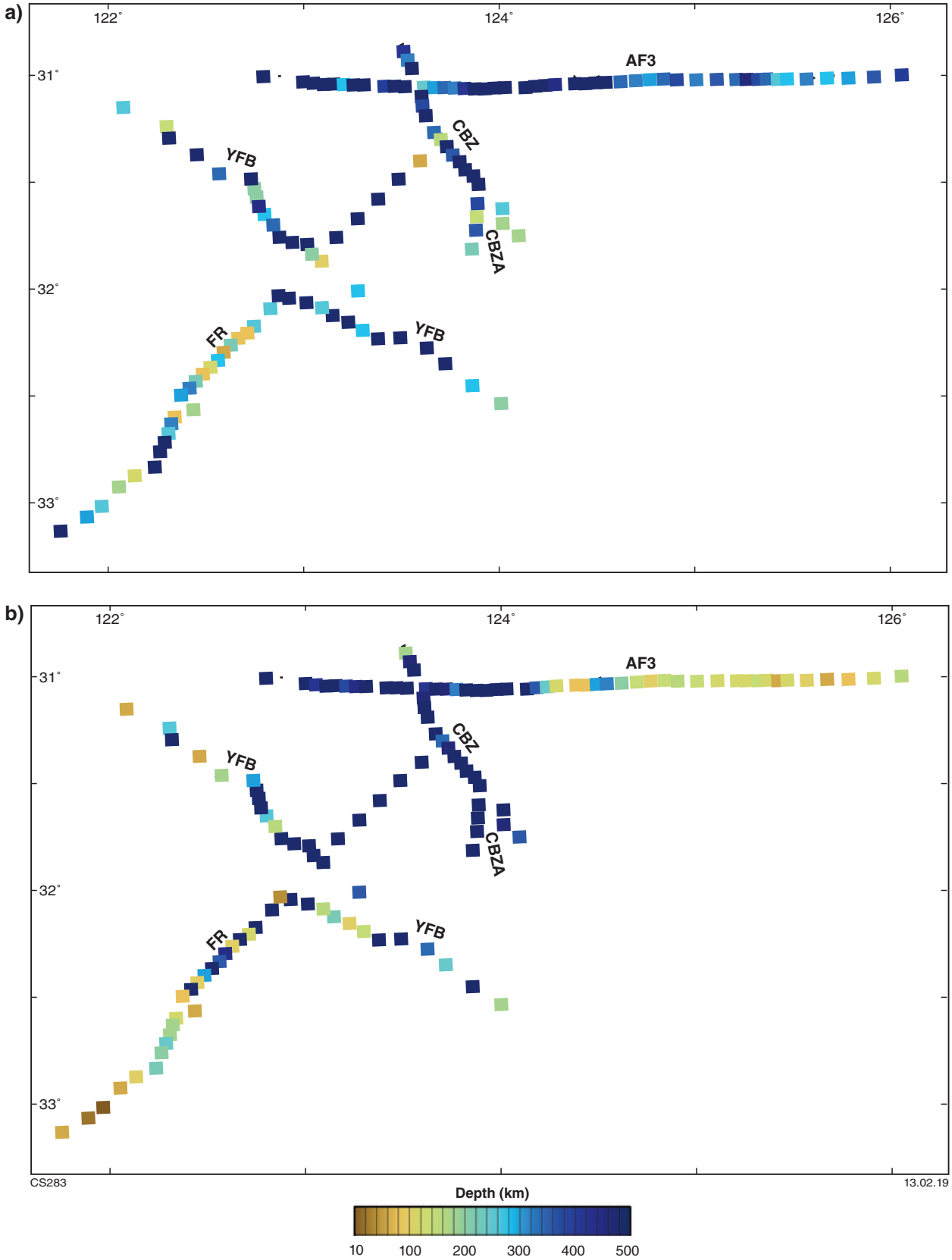

Figure 9. **Estimates for maximum penetration depths at 1000 s at each site: a) measured north–south directions; b) measured east–west directions**

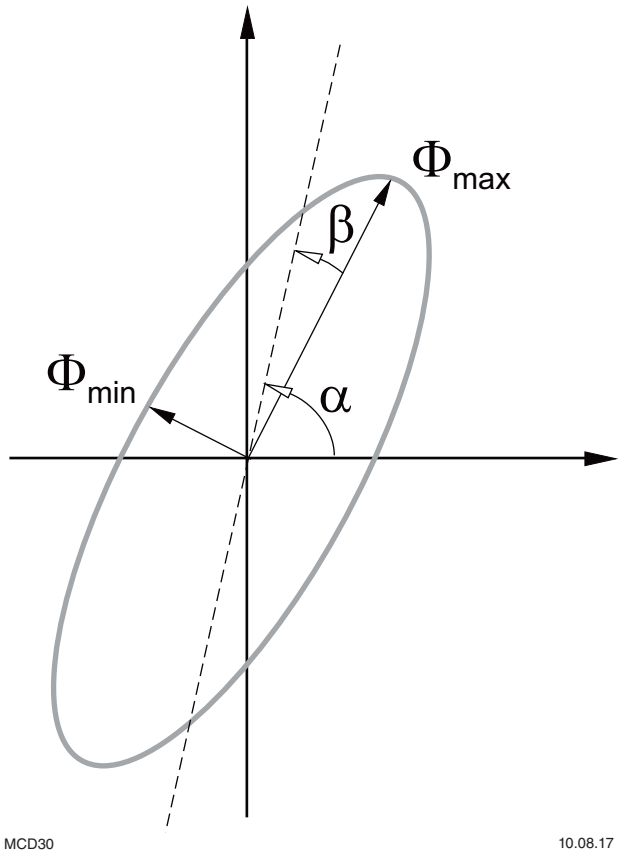

Figure 10. Graphical representation of the MT phase tensor illustrating parameters used to define the ellipse. From Caldwell et al. (2004)

Where lateral conductivity gradients exist along a profile within the Earth, vertical magnetic fields are created (in a 1D Earth, vertical magnetic fields are minimal). Induction arrows are the vector representations of the complex ratios of the vertical to horizontal magnetic fields. Both real and imaginary induction arrows can be produced because the ratio is complex. Here we have used the Parkinson convention, where real arrows point towards regions of low resistivity, or away from regions of high resistivity. The length of an arrow indicates the magnitude of the difference in resistivity. Where the electrical structure is 2D the real arrows will be parallel and oriented perpendicular to the geoelectric strike. Induction vectors have been plotted both in pseudosection format for each site at each period along each of the profiles, and in map view for all sites at specific periods (see strike analysis sections for each profile below).

The dimensionality of the MT data was further assessed using the phase-tensor method of Caldwell et al. (2004). Unlike many other dimensionality estimation methods, this technique analyses only the phase variations because these are unaffected by galvanic distortion associated with near-surface changes in electrical conductivity, and the method does not rely upon assumptions that the regional electrical structure is 1D or 2D. Three parameters are used to characterize the phase tensor: the maximum (Φmax) and minimum (Φmin) phase values, and the skew angle (β). The angle α is a measure of the tensor's orientation relative to the coordinate system and the ellipticity is a measure of the ratio of the maximum and minimum phase values. The phase tensor is commonly represented as an ellipse (Fig. 10), with the long and short axes of the ellipse representing the maximum and minimum phase values, respectively (the TE- and TM-modes), and the orientation (α–β) of the major axis representing the direction of maximum current flow, or geoelectric strike angle. At periods where the phase difference between the TE- and TM-modes is minimal (<10°) the data are deemed 1D, i.e. independent of geoelectric strike angle and the phase ellipse is a pseudocircle. With the influence of two-dimensionality, the ellipticity increases. Phase-tensor ellipses have been plotted in pseudosections for each station along each profile with red colours representing phase minima above 45°, generally indicating a change from resistive to more conductive rocks with depth, and blue colours below 45°, indicating a change from conductive to resistive units with depth (see strike analysis sections for each profile below).

In addition to phase-tensor analysis, Groom–Bailey decomposition analysis (Groom and Bailey, 1989) was applied to each site. Groom–Bailey decompositions provide a method to describe and separate the local parameters caused by galvanic distortions in the regional observed impedance tensor. This distortion modelling assumes that the regional structure is 2D but that the electric field data are galvanically distorted by local, near-surface features. The resulting preferred strike azimuth and the average phase difference between the conductive and resistive directions for one-decade period bandwidth are shown in Figure 11 for periods between 0.001 – 1000 s. Note that there is a 90° ambiguity inherent in phase-tensor analysis. Induction vectors can be helpful in resolving this ambiguity; alternatively, geological and geophysical information can be used to properly assign the TE- and TM-modes as current flow (the TE-mode) typically runs parallel to geological features.

A 3D subsurface results in a skewed ellipse with the main axis deflected by an angle β from the symmetry axis (dashed line in Fig. 10). The skews for each site along each profile are plotted with phase-tensor ellipses in pseudosection with the colour representing the skew value (β). Darker blue colours indicate a skew less than –5 and darker red colours indicate greater than +5. Empirically, $-5 < \beta < +5°$ means the data should be predominantly 2D. A skew outside this range is likely affected by 3D characteristics.

Dimensionality and strike analysis results

Analysis of the AF3 profile

Pseudosections of the apparent resistivities and phases have been plotted along the AF3 profile for each period of acquisition (Fig. 12). In general, the apparent resistivity sections display some vertical variations or streaks in the western half of the profile that might be suggestive of static shift effects; however, many of these variations are also observed in the phases. As phase lags are not affected by static shift, this is an indication of localized subsurface geological or structural variations. Both the apparent resistivity and phase pseudosections along the eastern half of the profile reveal a layered subsurface with minimal along-profile variation in both the TE- and TM-modes, an

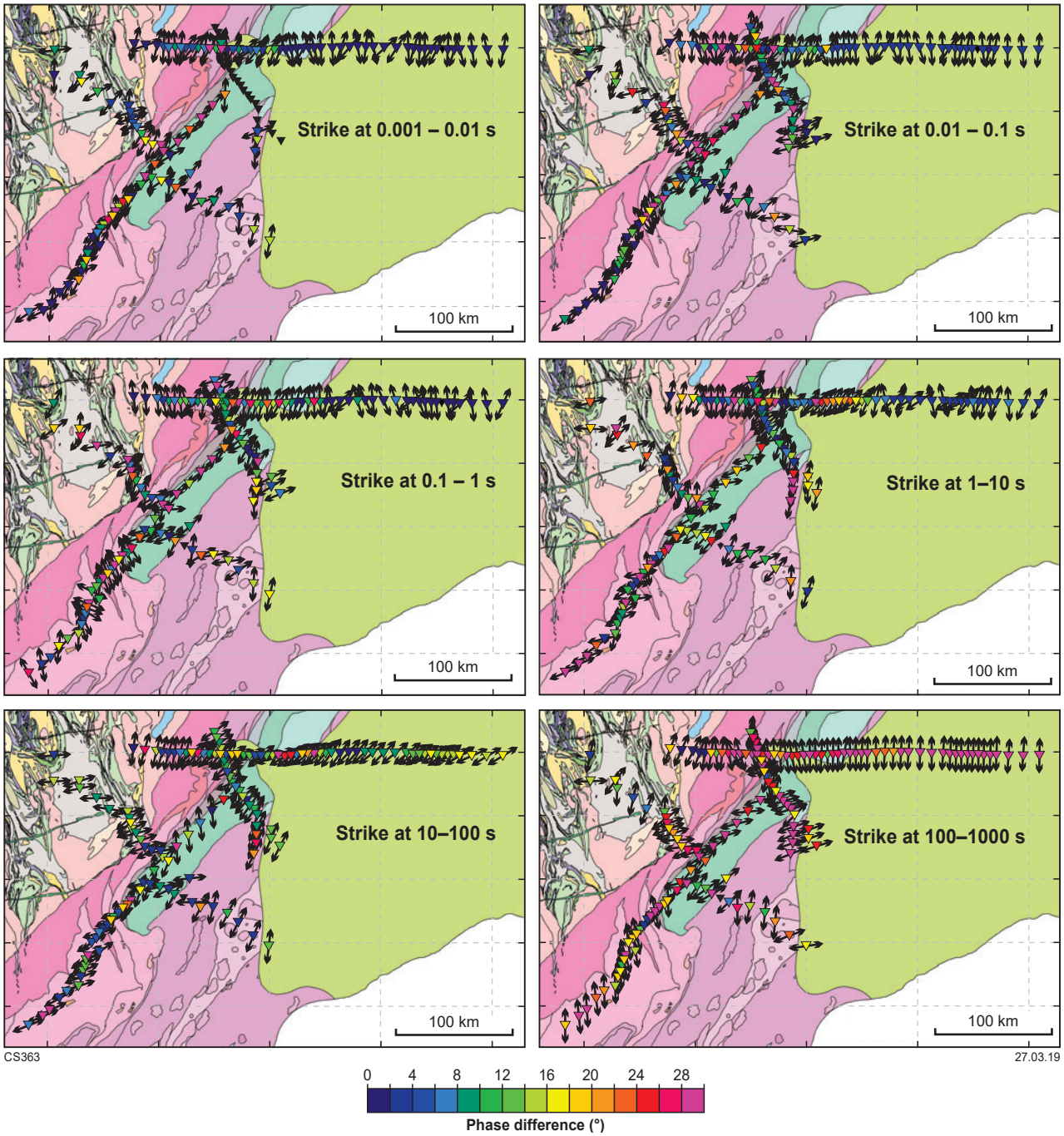

Figure 11. **Maps showing the preferred geoelectric strike direction at each site for six decade-period bands between 0.001 – 1000 s. The colour scale illustrates the maximum difference between the TM- and TE-mode phases**

indication that the data are largely 1D and independent of the strike angle.

The real induction vectors along the AF3 profile are shown in Figure 13. In general, induction vectors are small to periods of approximately 0.1 s. At periods between 0.1 and 1 s, the western half of the profile shows large induction vectors with large directional variations indicative of a complex 2D or 3D conductivity structure. The eastern half of the profile shows short induction vectors to periods of approximately 1 s. At periods between 1 and 10 s, moderate vector lengths along the whole profile are observed pointing approximately northward, an indication of the presence of a large conductive body that is off-profile to the north (Figs 13, 14). Between 10 and 100 s, the vectors rotate to point in an easterly direction. At periods greater than approximately 1000 s, induction vectors along the whole AF3 profile, and every other MT site in the survey, uniformly point towards the southeast, likely an influence of coastal seawater (Fig. 14).

The phase-tensor ellipses along the AF3 profile show that at periods between 0.01 and 1 s, the ellipse orientations along the western half of the profile change more rapidly and are most elongate, indicating a heterogeneous electrical structure (Fig. 15). This suggests that the varying ellipse orientations and induction vectors may be a result of structure within the upper crust. Minimum phases are below 45° to approximately 100 s and are likely to represent a resistive crust. The eastern half of the profile shows open ellipses to approximately 1 s, with north–south oriented, elongate ellipses observed at periods greater than 100 s likely a result of structure within the upper mantle. Here, phase minima are greater than 45° to periods of 0.1 s, and up to 1 s in the far east, indicating the presence of either a thick or a very conductive layer near the surface, possibly the effects of sedimentary rocks within the Eucla Basin or underlying Bight Basin (Fig. 1).

Plots of skew along the AF3 profile are shown in Figure 16. The central part of the profile shows evidence of strong 3D effects with skew values greater than 5 (or less than –5) at periods between 0.1 and 10 s, particularly at sites between af316 and af336, and at periods greater than 50 s at sites between af314 and af327. The westernmost sites show high skews at periods below 1 s, whereas the data east of site af337 are relatively unaffected by 3D distortion.

Strike direction calculated from the phase-tensor ellipses along the AF3 profile at six decade-period bands are plotted on rose diagrams, showing the modal value for each band (Fig. 17). Recall that there is 90° ambiguity inherent in phase-tensor analysis. In addition to observing changes with period (depth), the profile has been divided into four sections to identify changes in the geoelectric strike along the profile. Section A shows a high degree of scatter at periods shorter than 10 s, and shows a preference of 10–15° at longer periods. Section B has a wide range of strikes at periods below 1 s, but shows a preference of 20° (110°) at periods of 1–10 s, and 55° (145°) at periods of 10–100 s. Section C shows a consistent strike angle of 15–25° (105–115°) at periods below 1 s. Section D shows consistent strike angles of –10° to 0° at periods below 1 s, and 45–50° (135–140°) at periods between 10 and 100 s. All sites and all sections consistently show a strike direction of –5 to 10° at periods greater than 100 s. These results are consistent with the strike azimuths plotted from Groom–Bailey decompositions (Fig. 11). A strike angle of approximately 20° appears to satisfy most of the data at periods below 10 s for sections A, B and C, a strike of 50–55° for periods 1–100 s for sections C and D, and –5° to 10° for periods greater than 100 s.

Groom–Bailey decomposed data were generated at strike angles of 20°, 50° and 5°. Root mean square (RMS) values for each site at each period have been plotted to view which strike direction is appropriate for the different sections of the profile (Fig. 18). This plot shows that no single strike direction is able to fit all of the data. The black ovals mark sections of the profile where specific strike directions can be applied, i.e. RMS is low. At the eastern end of the profile, the 5° strike is preferable across the entire bandwidth. At periods below 100 s the data are insensitive to the strike direction, indicative of 1D structure, as suggested by the pseudosections in Figure 12. The western end of the profile is more complex, with no strike direction suitable for all periods. Strike directions of 5° and 20° produce much the same response, minimizing RMS between 0.1 and 100 s.

Analysis of the YFB profile

Pseudosections of phase and apparent resistivity along the YFB profile are shown in Figure 19. The apparent resistivities show significant vertical streaking beneath the central portion of the profile, an indication that static shift effects may still be present in the data. TEM data were only acquired at 13 of the 31 YFB sites, and only three of these were suitable to adjust for static shifts. The phases, however, also show significant variations, particularly in the central portion of the profile. The lateral changes in phase and differences between the TE- and TM-modes suggest that the data along most of the profile are 2D or 3D. This is consistent with phase differences >10% observed at most sites and at most frequencies (Fig. 11).

Induction vectors along the YFB profile are small below approximately 0.04 s, but are relatively large along the whole length of the profile at longer periods (Fig. 20). In general, at periods between 0.1 and 10 s, induction vectors roughly point to the northwest or southeast indicating that the geoelectric strike direction is northeasterly trending. At periods greater than 100 s, the induction vectors uniformly point towards the southeast, indicating the presence of an off-profile conductor, possibly an effect of the ocean to the southeast (Fig. 14).

Pseudosections of the phase ellipses for each site at each period along the YFB profile are shown in Figure 21. The phase ellipses are most elongate at periods below 1 s. The central part of the profile shows a general northwesterly to southeasterly trend in the phase ellipses; however, there is a 90º ambiguity and the strikes more likely run parallel to geological strike (northeasterly to southwesterly). At greater periods the ellipses are more open, but continue to trend northwest. Minimum phases are generally below 45º to approximately 100 s, suggestive of a resistive crust.

Plots of skew values along the YFB profile show that the data along the southeastern half of the profile are relatively unaffected by 3D distortions at periods below approximately 600 s (Fig. 22). The northwestern half of the profile shows some high skew values (less than –5 or greater than +5), generally between 1 and 10 s.

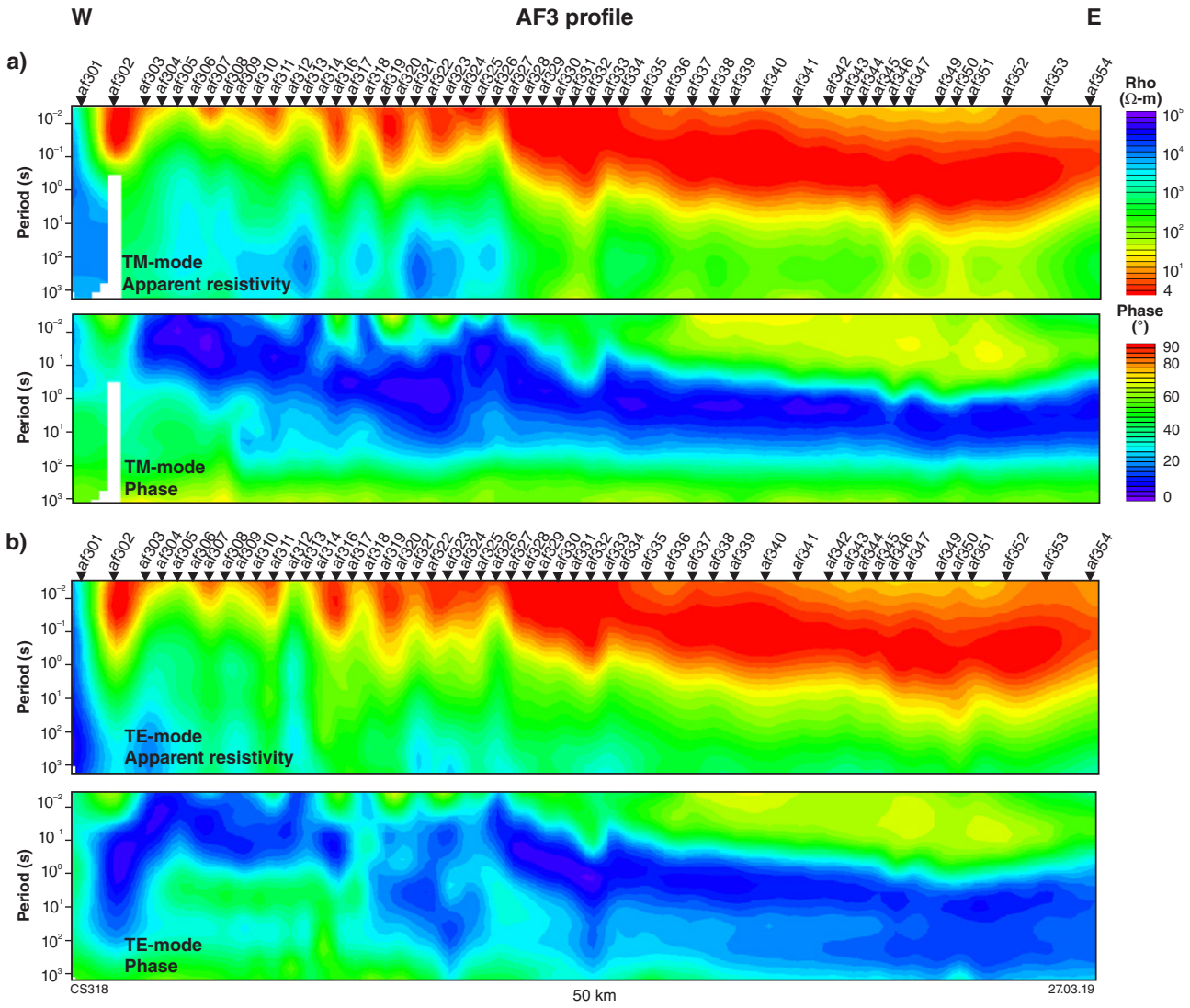

Figure 12. **Pseudosections of apparent resistivity and phase along the AF3 profile comprising data considered to have an acceptable signal-to-noise level: a) data in the TM-mode; b) data in the TE-mode**

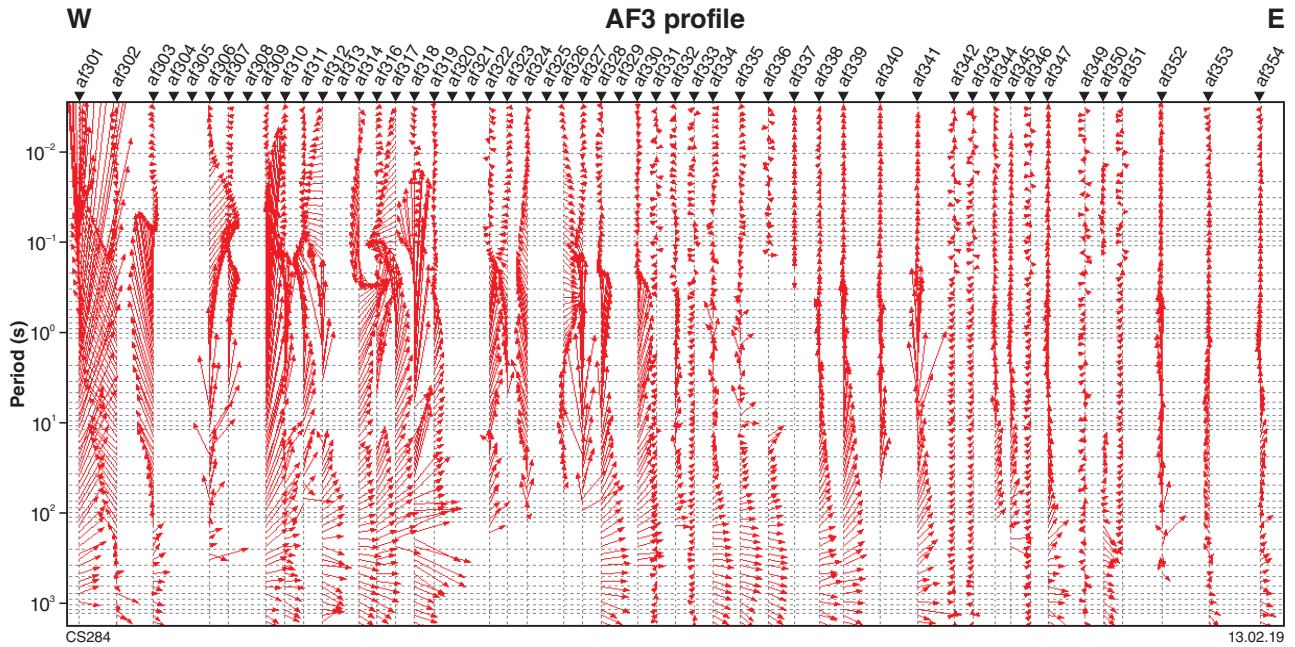

Figure 13. **Pseudosection display of induction arrows at each period along the AF3 profile**

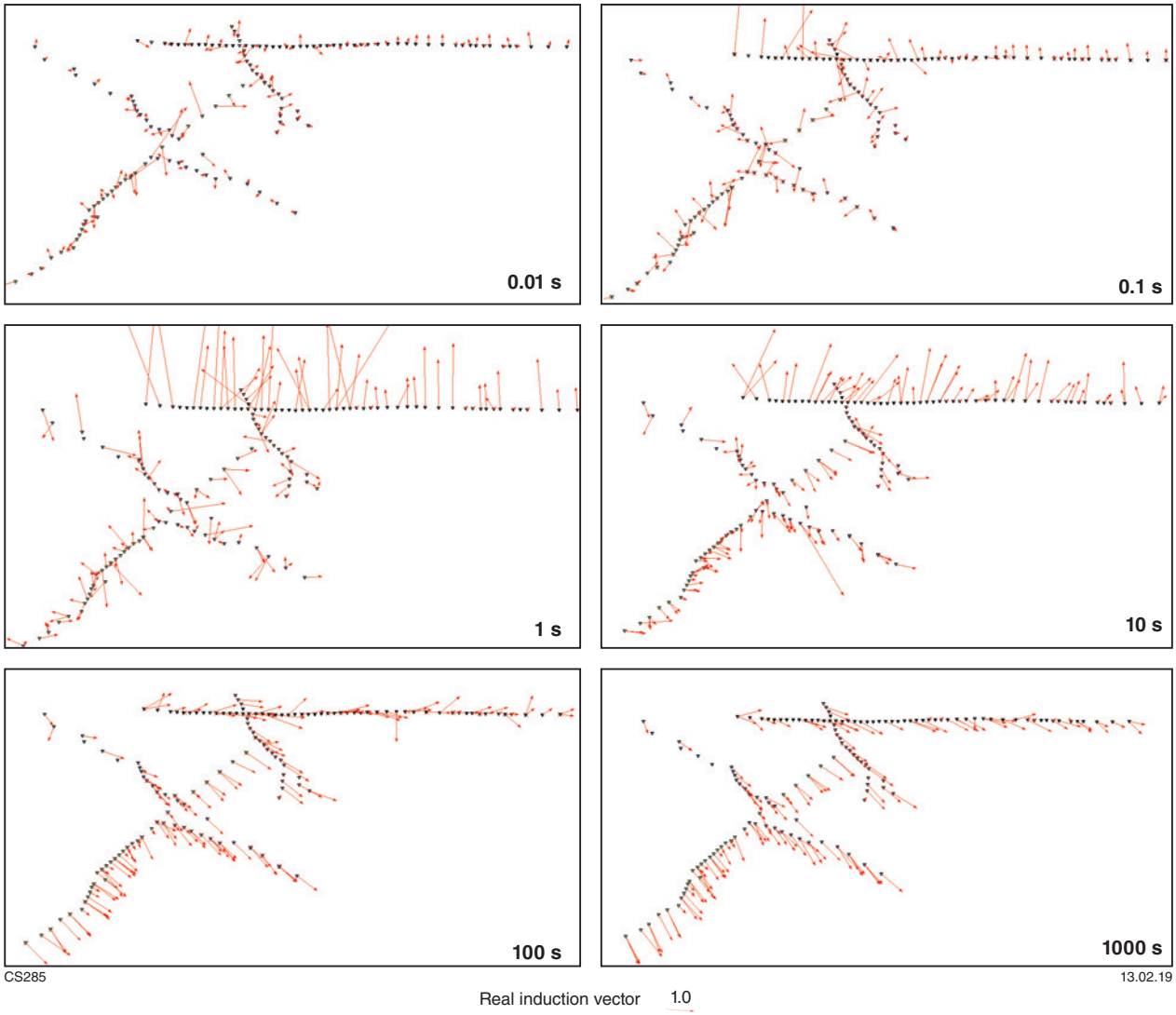

Figure 14. Map view of induction arrows at six different periods for all sites acquired along the AF3 profile

Strike directions calculated from phase-tensor analysis along the YFB profile for data in six decade-period bands along the whole profile and for four separate sections of the line are plotted in rose diagrams (Fig. 23). Where there is little scatter (an indication of a strong preference for a particular angle), a strike angle between 40° and 55° (130° and 145°) is apparent at periods between 0.01 and 0.1 s for sections B and D, and up to 10 s for section C. At all periods for section A, periods greater than 10 s for sections B and C, and 100 s for section D, there is a consistent strike angle of 165–175° (75–85°).

Groom–Bailey decomposed data were generated at strike angles of 40°, 55° and 70°. RMS values for each site at each period have been plotted to view which strike direction is appropriate for the different sections of the profile (Fig. 24). Again, no single strike direction is able to fit all of the data, and preferred strikes vary in a complex fashion depending on period and location.

Analysis of the CBZ profile

Phase pseudosections along the CBZ profile are shown in Figure 25. Both the apparent resistivity and phase data show strong lateral variation and significant differences between the TE- and TM-modes, an indication of 2D or 3D structure over most of the period range, particularly the central section of the profile. There is minimal vertical streaking in the apparent resistivities suggesting that static shift effects are minor.

In general, induction vectors are large at periods greater than 0.05 s (Fig. 26). At periods between 0.1 and 10 s, the vectors generally point in a northwesterly or southeasterly direction, suggesting a northeasterly trending geoelectric strike direction. As previously described, at periods greater than 100 s, the induction vectors uniformly point southeast towards the coast (Fig. 14).

Phase ellipses along the CBZ profile are elongate with varying trends at periods up to 1 s for the northwestern half of the profile (Fig. 27). The southeasternmost sites show elongate phase ellipses with a distinct east–west trend at

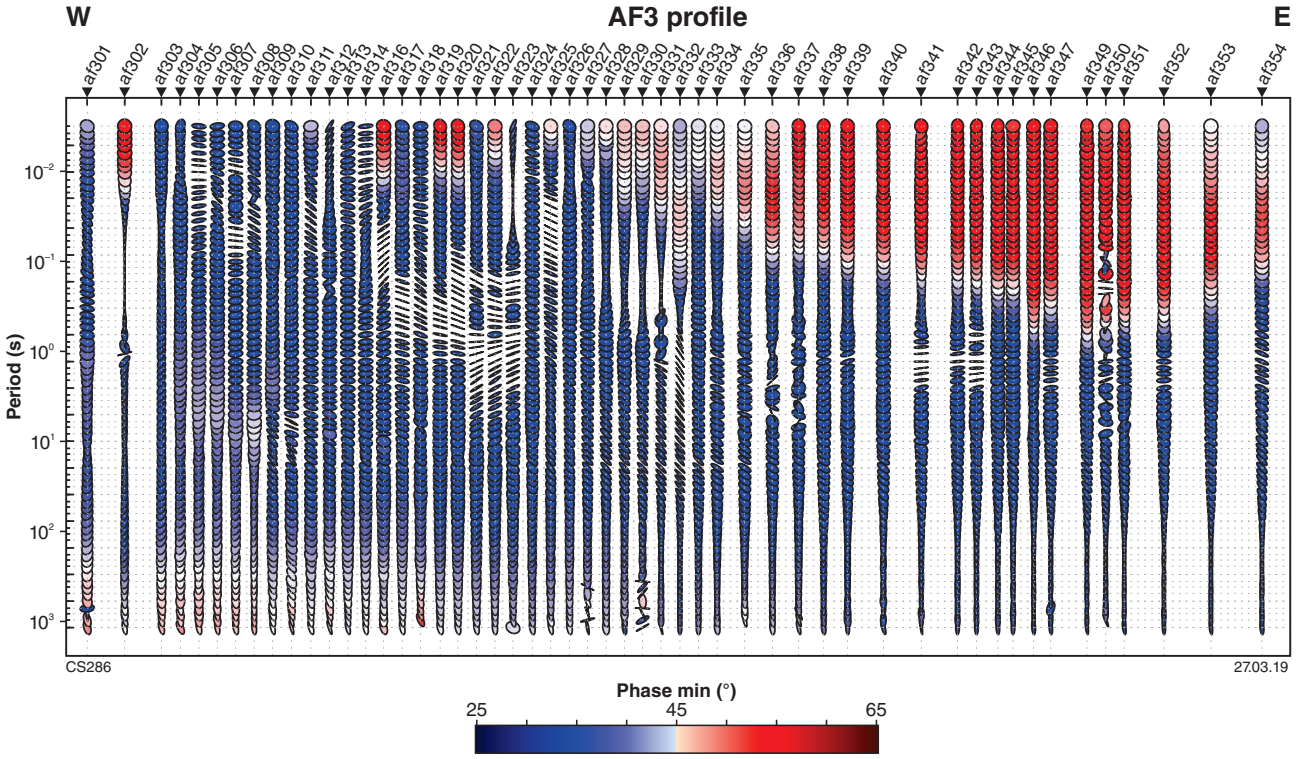

Figure 15. **Pseudosection display of MT phase ellipses and phase minima along the AF3 profile. The blue colours represent phase minima below 45°, generally indicating a change from conductive to resistive rocks with depth, and the red colours represent phase minima above 45°, generally indicating a change from resistive to more conductive rocks with depth**

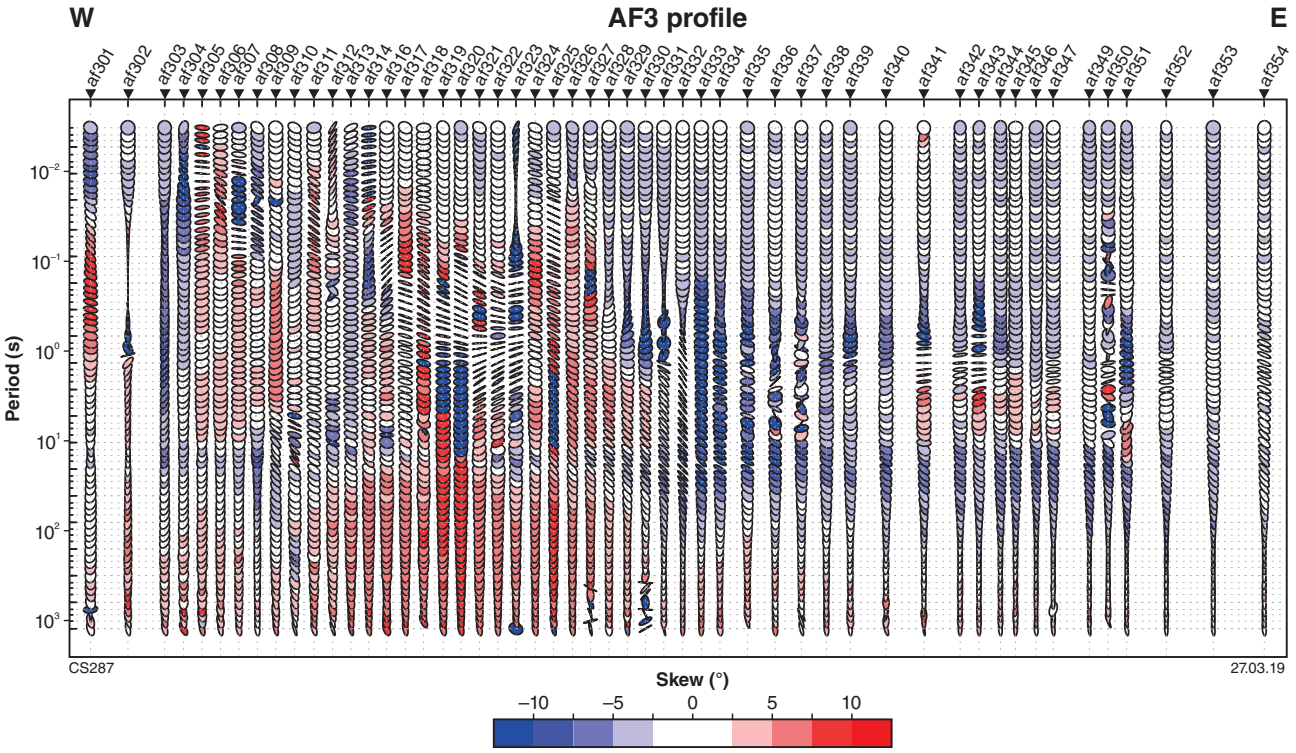

Figure 16. **Pseudosection display of MT phase ellipses and skew (β) along the AF3 profile. The darker blue colours represents skew values below −5° and the darker red colours represents skew values above +5°**

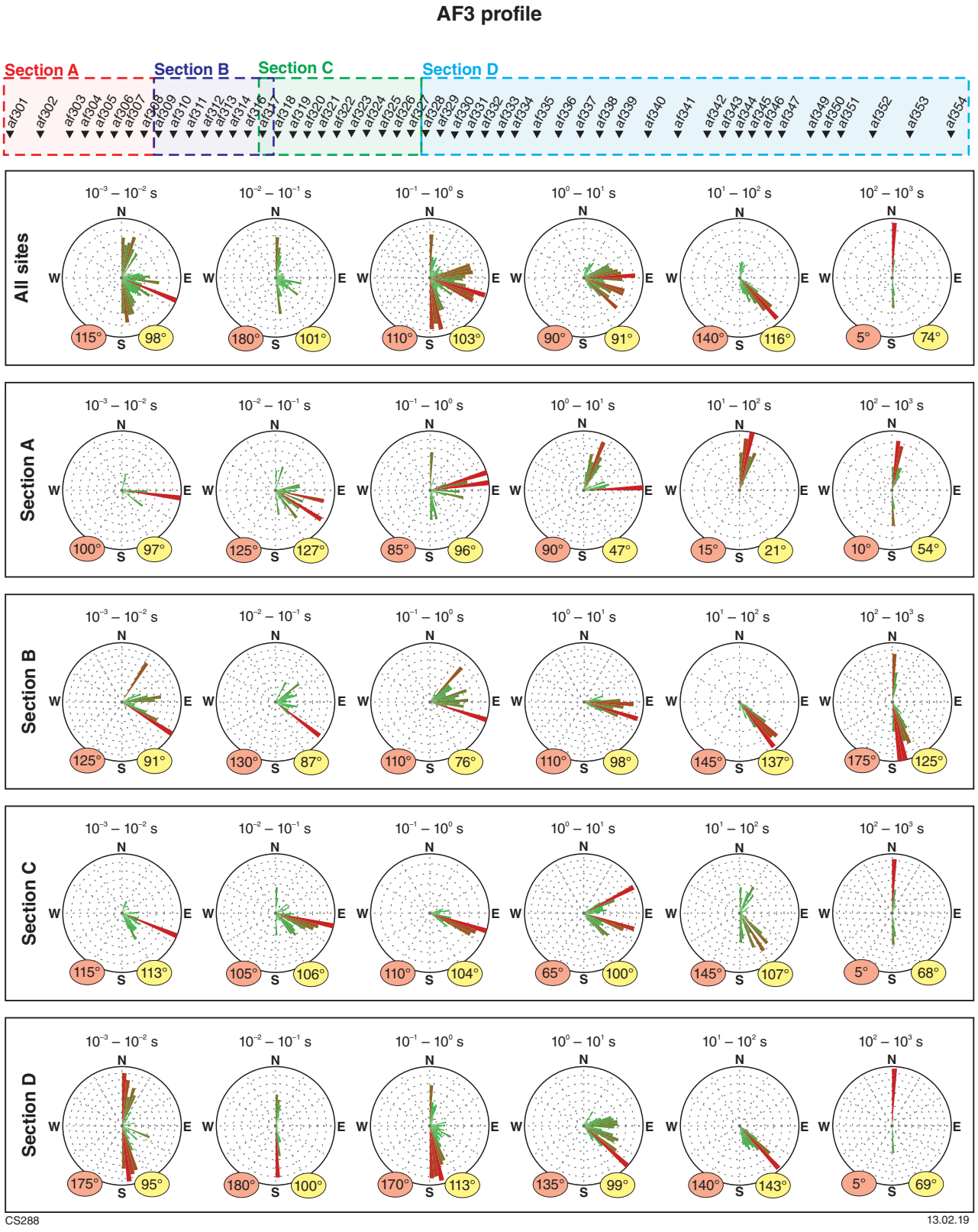

Figure 17. **Rose diagrams of phase-tensor ellipses and z-strike orientations at six decade-period bands for data along the entire AF3 profile, divided into four sections. The numbers in the red circles show the mode and the yellow circles show the median values**

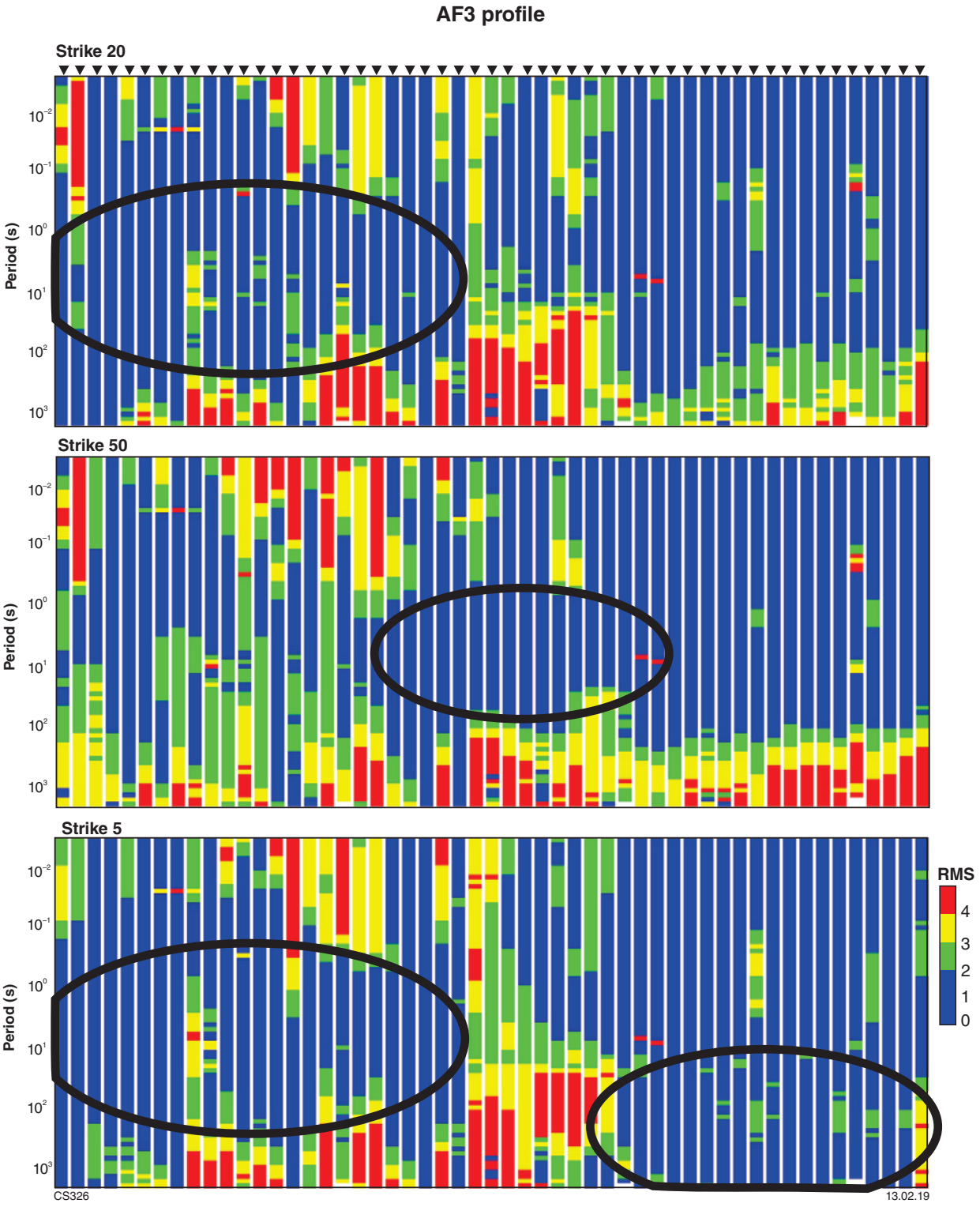

Figure 18. **RMS values calculated from Groom–Bailey decomposition at each site and each period along profile AF3 for three different strike directions: 20°, 50° and 5°. The black oval marks areas of the data that show a strong preference for a particular strike direction**

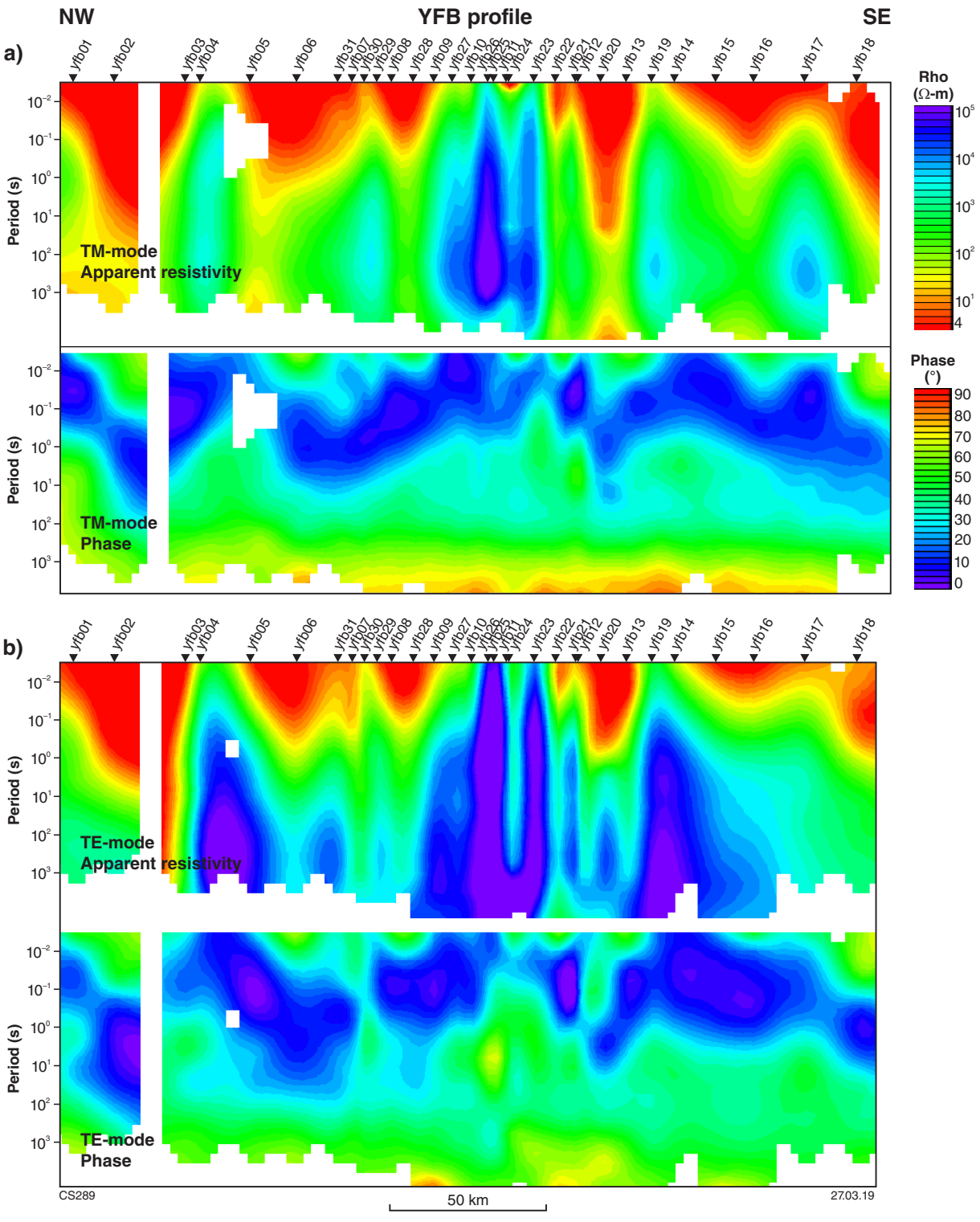

Figure 19. **Pseudosections of apparent resistivity and phase along the YFB profile comprising data considered to have an acceptable signal-to-noise level: a) data in the TM-mode; b) data in the TE-mode**

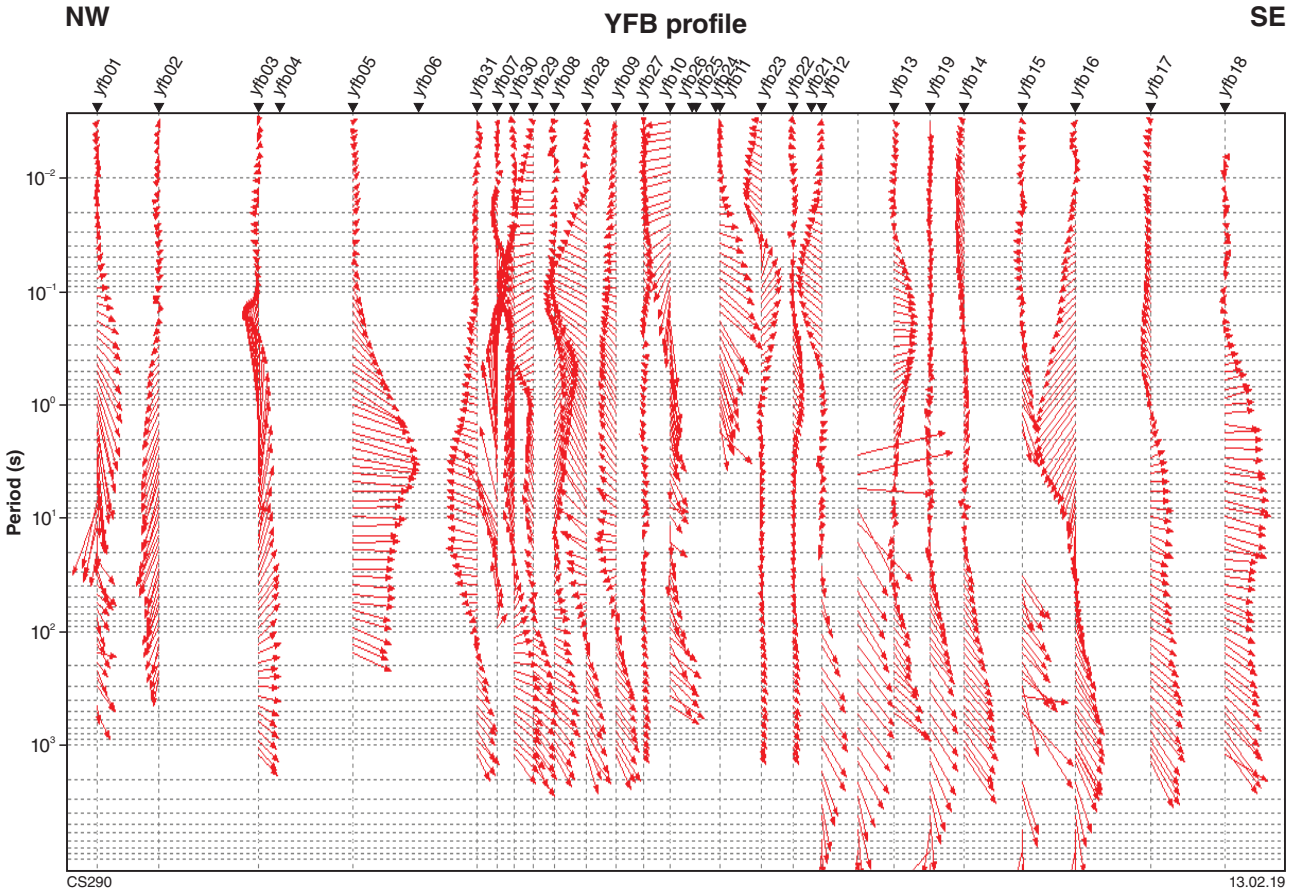

Figure 20. Pseudosection display of induction arrows at each period along the YFB profile

periods between 0.1 and 10 s. Skew values along the CBZ profile are shown in Figure 28. Most of the data between sites cbz10 and cbz19 are affected by 3D distortion at periods greater than 0.5 s. Along the whole profile, many of the sites have high skew values at periods greater than about 100 s.

Rose diagrams of the strike angles derived from phase-tensor analysis have been generated along the CBZ profile for six decade-period bands, for the whole profile, and for two separate sections of the profile (Fig. 29). Section A shows a lot of scatter in the strike directions at periods up to 100 s, where there is a preferred strike of 10º (100º). Azimuths plotted from Groom–Bailey decompositions show more consistent values of 35–55º at periods of 0.01 – 10 s (Fig. 11). Rose plots for section B show values ranging from 95–110º (5–20º) at periods up to 100 s, after which the mode is 175º (85º). These are consistent with Groom–Bailey decomposition results, with the exception of period bands 10–100 s showing strikes of 26–36º and 100–1000 s showing 69–74º.

Groom–Bailey decomposed data were generated at strike angles of 10°, 35° and 70°. RMS values for each site at each period have been plotted to view which strike direction is appropriate for the different sections of the profile (Fig. 30). The black ovals mark sections of the profile where specific strike directions can be applied, i.e. RMS is low. The strike of 10° produces the lowest RMS in the period range 0.1 – 100 s and extending to lower periods at the southern end of the profile.

Analysis of the FR profile

Pseudosections of the apparent resistivity and phases along the FR profile are shown in Figure 31. The apparent resistivity pseudosections show some vertical streaking in the central section of the profile, possibly due to static shift effects. The phase pseudosections show some along-profile lateral variations. This suggests that although the profile runs parallel to the regional geological trend, at least to the northeast of station fr11, some structures perpendicular to the profile could have been imaged.

With the exception of a few sites, induction vectors are long at most periods (Fig. 32). At periods up to approximately 10 s, induction vector directions are highly variable and are not particularly helpful in resolving the 90º strike ambiguity (Fig. 14). At periods greater than approximately 60 s, induction vectors uniformly point towards the southeast, i.e. towards the coast. Phase ellipses along the FR profile are shown in Figure 33. The four southwesternmost sites show open ellipses to periods of 0.2 s. At longer periods, the phase ellipses are elongate with a northwesterly to southeasterly trend. The central section of the profile shows a large degree of variation in the shape and orientation of the phase ellipses at periods

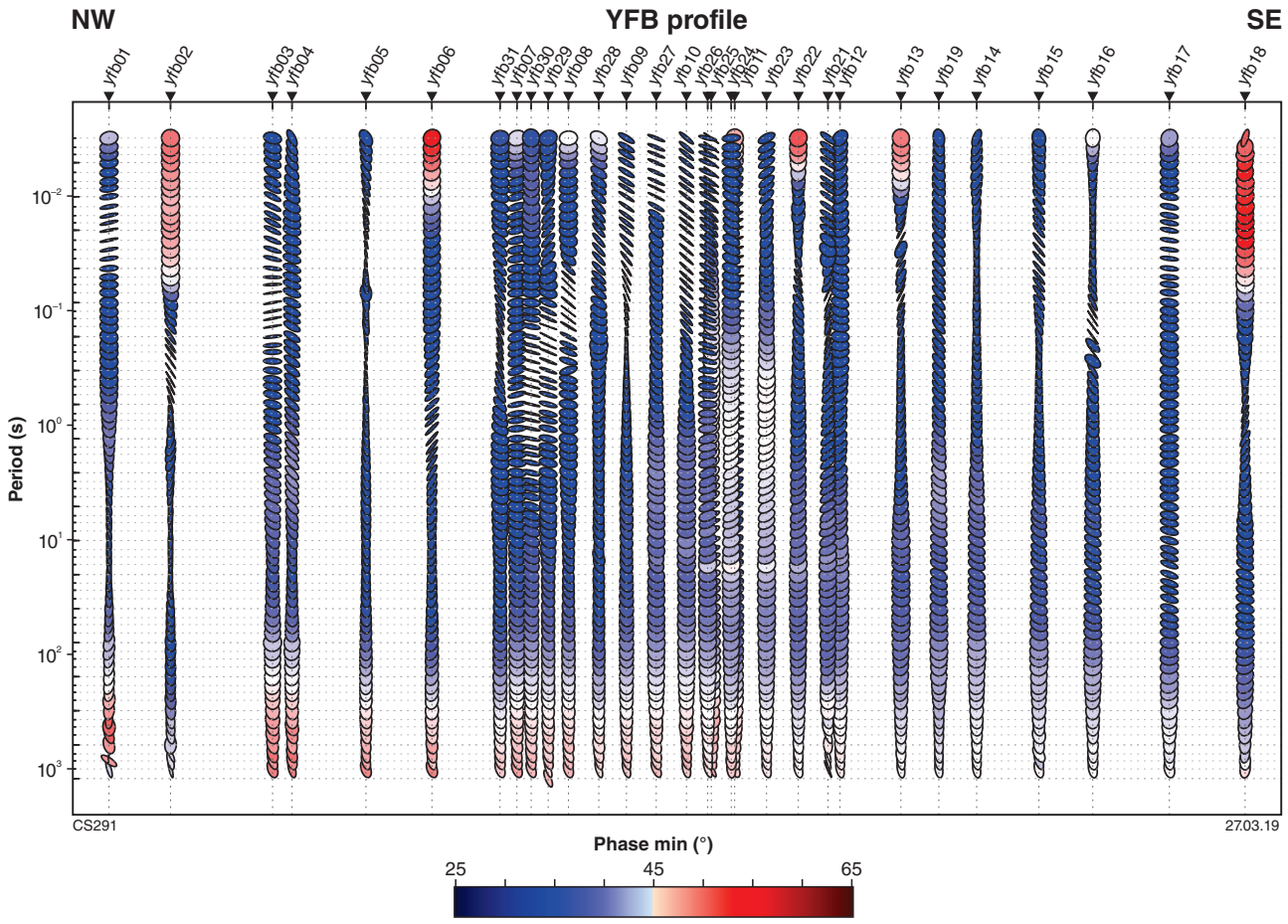

Figure 21. Pseudosection display of MT phase ellipses and phase minima along the YFB profile. The blue colours represent phase minima below 45°, generally indicating a change from conductive to resistive rocks with depth, and the red colours represent phase minima above 45°, generally indicating a change from resistive to more conductive rocks with depth

up to 1 s, indicating significant heterogeneity in the subsurface structure. At longer periods, the ellipses are less elongate with a northwesterly to southeasterly trend. The northeasternmost sites are most elongate at periods below 1 s, with a northwesterly to southeasterly trend.

Plots of skew along the FR profile are shown in Figure 34. Effects of 3D distortion are estimated to be most severe at the northeastern end of the profile, with high skew values observed at high frequencies for many sites and at periods greater than approximately 300 s (100 s in the central part of the profile).

Rose diagrams have been plotted for all sites along the FR profile and for four separate sections of the profile (Fig. 35). Section A shows no preferred strike angle at periods below 1 s; however, at periods of 1–100 s the data show less scatter, with strikes of 65–75º (155–165º). There is a consistent strike direction of 35–45º (125–135º) for section B at periods up to 0.1 s, and up to 1 s for section D, whereas section C shows a preference of 65–75º (155–165º). The deeper structure shows more consistency between the different sections, with values of 70–80º (160–170º) at periods of 10–100 s, and 80–90º (170–180º) at periods greater than 100 s. The rose diagrams agree with the results from Groom–Bailey decomposition analysis (Fig. 11).

Groom–Bailey decomposed data were generated at strike angles of –5°, 45° and 65°. RMS values for each site at each period have been plotted to view which strike direction is appropriate for the different sections of the profile (Fig. 36). The black ovals mark sections of the profile where specific strike directions can be applied, i.e. RMS is low. Strike directions are variable both in period and in location, possibly due to the profile being close to parallel to the geological strike.

2D data modelling

The WinGLink interpretation software package that implements the inversion algorithm of Rodi and Mackie (2001) was used to generate 2D models along the four profiles. Inversions were executed from the MT responses recalculated at the appropriate geoelectric strike directions. The inversion program searches for the smoothest, best-fit model with the least deviation from the starting model (Mackie and Madden, 1993). The models derived, therefore, represent the minimum structure required to fit the data with an acceptable misfit.

Models were generated along each profile using different components of the data, with and without the inclusion

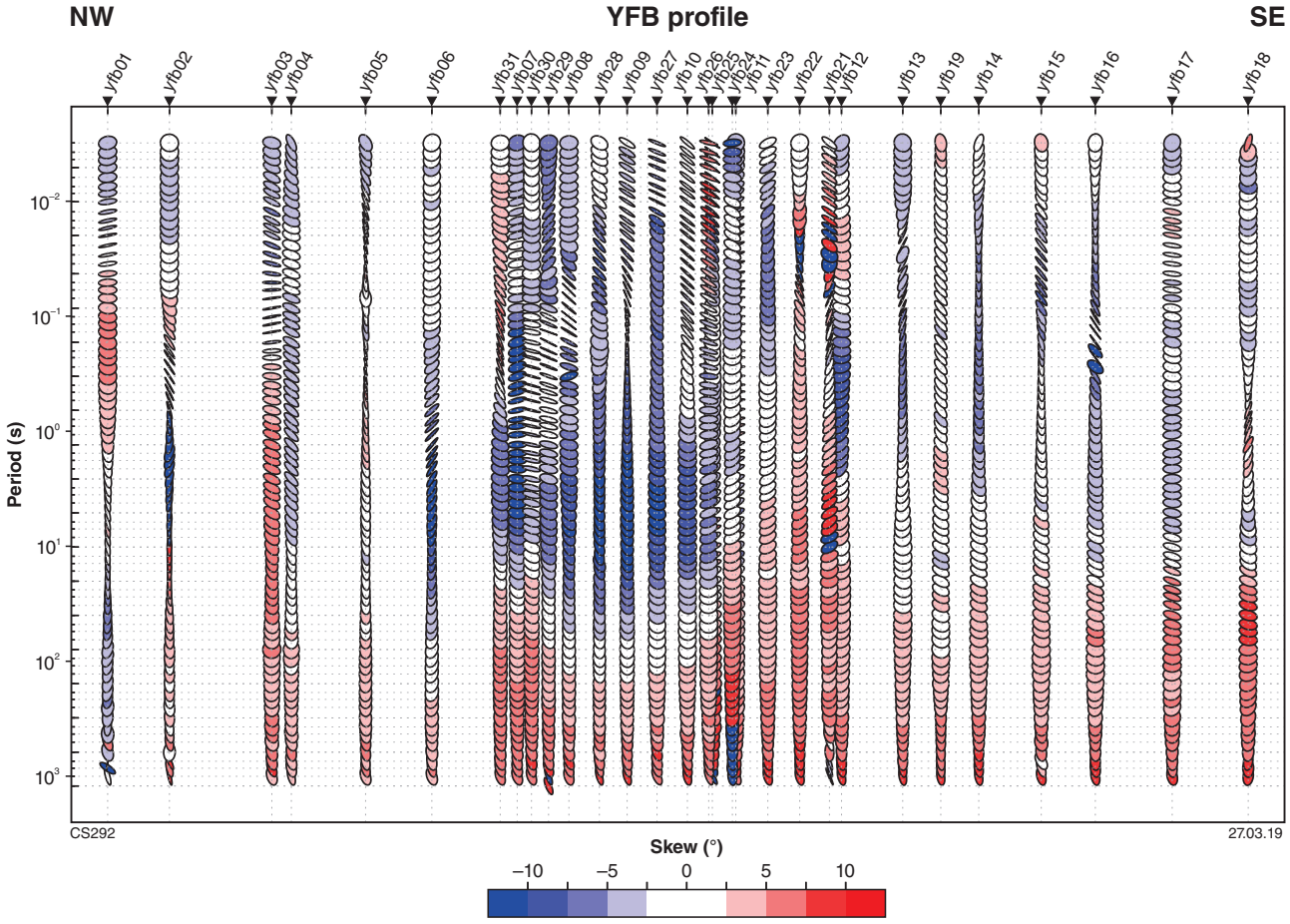

Figure 22. **Pseudosection display of MT phase ellipses and skew (β) along the YFB profile. The darker blue colours represents skew values below −5° and the darker red colours represents skew values above +5°**

of data deemed 3D, and at differing strike angles in order to assess the change in the observed conductivity structure and resolve features that are robust in the data. Each inversion included data in the period range of 0.004 – 1000 s, was initiated with a homogeneous half space of 500 Ω-m, and ran for a minimum of 200 iterations. The TE phases and apparent resistivities were set with an error floor of 7% and 15%, respectively. The TM error floors were set to 12% for apparent resistivities and 5% for phases. Where applicable, the Tipper error was set to an absolute value of 0.02. A uniform grid Laplacian operator and tau value of 3 were applied. The preferred models selected for each profile are those generated with MT data presumed to be affected by 3D distortion removed, with structure that appears to be robust between inversions using different data components and modelling parameters, and that have the lowest overall RMS value.

To test the reliability of the preferred resistivity model produced by the inversion, 'feature testing' was undertaken on various distinct conductive and resistive zones in each profile. This method involves removing and replacing conductivity values of a group of cells with the conductivity of the adjacent area. For example, in the case of discrete conductive zones in the upper crust, these are replaced with resistive values similar to those outside the feature being tested. A forward calculation is first performed on the data to assess the change in RMS value, then the resistivity in the area is 'fixed' and the inversion process re-started. This means the inversion algorithm is forced to try and match the observations using conductivity variations outside this area. This form of test is designed to see whether conductivity variations in another part of the model can be used to fit the data, i.e. does there need to be a zone of anomalous conductivity in the area being tested? The second type of feature test allowed the modelling algorithm to modify values within the test zone ('unfixed') to see if the anomalous zone reappears and if so, how its geometry is affected. This test is less rigorous than the first in terms of the presence or absence of a feature, but allows the reliability of the feature's geometry to be assessed, i.e. does it re-appear in the same form as in the original model? Details of feature testing of each profile are provided in Appendix 2.

2D modelling of the AF3 profile

Results of 2D modelling along AF3 profile are shown in Figure 37. Two-dimensional models were generated at strikes of 20°, 50° and 5° to observe how variations in the preferred geoelectric strike direction influences the inversion process, and to determine the most accurate 2D representation of the subsurface beneath the profile.

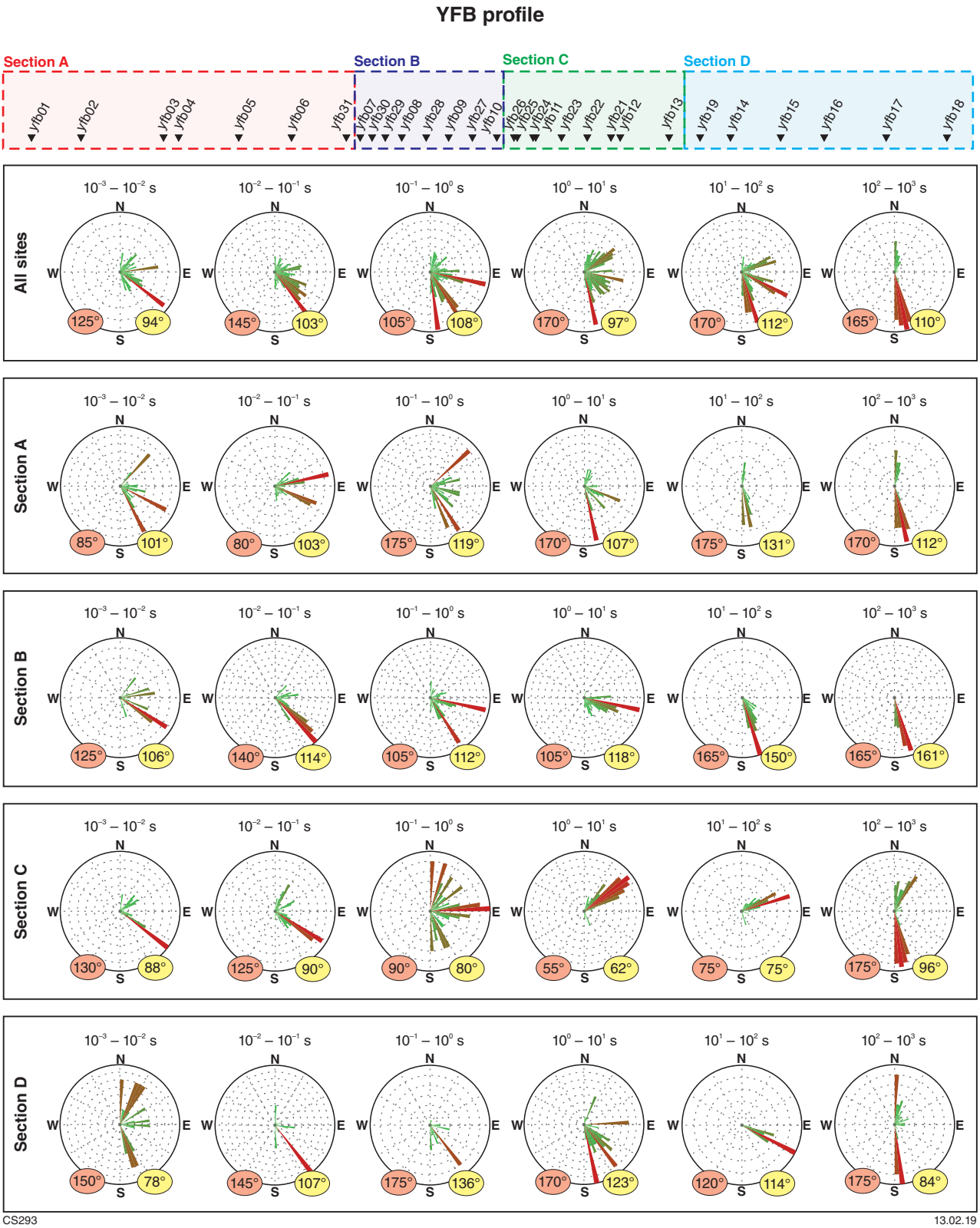

Figure 23. **Rose diagrams of phase-tensor ellipses and z-strike orientations at six decade-period bands for sites along the entire YFB profile, divided into four sections**

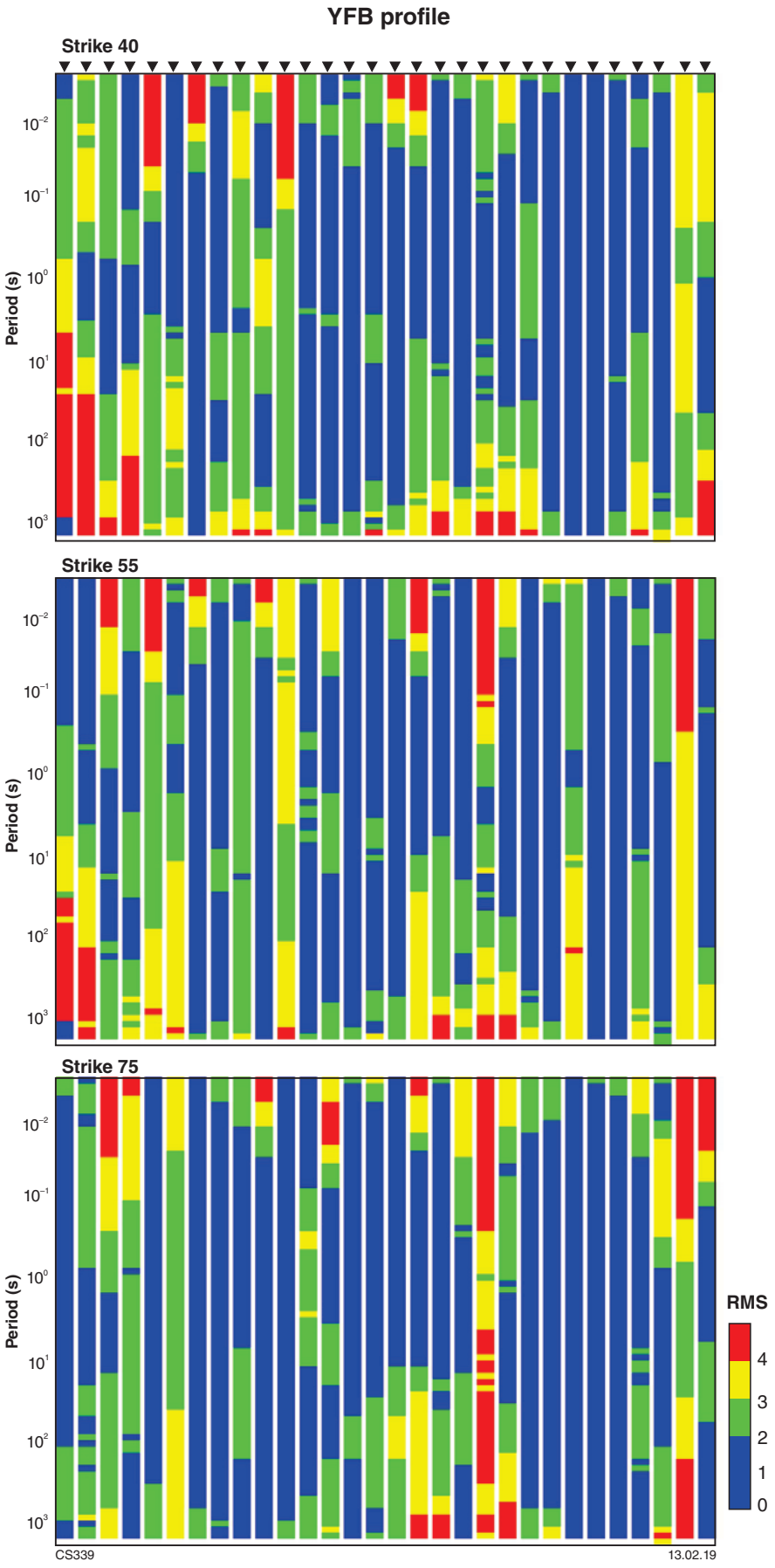

Figure 24. **RMS values calculated from Groom–Bailey decomposition at each site and each period along profile YFB for three different strike directions: 40°, 55° and 75°**

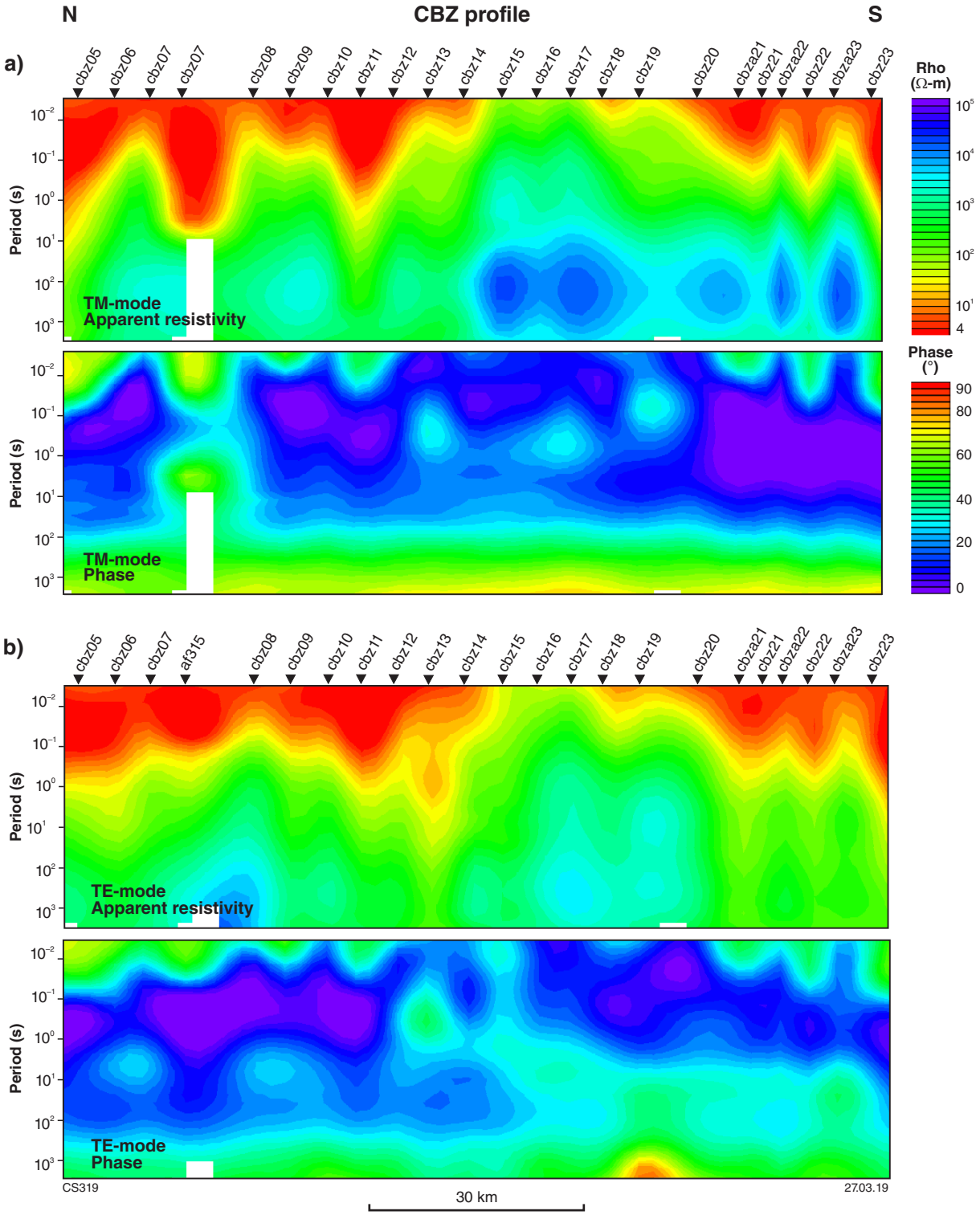

Figure 25. **Pseudosections of apparent resistivity and phase along the CBZ profile comprising data considered to have an acceptable signal-to-noise level: a) data in the TM-mode; b) data in the TE-mode**

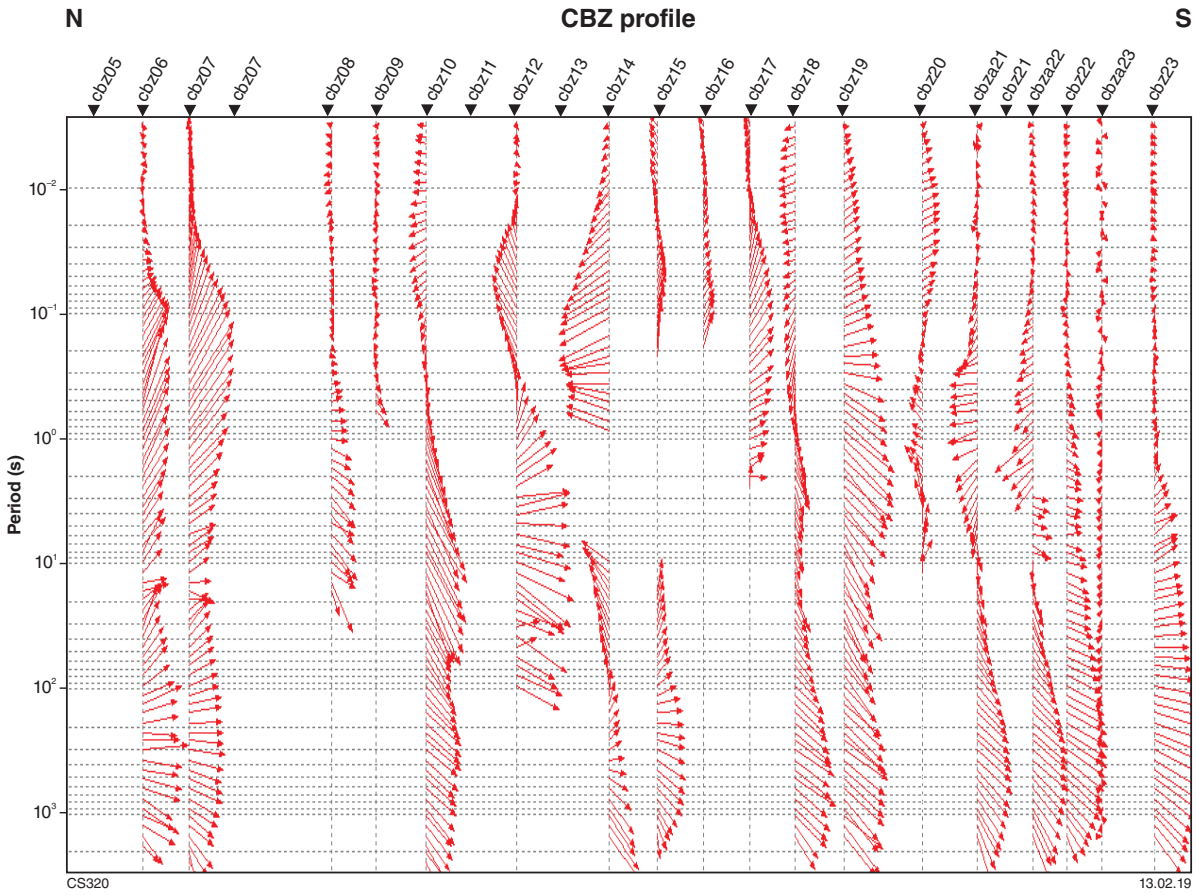

Figure 26. Pseudosection display of induction arrows at each period along the CBZ profile

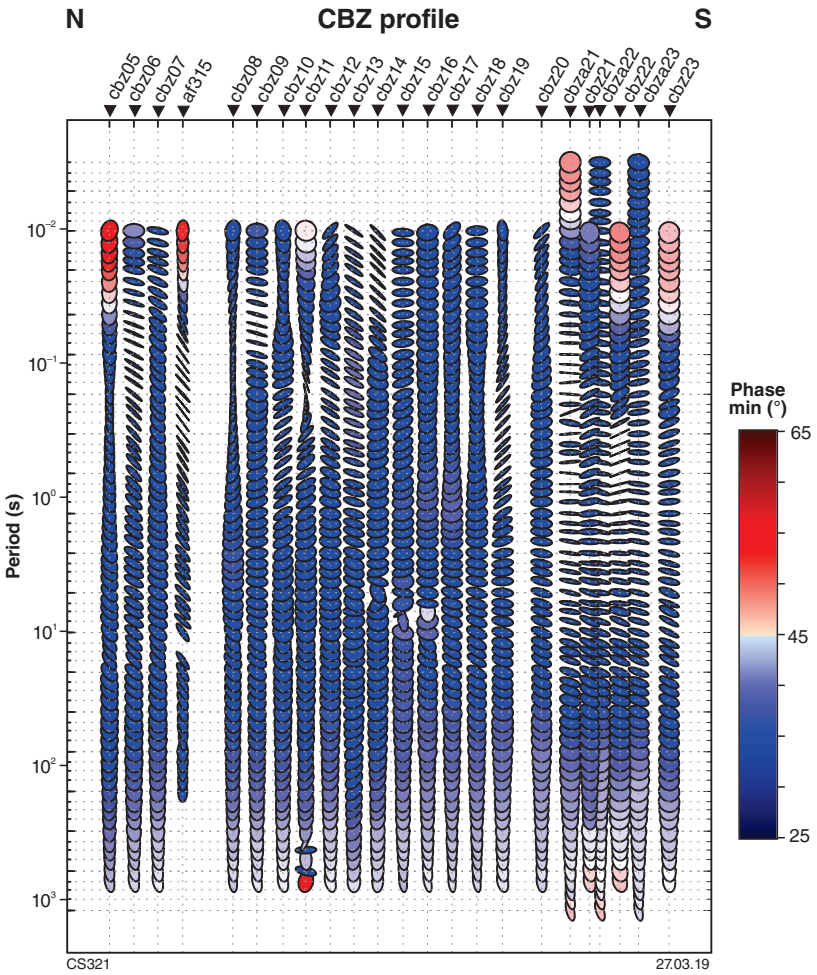

Figure 27. Pseudosection display of MT phase ellipses and phase minima along the CBZ profile. The blue colours represent phase minima below 45° generally indicating a change from conductive to resistive rocks with depth, and the red colours represent phase minima above 45°, generally indicating a change from resistive to more conductive rocks with depth

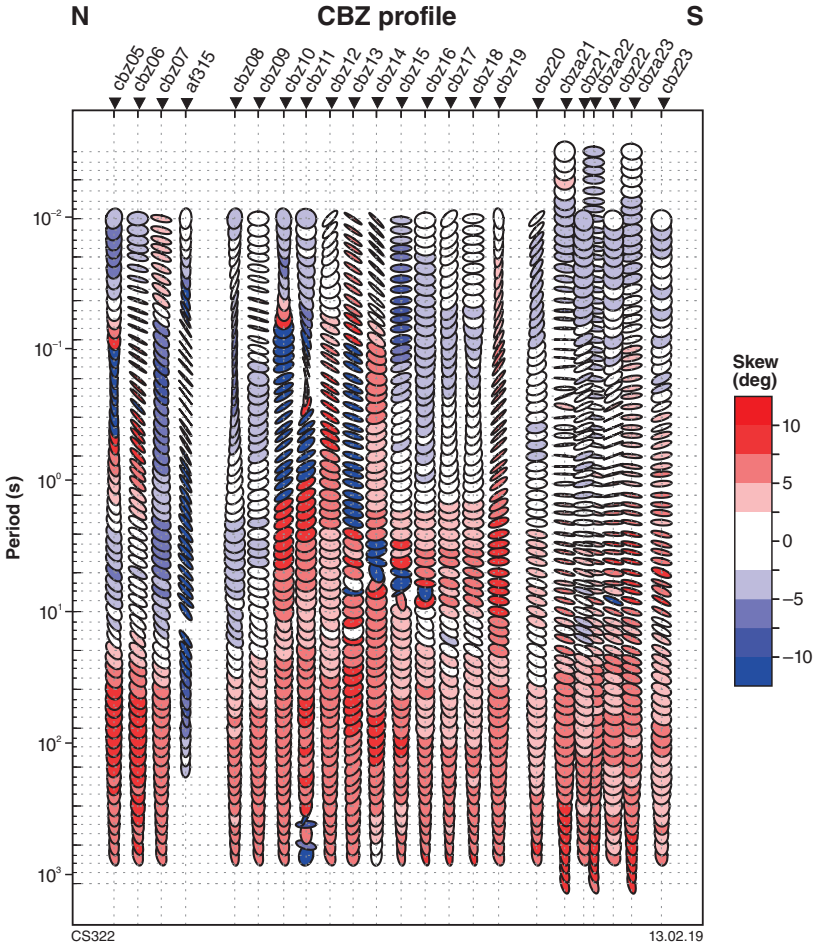

Figure 28. **Pseudosection display of MT phase ellipses and skew (β) along the CBZ profile. The darker blue colours represent skew values below −5° and the darker red colours represent skew values above +5°**

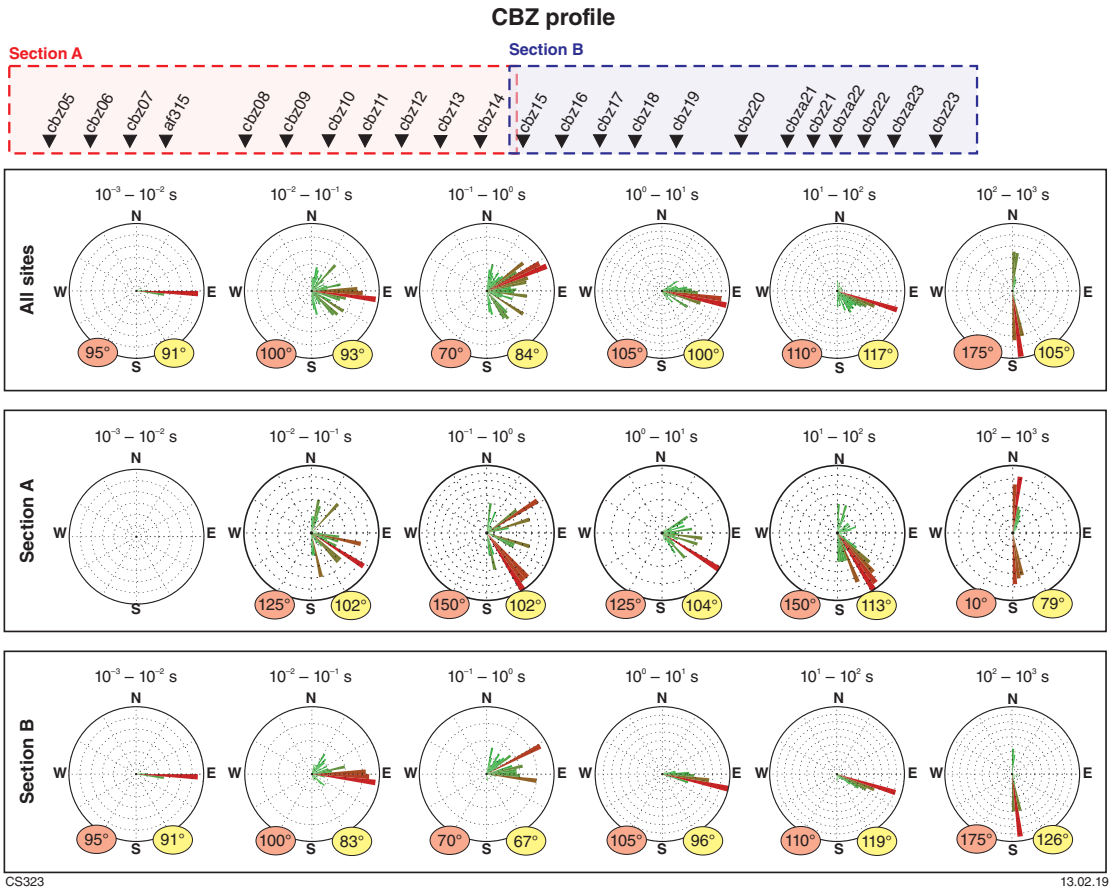

Figure 29. **Rose diagrams of phase-tensor ellipses and z-strike orientations at six decade-period bands for sites along the entire CBZ profile, the northern half of the CBZ profile (section A) and the southern half of the CBZ profile (section B)**

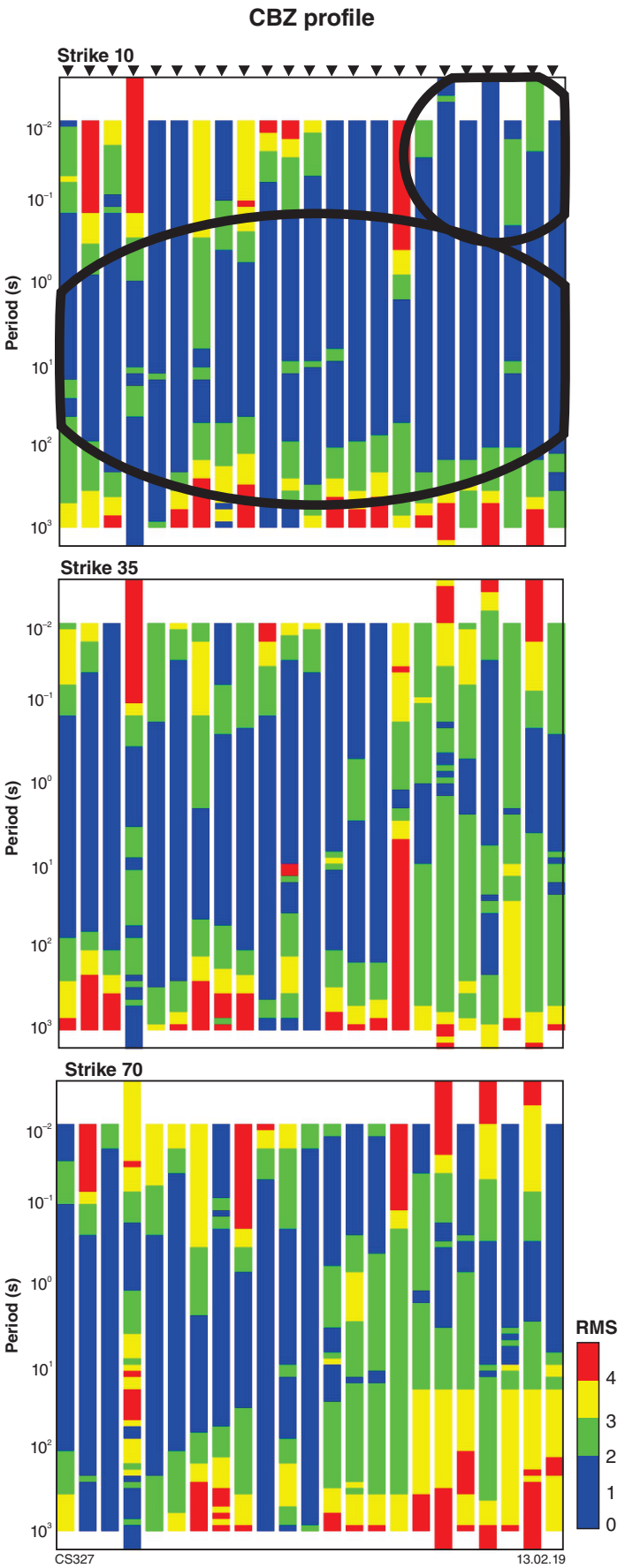

Figure 30. **RMS values calculated from Groom–Bailey decomposition at each site and each period along profile CBZ for three different strike directions: 10°, 35° and 70°. The black oval marks areas of the data that show a strong preference for a particular strike direction**

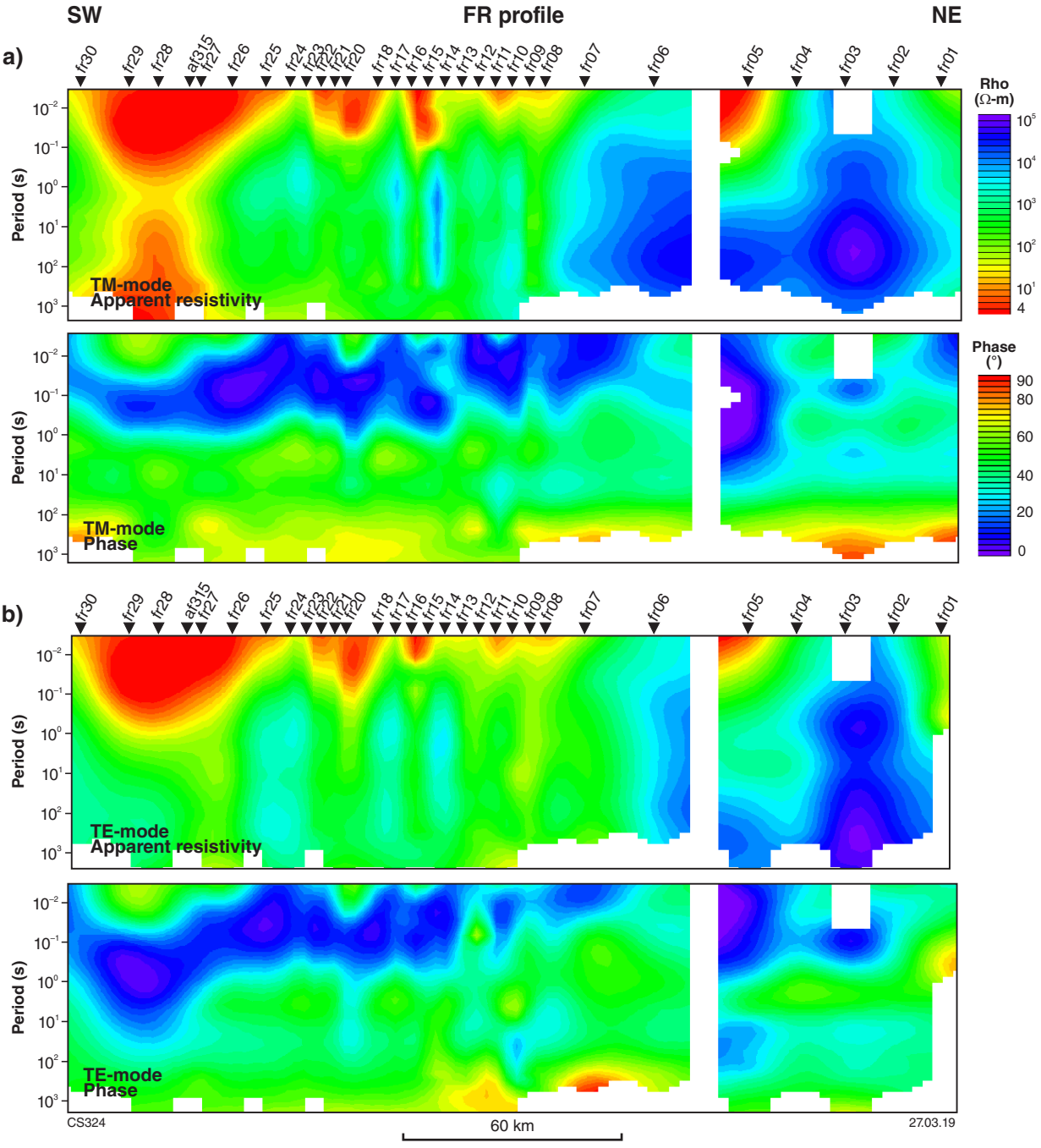

Figure 31. **Pseudosections of apparent resistivity and phase along the FR profile comprising data considered to have an acceptable signal-to-noise level: a) data in the TM-mode; b) data in the TE-mode**

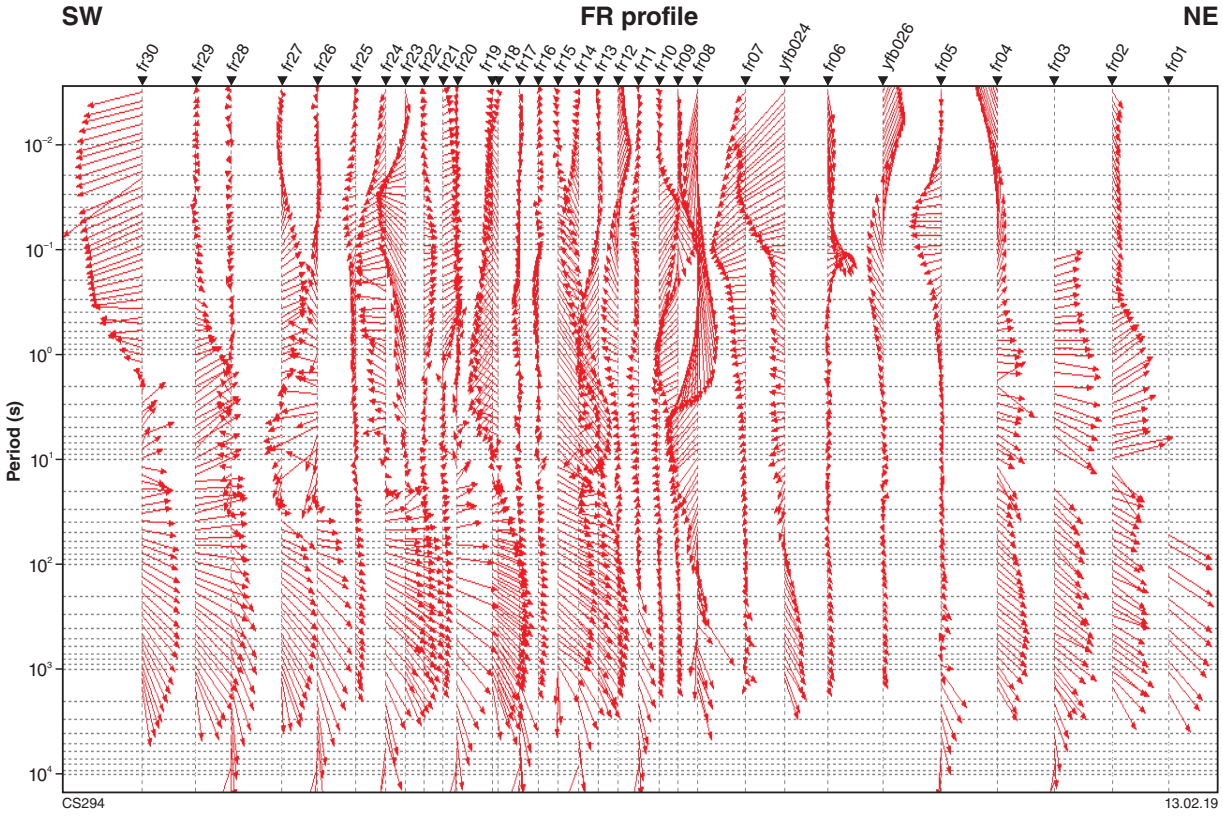

Figure 32. **Pseudosection display of induction arrows at each period along the FR profile**

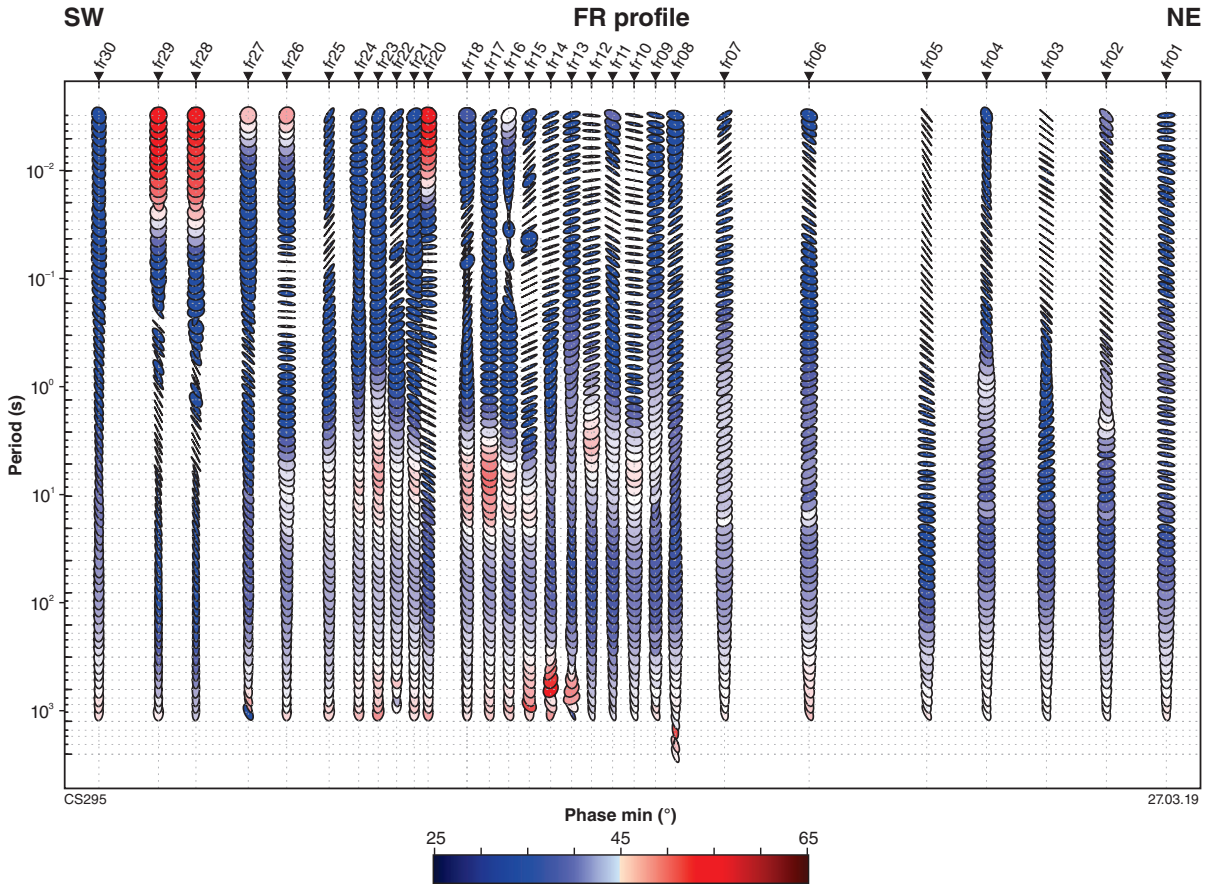

Figure 33. **Pseudosection display of MT phase ellipses and phase minima along the FR profile. The blue colours represent phase minima below 45°, generally indicating a change from conductive to resistive rocks with depth, and the red colours represent phase minima above 45°, generally indicating a change from resistive to more conductive rocks with depth**

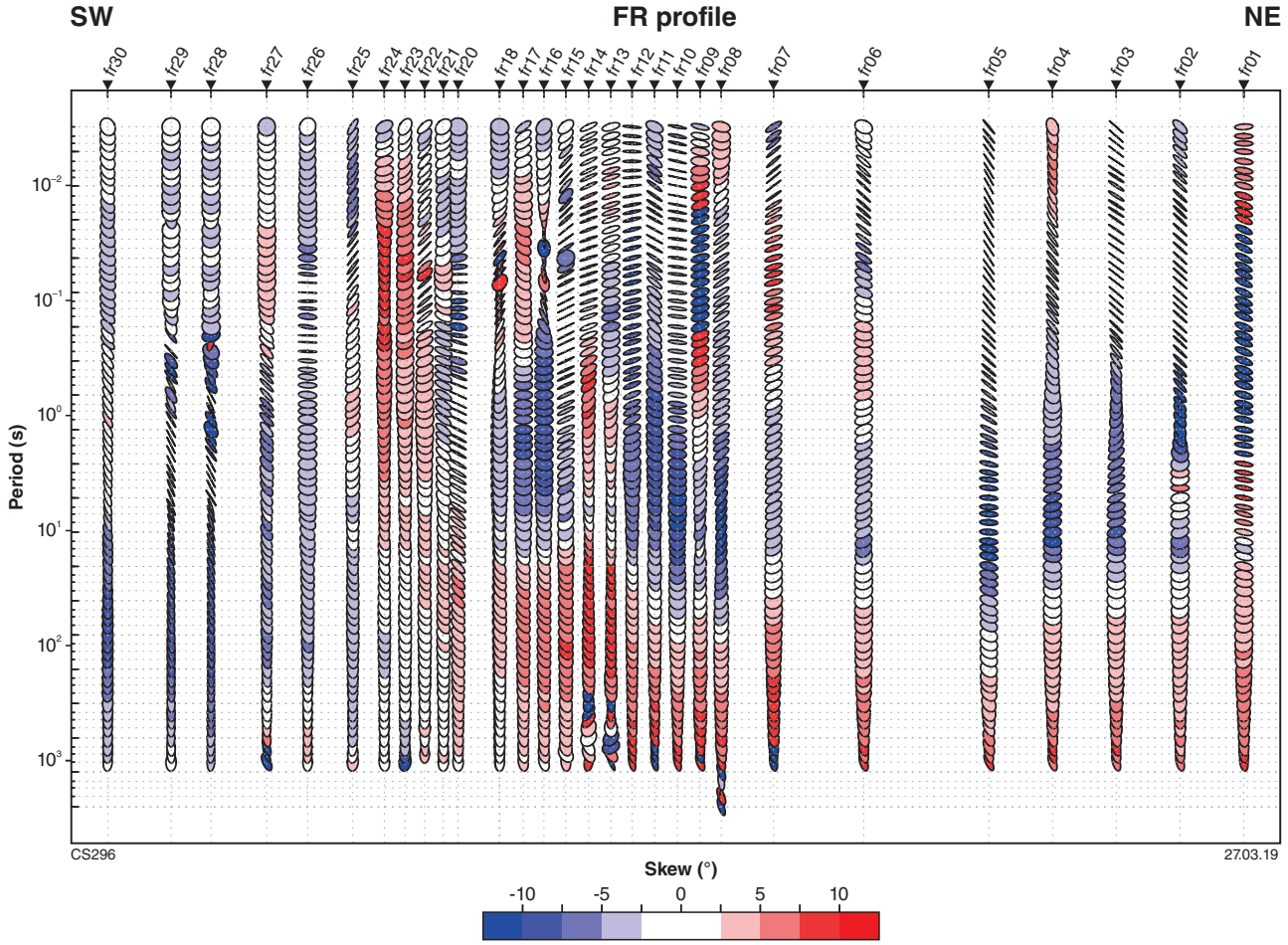

Figure 34. Pseudosection display of MT phase ellipses and skew (β) along the FR profile. The darker blue colours represent skew values below −5° and the darker red colours represent skew values above +5°

A strike of 20° is consistent with the orientation of localized structural features in section C of the rose plots and has been assigned to the TE-mode. A strike direction of 50° is roughly consistent with the predominant northeasterly trending regional geology, at least in the upper crust, and suggests that this direction corresponds to the TE-mode. A geoelectric strike of 5° is possibly a result of the effect of approximately north to northwesterly trending geological terrane boundaries and shear zones within the Eastern Goldfields Superterrane, at least in the western part of the profile.

Consistent with variable induction vectors and phase-tensor ellipses at short periods, the structure imaged beneath the western half of the profile at crustal depths is dependent on the assumed geoelectric strike angle. The structure imaged beneath the eastern half of the profile does not change significantly with different strike angles, with the exception of the large resistive feature below af333 and af334. The plots of the RMS values at each site for each strike direction (Fig. 37d) show that, for most of the profile, the model generated at a strike angle of 5º has the best fit to the data. Exceptions are beneath sites af307 through af320, where there is a preference for 50º.

Our preferred conductivity models along the AF3 profile are shown in Figure 38. These were generated using data edited for 3D effects and with geoelectric strike angles of 5° and 50°. The conductivity sections are overlain by the seismic reflection interpretations from Spaggiari and Occhipinti (2015) (Figs 38b,d). In both models, west of the Fraser Shear Zone, a resistive upper crust (>10 000 Ω-m) is imaged to approximately 20 km depth and is crosscut by several steeply west- or east-dipping, less resistive features (~500 Ω-m). Although much broader, some of these features roughly coincide with shear zones mapped at the surface and interpreted in potential field data. In the seismic reflection profile these shear zones have significantly shallower apparent dips, which are consistently to the east (Fig. 38b,d).

Beneath the resistive upper crust is a less resistive middle to lower crust layer (~500 Ω-m) that extends as far east as the Fraser Shear Zone. This roughly coincides with a zone of largely nonreflective lower crust below the Northern Foreland and Biranup Zone, which may be a zone of residual crustal melt (Spaggiari et al., 2014a). It also coincides with the zone of thicker crust detected in receiver function analysis (Sippl et al., 2017a). The crust–mantle boundary, based on the depth extent of conductive lower crustal material, is estimated at approximately 40–45 km

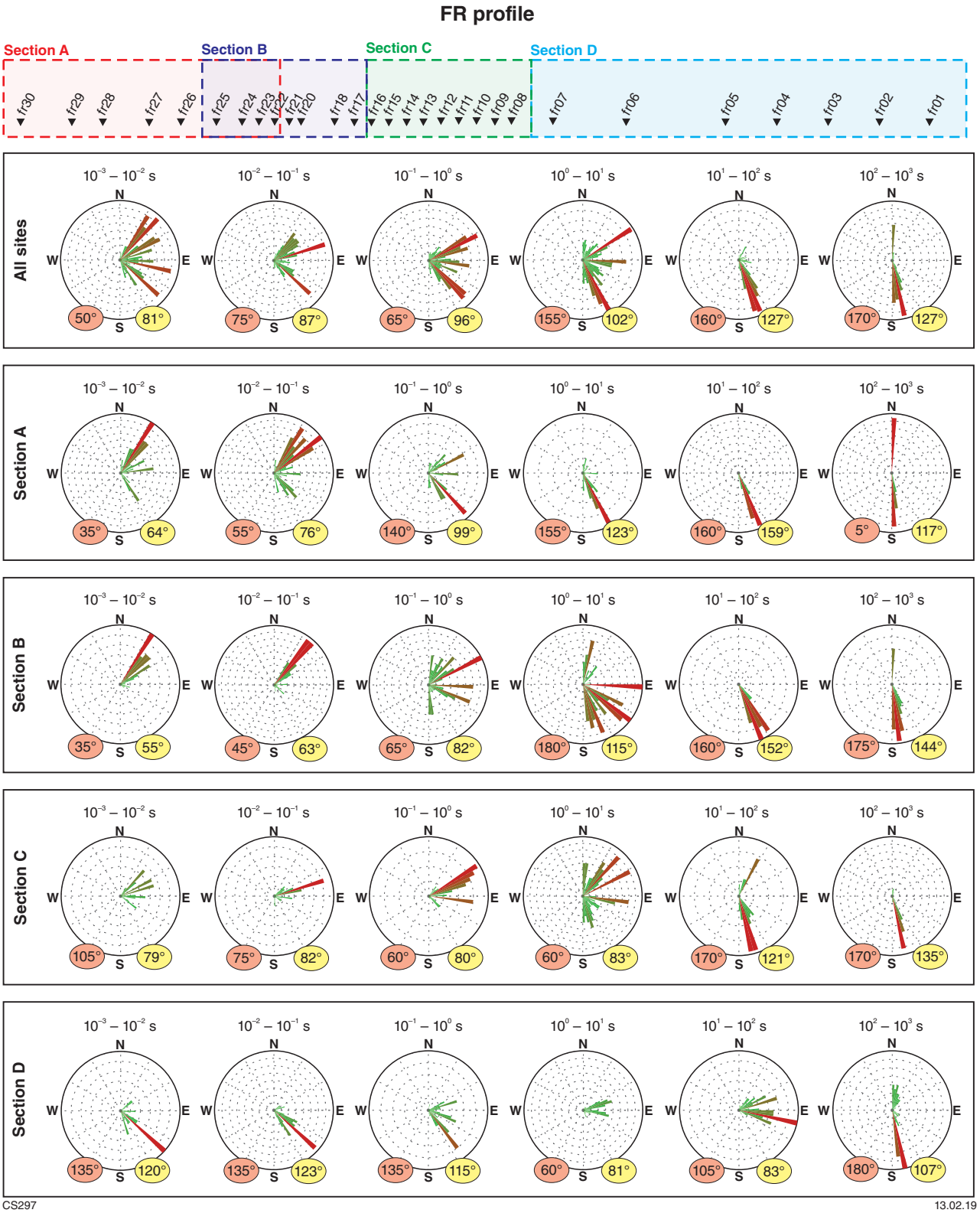

Figure 35. **Rose diagrams of phase-tensor ellipse and z-strike orientations at six decade-period bands for sites along the entire FR profile, divided into four sections**

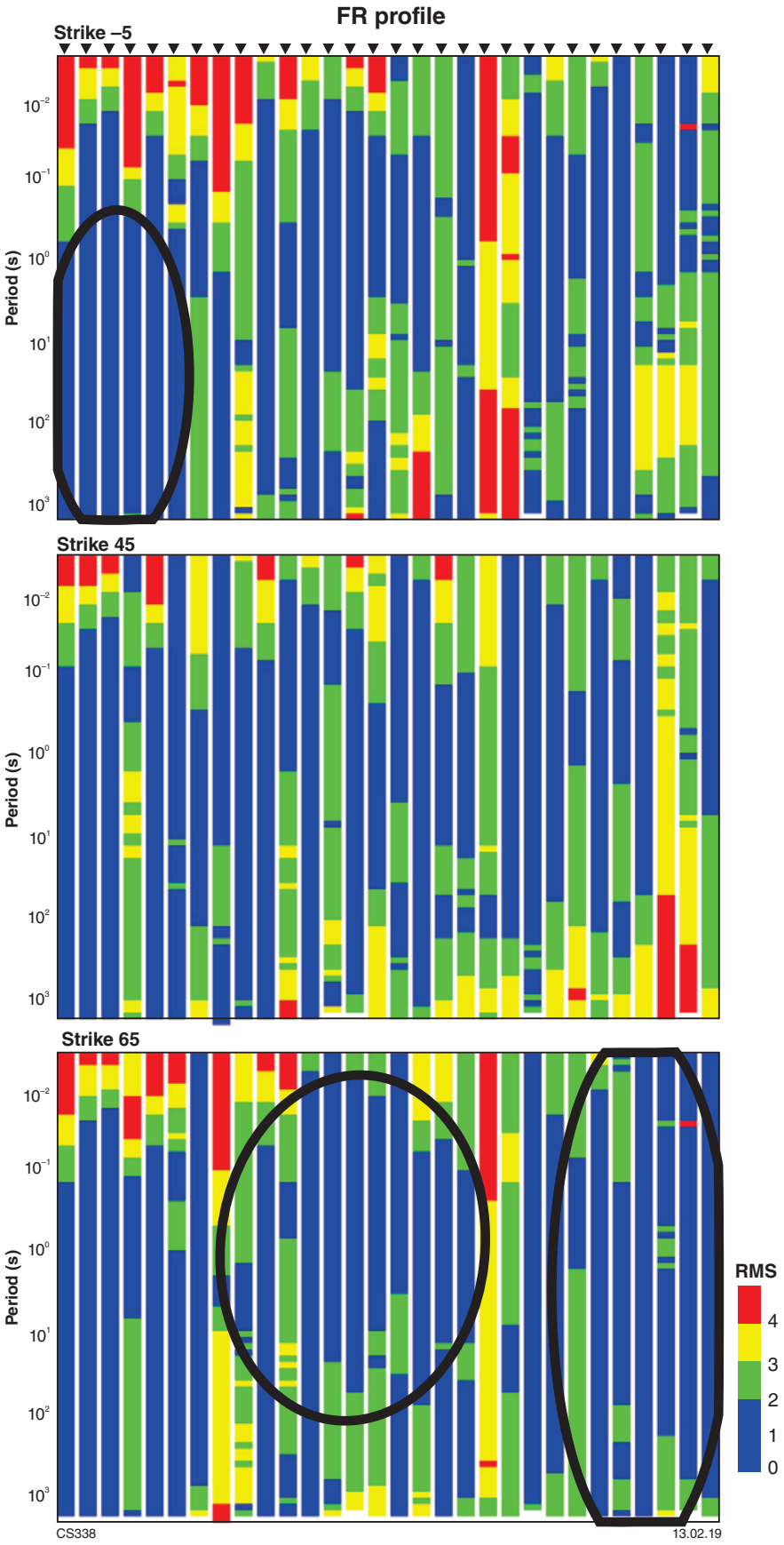

Figure 36. RMS values calculated from Groom–Bailey decomposition at each site and each period along Profile FR for three different strike directions: –5°, 45° and 65°. The black oval marks areas of the data that show a strong preference for a particular strike direction

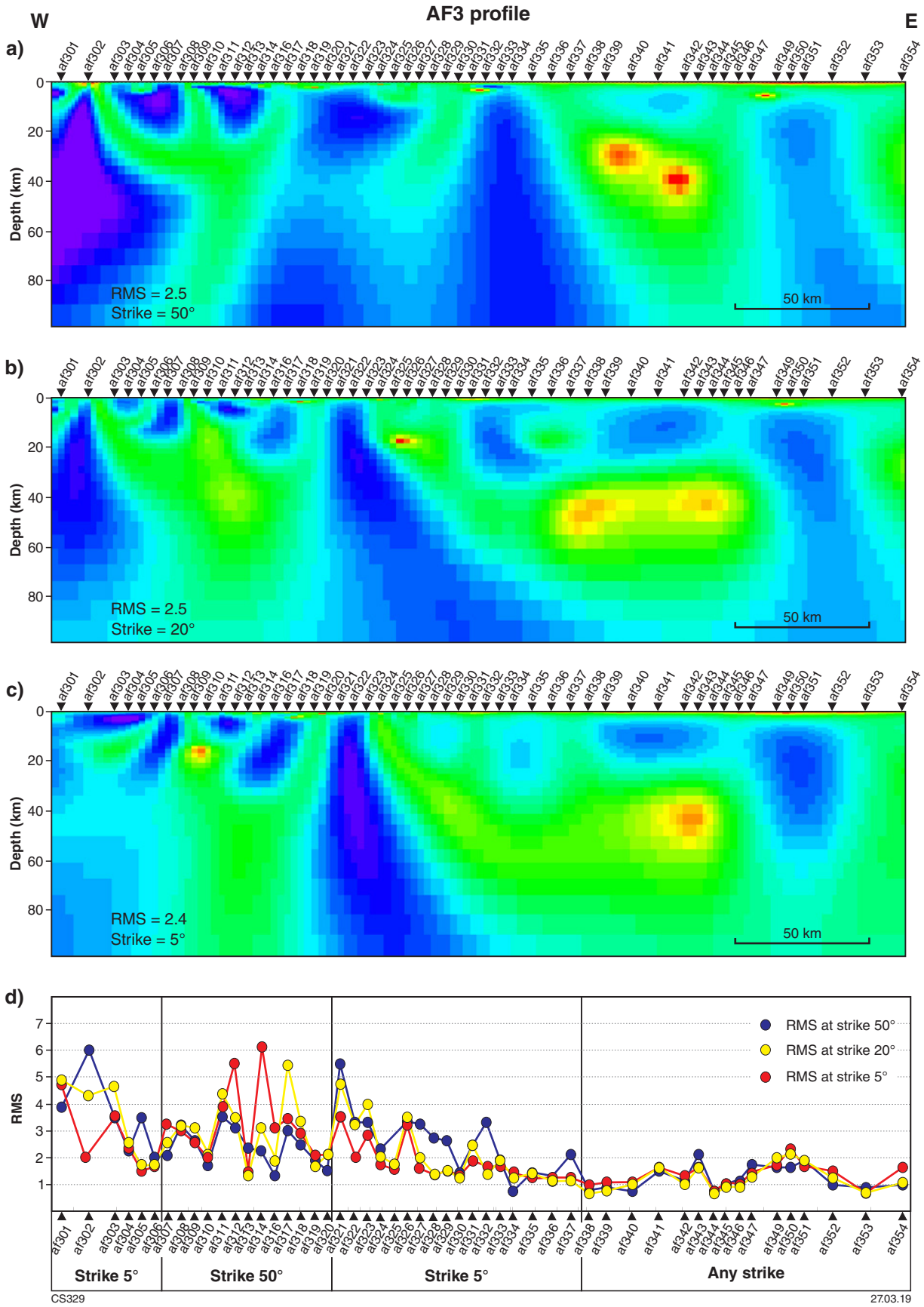

Figure 37. **Results of 2D modelling along the AF3 profile using all data not deemed exceptionally noisy, with the data rotated to the following geoelectric strike angles: a) 50°; b) 20°; c) 5°; d) RMS misfit values for each site along the profile for each model**

beneath this section of the MT profile, and this is consistent with the seismic reflection data (Fig. 3). Beneath sites af321–af323, directly east of the Fraser Shear Zone, the model shows high resistivities from 5 km depth down to the upper mantle, although there are some differences in the geometries of this feature between the two models at different strikes (Figs 38a,c). A similar resistive structure is seen at the western end of the profile beneath site af302. It is possible that the resistive feature below af302 represents typical Yilgarn crust, consistent with its location within the Eastern Goldfields Superterrane, whereas the resistive zone beneath sites af321–af323 is a local 'anomaly', within the Albany–Fraser Orogen. Farther to the east, the crust is locally resistive (~7000 Ω-m), tending to coincide with areas where the seismic interpretation includes large rafts of basement within Mesoproterozoic intrusions, although this zone is less pronounced in the model with the 50° strike. This resistive crust is also crosscut by several steeply dipping to subvertical, less resistive features, which are even broader than those to the west. There is some correspondence with known major shear zones, such as the Woodcutters Shear Zone, although again the dips are generally steeper than the apparent dips shown on the seismic interpretation. The Rodona Shear Zone overlies a region of more resistive crust, with less resistive crust in the hanging wall. The easterly dip seen in the seismic reflection profile is more pronounced in the model at 50° strike.

At mantle depths, the models show low resistivities with values generally less than 100 Ω-m. In the model at 5° strike, the lateral transition from more resistive to more conductive mantle is a steep boundary that occurs near the Fraser Shear Zone, whereas in the model at 50° strike, a broad resistive zone lies beneath the whole of the Fraser Zone. The model at 50° strike images the Fraser Zone as a V-shaped, less resistive zone, consistent with the seismic reflection profile interpretation and also gravity modelling (Brisbout, 2015). The MT data suggest this resistive feature extends all the way to the surface, albeit with some variation on geometry depending on model strike.

Feature testing has been undertaken to ascertain the robustness of several features along the AF3 profile (Fig. 38a). These include some of the near-vertical, low resistivity structures (features A, B and C), the absence of a lower crustal conductor beneath sites af302 and af322 (features D and E), the depth extent of the 'mantle' conductor east of the Fraser Zone (feature F), the change in upper mantle resistivity from west to east (feature H), and a zone of conductive mantle below the Northern Foreland (feature G). For each feature, the preferred model was altered and a forward inversion was run. Subsequent iterations were executed with the altered model fixed and unfixed to observe how the model adapts to the change (see Appendix 2). Of the conductive zones in the upper crust, the feature tests show that A is not well resolved but B and C are probably reliable components of the model. Features D and E represent lateral variations in lower crustal conductivity and are considered reliable. Features F and H were shown to be reliable aspects of the model, but feature G had little influence on the data fit, suggesting this feature is not a robust aspect of the model. Feature testing of features B, E and G was also conducted on the model at 50° strike (Fig. 38c), with similar results.

Conclusions based on 2D modelling

Feature testing shows that the relatively narrow conductive zones in the upper crust in the western part of the AF3 profile are a reliable feature of the models, apart from feature A. These features could be considered as related to major faults or shear zones, consistent with the interpretation of numerous faults or shear zones and structural complexity in this region based on the seismic reflection and other data (Spaggiari et al., 2014a; Spaggiari, 2016). However, the actual geometry of these faults and shear zones is difficult to reconcile with the MT data due its resolution, and as confirmed by the differences in the model obtained with different strike angles (Figs 37, 38). It is also likely that these structures are narrower than the conductive zones imaged. Furthermore, major faults or shear zones in the seismic interpretation have much shallower apparent dips than suggested by the MT data. Seismic reflection data can only image reflectors with dips up to approximately 60°, although steeply dipping structures can be interpreted where reflectors are systematically truncated. The disparity may also be a function of the complexity of the electrical conductivity structure as demonstrated by the various measures of geoelectrical strike, and that we are attempting to represent a 3D Earth with 2D profiles. Geological structural complexity is also problematic for the interpretation of seismic reflection 2D images (Spaggiari et al., 2014a). Furthermore, structurally controlled magmatism would no doubt have affected both electrical conductivity and acoustic impedance, so interpretations of already structurally complex regions are compounded. However, some broad-scale features can be resolved, and reasons for their presence speculated on.

The most interesting aspect of the conductivity section is the robust lateral change in both crust and mantle conductivity to the east of the Fraser Shear Zone. The extension of the change into the crust relies on the interpretation of the conductive crust below the Northern Foreland and Biranup Zone as a local 'anomaly'; however, this is consistent with the seismic interpretation and the robust nature of the resistive lower crustal regions comprising features D and E. It is also consistent with forward models of potential field data (Murdie et al., 2014). The seismic reflection data show a change in lower crustal seismic character at approximately this location, coinciding with the Gunnadorrah Seismic Province and also the zone of thicker crust — the 'Moho trough' of Sippl et al. (2017a). Thus, a major geological boundary in the vicinity of the Fraser Zone is identified in independent geophysical datasets. This is also consistent with geological observations of voluminous Mesoproterozoic magmatism and differences in structural evolution eastwards of the Fraser Shear Zone (Smithies et al., 2015; Spaggiari, 2016; Quentin de Gromard et al., 2017).

2D modelling of the YFB profile

Two-dimensional models generated along the YFB profile are shown in Figure 39. Modelling has been undertaken along the whole length of the YFB profile, with data rotated to geoelectric strike angles of 40°, 55° and 75°. Given that the regional geological trend of at least the upper crust is northeasterly to southwesterly, the TE-mode was assigned

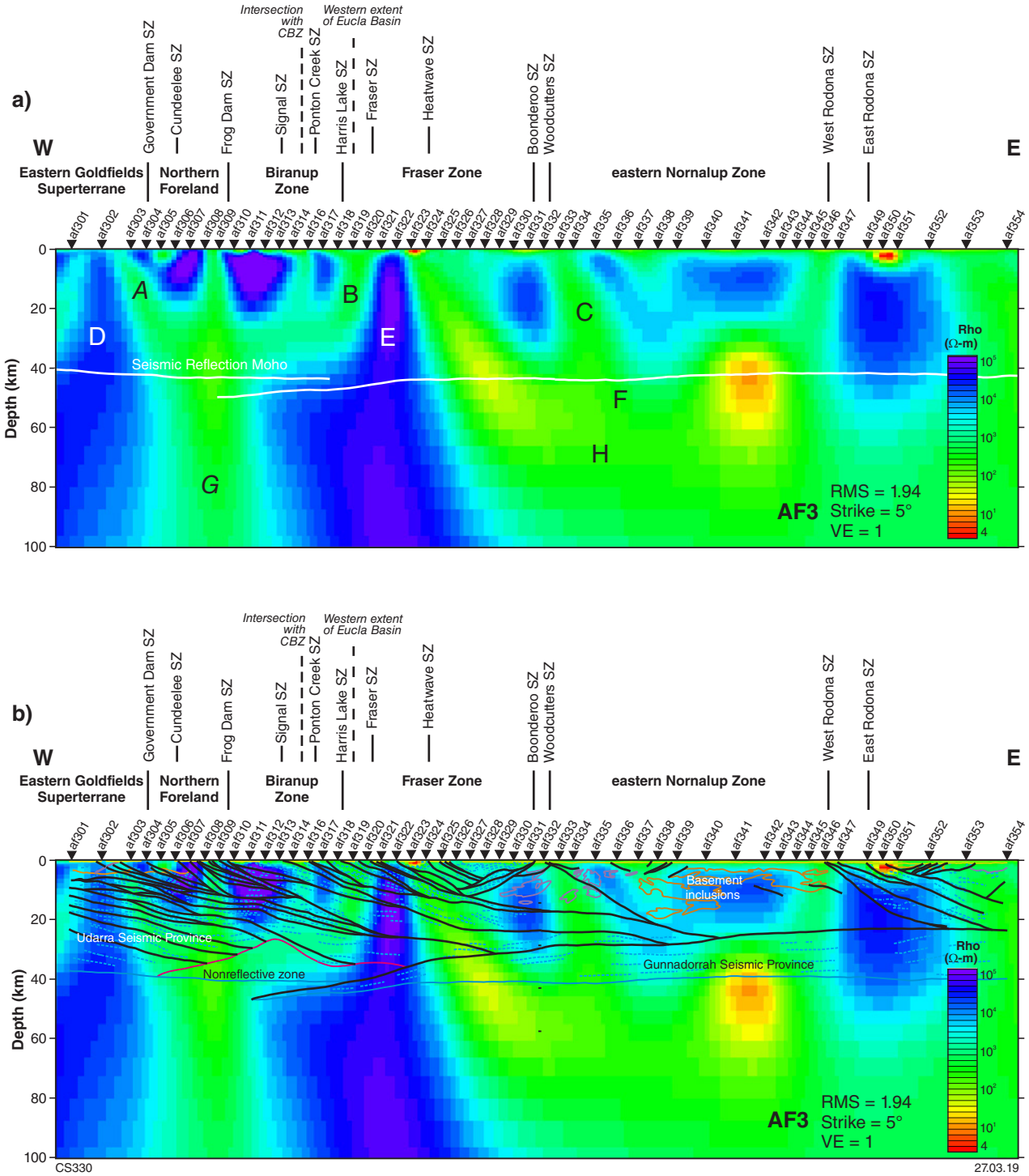

Figure 38. **Preferred 2D models along the AF3 profile. Warm colours represent areas that are conductive and blue colours represent areas that are resistive: a) model at a strike of 5° with letters that refer to the features tested (italicized letters indicate features that may not be reliable; see text and Appendix 2); b) conductivity section from a) overlain with interpretation of seismic reflection profile 12GA-AF3 (Spaggiari et al., 2014a); c) model at a strike of 50°; d) conductivity section from b) overlain with interpretation of seismic reflection profile 12GA- AF3 (Spaggiari et al., 2014a). VE, vertical exaggeration**

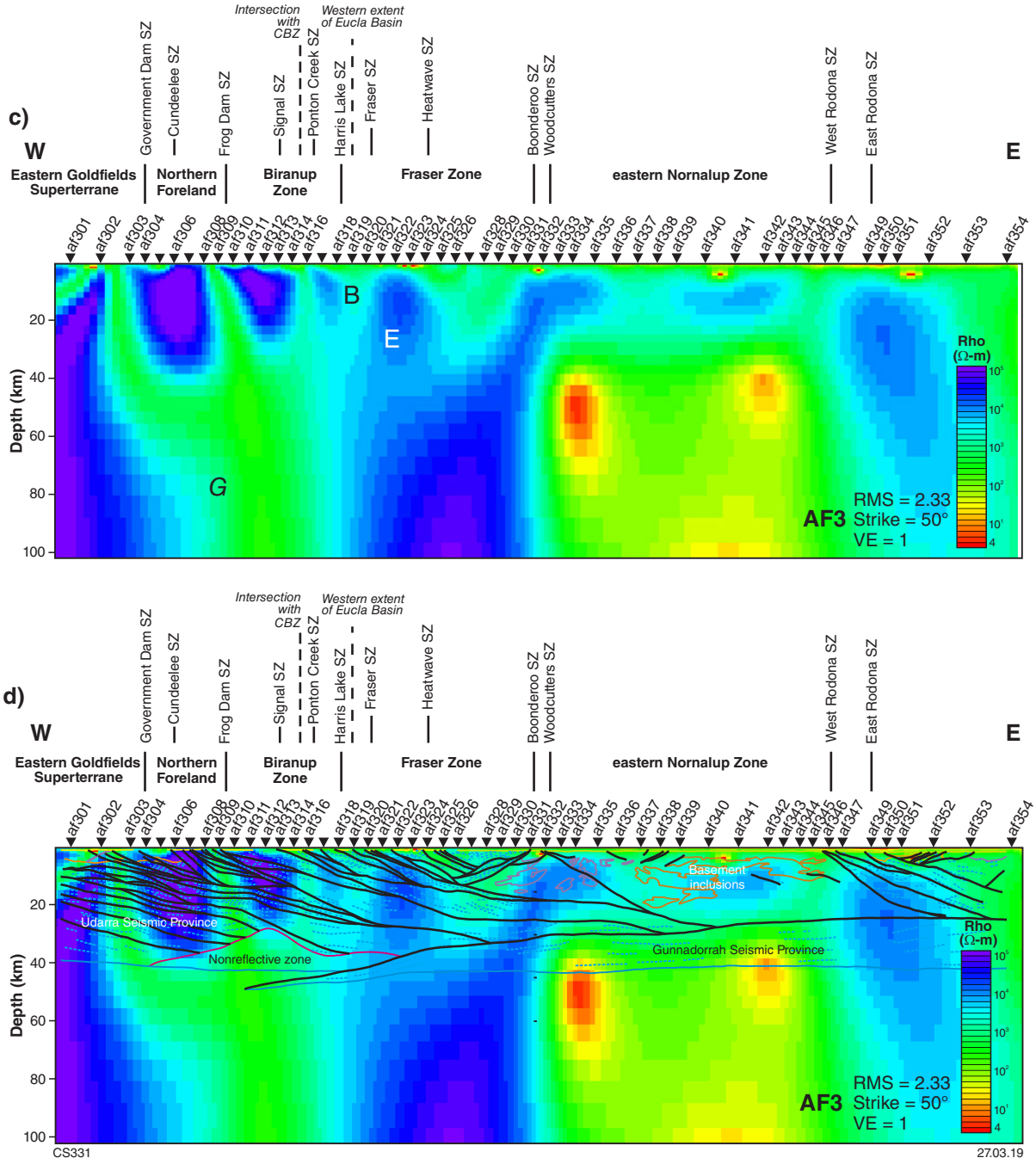

Figure 38. continued

to 40º and 55º, respectively. For a strike of 75º, the TE-mode was assigned perpendicular to the profile direction. Although there is some variation between models of differing strike angles, many features appear to be robust, with the lowest overall RMS value obtained equally with data rotated to strike angles of 40° and 55º. RMS values plotted for each site at each strike direction also show that a strike of 55º is suitable for most sites along the profile.

Data exhibiting high skew values were edited and recalculated at a geoelectric strike angle of 55° prior to generating our preferred model along the YFB profile (Fig. 40). This profile is close to one of the sections generated using receiver functions (Fig. 1) and the estimated depth to the mantle (Fig. 5b) is overlain on the conductivity cross-section. Relatively high conductivity values (generally >500 Ω-m) are observed at crustal depths beneath much of the Eastern Goldfields Superterrane of the Yilgarn Craton, although data are sparse there. Between stations yfb05 and yfb31 there is a resistive zone beneath northwesterly trending greenstones of the Kurnalpi Terrane that are parallel to the profile. This resistive zone (yfb05–yfb31) coincides with the northwestern limit of both the Rason Regional Gravity Low and the zone of thicker crust detected in the passive seismic results (Fig. 2; Sippl et al., 2017a). Station yfb06 is roughly along strike in a northeasterly direction from af302 in the AF3 profile (Fig. 38), where resistive crust is also apparent. It is therefore feasible that this resistive zone may in part correspond with the northwestern limit of the Rason Regional Gravity Low and zone of thicker crust. Southeast of site yfb31, the crust is resistive (>10 000 Ω-m) to approximately 35 km depth and is crosscut by several steeply dipping, less resistive features. Whether these features are related to structurally controlled zones of magmatism or major structures is unclear. However, yfb09 lies near the Frog Dam Shear Zone and boundary between the Northern Foreland and Biranup Zone, yfb10 lies near the Fraser Shear Zone and western edge of the Fraser Zone, and yfb12 lies near the Newman Shear Zone and eastern side of the Fraser Zone. Beneath the resistive crust, there is a moderately conductive layer (~500 Ω-m) that lies at depths between 35 and 60 km. This is consistent with results along the AF3 profile. Similar to the AF3 profile, lateral variations are observed within the upper mantle, with values of approximately 2000 Ω-m imaged beneath the Albany–Fraser Orogen and values of about 10 000 Ω-m towards the northwest.

Feature testing has been undertaken along the YFB profile to assess the robustness of the conductivity structure image (Fig. 40; Appendix 2). These include some of the near-vertical, low resistivity structures in the upper crust (features A and B), the resistive lower crust (feature C), continuity and depth of the lower crustal/upper mantle conductive zone (features D and E), and the change in upper mantle resistivity from northwest to southeast (features F, G and H). As described in Appendix 2, feature B is well resolved but feature A less so. The zone of resistive lower crust (feature C) is considered reliable. The depth to feature D is considered reliable, implying a conductive mantle in this area. Feature E is a narrow, low conductivity zone in the upper mantle, and was designed to test the sensitivity of the modelling to such features. Feature testing suggested features of this width are not resolvable in the data. Testing of feature F suggested the data may not be sensitive to the area directly beneath the lower crustal conductor at the northwest end of the profile. However, testing suggests the data are sensitive to the deeper structure and that the lateral changes in upper mantle resistivity structure are robust (features G and H).

Conclusions based on 2D modelling

The spacing and linearity of the stations in the YFB profile are quite variable due to access constraints. In particular, aspects of the model to the northwest of yfb05 should be considered with caution. Along-strike differences between the AF3 and YFB models may be attributed to the profile orientations, slightly larger station spacing along YFB, and the fact that many stations along YFB are projected from almost 20 km along-strike onto the profile plane. Also, data from sites located directly southeast of the Fraser Shear Zone, where the resistive lower crust was expected based on results from the other profile, had the phases in one mode out-of-quadrant even with repeated data acquisitions (Fig. 6d). This indicates severe localized distortion and only one mode of data was usable in the inversion. It should also be noted that there are significant along-strike geological differences, particularly the width of the Northern Foreland and Biranup Zone, and the composition and structure of the Fraser Zone (Spaggiari, 2016).

Acknowledging the points made above, an obvious discrepancy between the results from the YFB and AF3 profiles is that on the YFB profile the lateral change in mantle conductivity occurs northwest of the Northern Foreland, but on the AF3 profile it occurs at approximately the western edge of the Fraser Zone at 5° strike, and west of the eastern Nornalup Zone at 50° strike (Fig. 38). This may be a matter of lateral resolution at the depths of interest. Although the location of this change is disputable, as with the AF3 profile, there is good evidence for a lateral change in the electrical properties of the upper mantle near the northwestern margin of the east Albany–Fraser Orogen. This change is consistent with either a fundamental geological boundary, or at the very least, a change in upper mantle character between the east Albany–Fraser Orogen and the non-reworked portion of the Yilgarn Craton.

2D modelling of the CBZ profile

Results of 2D modelling using all of the acquired data along the CBZ profile are shown in Figure 41 for geoelectric strikes of 35°, 10° and 70°. Significant differences are observed between the models at differing strike angles, particularly at depths greater than 20 km. The most significant difference is the thickness of two resistive crustal units, separated by a near-vertical, low resistivity zone, that vary in depth extent from 20 to 55 km between the models. These large differences indicate the data are strongly 2D or 3D. The lower overall RMS value was obtained at a strike of 10°. Our preferred model along the CBZ profile, using data edited for high skew values at a strike of 10°, is shown in Figure 42. Note that a strike of 10° is only about 20–30° from the strike of the profile trace and may result in unreliable models.

The model shows moderate to low resistivities (50–500 Ω-m) beneath part of the Biranup Zone and the westernmost part of the Fraser Zone, between cbz09 and the Spy Hill Shear Zone, to depths of 20–30 km. High

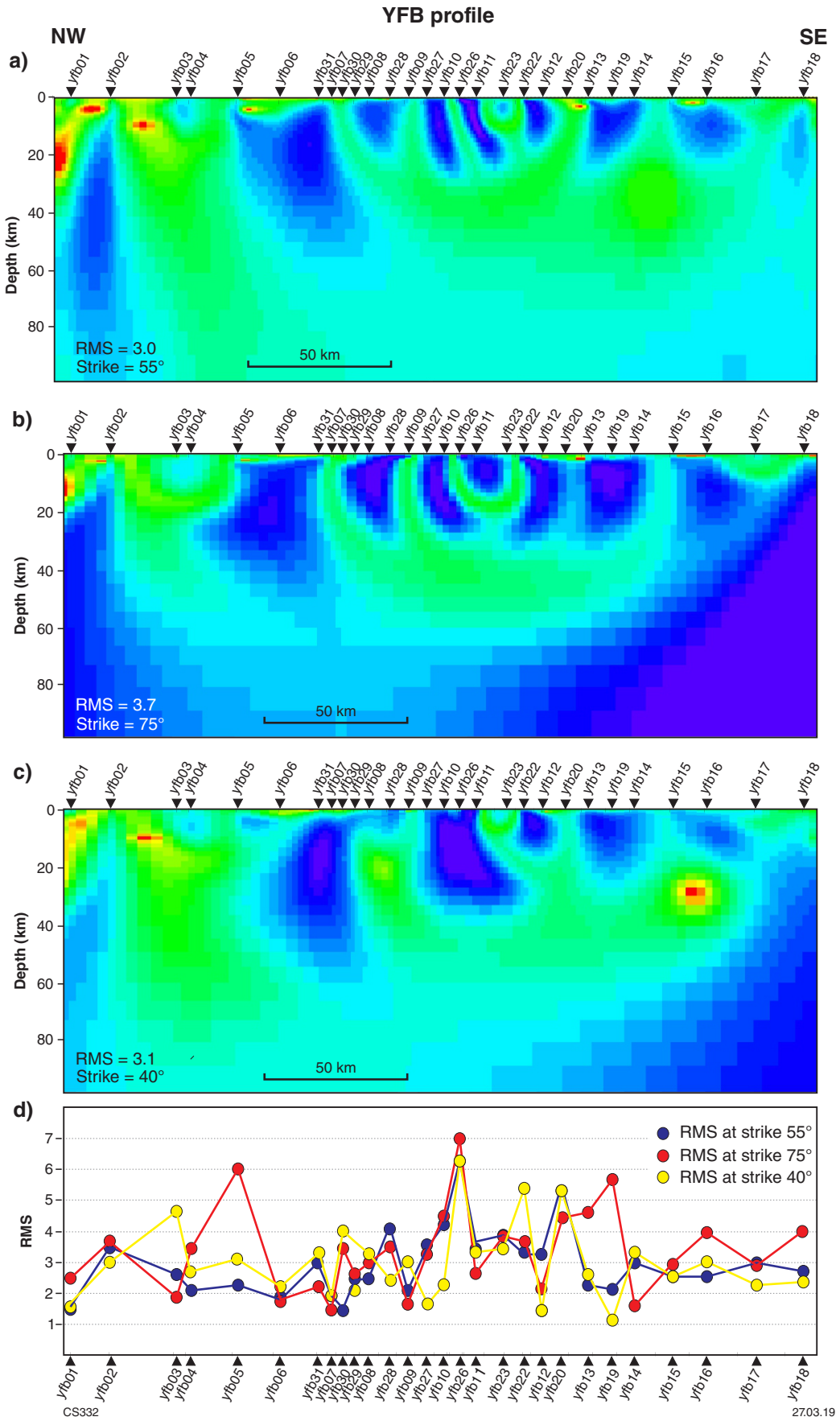

Figure 39. **Results of 2D modelling along the YFB profile using all data not deemed exceptionally noisy, with data rotated to the following geoelectric strike angles: a) 55°; b) 75°; c) 40°; d) RMS misfit values for each site along the profile for each model**

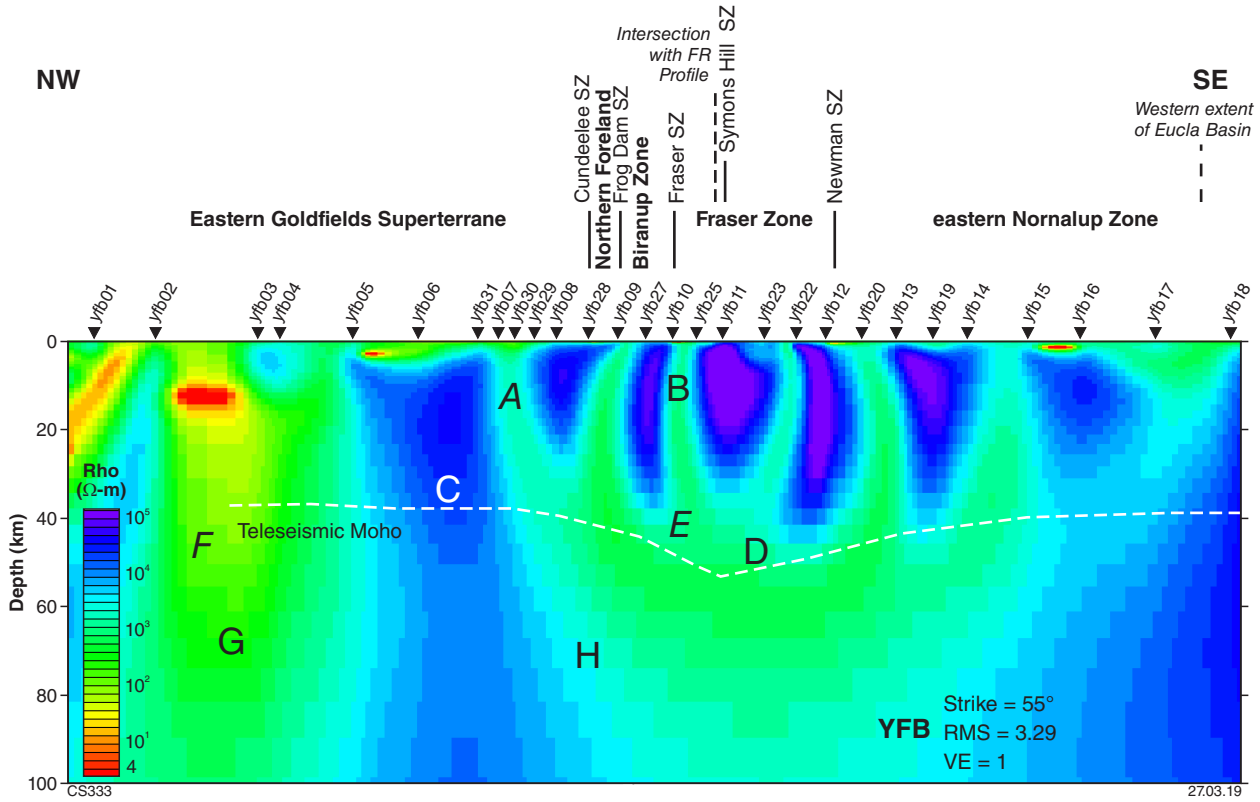

Figure 40. **The preferred 2D model along the YFB profile. Warm colours represent areas that are conductive and blue colours represent areas that are resistive. The letters refer to features tested (italicized letters indicate features that may not be reliable; see text and Appendix 2)**

resistivities are observed through to the upper mantle beneath cbz12, which corresponds to the Spy Hill Shear Zone within the Fraser Zone. Low resistivities at lower crustal depths are broadly consistent with results along the AF3 and FR profiles. Beneath most of the Fraser Zone, crust is resistive (>10 000 Ω-m) to approximately 20 km and is cut by near-vertical, low resistivity features (~1000 Ω-m). Between sites cbz12 and cbz21, the lower crust is imaged as moderately resistive, with values of approximately 1000 Ω-m to depths of 35–40 km; however, the depth to this layer is largely variable at differing strikes so the depth estimate is deemed unreliable. Southeast of site cbz21, high resistivities (>10 000 Ω-m) are imaged from <5 km depth through to the upper mantle.

Feature testing was undertaken on eight features of the preferred conductivity model (Fig. 42; Appendix 2). Feature A is a resistive zone in the upper crust, and features B and C are conductive zones in the upper crust, such as those seen on several profiles. All three features are considered reliable. Features D and E are areas of resistive lower crust, and these two are considered reliable. The depth to the top of Feature F is not a reliable component of the model and if the feature was in the upper mantle, this would be consistent with the data from AF3. Tests on conductivities in the upper mantle indicated features G and H were reliable.

Conclusions base on 2D modelling

The CBZ results are probably less reliable than those from the adjacent profiles, given that the electrical strike angle is nearly parallel to the trend of the section. The absence of a conductive mantle to the southeast may be a function of the insensitivity of the data to the depth of the conductive feature modelled in the lower crust. Most of the narrow conductive zones in the upper crust roughly coincide with known shear zones, although are much broader. The resistive crust under the western part of the eastern Nornalup Zone is similar to that defined in the AF3 profile at a strike of 50°.

2D modelling of the FR profile

Models have been generated with TE-mode recalculated at –5°, –45° and –25° (TM-mode at 85°, 45° and 65°, respectively; Fig. 43). Geoelectric strikes of –45° and –25° are roughly perpendicular to upper-crustal regional geological trends for the southwestern half of the profile, but are parallel to regional geological trends along the northeastern half of the profile, which corresponds to the Fraser Zone. The 90° ambiguity allows for strikes of –45° and –25°, which could be interpreted to relate to the northwesterly trends of greenstone belts and major structures in the Yilgarn Craton, as shown in regional gravity and magnetic data (Fig. 2). The seismic reflection

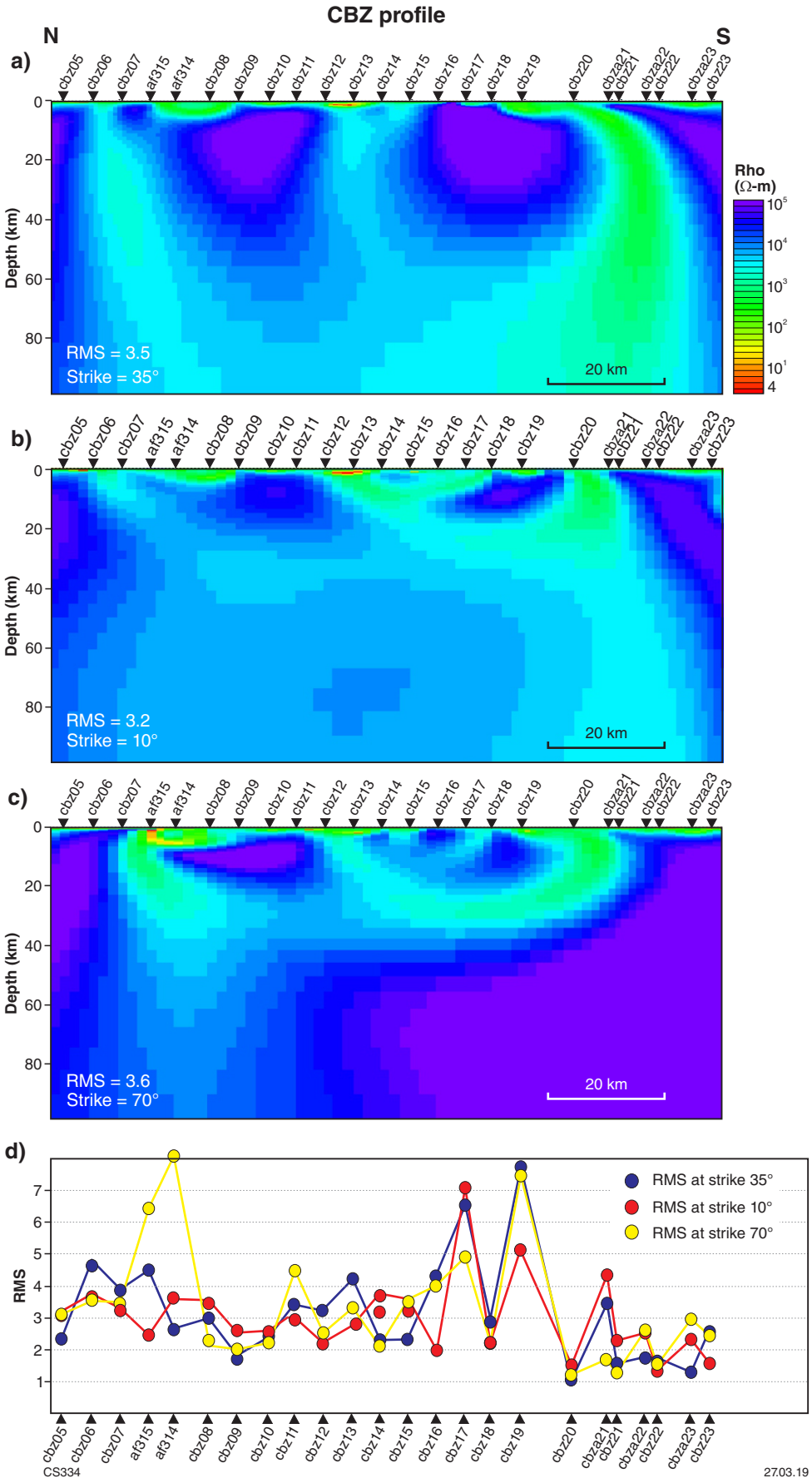

Figure 41. **Results of 2D modelling along the CBZ profile using all data not deemed exceptionally noisy, with data rotated to the following geoelectric strike angles: a) 35°; b) 10°; c) 70°; d) RMS misfit values for each site along the profile for each model**

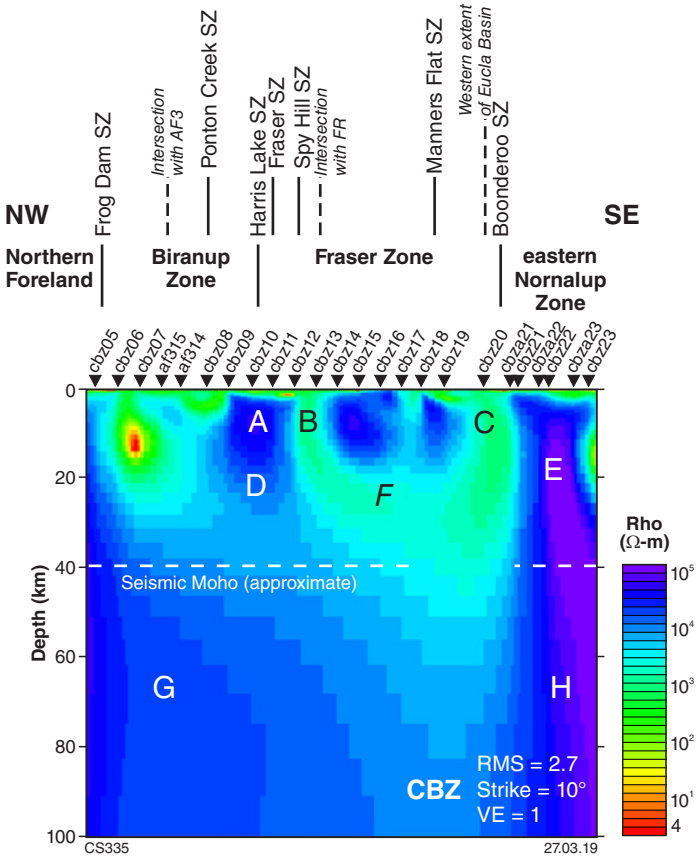

Figure 42. **The preferred 2D model along the CBZ profile. Warm colours represent areas that are conductive and blue colours represent areas that are resistive. The letters refer to features tested (italicized letters indicate features that may not be reliable; see text and Appendix 2)**

profiles suggest Yilgarn Craton crust underlies the Biranup and Fraser Zones (Fig. 3), which would be consistent with TE-mode perpendicular to the FR profile. However, given the degree of Proterozoic reworking, it is highly likely that where the Yilgarn trends have been subjected to Proterozoic deformation and magmatism, they have been greatly modified so that the geological strike at depth is dominantly northeasterly, as indicated by passive seismic data (Sippl et al., 2017a,b).

Results of 2D modelling along the FR profile using all of the data not deemed excessively noisy or 3D are shown in Figure 44. The models generated at differing strike angles show strong similarities in the subsurface conductivity structure. There is little difference in the overall model RMS value, which ranges from 3.7 for a strike of –5° to 3.5 for a strike of –25°. High RMS values are observed for the northeasternmost sites; however, it is presumed that for these sites the profile runs along strike at crustal depths and the TE- and TM-modes have been assigned incorrectly.

The preferred model along the FR profile was generated with TE-mode data at a strike of –25° (Fig. 44). The southwestern half of the profile exhibits moderate resistivities (1000 Ω-m) to at least 10 km beneath the Biranup Zone. The Biranup Zone, in general, shows high resistivities (>10 000 Ω-m) to at least 20 km depth that are cut by moderately to steeply dipping, less resistive features. Some of these features may relate to major shear zones, although they are much broader than the shear zones themselves. The Bishops Hat Shear Zone and a shear zone-bound sliver of Northern Foreland are examples. Beneath the resistive upper crust of the Biranup Zone there is a moderately conductive zone (~500 Ω-m) at lower crustal depths. Where the profile crosses the Fraser Shear Zone, there is a sharp boundary between the conductive material to the southwest, and a very resistive lower crust and upper mantle to the northeast. As the crustal structure to the northeast is likely parallel to profile orientation, the conductivity models are deemed unreliable; however, this change appears to continue into the upper mantle and a similar observation is noted along the AF3 profile. Along the length of the FR profile, significant variations are imaged in both the crust and the upper mantle.

Feature testing undertaken along the FR profile was performed on some of the near-vertical, low resistivity structures in the upper crust (features A, B and C), the continuity and thickness of the lower crustal conductor (features D, E, F and G), and the change in upper-mantle resistivity from southwest to northeast (features H and I; Fig. 44). Features A, B and C were found to be reliable aspects of the conductivity model. Features D and E are less reliable. The high resistivities in the vicinity of F are reliable, but not feature G. Features H and I are reliable, supporting the observed lateral change in resistivity in the mantle. Of possible significance is a low resistivity zone (feature C) that broadly corresponds to the Nova–Bollinger Ni–Cu deposit, which is located about 8 km southeast of fr05 (Fig. 2), and southeast of the Symons Hill Shear Zone.

Conclusions based on 2D modelling

The FR profile was designed to detect the effects of deep structures trending roughly northwest–southeast, which potentially correlate with the southward extensions of major terrane-bounding faults and shear zones in the Yilgarn Craton. A change in mantle resistivity near the southwestern end of the Fraser Zone is consistent with the along-strike change in surface geology in this area, and with the different structure of the Moho observed in the receiver function data. The location of the change in resistivity roughly coincides with the southward extension of the boundary between the Kalgoorlie and Kurnalpi Terranes.

The complexity of the upper-crustal structure in the southwestern part of the FR profile is difficult to reconcile in the MT data, as it is in other geophysical datasets because of intersecting units and the 'S-bend' feature (Spaggiari et al., 2014a; Spaggiari, 2016; Quentin de Gromard et al., 2017). However, a narrow, less resistive zone (feature B) coincides with the Biranup Zone, and the shear zone-bounded sliver of Northern Foreland rocks west of this correlates with a more resistive zone (Fig. 44). In the northeastern part of the FR profile, the pattern of a resistive crust cut by narrow, more conductive zones, as observed in other profiles, is repeated. This indicates variable resistivity within the Fraser Zone. A less resistive zone is evident below the projected position of the Nova–Bollinger Ni–Cu deposit (feature C, Figs 44, 45).

The deep lateral change in resistivity of the mantle is a robust feature of the model, and corresponds with the southern termination of the Fraser Zone. The other profiles suggest the Proterozoic mantle is more conductive than the

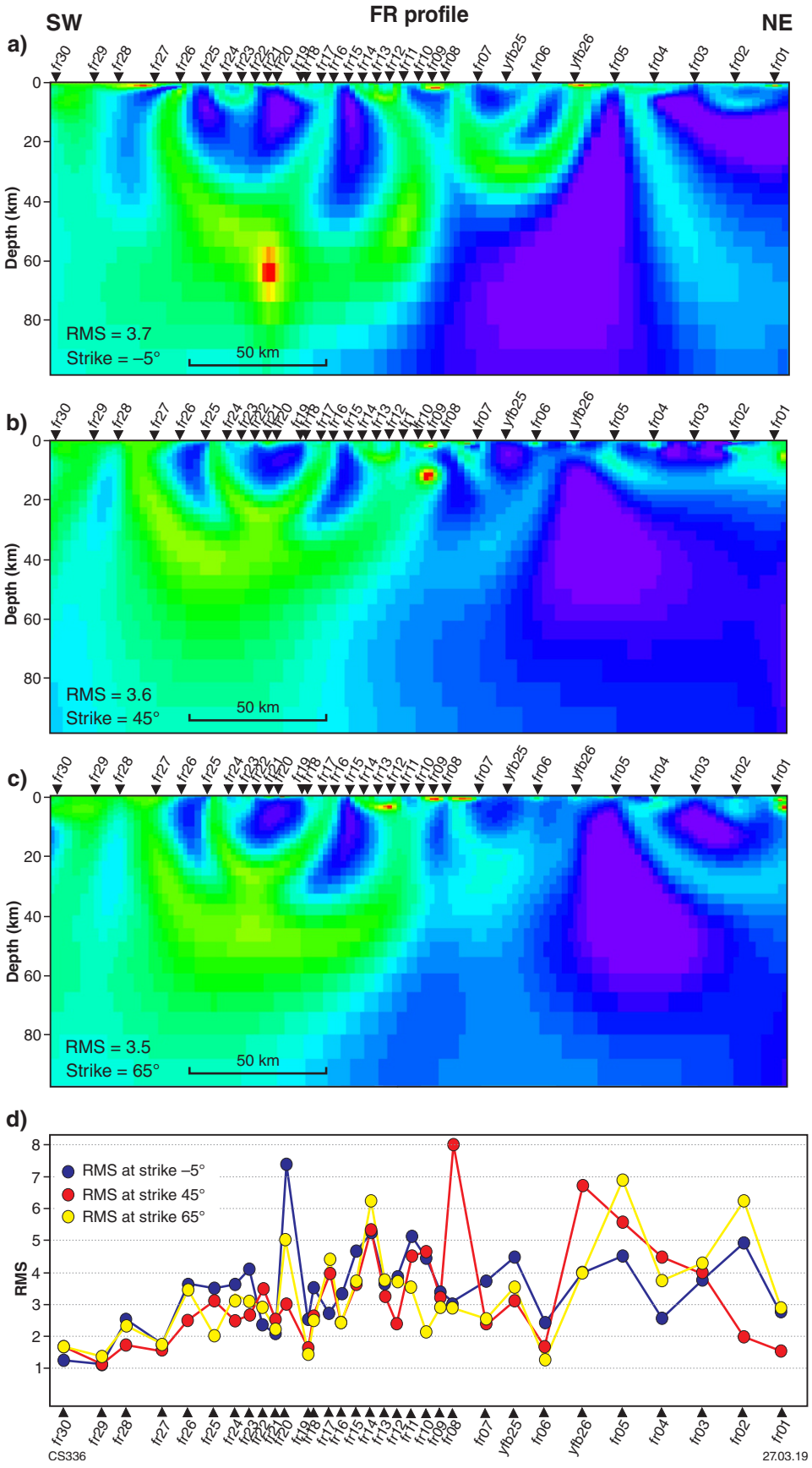

Figure 43. **Results of 2D modelling along the FR profile using all data not deemed exceptionally noisy, with data rotated to the following geoelectric strike angles: a) –5°; b) 45°; c) 65°; d) RMS misfit values for each site along the profile for each model**

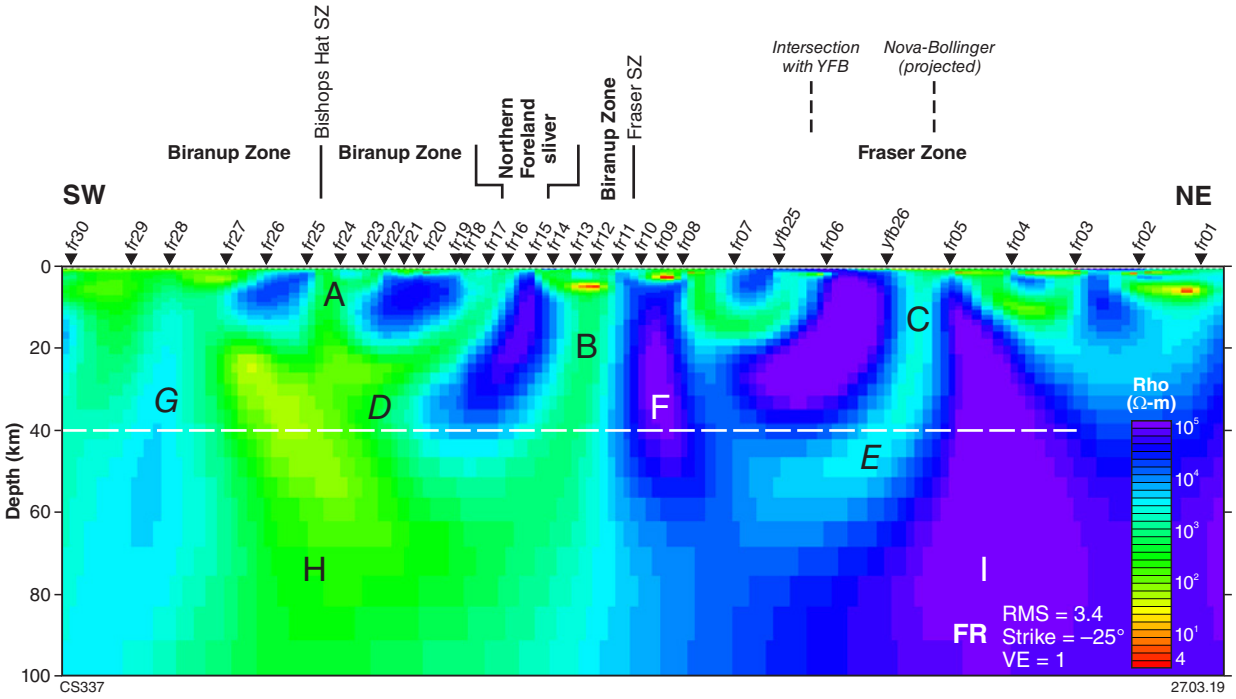

Figure 44. **The preferred 2D model along the FR profile. Warm colours represent areas that are conductive and blue colours represent areas that are resistive. The letters refer to features tested (italicized letters indicate features that may not be reliable; see text and Appendix 2)**

Archean mantle and, as such, is expected to be relatively conductive in this profile. The fact that the FR profile is close to geological strike, at least within the Fraser Zone, may have affected the result. One possible explanation is that the transect may lie close to the conductivity boundary observed along both the AF3 and YFB profiles, which in turn is at an oblique angle to both the surface geological strike and the FR transect itself. Furthermore, this conductivity boundary is potentially more geometrically complex than can be resolved here. Note that the axis of the zone of increased crustal thickness, plotted on Figure 2, shows the southwestern half of the FR profile following the axis, but the two diverge to the north. It is speculated that the conductive lower crust on the FR profile is related to the along-strike continuation of the conductive zone that coincides with the lower-crustal, nonreflective zone described in the AF3 profile.

3D data modelling

Traditional applications of the MT method have relied on the assumption that resistivity variations can be represented in a 2D space. However, 3D near-surface complications can severely distort electric fields, causing variations in geoelectric strike as well as static shift. In 2D inversions these complications must be dealt with through rigorous strike analysis, decomposition analysis, static shift removal and internal competency tests before a reasonable 2D interpretation can be made. In 3D inversion, near-surface complications can be modelled directly, simplifying the process. The parallelized forward inversion code ModEM, of Egbert and Kelbert (2012), was used to generate 3D models of the subsurface beneath the survey area. The inversion code is based on a standard, minimum-structure, nonlinear conjugate gradients algorithm. Within the inversion process, the ModEM algorithm seeks to minimize the penalty function Φ, which consists of a data regularization and a model regularization term (Egbert and Kelbert, 2012):

$$\Phi(m,d) = (d - f(m))TC - 1d(d - f(m)) + \lambda(m - m0)$$
$$TC - 1m(m - m0)$$

Equation 1

where d is the observed data, and m is an M-dimensional Earth conductivity model parameter vector that provides an adequate fit to d. Here, f(m) defines the forward mapping, Cd (see below) the data covariance, m0 the prior model, Cm (see below) the model covariance or regularization term, and λ is a trade-off parameter.

Parameter testing of the 3D model

A series of inversion parameters and settings were varied in order to determine their influence on the final inversion results, and to identify optimal inversion parameters for the Albany–Fraser MT dataset. Parameters tested include the trade-off value λ, the model regularization parameters (smoothing and a priori model), the frequency ranges included in the inversion and the orientation of the inversion coordinate system. Models were generated using data from the full impedance tensor (Z) independently, and from Z with the vertical transfer function (VTF) data. These initial inversions were performed on a subset of the data (termed ‘Center models’) comprising the central 79 sites (Fig. 45). The central portion of each mesh consists of cells that are 2500 x 2500 m and is padded by 10 cells on each side. The mesh consists of 50 layers, with a top layer that is 25 m thick and that extends to a depth of

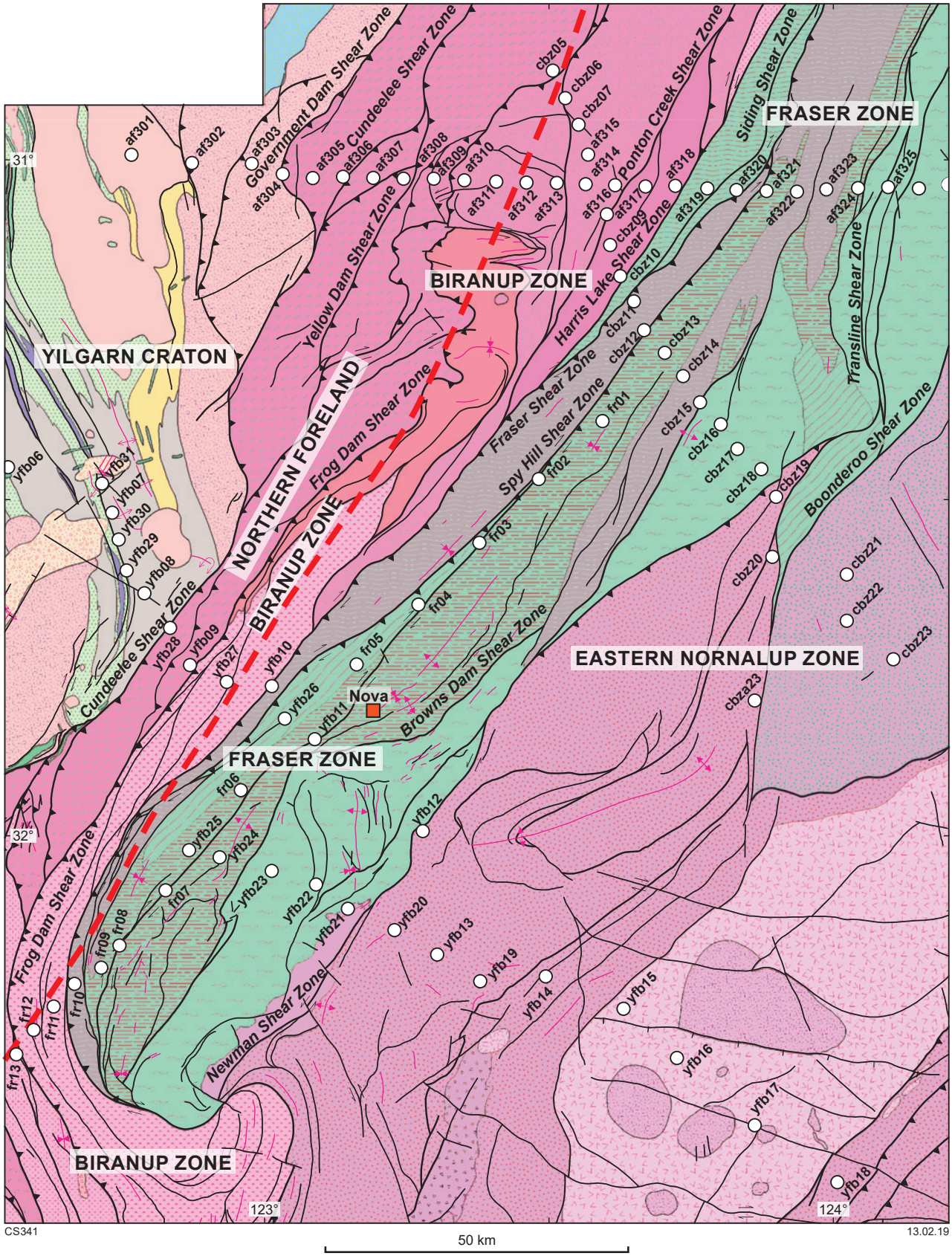

Figure 45. **Extract from Spaggiari (2016) of the east Albany–Fraser Orogen pre-Mesozoic bedrock map of the central region of the MT survey area used for 3D modelling. The MT stations are labeled and shown as white dots. The axis of the zone of thicker crust is marked with a red dashed line. Refer to Spaggiari (2016) for information on individual units and structures**

500 km. The results of the variation of inversion parameters are summarized in Table 2.

Lambda and smoothing parameters

Values of 1000 (Fig. 46a), 100 (Fig. 46b), and 1 (Fig. 46c) were tested for the initial damping parameter (λ). A λ of 1 yielded the lowest RMS value of 1.84 in the fewest number of iterations (Table 2).

The model covariance matrix (Cm) characterizes the expected magnitude and smoothness of resistivity variations relative to the prior model. It is specified in terms of 3D smoothing and scaling operators similar to the scheme of Siripunvaraporn and Egbert (2000). The inversion algorithm does not only distinguish between different smoothing parameters in horizontal and vertical directions, but also allows for different horizontal smoothing parameters in each layer. The ModEM algorithm penalizes smoothed deviations from a prior model as part of the model update process, and the inversion tends to keep or return to the assumed prior resistivities where the model is poorly constrained.

For the Center 3D models, horizontally isotropic smoothing was applied to the data in the geographic coordinate system. Values tested include a uniform smoothing of 0.3 in the two horizontal and vertical directions (Fig. 46d), increased horizontal smoothing in the top layers with values of 0.5 to 0.3 by layer 16 (equivalent to approximately 750; Fig. 46c), and increased horizontal smoothing in the top layers with a vertical value of 0.1 (Fig. 46e). The lowest RMS value of 1.84 was obtained by using a higher near-surface smoothing value and a deeper horizontal and vertical value of 0.3 (Fig. 46c). This model also shows smoother near-surface structure and higher resolution at greater depths (to 40–50 km).

Starting resistivity value

Variations in the starting model were tested to determine a reasonable prior model or background resistivity model, which is used by the ModEM inversion scheme both to define the penalty functional, and as a starting point for the optimization. Independent models were initiated with uniform resistivity values of 50, 100, 500, 1000 and 2000 Ω-m. Subsequently a coarse 3D bathymetry of the seawater south of the Australian coastline, with a value of 0.3 Ω-m, was included in the starting model and fixed during inversions (Fig. 47; Table 2).

With the exception of the deep subsurface of the southeast section of the survey area, the overall conductivity structure remains robust between the different models. With a uniform starting model, the lowest RMS values obtained were 1.829 with a starting resistivity of 100 Ω-m and 1.844 with a starting resistivity of 500 Ω-m. However, the total number of iterations required to reach these values was 259 and 172, respectively (Table 2). Due to the similarities in the final conductivity structure and RMS value, and the long computing time required for each iteration, a starting value of 500 Ω-m was chosen for further inversions.

Significant differences are observed in the deep conductivity structure (>20 km) beneath the southeastern end of 2D profile YFB between the models with varying starting values. The conductivity values remain closer to those of the starting model, an indication that the data in this region are not sensitive to the deep structure.

Error floor

Impedance error floors were systematically set to 7%, 5% and 3% of $|Zxy*Zyx|^{1/2}$, for both the diagonal and off-diagonal elements, to determine the appropriate error floor that yields a reasonable RMS value (Fig. 48). For the VTF data, constant error bounds of 0.03 were applied. Results show that the 3D resistivity structure beneath the survey area is similar for each of the three models. The RMS values obtained after over 200 iterations were 1.85 at an error floor of 7%, 2.81 at 5%, and 4.45 at 3%. We opted to use an impedance error floor of 5% for the preferred models, the lowest error floor that yields an acceptable misfit value.

Frequency ranges and data type

Preliminary 3D inversion results indicate that the models are not well resolved at depths greater than approximately 40 km when inverting the entire frequency spectrum. The data were divided into three separate frequency ranges: high frequencies (hf) that include 12 periods between 0.007 and 12 s, low frequencies (xl) that include 12 periods between 2.5 and 1500 s, and the full range of frequencies (19f) consisting of 19 periods between 0.007 and 2000 s. Using the data from Z, models were initially generated using the hf data only, then the xl only data were inverted using the final model of the hf data as the starting model, and finally the 19f data were used (Fig. 49a). In an attempt to further resolve the deeper structure, the xl data were modelled first, followed by the hf data and finally the 19f data (Fig. 49b). When the low frequency data were inverted first, conductivity variations were imaged at slightly greater depths (up to 50 km) and the final RMS value was significantly improved, resulting in a value of 2.30.

The full impedance tensor (Z) and VTF data were inverted together using the data at the xl range, then the hf range, and finally over the full 19f range (Fig. 49c). Results show that the resistive crustal-scale features extend to much greater depths when the transfer function data are included, particularly along the northern extent of the survey area. These results are more consistent with the models generated along the 2D profiles. Final models presented here include Z only and Z with the VTF data, and were generated by initially inverting the long-period data only, then adding the full frequency range.

Orientation of coordinate system

ModEM uses a Cartesian, right-handed coordinate system with Z pointing positive downwards where data need to be rotated to align with the inversion coordinate system. We tested the inversion coordinate systems with the x-axis aligned with geographic north (0°), and with the dominant geoelectric strike directions of 30° and 48° (Fig. 50). With the model mesh and data at 0° (Fig. 50a), the model grid dimensions are 96 x 78 x 50 (rows, columns and depth layers, respectively). At an angle of 48° (Fig. 50c), the model grid dimensions are 96 x 100 x 50 and at 30° (Fig. 50e), 97 x 100 x 50.

Table 2. List and root-mean-square (RMS) results of variations in 3D inversion parameters and settings for the models generated from the Albany–Fraser MT dataset. Annotations for period ranges are: hf = 12 periods at 0.007 – 12 s, xl = 12 periods at 2.5 – 1500 s, and 19f = 19 periods at 0.007 – 2000 s

Data set	*Rotation (°)*	*Data*	*Error floor (%)*	*Frequencies*	*λ*	*Smoothing*	*Starting resistivity*	*Iterations*	*RMS*	*Figure*
Center	0	Full tensor	7.00	hf – xl – 19f	100	x = y = z = 0.3	500	158	2.61	46d
Center	0	Full tensor	7.00	hf – xl – 19f	100	x = y = 0.5 – 0.3, z = 0.3	500	167	2.225	46b
Center	0	Full tensor	7.00	hf – xl – 19f	1000	x = y = 0.5 – 0.3, z = 0.3	500	196	2.176	46a
Center	0	Full tensor	7.00	hf – xl – 19f	1	x = y = 0.5 – 0.3, z = 0.3	500	172	1.844	46c, 47c, 48a
Center	0	Full tensor	7.00	hf – xl – 19f	1	x = y = 0.5 – 0.3, z = 0.1	500	271	2.001	46e
Center	0	Full tensor	3.00	hf – xl – 19f	1	x = y = 0.5 – 0.3, z = 0.3	500	309	4.449	48c
Center	0	Full tensor	5.00	hf – xl – 19f	1	x = y = 0.5 – 0.3, z = 0.3	500	274	2.806	48b,49a
Center	0	Full tensor	7.00	hf – xl – 19f	1	x = y = 0.5 – 0.3, z = 0.3	50	248	1.969	47a
Center	0	Full tensor	7.00	hf – xl – 19f	1	x = y = 0.5 – 0.3, z = 0.3	100	259	1.826	47b
Center	0	Full tensor	7.00	hf – xl – 19f	1	x = y = 0.5 – 0.3, z = 0.3	1000	182	2.007	47d
Center	0	Full tensor	7.00	hf – xl – 19f	1	x = y = 0.5 – 0.3, z = 0.3	2000	205	2.137	47e
Center	0	Full tensor	5.00	xl – hf – 19f	1	x = y = 0.5 – 0.3, z = 0.3	500	284	2.301	49b, 50a
Center	0	Full tensor	7.00	hf – xl – 19f	1	x = y = 0.5 – 0.3, z = 0.3	500+ocean	255	1.706	47f
Center	0	Full tensor	5.00	xl – hf – 19f	1	x = y = 0.5 – 0.3, z = 0.3	500+ocean	313	2.811	51a, 52a
Center	0	Full tensor + VTF	5.00	xl – hf – 19f	1	x = y = 0.5 – 0.3, z = 0.3	500+ocean	263	2.845	51b, 52b
Center	48	Full tensor	5.00	xl – hf – 19f	1	x = y = 0.5 – 0.3, z = 0.3	500	271	2.545	50c
Center	30	Full tensor	5.00	xl – hf – 19f	1	x = y = 0.5 – 0.3, z = 0.3	500	263	2.28	50e
Center	30	Full tensor + VTF	5.00	xl – hf – 19f	1	x = y = 0.5 – 0.3, z = 0.3	500+ocean	296	3.324	51d
Center	30	Full tensor	5.00	xl – hf – 19f	1	x = y = 0.5 – 0.3, z = 0.3	500+ocean	245	2.381	51c
Center	30	Full tensor + VTF	5.00	xl – hf – 19f	1	x = 0.5 – 0.3, y = 0.5, z = 0.3	500+ocean	301	3.739	51e
All	all data	Full tensor	5.00	xl – hf – 19f	1	x = y = 0.5 – 0.3, z = 0.3	500+ocean	310	3.737	52c, 53a
All	all data	Full tensor + VTF	5.00	xl – hf – 19f	1	x = y = 0.5 – 0.3, z = 0.3	500+ocean	286	4.182	52d, 53b

Note: hf, high frequencies; xl, low frequencies; 19f, full range of frequencies of 19 periods; λ, initial damping parameter

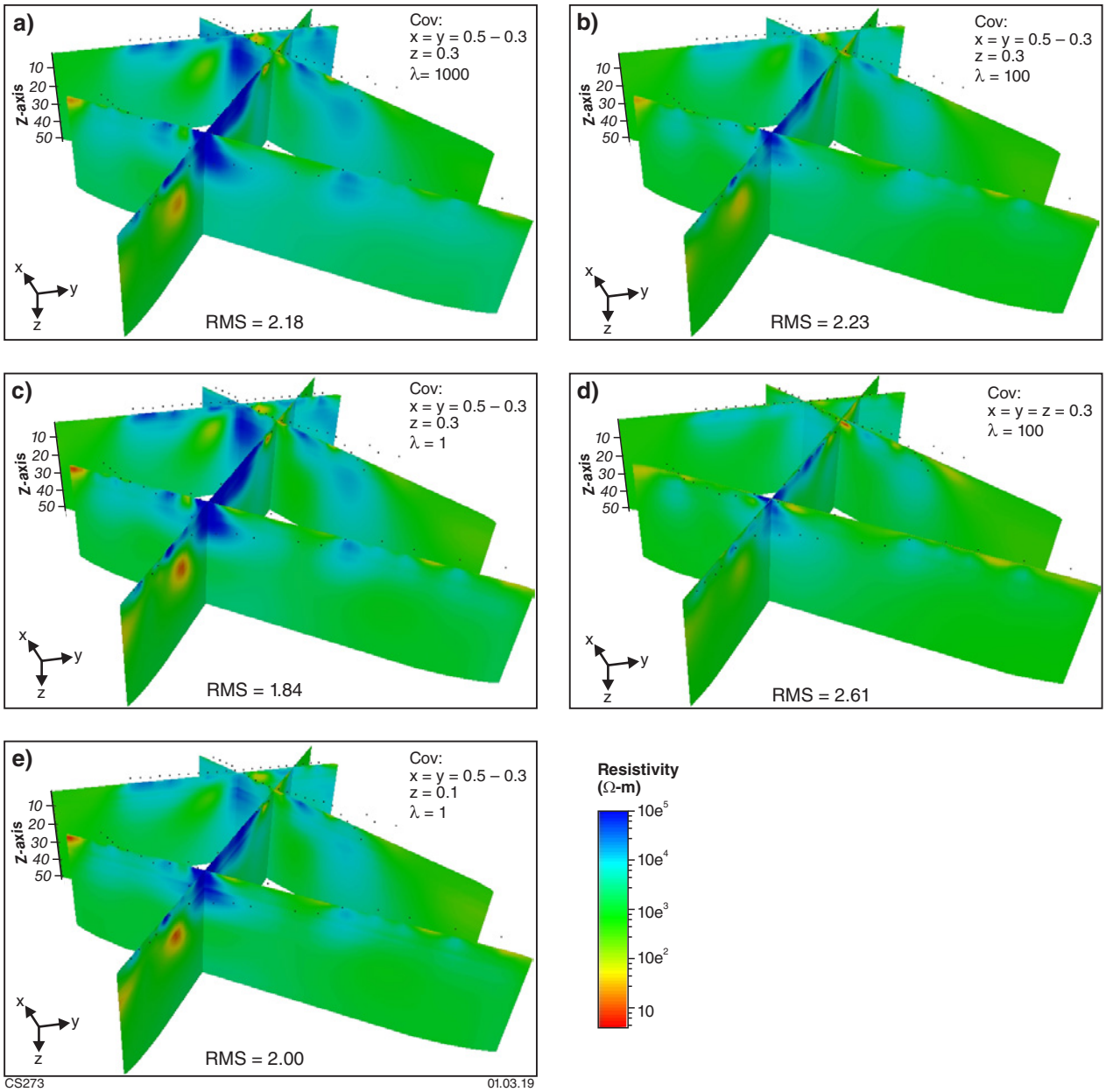

Figure 46. Results of 3D inversions using various initial damping factors (λ) and smoothing parameters

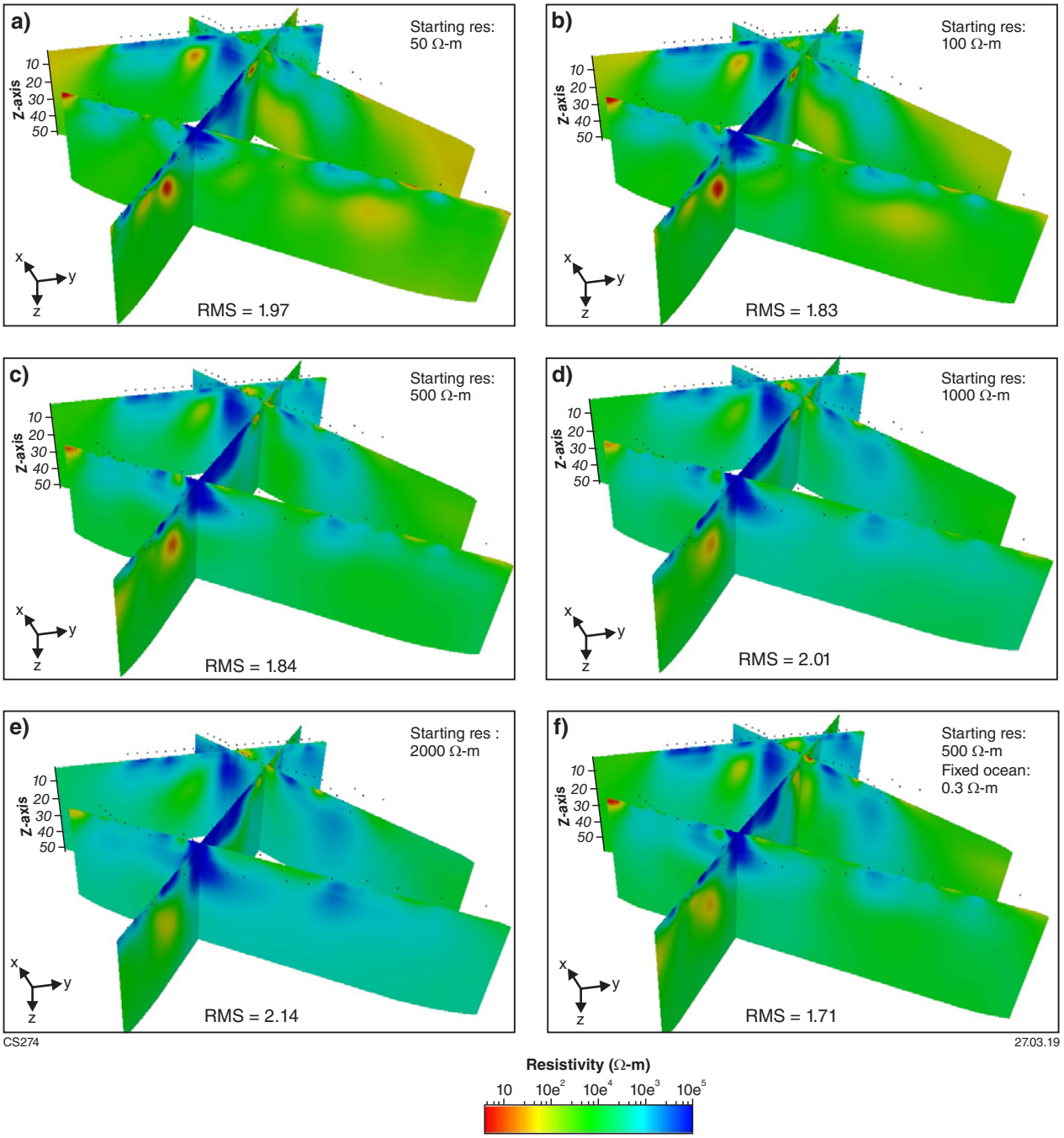

Figure 47. **Results of 3D inversions using various starting models: a) uniform grid of 50 Ω-m; b) 100 Ω-m; c) 500 Ω-m; d) 1000 Ω-m; e) 2000 Ω-m; f) starting land resistivity value of 500 Ω-m and fixed ocean value of 0.3 Ω-m**

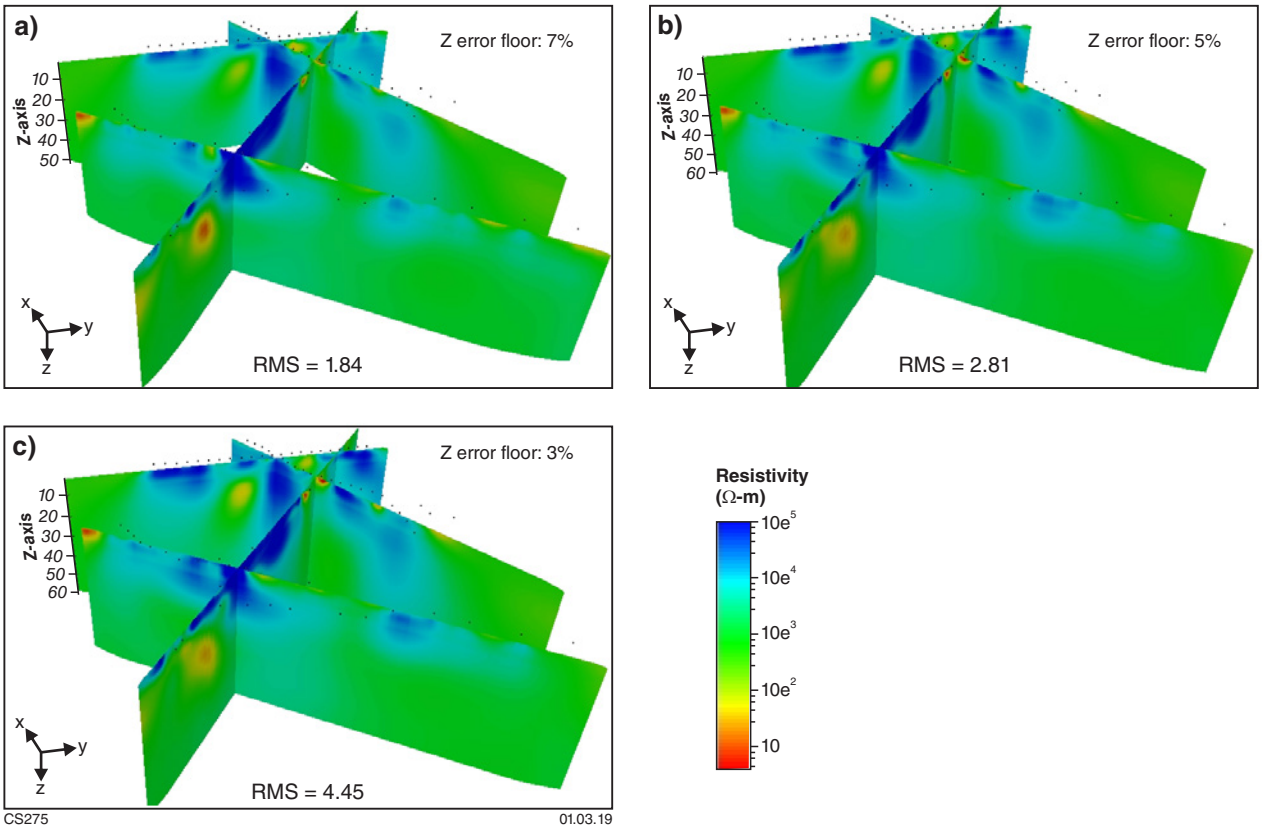

Figure 48. Results of 3D inversions using various impedance error floor values: a) 7%; b) 5%; c) 3%

The inversion results show some differences in the conductivity structure depending on the coordinate system of the mesh and data, indicating that the models are dependent on the geoelectric strike angle. The lowest RMS value of 2.28, using data from Z only, was obtained with the x-axis and data at a strike angle of 30° (Fig. 50e); however at geographic north, the RMS value was only slightly higher at 2.30. It has been shown that where the data are strongly 2D with a uniform geoelectric strike, directly rotating the mesh might be more accurate (e.g. Tietze and Ritter, 2013). However, as the regional Albany–Fraser MT dataset has variable geoelectric strikes across the survey area, and low RMS values are observed, our preferred models have been generated using the geographic north (0°) coordinate system.

In modelling the Albany–Fraser MT dataset, horizontally isotropic smoothing was applied to the data in the geographic coordinate system. Where the model and data were rotated to a geoelectric strike direction of 30°, both horizontal isotropic smoothing and increased smoothing parallel to strike was applied in separate inversions. This model was generated using a starting model that included bathymetry information, which is discussed in the next section.

Effects of ocean bathymetry in the starting model

Coarse 3D bathymetry was included as a priori information to observe the effects of nearby seawater on the resulting models (Fig. 51). A resistivity of 0.3 Ω-m was assigned to the seawater and these cells of the model were fixed for all subsequent inversions. The remaining cells were set to 500 Ω-m. Inversions were executed at geographic coordinates using horizontally isotropic model smoothing (Fig. 51a,b), and at 30° using both horizontally isotropic smoothing (Fig. 51c,d) and with smoothing increased parallel to strike (Fig. 51e).

Ocean depths within 200 km of the nearest MT site are shallow (<500 m) and the inclusion of bathymetric information does not appear to have much influence on the resulting resistivity model. RMS values are comparable or slightly improved when modelling the impedance tensor and VTF data together. Increased smoothing along geoelectric strike direction yielded a model with a significantly higher RMS value of 3.73 (Fig. 51e). Preferred models have been generated using the ocean depth information in the a priori models.

Preferred 3D models

Our preferred models for the Center dataset and the entire dataset are shown in Figures 52 and 53. The Center model has a mesh comprising 96 rows, 78 columns, and 50 depth layers, with the central portion consisting of cells that are 2500 x 2500 m and padded by 10 cells on each side. The whole data model has a mesh of 85 rows, 121 columns and 50 depth layers, where the central portion consists of cells that are 4000 x 4000 m.

The models were generated with the x-axis aligned at geographic north (0°), from a starting model of 500 Ω-m for land resistivity and ocean resistivity fixed at 0.3 Ω-m. We used an error floor of 5% of $|Zxy*Zyx|^{1/2}$ for both the diagonal and off-diagonal elements, and constant error bounds of 0.03 for the VTF data. Increased horizontal smoothing in the top layers with values of 0.5 to 0.3 by layer 16 was applied with a vertical smoothing value of 0.3.

The preferred models for the Center dataset yielded an RMS value of 2.81 using data from the full impedance tensor (Fig. 52a) and data from the full impedance tensor and VTF (Fig. 52b). Map view slices of the preferred models are shown in Figure 53 at depths of 1, 5, 10, 20, 30, 40 and 50 km. The preferred models for the whole dataset resulted in a final RMS value of 3.74 using the full impedance tensor only (Fig. 52c) and 4.18 using the full impedance tensor and VTF data (Fig. 52d). The fit of the data to the final whole dataset model is illustrated in Figure 54. In general, there is a reasonable fit for most of the data with values <5.0, particularly with the Z components and the total RMS values. However, at the sites at the eastern end of the AF3 transect, the model poorly fits the data in all inverted components. The poor fit at these sites may be due to a lack of 3D site coverage.

Interpretation of the 3D model

The results of the 3D inversion can be used to interpret regional, large-scale conductivity features with greater reliability than the 2D inversions. However, due to limitations on inversion control, mesh discretization of the subsurface and computational requirements in 3D inversion, 2D models are currently better at providing detailed resolution of small-scale features.

Figure 53 shows depth slices at a range of depths up to 50 km. Slices at shallower depths show discrete zones of varying conductivity, indicating that the scale of electrical variations is much smaller than the sampling interval. At depths greater than about 10 km, the variations become smoother, but there are still few features which can be correlated between the different profiles.

Where the AF3 profile crosses the Northern Foreland a zone of higher resistivity is evident (labelled A in Fig. 53). This zone is apparent in the 5 to 50 km depth slices, which indicates that it extends from the upper crust to the upper mantle. However, there appears to be little evidence for it to the southwest where the YFB profile crosses the Northern Foreland, although in that area the Northern Foreland is

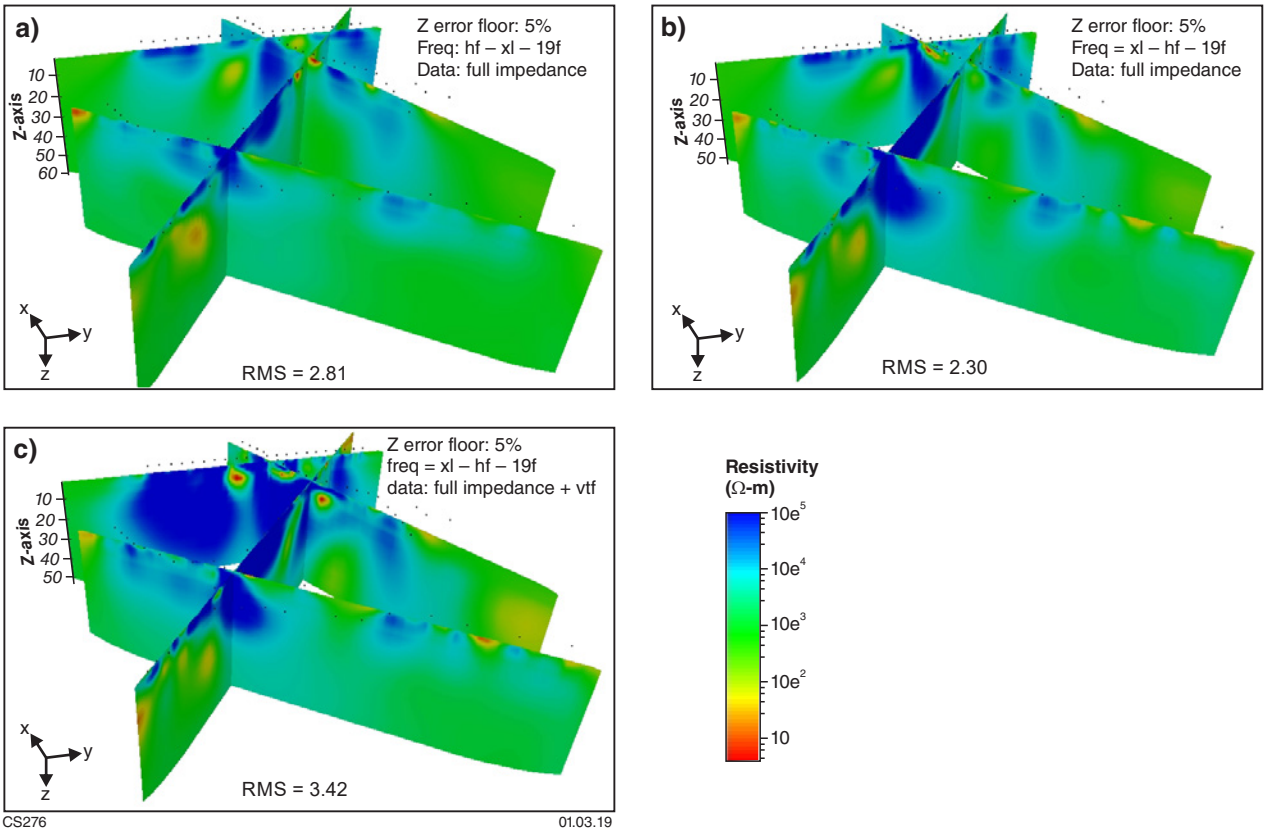

Figure 49. **Results of 3D inversions using varying frequency ranges and data types: a) inversion of the full impedance tensor data at high frequency range followed by addition of the low frequency data; b) inversion of the full impedance tensor data at low frequency range followed by addition of the high frequency data; c) inversion of the full impedance tensor data and vertical field data. Frequency ranges: hf = 12 periods between 0.007 – 12 s; xl = 12 periods between 2.5 – 1500 s, and 19f = 19 periods between 0.007 – 2000 s**

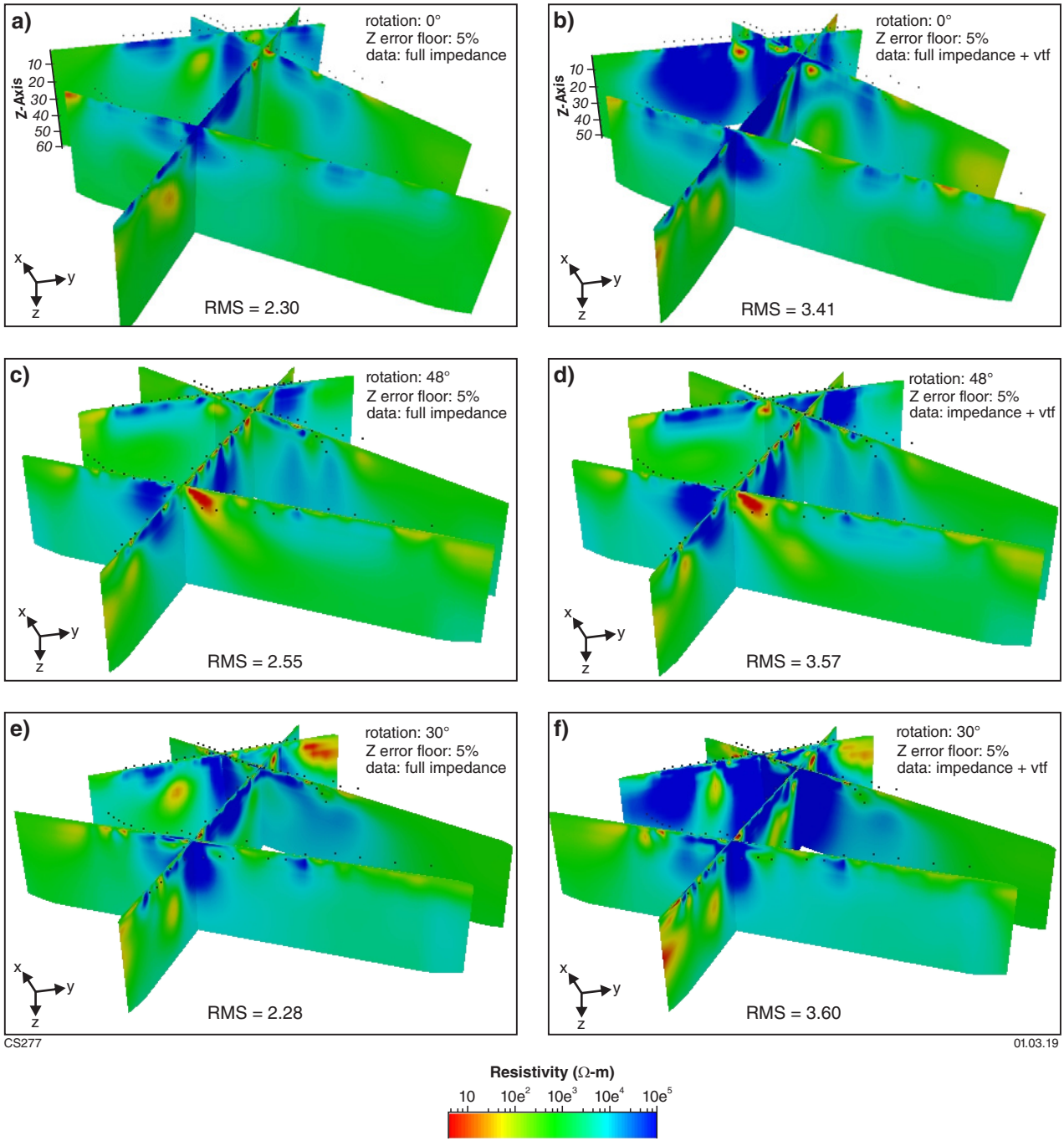

Figure 50. **Results of 3D inversions with x-axis of mesh and data aligned with: a) geographic north (0°) using the full impedance tensor only; b) geographic north (0°) using the full impedance tensor and the vertical field data; c) the dominant geoelectric strike direction of 30° inverting the full impedance tensor only; d) the dominant geoelectric strike direction of 30° inverting the full impedance tensor and the vertical field data; e) the dominant geoelectric strike direction of 48° inverting the full impedance tensor; f) the dominant geoelectric strike direction of 48° inverting the full impedance tensor and the vertical field data**

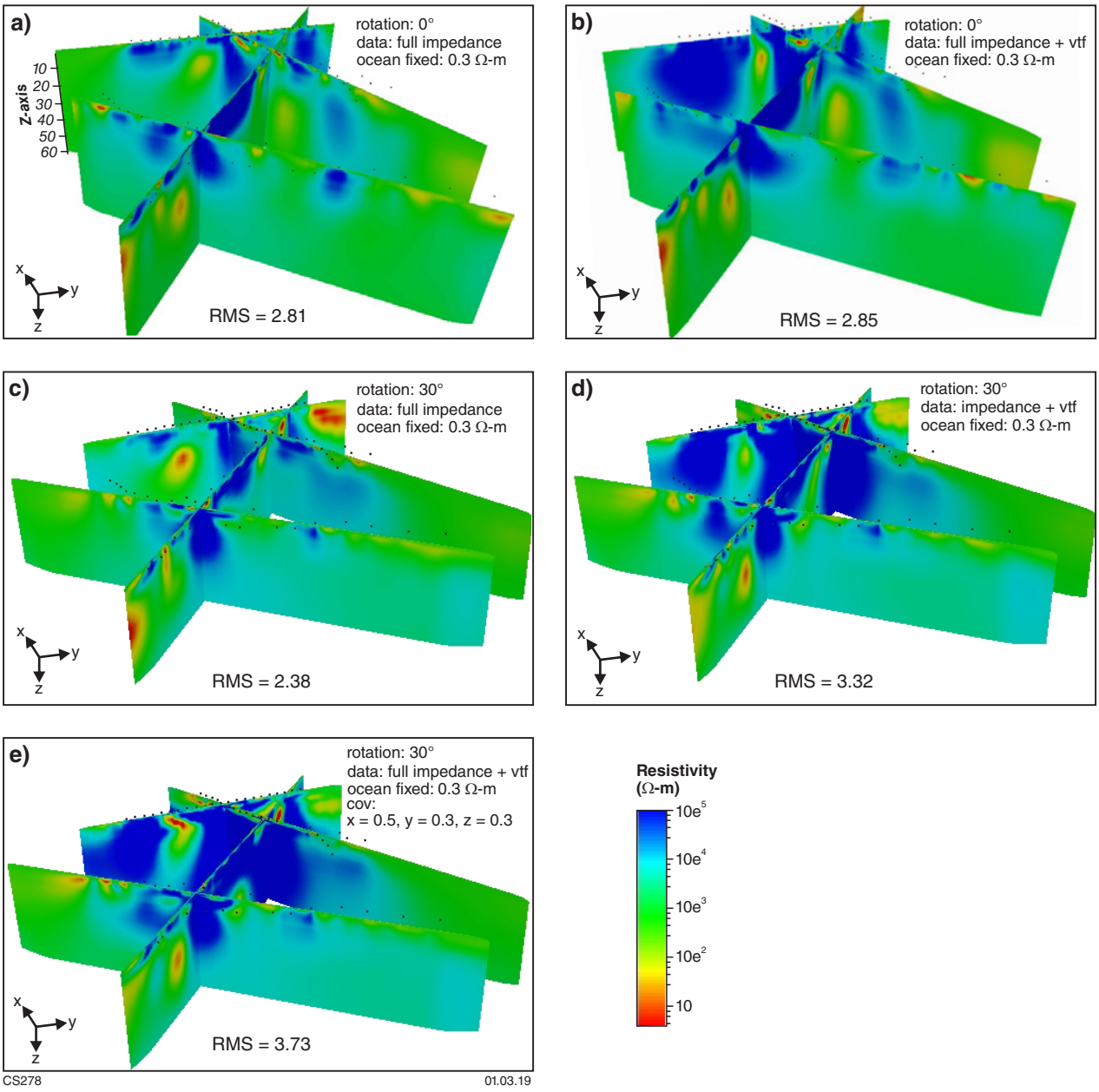

Figure 51. **Results of 3D inversion using a fixed ocean resistivity value of 0.3 Ω-m in the starting models and inverting: a) the full impedance tensor data at geographic north; b) the full impedance tensor and VTF data at geographic north; c) the full impedance tensor at 30° with uniform horizontal smoothing; d) the full impedance tensor with VTF data at 30° with uniform horizontal smoothing; e) the full impedance tensor with VTF data at 30° with increased smoothing along geoelectric strike**

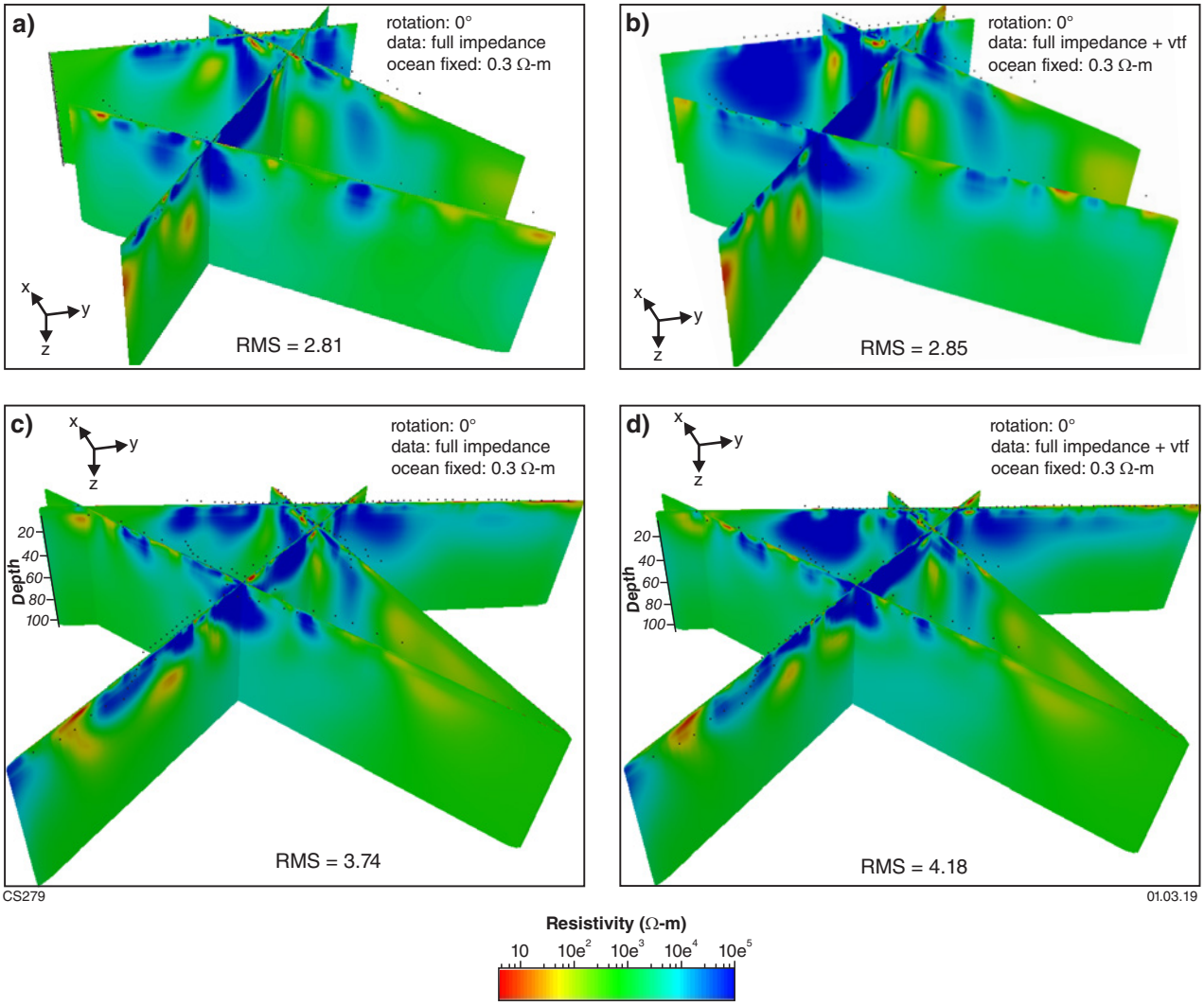

Figure 52. **Preferred 3D model results displayed along the four 2D profile traces: a) the central dataset using the full impedance tensor only; b) the central dataset using the full impedance tensor plus the VTF data; c) the whole dataset using the full impedance tensor only; d) the whole dataset using the full impedance tensor plus the VTF data**

much narrower (Fig. 40). Furthermore, this portion of the AF3 profile coincides with the Rason Regional Gravity Low, whereas the YFB profile follows a northwesterly trending greenstone belt from station yfb031 through to yfb008, and intersects the Cundeelee Shear Zone and Northern Foreland at yfb028 (Fig. 2).

Another zone of higher resistivity (labelled B in Fig. 53) occurs near the intersection of the CBZ and AF3 profiles. Its northwestern side coincides with the axis of the zone of thicker crust, here beneath the Biranup Zone (Fig. 38), determined using receiver function data (Sippl et al., 2017a). At crustal depths this may correlate with the resistive zone on the FR and YFB profiles (labelled C in Fig. 53), trending parallel to the axis of thicker crust. It also suggests the presence of resistive crust within part of the Fraser Zone itself. However, the crust is more conductive farther southwest along the axis of thicker crust (northwest of label C, Fig. 53), particularly below the interpreted base of the Fraser Zone at a depth of about 15 km. This more conductive region may correlate with the lower crustal, nonreflective zones observed in the seismic profiles, which appear to be located in the zone of thicker crust (Sippl et al., 2017a). At crustal depths between 20 and 30 km is a resistive zone that could be linked between the AF3 and CBZ profiles (labelled D in Fig. 53).

The trends of the deep conductivity zones appear to follow that of the zone of greater crustal thickness, slightly oblique to the dominant northeasterly geological trend of the upper crust in the east Albany–Fraser Orogen. As with other geophysical datasets (e.g. seismic reflection, passive seismic, gravity) it is apparent that the lower crust, and perhaps parts of the middle and lower crust, may have different geological trends to the upper crust. This likely reflects significant detachment and perhaps rotation during Proterozoic magmatism and deformation. A lack of evidence of the northwesterly trending Yilgarn Craton terrane boundaries below the orogen are consistent with this, and suggests that these boundaries are now cryptic due to Proterozoic modification. As with the 2D profiles, there is some evidence for a more conductive Proterozoic

mantle compared to the Archean mantle, with less variation to the southeast. This change is in the vicinity of the zone of increased crustal thickness.

Discussion

Upper to middle crustal structure

Beneath the northwestern extent of the YFB profile, the Yilgarn Craton shows anomalously low resistivities within the upper crust compared to the high resistivities typically imaged beneath stable Archean cratons (see examples in Evans et al., 2005; Spratt et al., 2009; Spratt et al., 2014). These low resistivities may be the result of graphite or sulfide mineralization along fault planes or within metasedimentary units (e.g. the black shales in the Black Flag Group within the Norseman–Wiluna Greenstone belt; Hand et al., 2009). Alternatively, they could be the result of focused paleo fluid flow along gently dipping, mid-crustal detachments within the Eastern Goldfields Superterrane, as suggested by Drummond et al. (2004).

The northwestern extent of the Northern Foreland is not distinct in the upper crust in the YFB and AF3 profiles, due to the variability in resistivity. Therefore, there is no clear distinction between the Yilgarn Craton and the adjacent Albany–Fraser Orogen units in the MT data, although some major structures do coincide with changes in resistivity (e.g. the Government Dam Shear Zone on AF3, Fig. 38). The low resistivity of this part of the Yilgarn Craton and also the variability in the Northern Foreland and the Biranup Zone is likely due to overprinting effects from orogenesis and reworking of the craton margin. The variable resistivity in the middle to upper crust also coincides with the zone of thicker crust (Figs 38, 40).

The 2D images of electrical conductivity reveal several features in common. In general, along each of the four profiles the units within the Albany–Fraser Orogen show high resistivities with values >10 000 Ω-m. These units are cut by steeply dipping or near-vertical, less resistive zones, some of which are potentially linked to major shear zones. The high resistivities are consistent with deformed amphibolite to granulite facies rocks, such as gneisses, which are common throughout the orogen. These values are observed in other Proterozoic orogenic domains, such as the Wopmay Orogen in the Northwest Territories, Canada (Spratt et al., 2009), and the Musgrave Province in central Australia (Selway et al., 2011). The less resistive, steeply dipping or near-vertical features are not highly conductive as they are still within the range typical of crystalline rocks, with values greater than 2000 Ω-m (Fig. 7), and are visible by MT methods due to the extremely resistive nature of the host rock. These values would fit with these zones being attributed to Proterozoic magmatism, most of which was likely syn-orogenic (Spaggiari et al., 2014b; Smithies et al., 2015). However, if these features are interpreted as shear zones, the moderate values would suggest that they are dry and contain minimal mineralization. Most of these features (or potential shear zones) are shown to extend to lower crustal depths, and some may extend deeper; however, the presence of a lower crustal conductor (described below) masks their conductivity signature at depth.

If interpreted as shear zones, the steep or near-vertical orientations suggest strike-slip deformation, possibly during Stage II of the Albany–Fraser Orogeny. The strongest candidate for this type of interpretation is the Fraser Shear Zone, which clearly shows dextral strike-slip kinematics (Spaggiari et al., 2011; Quentin de Gromard et al., 2017) and records Stage II activity (Kirkland et al., 2016). However, in the seismic interpretation the Fraser Shear Zone has an apparent dip of about 40° to the east, although this would be a minimum because the profile is not perpendicular to strike (Fig. 1).

In the MT AF3 profile modelled at 5° strike, the Fraser Shear Zone intersects the top of the western side of the resistive zone (at af320; Fig. 38a,b), which has an apparent dip of about 80° to the west. The eastern side of the resistive zone has an apparent dip of 75° east, which does not coincide with any known shear zones (although it is feasible that this could correspond to the Woodcutters Shear Zone), and it has a steeper dip than that interpreted in the seismic profile (near af332; Fig. 38a,b). In the MT AF3 profile modelled at 50° strike, the Fraser Zone appears to have a similar V-shaped geometry to that interpreted in the seismic profile, denoted as a less resistive region flanked and underlain by regions of higher resistivity, and the fit between the two datasets for the Fraser Shear Zone is much better (Fig. 38c,d). The Fraser Zone itself is perhaps characterized by highly variable resistivity, as suggested by the 2D profiles (Figs 38, 40, 42, 44).

Lower crustal conductive layer and the Moho

Although the causes remain uncertain, MT studies worldwide have revealed much of the lower continental crust to have relatively uniform, reduced resistivities, typically 10–100 times less resistive than middle to upper crustal values (Fig. 7; Jones, 1992; Hyndman et al., 1993; Spratt et al., 2014). The two most widely supported candidates for these observations in stable continental regions include ionic conduction through interconnected saline pore fluids, and/or electronic conduction through metasedimentary rocks, likely through thin layers of graphite films or sulfides. Studies are hindered by the need to recreate extreme conditions of temperature and pressure in the laboratory and the impossibility of accounting for the effects of time. The argument that saline fluids in the Archean crust cause reduced resistivity is weakened by long resident times, a lack of fluid regeneration mechanisms, and the fact that there are petrographic grounds for suggesting the absence of free water in the deep crust. The enhanced lower crustal conductivity observed in our profiles could be caused by the presence of metasedimentary rocks with a dry granulite mineralogy, which were buried during orogenesis (e.g. Spratt et al., 2014).

Where the lower crust is resistive, the crust–mantle boundary can be observed electrically (see the Slave Craton as an example; Jones and Ferguson, 2001). However, the enhanced conductivity within the crust of the Yilgarn Craton inhibits the MT data from imaging the base of the crust and it has been shown that model resolution is poor at 40–60 km beneath the northwesternmost extent of the YFB profile (Fig. 40). Beneath the Northern Foreland

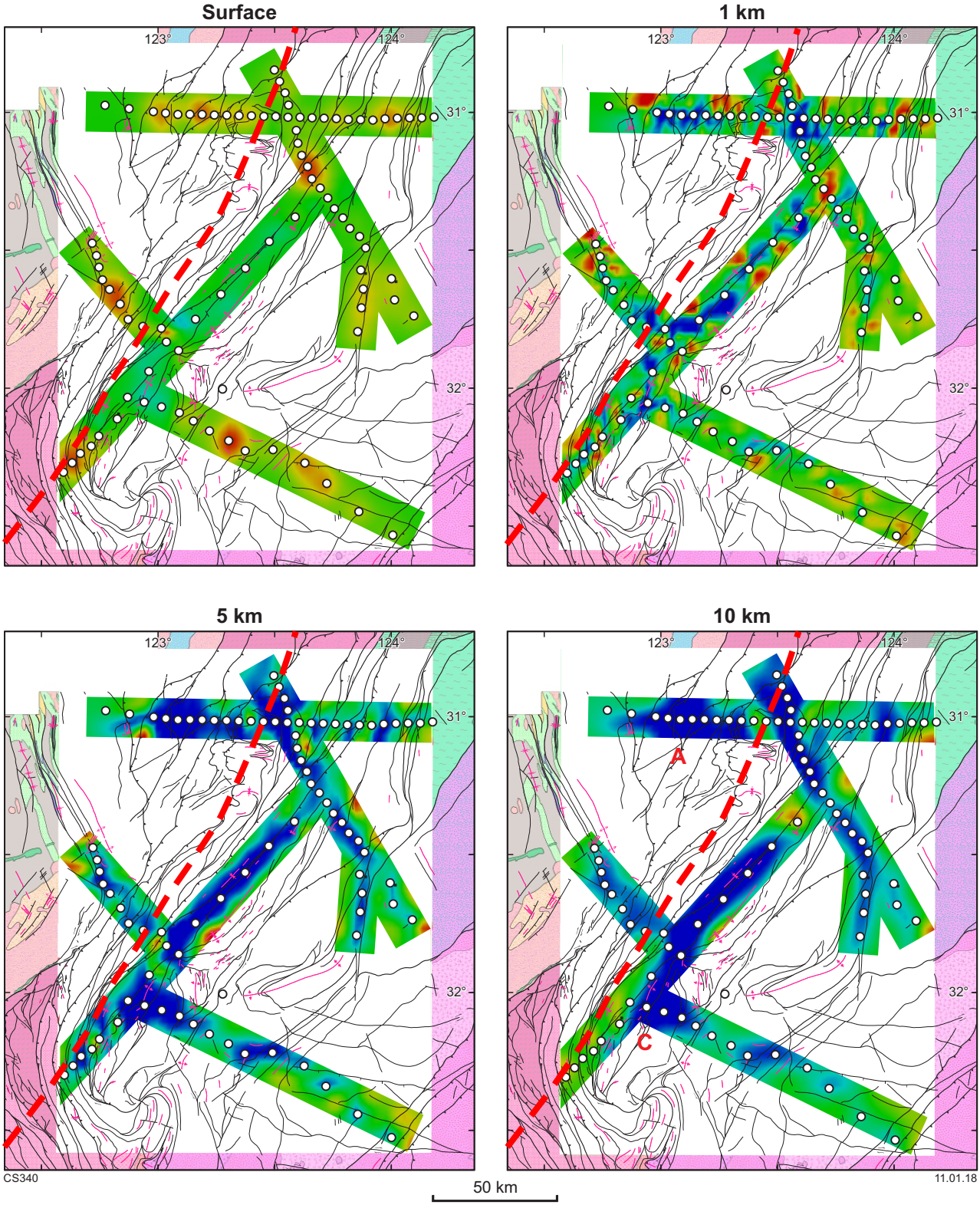

Figure 53. **Horizontal slices through the preferred 3D model of the central region using the full impedance tensor plus the VTF data, displayed as map view slices for depths of 0, 1, 5, 10, 20, 30, 40 and 50 km. The red dashed line shows the approximate axis of the zone of thickened crust, derived from passive seismic data and receiver function analysis (Sippl et al., 2017a). See text for explanations of letter symbols**

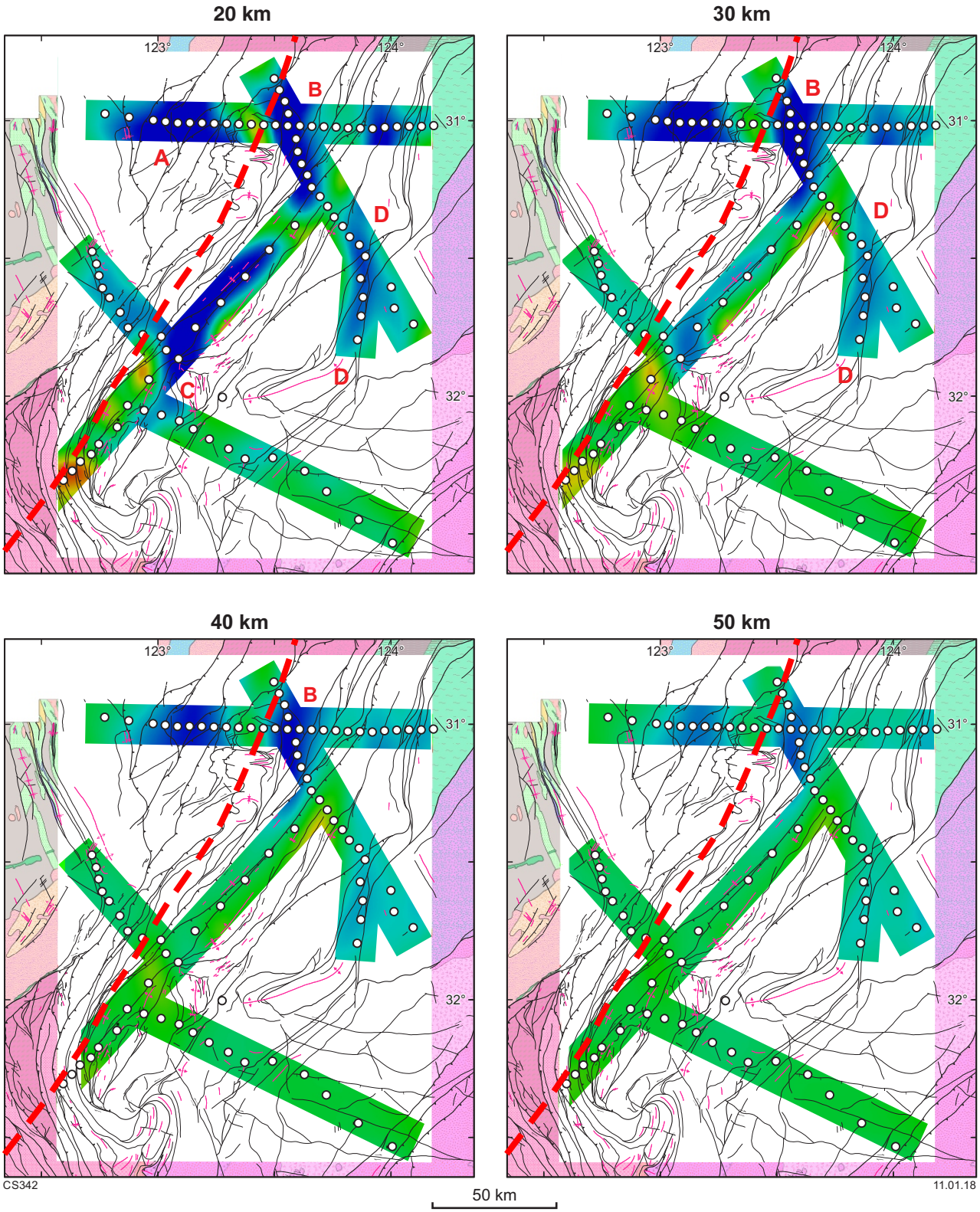

Figure 53. continued

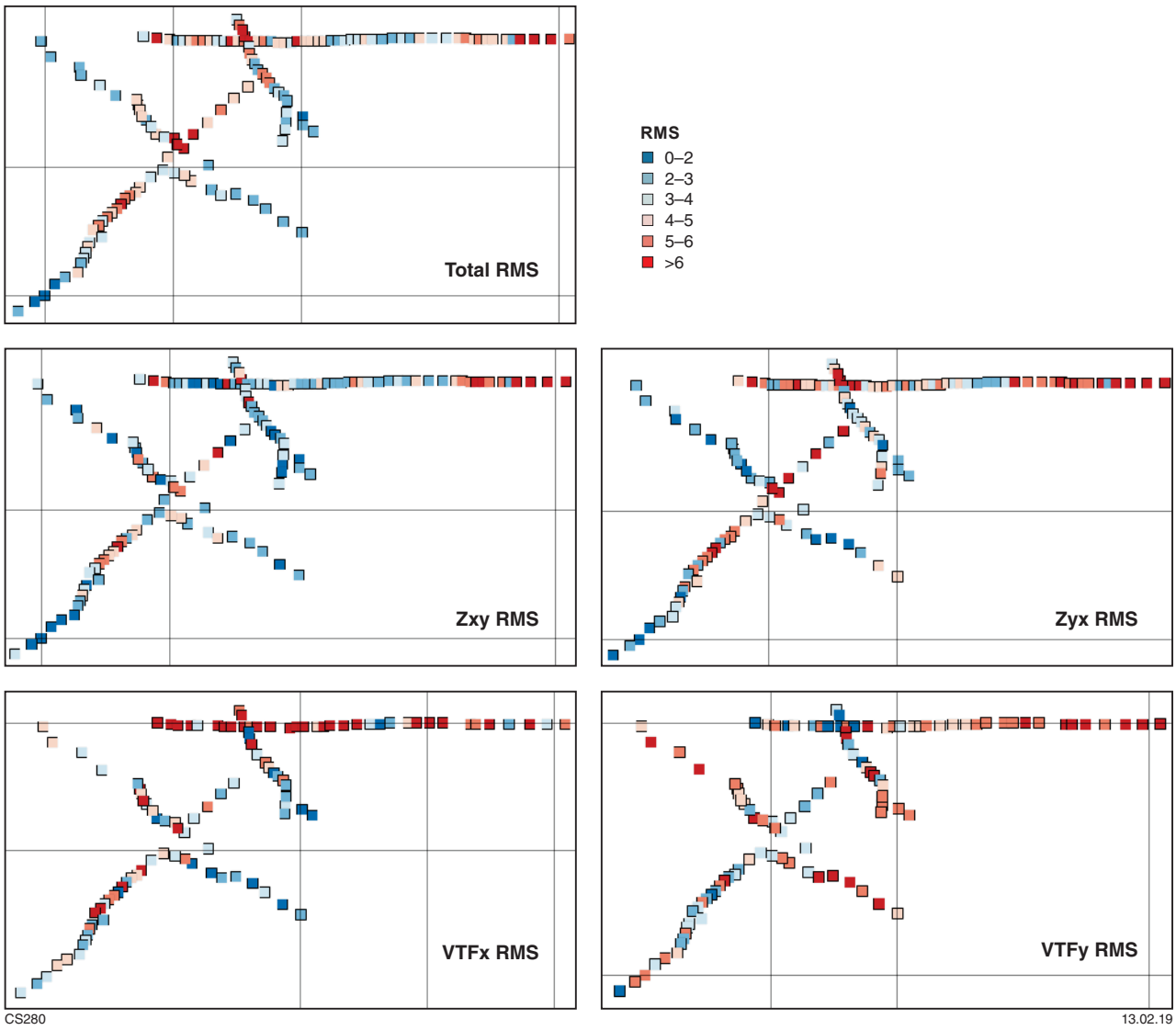

Figure 54. **RMS model fit values plotted at each site. Blue squares represent a good fit to the data and red squares represent a poor fit**

and the Biranup Zone, moderately low resistivities are observed at lower crustal depths beneath each of the four profiles, impeding accurate estimates for the electric Moho depth. However, along the AF3 and CBZ profiles, an increase in resistivity is observed from 35 to 40 km that is consistent with seismically derived crustal depth estimates. Beneath the Fraser Zone and eastern Nornalup Zone, high resistivities are imaged to approximately 40 km depth in the AF3, YFB and FR profiles. This is not observed along the CBZ profile, but feature testing has shown that the structure at these depths is not reliable.

Mantle structure

In general, high resistivities are imaged beneath the Yilgarn Craton, the Northern Foreland and the Biranup Zone, and lower resistivities to the east beneath the Fraser and eastern Nornalup Zones. This is consistent with old, colder, stable lithosphere beneath the Archean Yilgarn Craton that is juxtaposed against juvenile, more fertile Proterozoic upper mantle beneath the orogenic belt.

The complex tectonic history of the Albany–Fraser Orogen has resulted in a deep structure that is largely 3D. This is evident in the variation in geoelectric strike direction laterally and with depth in the MT dataset and in the high skew values observed at long periods. Two-dimensional models of the deep structure are, therefore, unreliable with large differences in models derived at differing strike angles. However, there do not appear to be any anomalous zones of enhanced conductivity, such as the Central Slave Mantle conductor observed beneath the Slave Craton (Jones et al., 2003).

Conclusions

Magnetotelluric investigations of the Albany–Fraser Orogen have imaged the regional conductivity structure of the crust and uppermost mantle beneath four transects. Strike and dimensionality analysis reveal that the regional geoelectric strike is variable across the survey area and with depth. However, locally 2D models can still be reliable.

The models identify near-vertical, low resistivity zones that crosscut a resistive upper crust. Some of these features can be correlated with major shear zones and tectonic unit boundaries, or the effects of these structures within the Albany–Fraser Orogen. A conductive zone in the lower crust, below the Northern Foreland and the Biranup Zone, coincides with a nonreflective zone observed in seismic reflection data, and with a region of thicker crust determined from passive seismic data. This and other conductivity variation in the deep crust and mantle are locally oblique to surface geological strike, suggesting there may be detachment of upper and lower crustal geology.

Acknowledgements

We thank Moombarriga Geoscience for data acquisition, and Ray Addenbrooke for field support. This work was supported by resources provided by the Pawsey Supercomputing Centre with funding from the Australian Government and the Government of Western Australia.

References

Adetunji, AQ, Ferguson, IJ and Jones, AG 2014, Crustal and lithospheric scale structures of the Precambrian Superior–Grenville margin: Tectonophysics, v. 614, p. 146–169, doi:10.1016/j.tecto2013.12.008.

Aitken, ARA, Betts, PG, Young, DA, Blankenship, DD, Roberts, JL and Siegert, MJ 2016, The Australo-Antarctic Columbia to Gondwana transition: Gondwana Research, v. 29, 136–152.

Aitken, AR, Dentith, MC, Evans, SF, Gallardo, LA, Joly, A, Thiel, S, Smithies RH and Tyler, IM 2013, Imaging crustal structure in the west Musgrave Province from magnetotelluric and potential field data: Geological Survey of Western Australia, Report 114, 81p.

Banks, RJ, Livelybrooks, D, Jones, P and Longstaff, R 1996, Causes of high crustal conductivity beneath the Iapetus suture zone in Great Britain: Geophysical Journal International, v. 124, Issue 2, p. 433–455, doi:10.1111/j.1365-246X.1996.tb07031.

Bennett, M, Gollan, M, Staubman, M and Bartlett, J 2014, Motive, means, and opportunity: Key factors in the discovery of the Nova–Bollinger magmatic nickel-copper sulfide deposits in Western Australia: Society of Economic Geologists, Special Publication 18, p. 301–320.

Blenkinsop, TG and Doyle, M 2014, Structural controls on gold mineralisation on the margin of the Yilgarn Craton, Albany–Fraser Orogen: the Tropicana deposit, Western Australia: Journal of Structural Geology, v. 67, p. 189–204.

Bodorkos, S and Clark, DJ 2004a, Evolution of a crustal-scale transpressive shear zone in the Albany–Fraser Orogen, SW Australia: 2. Tectonic history of the Coramup Gneiss and a kinematic framework for Mesoproterozoic collision of the West Australian and Mawson cratons: Journal of Metamorphic Geology, v. 22, no. 8, p. 713–731.

Bodorkos, S and Clark, DJ 2004b, Evolution of a crustal-scale transpressive shear zone in the Albany–Fraser Orogen, SW Australia: 1. P–T conditions of Mesoproterozoic metamorphism in the Coramup Gneiss: Journal of Metamorphic Geology, v. 22, no. 8, p. 691–711.

Bostick, FX 1977, A simple almost exact method of magnetotelluric analysis, in Processing workshop on electrical methods in geothermal exploration: US Geological Survey, p. 174–183.

Brisbout, LI 2015, Determining crustal architecture in the east Albany–Fraser Orogen from geological and geophysical data: Geological Survey of Western Australia, Report 152, 52p.

Cagniard, L 1953, Basic theory of the magnetotelluric method of geophysical prospecting: Geophysics, v. 18, p. 605–635.

Caldwell, TG, Bibby, HM and Brown, C 2004, The magnetotelluric phase tensor: Geophysical Journal International, v. 158, p. 457–469.

Cassidy, KF, Champion, DC, Krapež, B, Barley, ME, Brown, SJA, Blewett, RS, Groenewald, PB and Tyler, IM 2006, A revised geological framework for the Yilgarn Craton, Western Australia: Geological Survey of Western Australia, Record 2006/8, 8p.

Clark, DJ, Hensen, BJ and Kinny, PD 2000, Geochronological constraints for a two-stage history of the Albany–Fraser Orogen, Western Australia: Precambrian Research, v. 102, no. 3, p. 155–183.

Clark, C, Kirkland, CL, Spaggiari, CV, Oorschot, C, Wingate, MTD and Taylor, R 2014, Proterozoic granulite formation driven by magmatism: an example from the Fraser Range Metamorphics, Western Australia: Precambrian Research, v. 240, p. 1–21.

Constable, SC 2006, SEO3: A new model of olivine electrical conductivity: Geophysical Journal International, v. 166, p. 435–437.

Doyle, MG, Fletcher, IR, Foster, J, Large, R, Mathur, R, McNaughton, NJ, Meffre, S, Muhling, JR, Phillips, D and Rasmussen, B 2015, Geochronological constraints on the Tropicana Gold Deposit and Albany–Fraser Orogen, Western Australia: Economic Geology, v. 110, p. 1–32.

Drummond, BJ, Hobbs, BE and Goleby, BR 2004, The role of crustal fluids in the tectonic evolution of the Eastern Goldfields Province of the Archaean Yilgarn Craton, Western Australia: Earth and Planetary Science Letters, v. 56, p. 1163–1169.

Duba, AL and Shankland, TJ 1982, Free carbon and electrical conductivity in the Earth's mantle: Geophysical Research Letters, v. 9, p. 1271–1274.

Ducea, MN and Park, SK 2000, Enhanced mantle conductivity from sulfide minerals, southern Sierra Nevada, California: Geophysical Research Letters, v. 27, p. 2405–2408.

Eaton, DW, Darbyshire, F, Evans, RL, Grutter, H, Jones, AG and Yuan, X 2009, The elusive lithosphere-asthenosphere boundary (LAB) beneath cratons: Lithos, v. 109, p. 1–22.

Egbert, GD and Kelbert, A 2012, Computation recipes for electromagnetic inverse problems: Geophysical Journal International, v. 189(1), p. 251–267.

Evans, S 2012, Conductivity of Earth materials, in The magnetotelluric method: theory and practice edited by AD Chave and AG Jones: Cambridge University Press, New York, US, p. 50–95.

Evans, S, Jones, AG, Spratt, J and Katsube, J 2005, Central Baffin electromagnetic experiment (CBEX): mapping the North American Central Plains (NACP) conductivity anomaly in the Canadian arctic: Physics of the Earth and Planetary Interiors, v. 150, p. 107–122.

Fitzsimons, ICW 2003, Proterozoic basement provinces of southern and southwestern Australia and their correlation with Antarctica: Geological Society of London Special Publication, v. 206, p. 93–130.

Fraser, AR and Pettifer, GR 1980, Reconnaissance gravity surveys in WA and SA, 1969–1972: Australian Bureau of Mineral Resources, Geology and Geophysics Bulletin 196, 60p.

Gamble, TD, Goubau, WM and Clarke, J 1979, Magnetotellurics with a remote reference: Geophysics, v. 44, p. 53–68.

Geological Survey of Western Australia 2017, Compilation of geochronology information, 2017: Geological Survey of Western Australia, digital data package.

Glover, PWJ, Pous, J, Queralt, P, Munoz, J-A, Liesa, M and Hole, MJ 2000, Integrated two-dimensional lithospheric conductivity modeling in the Pyrenees using field-scale and laboratory measurements: Earth and Planetary Science Letters, v. 178, p. 59–72.

Groom, RW and Bailey, RC 1989, Decomposition of magnetotelluric impedance tensors in the presence of local three-dimensional galvanic distortion: Journal of Geophysical Research, v. 94, p. 1913–1925.

Haak, V and Hutton, VRS 1986, Electrical resistivity in continental lower crust, *in* The nature of the lower continental crust *edited by* JB Dawson, DA Carswell, J Hall and KH Wedepohl: Geological Society of London, Special Publication 24, p. 35–49.

Hand, JL, Cas, RAF, Ong, L, Brown, SJA, Krapež, B and Barley, ME 2009, Syn- and post-eruptive volcaniclastic sedimentation in late Archaean subaqueous depositional systems of the Black Flag Group, Eight Mile Dam, Kalgoorlie, Western Australia, *in* Precambrian sedimentary environments: a modern approach to ancient depositional systems *edited by* W Altermann and P Corcoran: Wiley; International Association of Sedimentologists Series Special Publication, v. 18, no. 33, p. 235–258, doi:10.1002/9781444304312.ch10.

Hyndman, RD, Vanyan, LL, Marquid, G and Lay, LK 1993, The origin of electrically conductive lower continental crust: saline water or graphite?: Physics of the Earth and Planetary Interiors, v. 81, p. 325–345.

Jones, AG 1992, Electrical conductivity of the continental lower crust, *in* Continental lower crust *edited by* DM Fountain, RJ Arculus and RW Kay: Elsevier, Amsterdam, Chapter 3, p. 81–143.

Jones, AG 1999, Imaging the continental upper mantle using electromagnetic methods: Lithos, v. 48, p. 57–80.

Jones, AG 2006, Electromagnetic interrogation of the anisotropic Earth: looking into the Earth with polarized spectacles: Physics of the Earth and Planetary Interiors, v. 158, p. 281–291.

Jones, AG, Craven, JA, McNeice, GA, Ferguson, IJ, Boyce, T, Farquharson, C and Ellis, RG 1993, North American Central Plains conductivity anomaly within the Trans-Hudson Orogen in northern Saskatchewan: Geology, v. 21, p. 1027–1030.

Jones, AG, Evans, RL and Eaton, DW 2009, Velocity-conductivity relationships for mantle mineral assemblages in Archean cratonic lithosphere based on a review of laboratory data and Hashin-Shtrikman external bounds: Lithos, v. 109, p. 131–143.

Jones, AG and Ferguson, IJ 2001, The electric Moho: Nature, v. 409, p. 331–333.

Jones, AG, Fullea, F, Evans, RL and Muller, MR 2012, Calibrating laboratory-determined models of electrical conductivity of mantle minerals using geophysical and petrological observations: Geochemistry, Geophysics, Geosystems, v. 13, Q06010, doi: 10.1029/2012GC004055.

Jones, AG and Jödicke, H 1984, Magnetotelluric transfer function estimation improvement by a coherence based rejection technique (EM1.5), in Abstract Volume: 54th Society of Exploration Geophysics Annual General Meeting, Atlanta, Georgia, US, 1984 SEG Expanded Abstracts v. 3, p. 51–55.

Jones, AG, Ledo, J and Ferguson, IJ, 2005, Electromagnetic images of the Trans-Hudson orogen: the North American Central Plains anomaly revealed: Canadian Journal of Earth Sciences, v. 42, p. 457–478, doi:10.1139/E05-018.

Jones, AG, Lezaeta, P, Ferguson, IJ, Chave, AD, Evans, R, Garcia, X and Spratt, J 2003, The electrical structure of the Slave Craton: Lithos, v. 71, p. 505–527.

Karato, S 1990, The role of hydrogen in the electrical conductivity of the upper mantle: Nature, v. 347, p. 272–273.

Karato, S 2006, Influence of hydrogen-related defects on the electrical conductivity and plastic deformation of mantle minerals: a critical review, *in* Earth's Deep Water Cycle *edited by* SD Jacobson and S van der Lee: American Geophysical Union, Washington DC, US, p. 113–129.

Kirkland, CL, Spaggiari, CV, Johnson, TE, Smithies, RH, Danišík, M, Evans, N, Wingate, MTD, Clark, C, Spencer, C, Mikucki, E and McDonald, BJ 2016, Grain size matters: implications for element and isotopic mobility in titanite: Precambrian Research, v. 278, p. 283–302.

Kirkland, CL, Spaggiari, CV, Pawley, MJ, Wingate, MTD, Smithies, RH, Howard, HM, Tyler, IM, Belousova, EA and Poujol, M 2011, On the edge: U–Pb, Lu–Hf, and Sm-Nd data suggests reworking of the Yilgarn Craton margin during formation of the Albany–Fraser Orogen: Precambrian Research, v. 187, p. 223–247.

Kirkland, CL, Spaggiari, CV, Smithies, RH and Wingate, MTD 2014, Cryptic progeny of craton margins: geochronology and isotope geology of the Albany–Fraser Orogen with implications for evolution of the Tropicana Zone, *in* Albany–Fraser Orogen seismic and magnetotelluric (MT) workshop 2014: extended abstracts *compiled by* CV Spaggiari and IM Tyler: Geological Survey of Western Australia, Record 2014/6, p. 89–101.

Korsch, RJ, Spaggiari, CV, Occhipinti, SA, Doublier, MP, Clark, DJ, Dentith, MC, Doyle, MG, Kennett, BLN, Gessner, K, Neumann, NL, Belousova, EA, Tyler, IM, Costelloe, RD, Fomin, T and Holzschuh, J 2014, Geodynamic implications of the 2012 Albany–Fraser deep seismic reflection survey: a transect from the Yilgarn Craton across the Albany–Fraser Orogen to the Madura Province, *in* Albany–Fraser Orogen seismic and magnetotelluric (MT) workshop 2014: extended abstracts *compiled by* CV Spaggiari and IM Tyler: Geological Survey of Western Australia, Record 2014/6, p. 142–173.

Kositcin, N, Brown, SJA, Barley, ME, Krapež, B, Cassidy, KF and Champion, DC 2008, SHRIMP U–Pb zircon age constraints on the Late Archaean tectonostratigraphic architecture of the Eastern Goldfields Superterrane, Yilgarn Craton, Western Australia: Precambrian Research, v. 161, p. 5–33.

Kurtz, RD, Craven, JA, Niblett, ER and Stevens, RA 1993, The conductivity of the crust and mantle beneath the Kapuskasing Uplift: Electrical anisotropy in the upper mantle: Geophysical Journal International, v. 113, p. 167–176.

Ledo, J. and Jones, AG 2005, Upper mantle temperature determined from combining mineral composition, electrical conductivity laboratory studies and magnetotelluric field observations: application to the Intermontane Belt, Northern Canadian Cordillera: Earth and Planetary Science Letters, v. 236, p. 479–493.

Lowry, DC 1970, Geology of the Western Australian part of the Eucla Basin: Geological Survey of Western Australia, Bulletin 122, 201p.

Mackie, RL and Madden, TR 1993, Three dimensional magnetotelluric inversion using conjugate gradients: Geophysical Journal International, v. 115, p. 215–229.

Maier, WD, Smithies, RH, Spaggiari, CV, Barnes, SJ, Kirkland, CL, Kiddie, O and Roberts, MP 2016, The evolution of mafic and ultramafic rocks of the Mesoproterozoic Fraser Zone, Albany–Fraser Orogen, and implications for Ni–Cu sulfide potential of the region: Geological Survey of Western Australia, Record 2016/8, 49p.

McCuaig, TC, Beresford, S, Hronsky, J 2010, Translating the mineral systems approach into an effective exploration targeting system: Ore Geology Reviews, v. 38, p. 128–138.

Morrissey, LJ, Payne, JL, Hand, M, Clark, C, Taylor, R, Kirkland, CL, Kylander-Clark, A 2017, Linking the Windmill Islands, east Antarctica and the Albany–Fraser Orogen: insights from U–Pb zircon geochronology and Hf isotopes: Precambrian Research, v. 293, p. 131–149.

Murdie, RE, Gessner, K, Occhipinti, SA, Spaggiari, CV and Brett, J 2014, Interpretation of gravity and magnetic data across the Albany–Fraser Orogen, *in* Albany–Fraser Orogen seismic and magnetotelluric (MT) workshop 2014: extended abstracts *compiled by* CV Spaggiari and IM Tyler, Geological Survey of Western Australia, Record 2014/6, p. 118–134.

Nelson, KD, Zhao, W, Brown, LD, Kuo, J, Che, J, Liu, X, Klemperer, SL, Makovsky, Y, Meissner, R, Mechie, J, Kind, R, Wenzel, F, Ni, J, Nabelek, J, Chen, L, Tan, H, Wei, W, Jones, AG, Booker, J, Unsworth, M, Kidd, WSF, Hauck, M, Alsdorf, D, Ross, A, Cogan, M, Wu, C, Sandvol, E and Edwards, M 1996, Partially molten middle crust beneath southern Tibet: an initial synthesis of Project INDEPTH results: Science, v. 274, p. 1684–1688.

Niblett, ER and Sayn-Wittgenstein, C 1960, Variation of electrical conductivity with depth by the magnetotelluric method: Geophysics, v. 25, p. 998–1008.

Pawley, MJ, Wingate, MTD, Kirkland, CL, Wyche, S, Hall, CE, Romano, SS and Doublier, MP 2012, Adding pieces to the puzzle: episodic crustal growth and a new terrane in the northeast Yilgarn Craton,

Western Australia: Australian Journal of Earth Sciences, v. 59, no. 5, p. 603–623.

Poe, BT, Romano, C, Nestola, F and Smyth, JR 2010, Electrical conductivity anisotropy of dry and hydrous olivine at 8 Gpa: Physics of the Earth and Planetary Interiors, v. 181, no. 3, p. 103–111.

Quentin de Gromard, R, Spaggiari, CV, Munro, MA, Sapkota, J and De Paoli, M 2017, SGTSG 2017 Albany–Fraser Orogen pre-conference field trip: transect across an Archean craton margin to a Proterozoic ophoilite: Geological Survey of Western Australia, Record 2017/14, 100p.

Rodi, W and Mackie, RL 2001, Nonlinear conjugate gradients algorithm for 2-D magnetotelluric inversion: Geophysics, v. 66, p. 174–187.

Schmucker, U 1970, An introduction to induction anomalies: Journal of Geomagnetism and Geoelectricity, v. 22, p. 9–33.

Selway, KM, Hand, M, Payne, JL, Heinson, GS and Reid, A 2011, Magnetotelluric constraints on the tectonic setting of Grenville-aged orogenesis in central Australia: Journal of the Geological Society of London, v. 168, p. 251–264

Sippl, C, Brisbout, LJ, Spaggiari, CV, Kennett, BLN, Tkalčić, H, Murdie, R and Gessner, K 2017a, Crustal structure and tectonic evolution scenarios for the east Albany–Fraser Orogen, Western Australia, from passive seismic and gravity anomaly data: Precambrian Research, v. 296, p. 78–92.

Sippl, C, Kennett, BLN, Tkalčić, H, Gessner, K and Spaggiari, CV 2017b, Crustal surface-wave velocity structure of the east Albany–Fraser Orogen, Western Australia, from ambient noise recordings: Geophysical Journal International, v. 210, no. 3, p. 1641–1651.

Siripunvaraporn, W and Egbert, G 2000, An efficient data-subspace inversion method for 2D magnetotelluric data: Geophysics, v. 65, p. 791–803.

Smithies, RH, Spaggiari, CV, Kirkland, Howard, HM and Maier, WD 2013, Petrogenesis of gabbros of the Mesoproterozoic Fraser Zone: constraints on the tectonic evolution of the Albany–Fraser Orogen: Geological Survey of Western Australia, Record 2013/5, 29p.

Smithies, RH, Spaggiari, CV and Kirkland, CL 2015, Building the crust of the Albany–Fraser Orogen; constraints from granite geochemistry: Geological Survey of Western Australia, Report 150, 49p.

Spaggiari, CV 2016, Pre-Mesozoic 1:250 000 interpreted bedrock geology of the east Albany–Fraser Orogen (digital map layer), *in* East Albany–Fraser Orogen 2016: Geological Survey of Western Australia, Geological Exploration digital data package.

Spaggiari, CV, Bodorkos, S, Barquero-Molina, M, Tyler, IM and Wingate, MTD 2009, Interpreted bedrock geology of the south Yilgarn and central Albany–Fraser Orogen, Western Australia: Geological Survey of Western Australia, Record 2009/10, 84p.

Spaggiari, CV, Kirkland, CL, Smithies, RH, Occhipinti, SA and Wingate, MTD 2014b, Geological framework of the Albany–Fraser Orogen, *in* Albany–Fraser Orogen seismic and magnetotelluric (MT) workshop 2014: extended abstracts *compiled by* CV Spaggiari and IM Tyler: Geological Survey of Western Australia, Record 2014/6, p. 12–27.

Spaggiari, CV, Kirkland, CL, Smithies, RH, Wingate, MTD and Belousova, E 2015, Transformation of an Archean craton margin during Proterozoic basin formation and magmatism: the Albany–Fraser Orogen, Western Australia: Precambrian Research, v. 266, p. 440–466.

Spaggiari, CV, Kirkland, CL, Pawley, MJ, Smithies, RH, Wingate, MTD, Doyle, MG, Blenkinsop, TG, Clark, C, Oorschot, CW, Fox, LJ and Savage, J 2011, The geology of the east Albany–Fraser Orogen — a field guide: Geological Survey of Western Australia, Record 2011/23, 97p.

Spaggiari, CV, Occhipinti, SA, Korsch, RJ, Doublier, MP, Clark, DJ, Dentith, MC, Gessner, K, Doyle, MG, Tyler, IM, Kennett, BLN, Costelloe, RD, Fomin, T and Holzschuh, J 2014a, Interpretation of Albany–Fraser seismic lines 12GA-AF1, 12GA-AF2 and 12GA-AF3: implications for crustal architecture, *in* Albany–Fraser Orogen seismic and magnetotelluric (MT) workshop 2014: extended abstracts *compiled by* CV Spaggiari and IM Tyler: Geological Survey of Western Australia, Record 2014/6, p. 28–51.

Spaggiari, CV and Occhipinti, SA 2015, Interpreted pre-Mesozoic bedrock geology of the northeast region of the Albany–Fraser Orogen including seismic line GA12–T1 (1:250 000), *in* Albany–Fraser Orogen seismic and magnetotelluric (MT) workshop 2014: extended abstracts *compiled by* CV Spaggiari and IM Tyler: Geological Survey of Western Australia, Record 2014/6, Plate 1.

Spaggiari, CV and Smithies, RH (compilers) 2015, Eucla basement stratigraphic drilling results release workshop: extended abstracts: Geological Survey of Western Australia, Record 2015/10, 70p.

Spratt, JE, Jones, AG, Nelson, KD, Unsworth, MJ and the INDEPTH team 2005, Crustal structure of the India–Asia collision zone, southern Tibet, from INDEPTH-MT investigations: Physics of the Earth and Planetary Interiors, v. 150, issues 1–3, p. 227–237.

Spratt, JE, Jones, AG, Jackson, V, Collins, L and Avdeeva, A 2009, Lithospheric geometry of the Wopmay Orogen from a Slave Craton to Bear Province magnetotelluric transect: Journal of Geophysical Research, v. 114, B01101, doi:10.1029/2007JB005326.

Spratt, JE, Jones, AG, Corrigan, D and Hogg, C 2013, Lithospheric geometry revealed by deep-probing magnetotelluric surveying, Melville Peninsula, Nunavut: Geological Survey of Canada, Current Research 2013-12, 14p., doi:10.4095/292482

Spratt, JE, Skulski, T, Craven, JA, Jones, AG, Snyder, DB and Kiyan, D 2014, Magnetotelluric investigations of the lithosphere beneath the central Rae craton, Mainland Nunavut, Canada: Journal of Geophysical Research, p. 2415–2439, doi:10.1002/2013JB010221.

Tassell, H and Goncharov, A 2006, Geophysical evidence for a deep crustal root beneath the Yilgarn Craton and Albany-Fraser Orogen, Western Australia, in Australian Earth Sciences Convention 2006: conference abstracts: Geological Society of Australia; Australian Earth Sciences Convention, Melbourne, Victoria, 2–8 July 2006, 6p.

ten Grotenhuis, SM, Drury, MR, Peach, CJ and Spiers, CJ 2004, Electrical properties of fine-grained olivine: Evidence for grain boundary transport: Journal of Geophysical Research, v. 109, B06203, doi:10.1029/2003JB002799.

Tietze, K and Ritter, O 2013, Three-dimensional magnetotelluric inversion in practice — the electrical conductivity structure of the San Andreas Fault in Central California: Geophysical Journal International, v. 195, issue 1, p. 130–147, doi:10.1093/gji/ggt234.

Unsworth, MJ, Jones, AG, Wei, W, Marquis, G, Gokarn, SG, Spratt, JE and the INDEPTH-MT team 2005, Crustal rheology of the Himalaya and Southern Tibet inferred from magnetotelluric data: Nature, v. 438, p. 78–81.

Wait, JR 1962, Theory of magnetotelluric fields: Journal of Research of the National Bureau of Standards, Radio Propagation, v. 66d, p. 509–541.

Wight, DE and Bostick, FX 1981, Cascade decimation — a technique for real time estimation of power spectra, in Proceedings: Institute of Electrical and Electronic Engineers; International conference on acoustics, speech and signal processing, Atlanta, Georgia, US, 30 March 1981, p. 626–629.

Wu, X, Ferguson, IJ and Jones, AG 2002, Magnetotelluric response and geoelectric structure of the Great Slave Lake shear zone: Earth and Planetary Science Letters, v, 196, p. 35–50.

Wyche, S, Kirkland, CL, Riganti, A, Pawley, MJ, Belousova, E and Wingate, MTD 2012, Isotopic constraints on stratigraphy in the central and eastern Yilgarn Craton, Western Australia: Australian Journal of Earth Sciences, v. 59, p. 657–670.

Appendix 1

Appendix 1 shows the unedited apparent resistivity and phase response curves as a function of period for each of the MT sites acquired. The black squares show data in the xy mode in the geographic north direction and the open squares show data in the perpendicular yx mode.

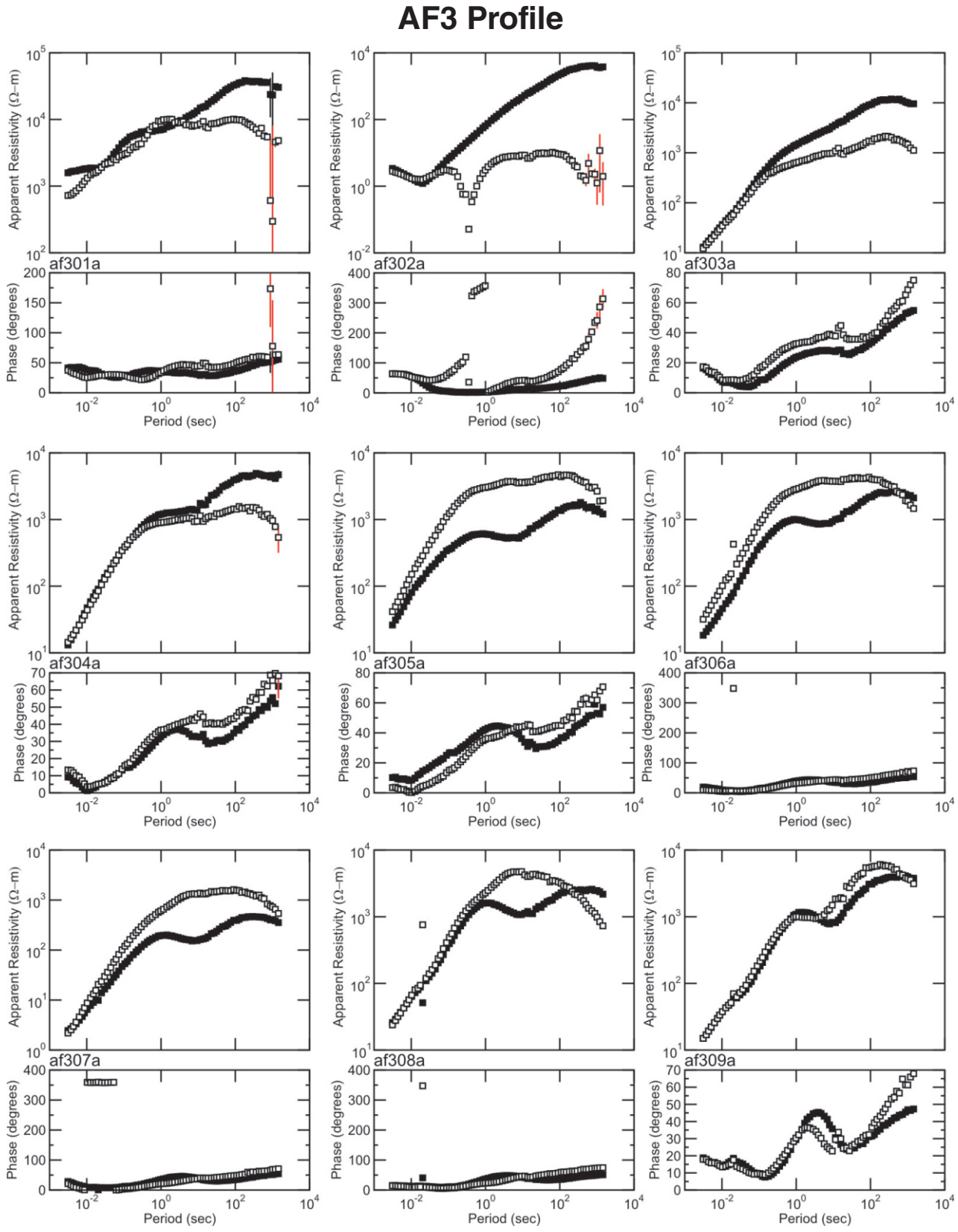

Figure 1.1. Stations af301–af309 along the AF3 profile

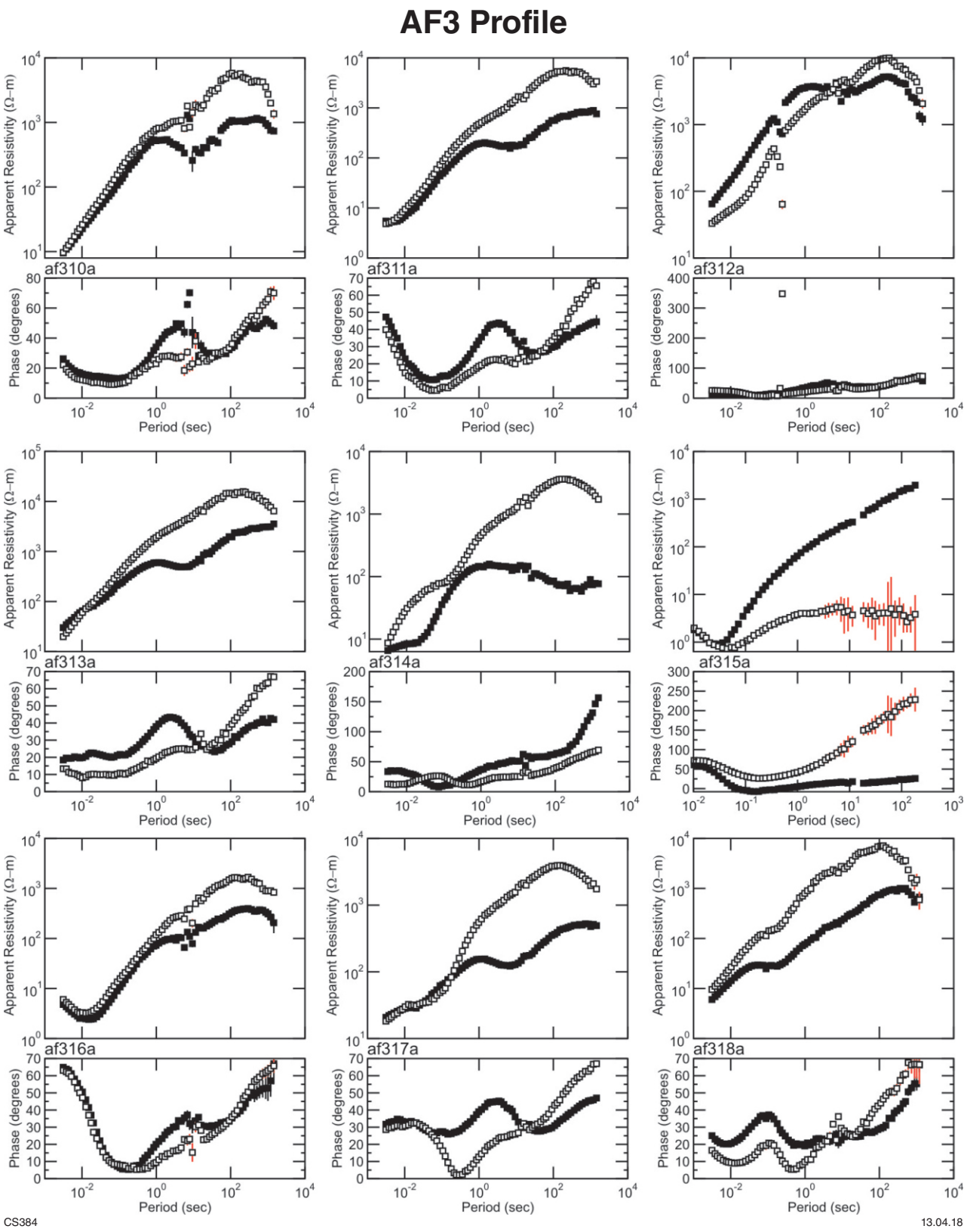

Figure 1.2. Stations af310–af318 along the AF3 profile

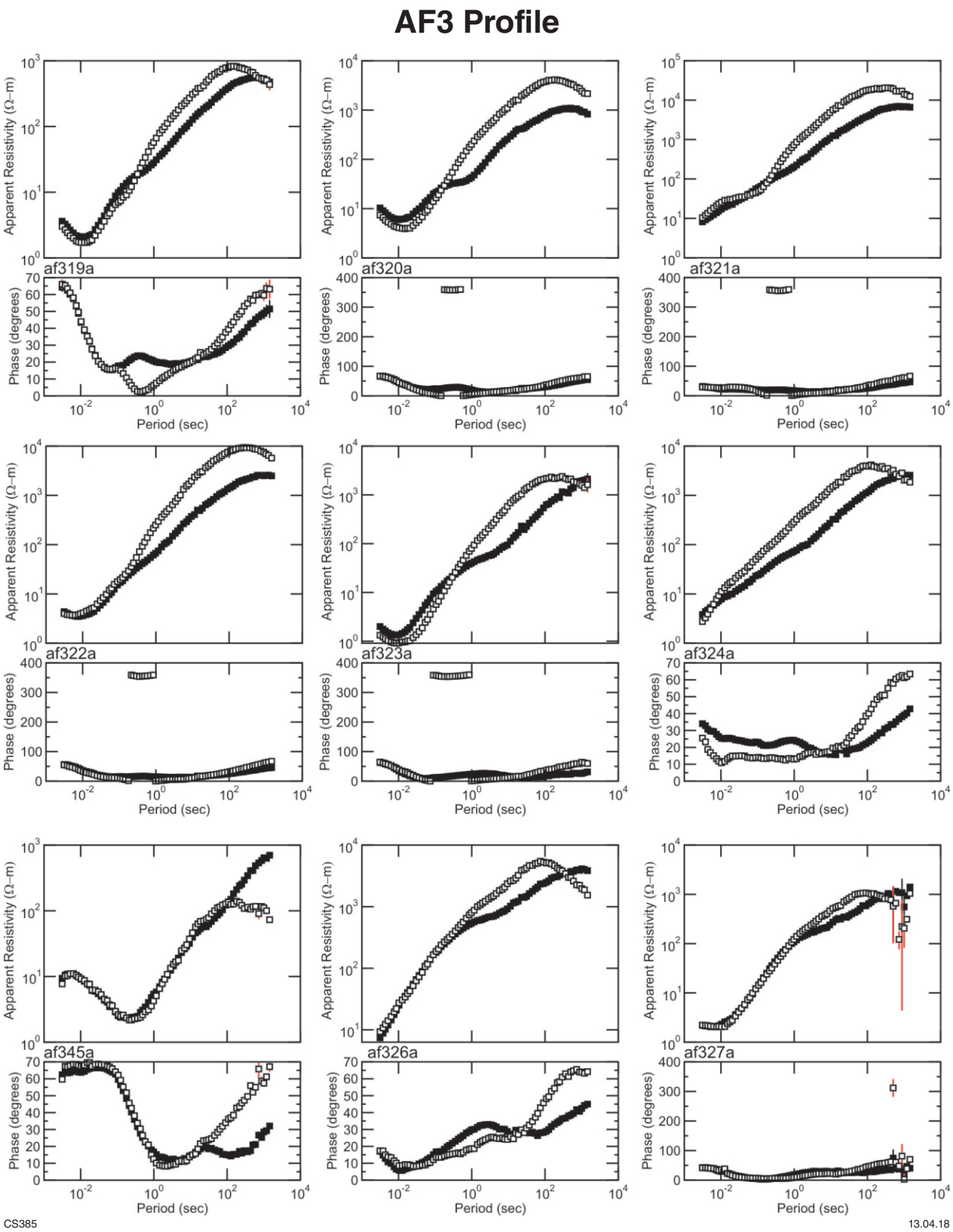

Figure 1.3. Stations af319–af327 along the AF3 profile

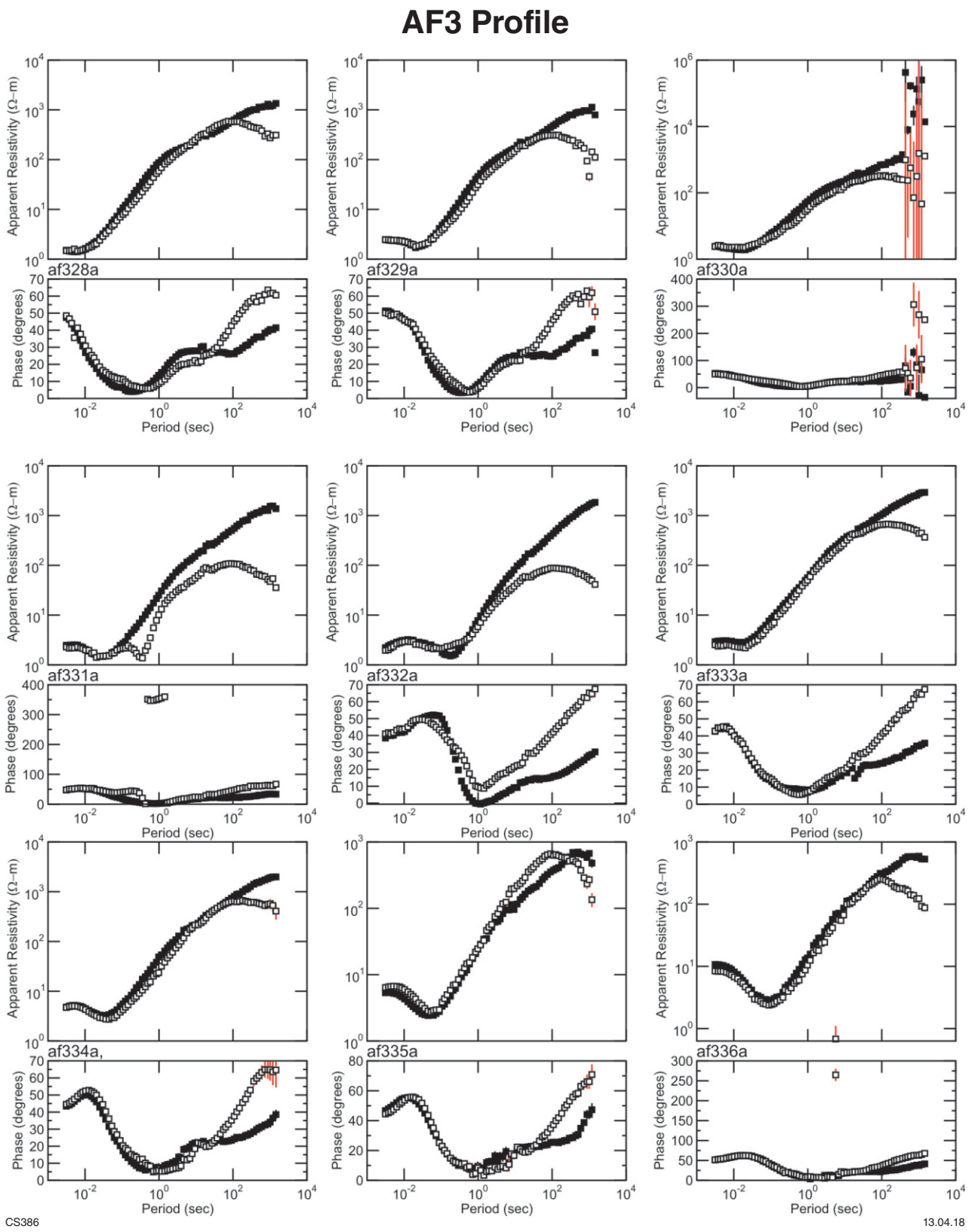

Figure 1.4. Stations af328–af336 along the AF3 profile

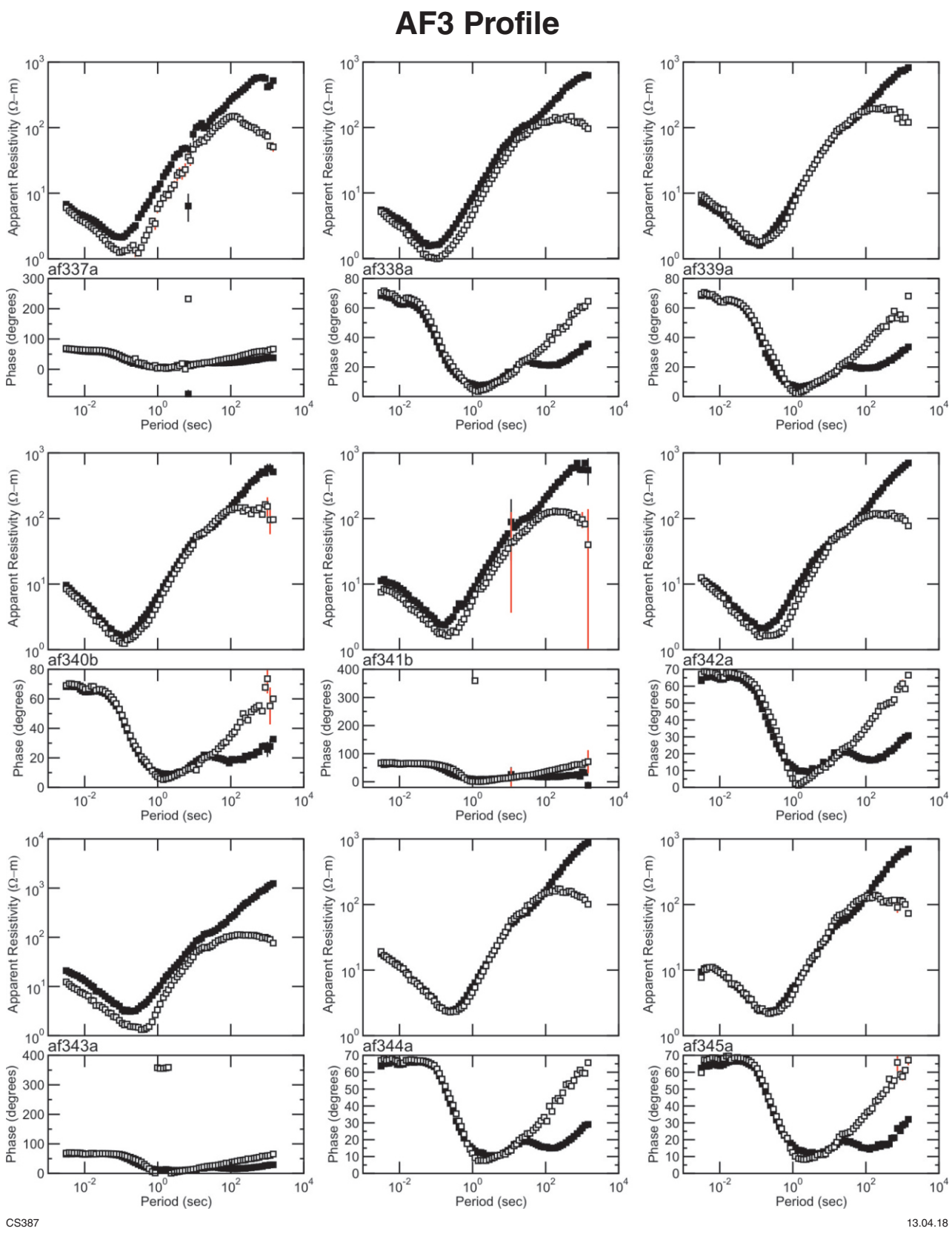

Figure 1.5. Stations af337–af345 along the AF3 profile

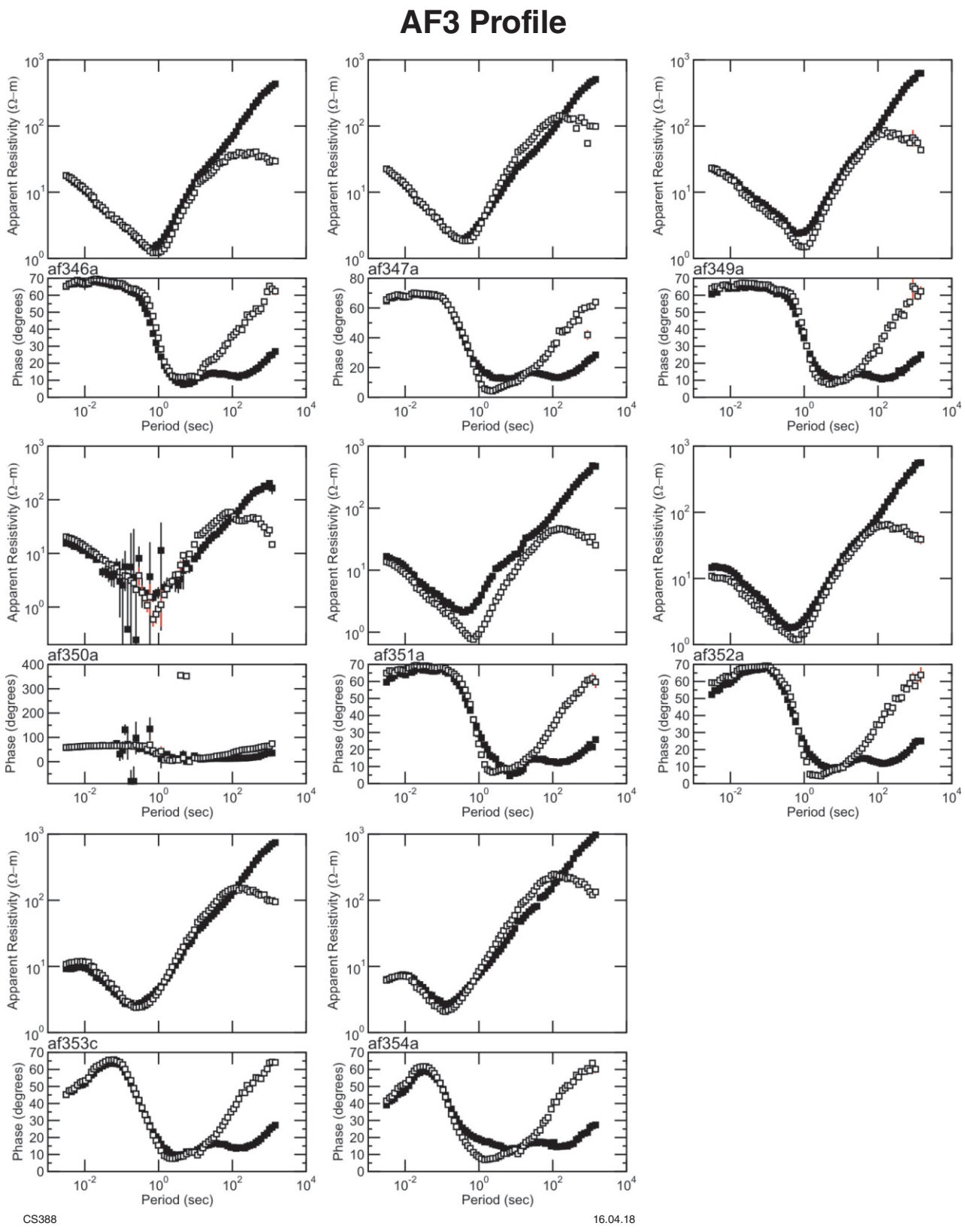

Figure 1.6. Stations af346–af354 along the AF3 profile

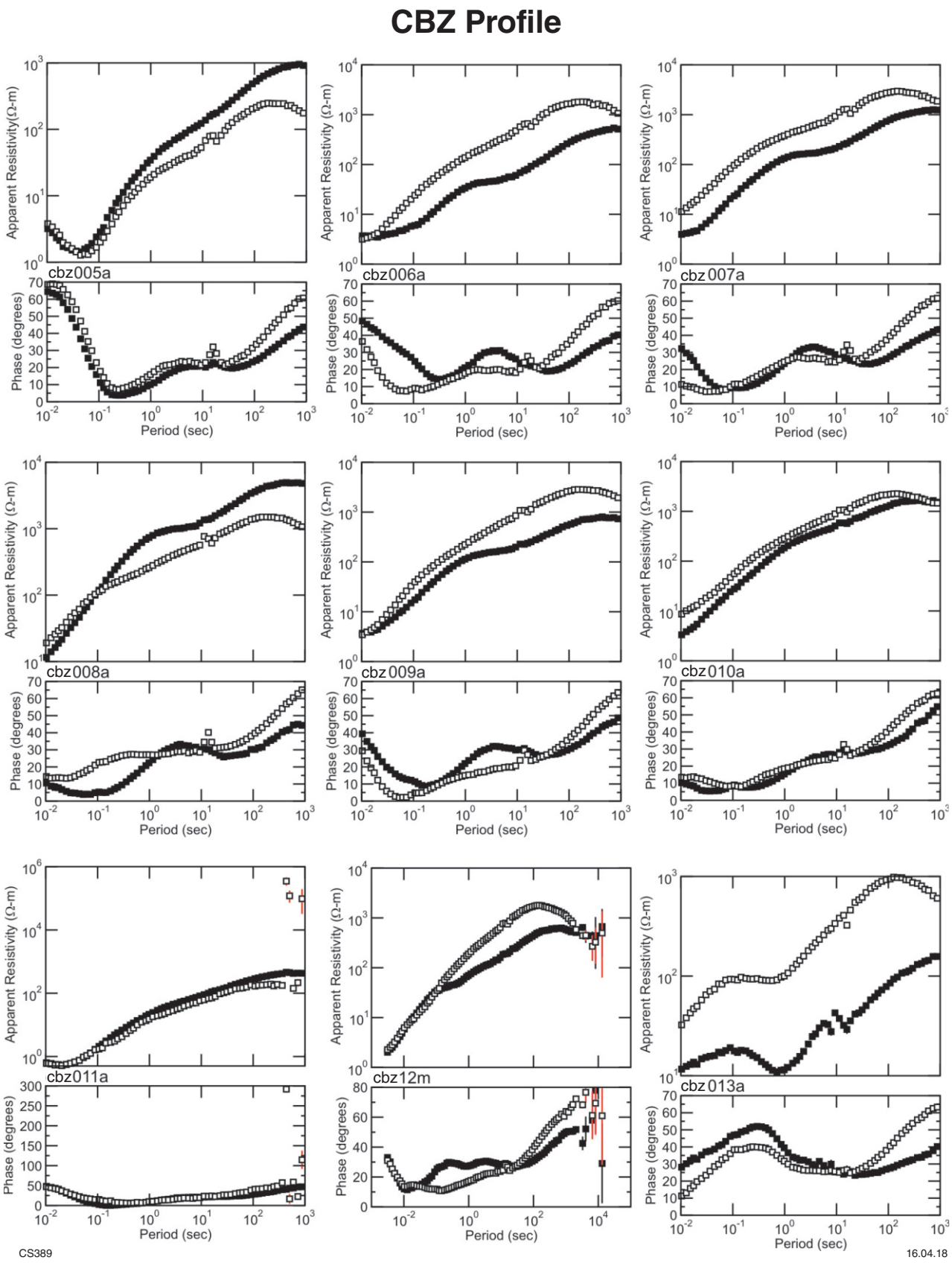

Figure 1.7. Stations cbz005–cbz013 along the CBZ profile

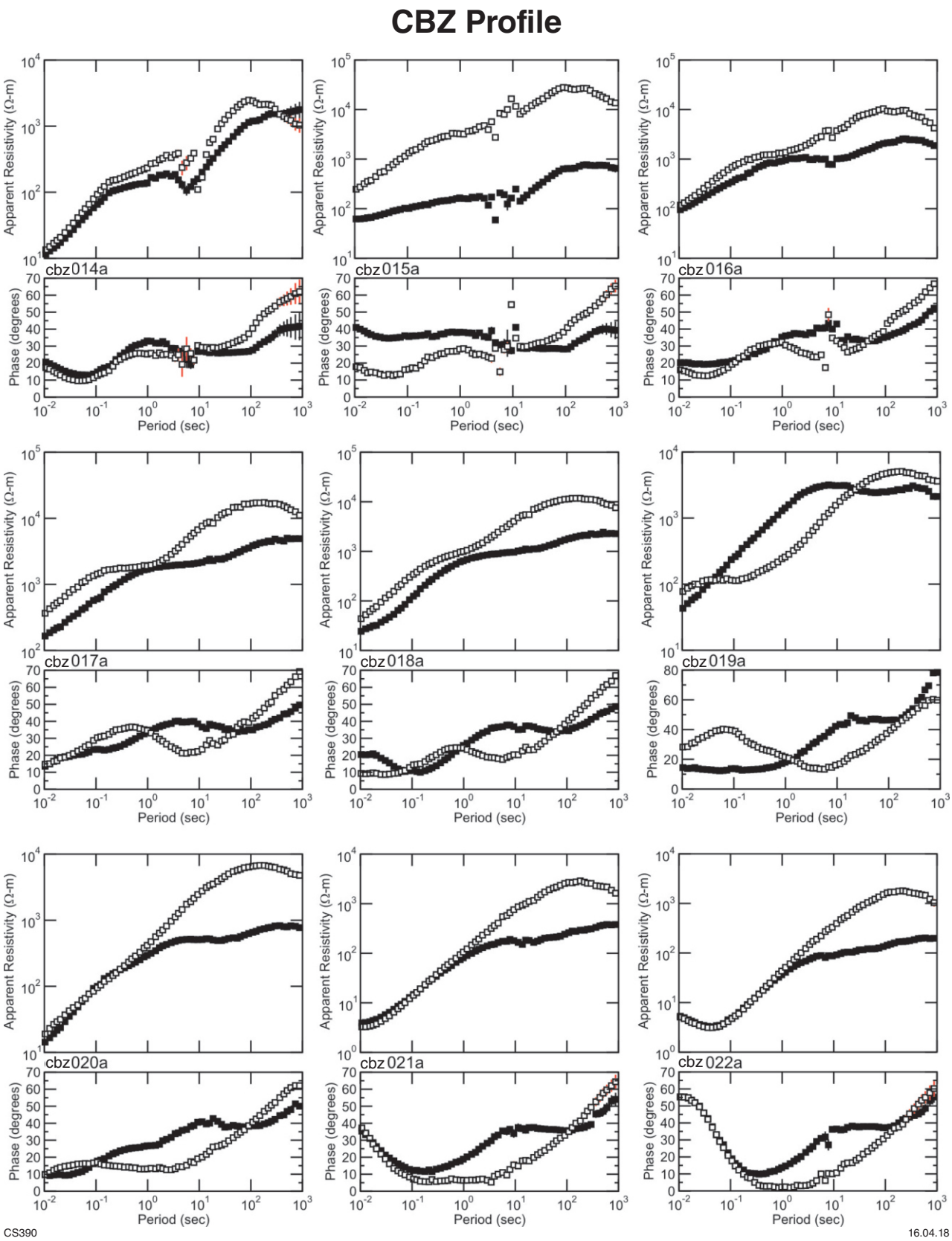

Figure 1.8. Stations cbz014–cbz022 along the CBZ profile

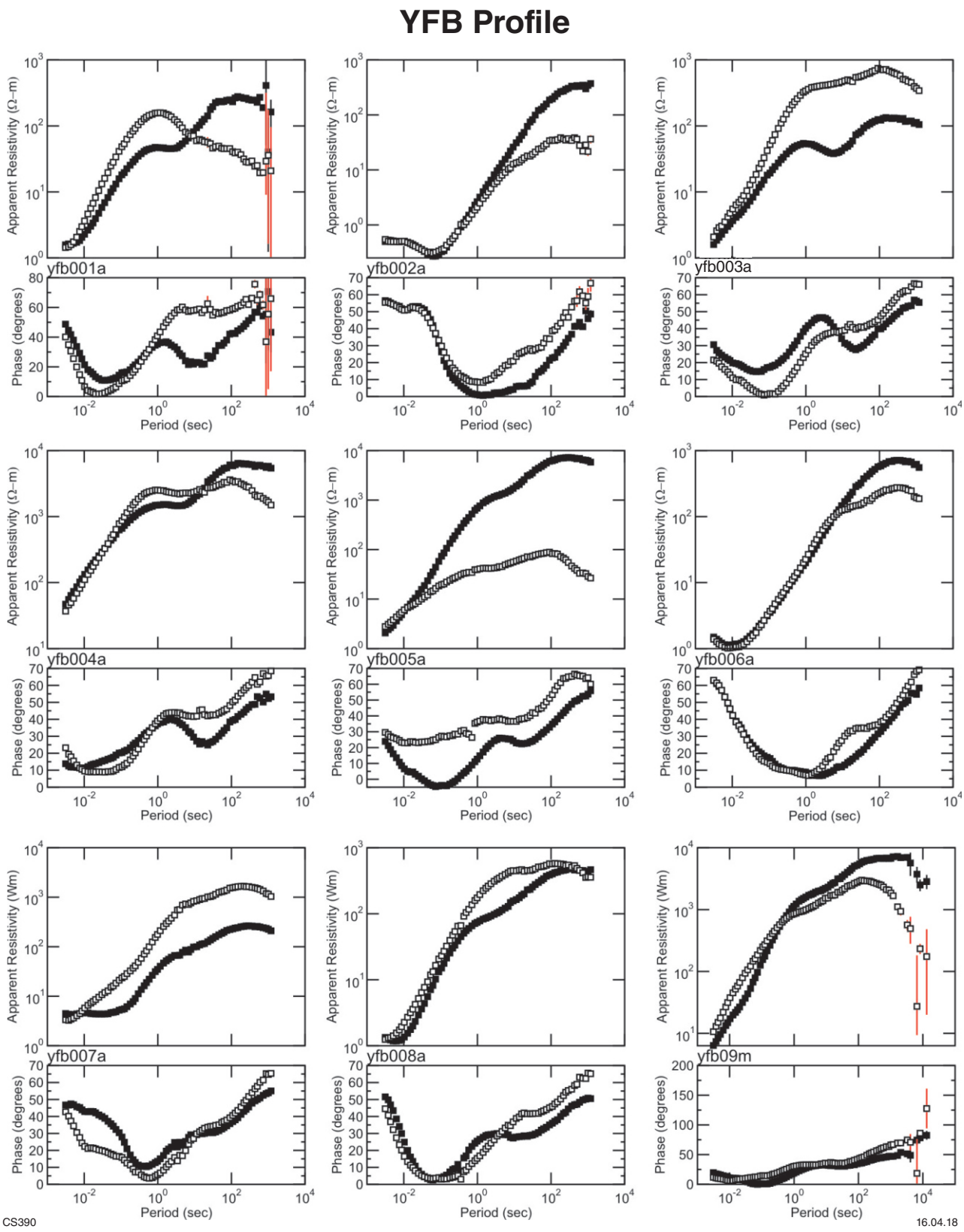

Figure 1.9. Stations yfb001–yfb009 along the YFB profile

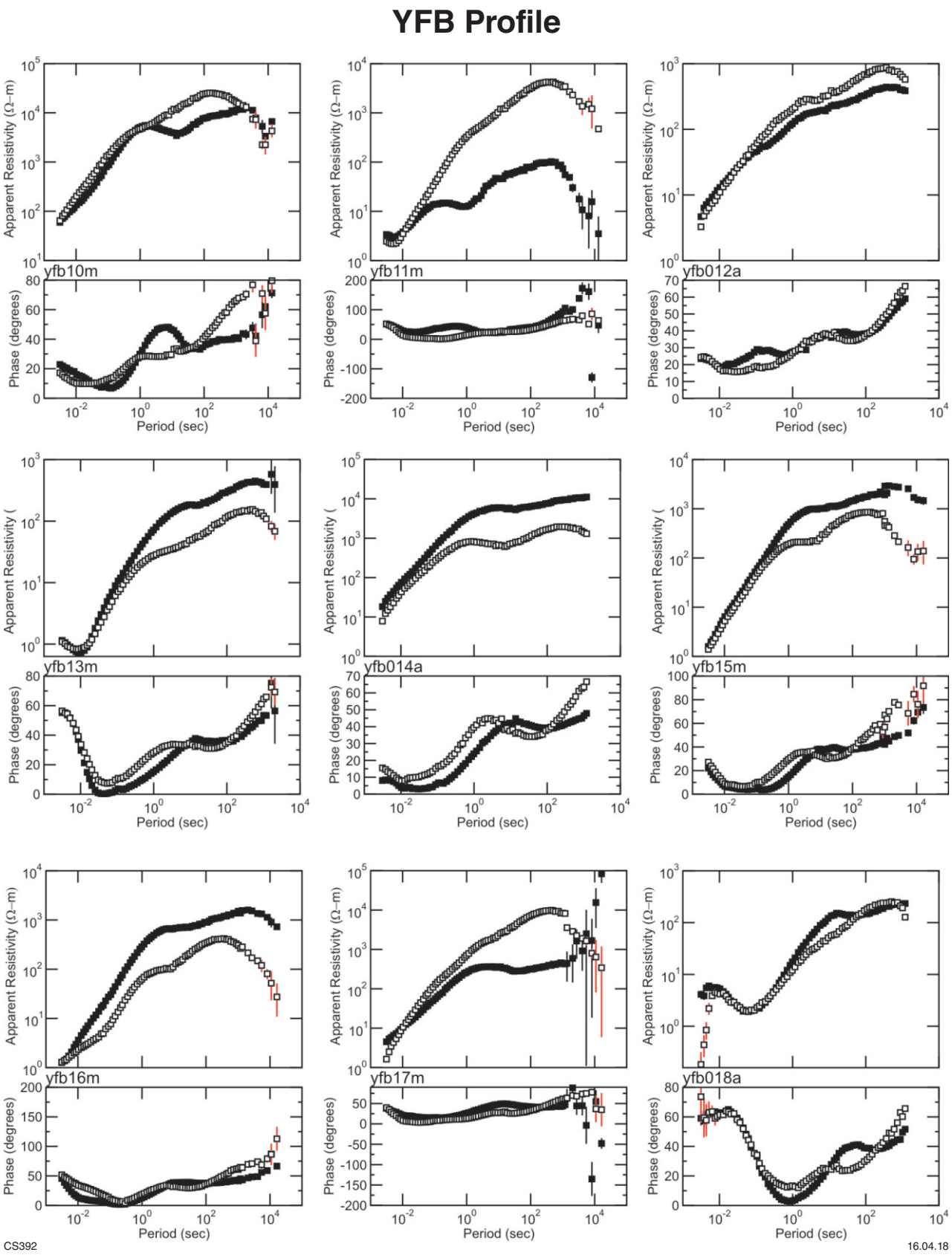

Figure 1.10. Stations yfb010–yfb018 along the YFB profile

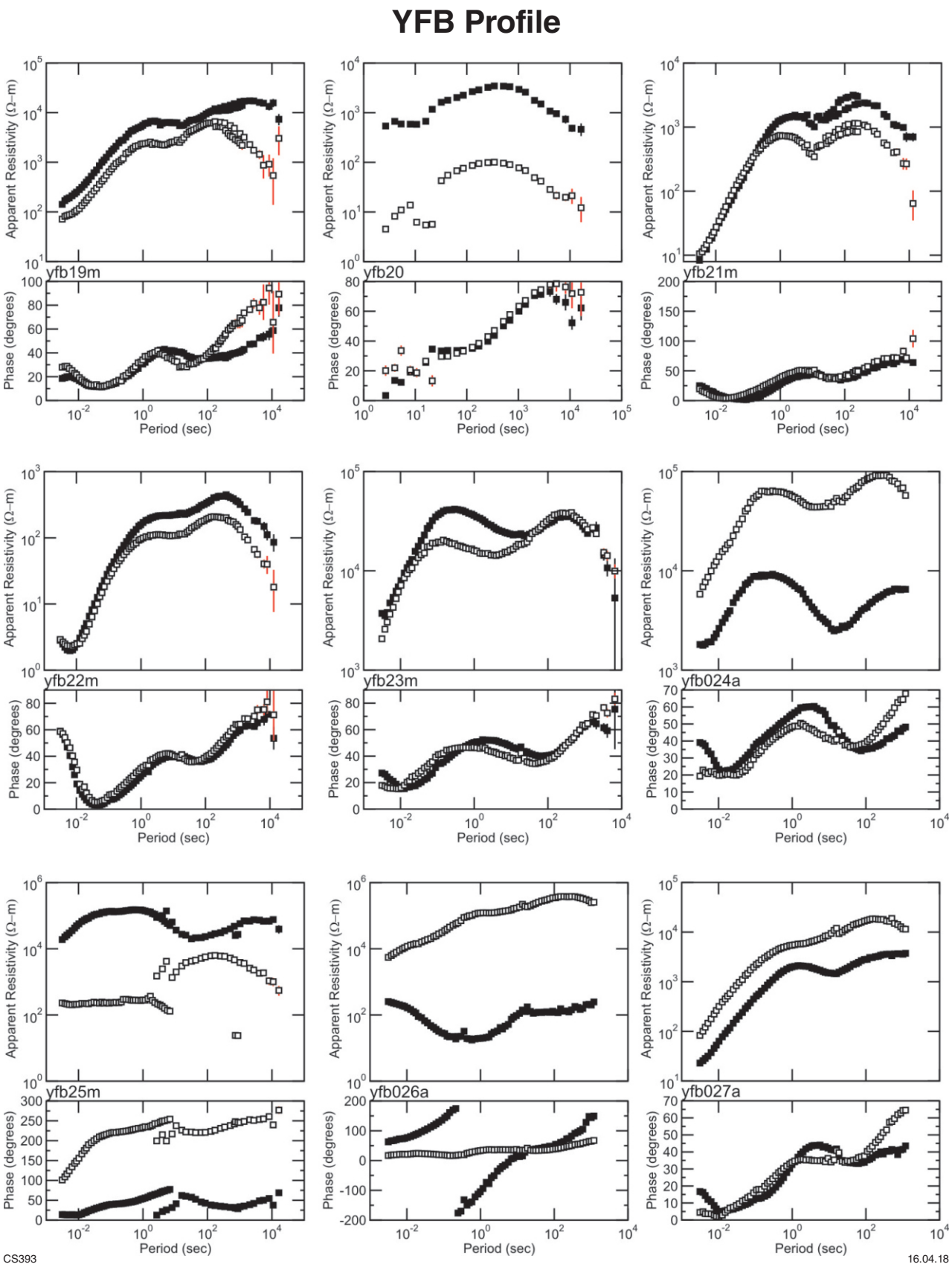

Figure 1.11. Stations yfb019–yfb027 along the YFB profile

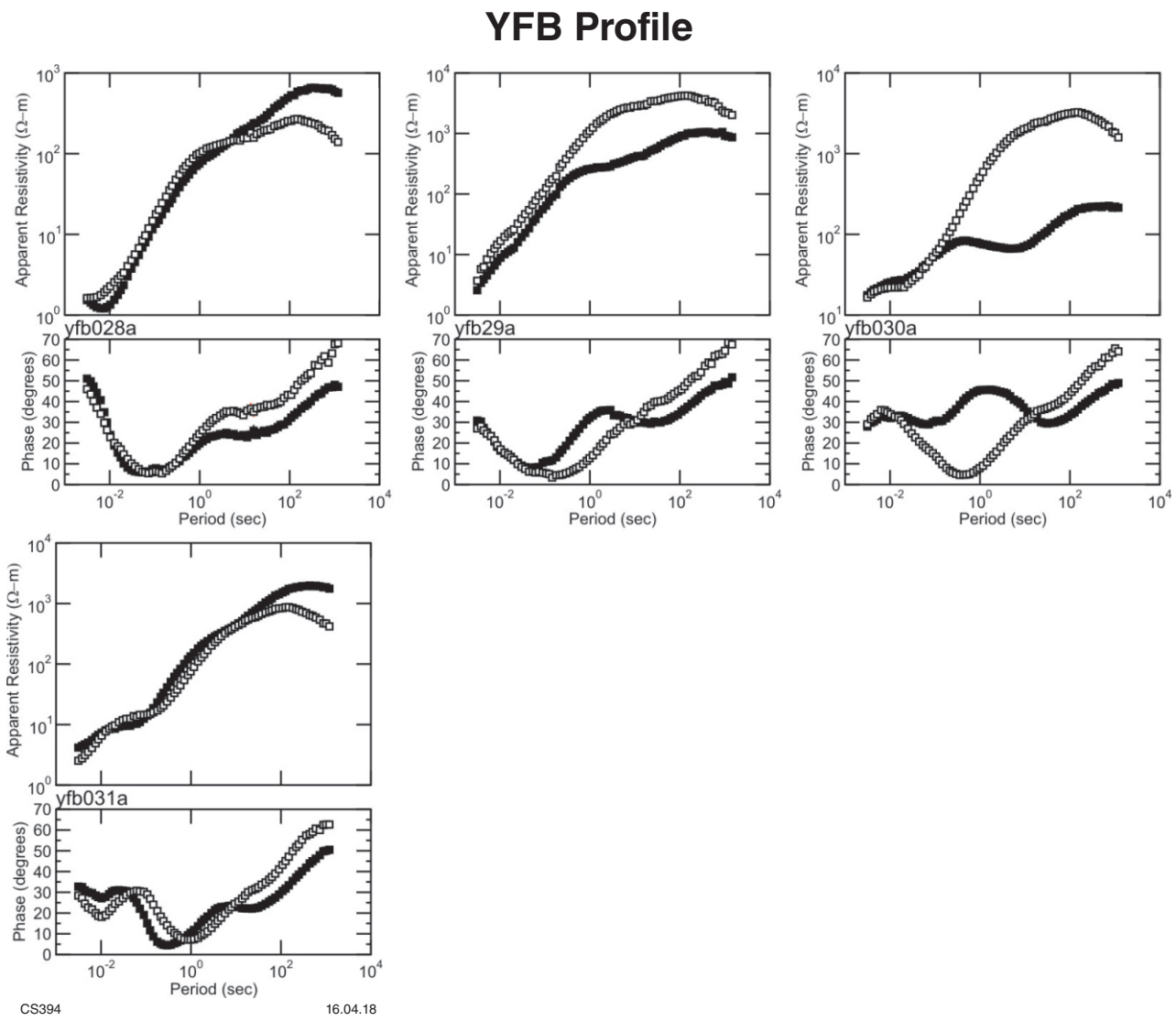

Figure 1.12. Stations yfb028–yfb031 along the YFB profile

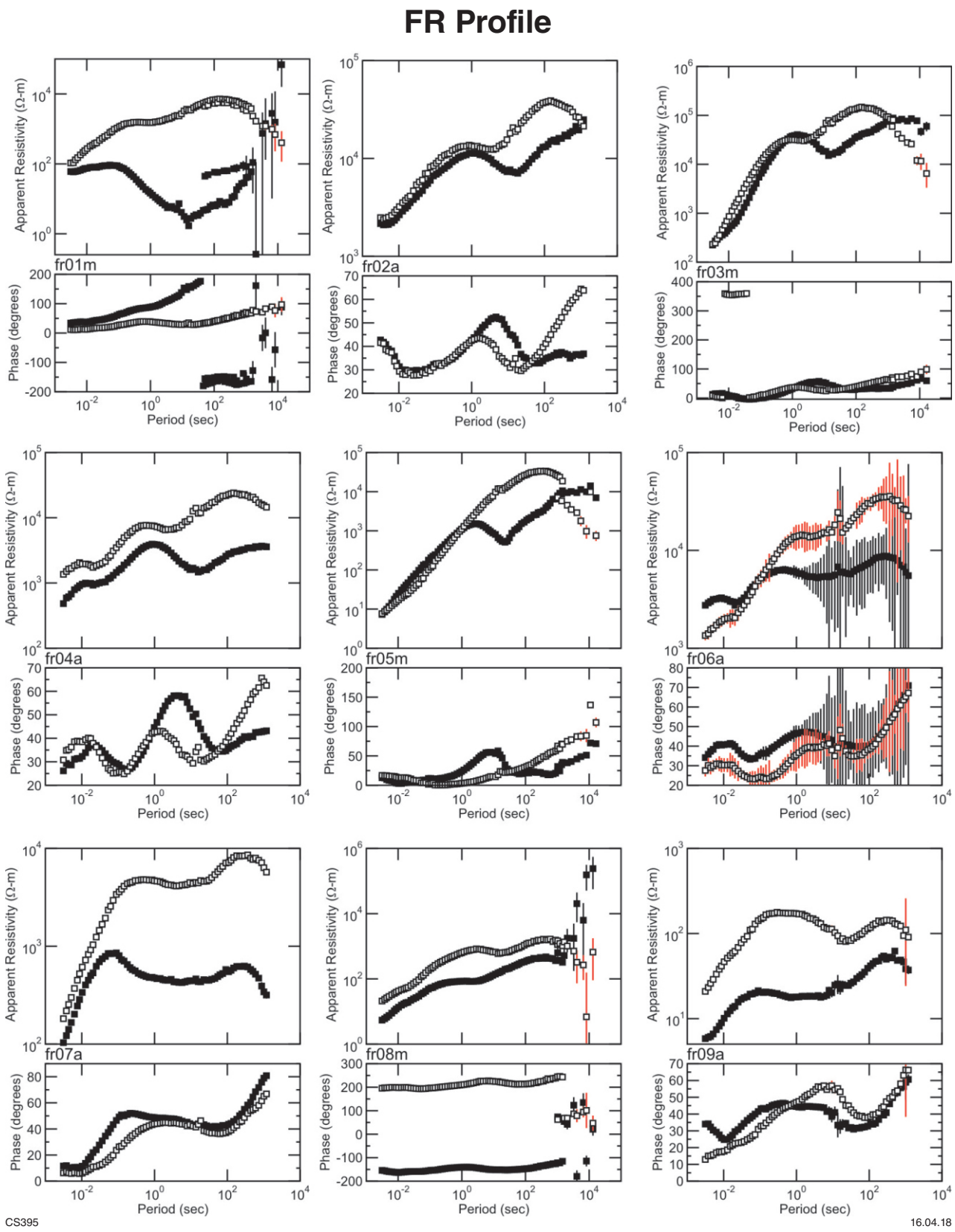

Figure 1.13. Stations fr01–fr09 along the FR profile

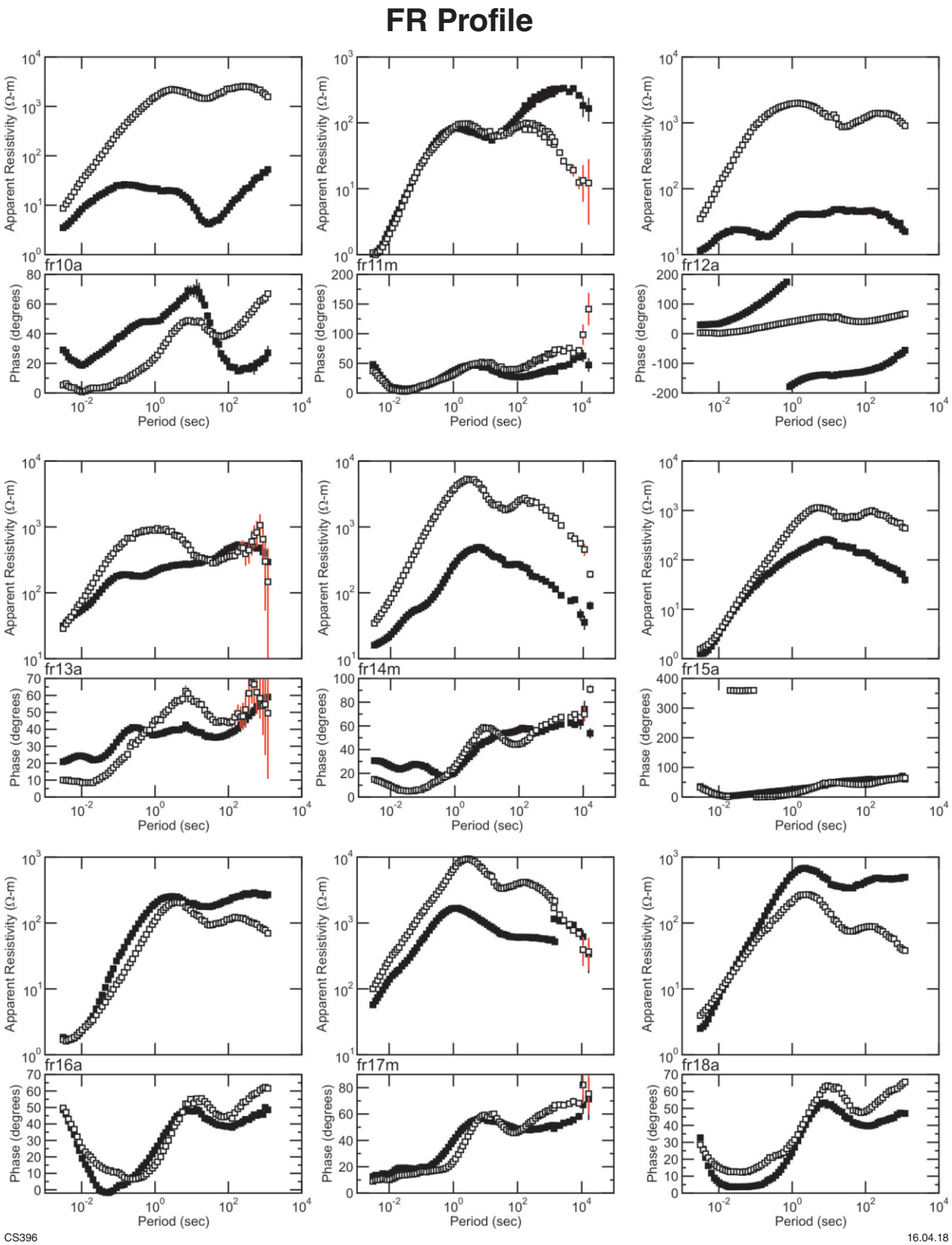

Figure 1.14. Stations fr10–fr18 along the FR profile

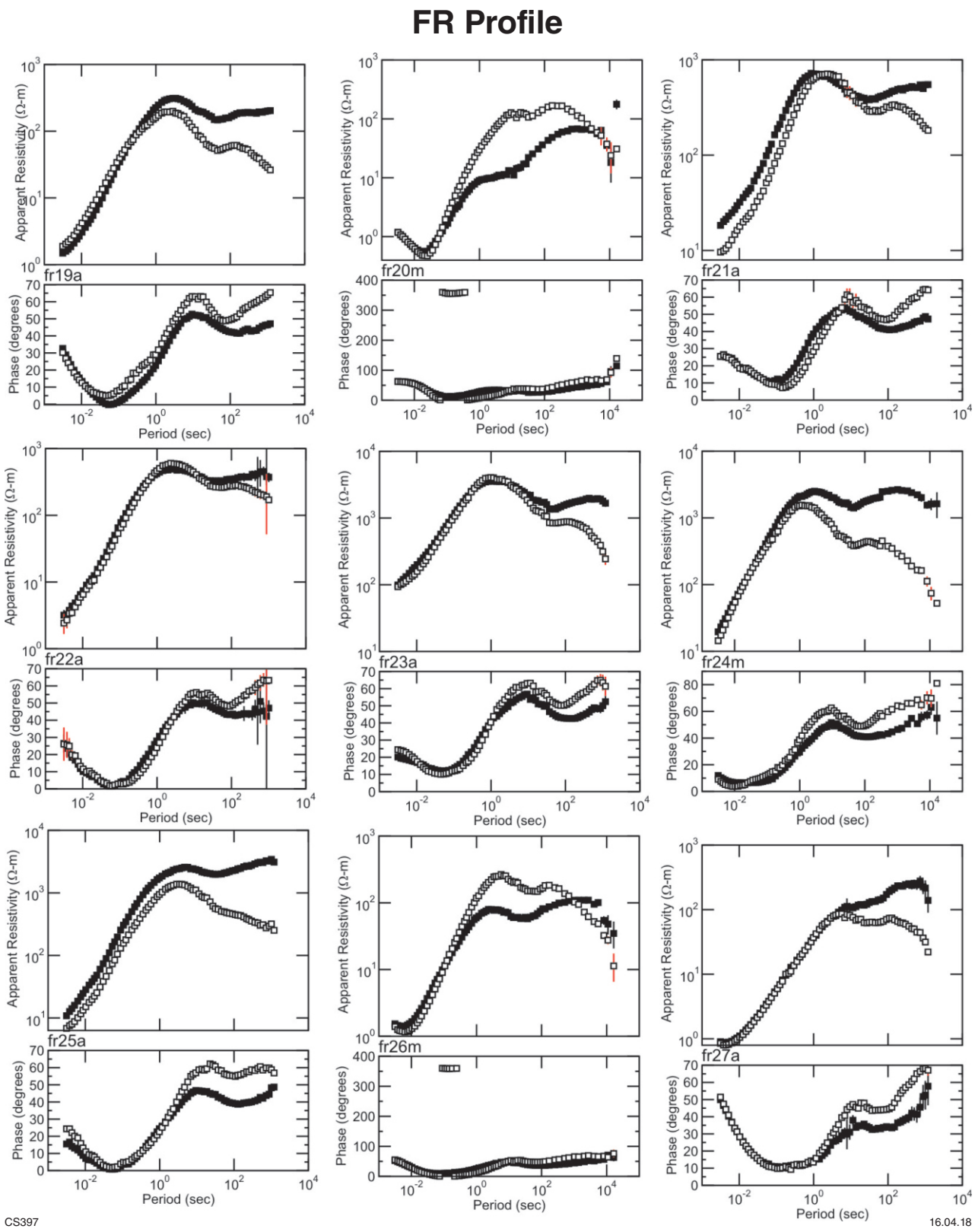

Figure 1.15. Stations fr19–fr27 along the FR profile

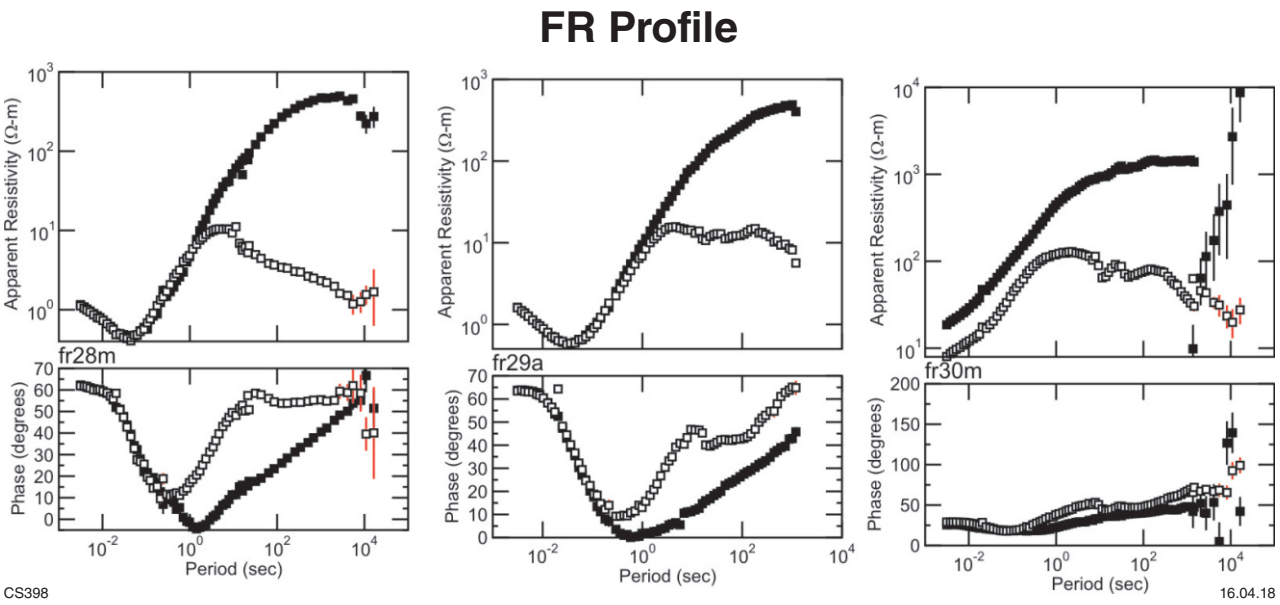

Figure 1.16. Stations fr28–fr30 along the FR profile

Appendix 2

AF3 profile

Eight aspects of the preferred conductivity model from profile AF3 (Fig. 38) were tested.

Three of the upper crustal, near-vertical structures were tested by replacing the low resistivities with higher values consistent with neighbouring cells (Fig. 2.1). Each saw a small increase in the forward calculated RMS value; however, the increase was minimal (1.96 – 1.98) for feature C. Both fixed and unfixed the altered feature A area resulted in equal RMS values that were slightly lower than that for the original model (Fig. 2.1b,c). With the area fixed, the model did not change significantly, but did return to the original model when unfixed. This indicates that feature A is not well resolved. In the case of feature B, subsequent inversions resulted in lower resistivities adjacent to or below the fixed area (Fig. 2.1d). With the areas unfixed, features B and C returned to the original model and had the lowest RMS values (Fig. 2.1e,g). The small changes in overall RMS value may be a result of misfit averaging over a long profile with many sites. Note that with MT data, the area sampled beneath each site is larger with longer periods. Therefore, changes at shallow depths will affect fewer sites than changes at deeper levels. It is concluded that the features B and C are generally a reliable aspect of the model.

Two areas of resistive lower crust were tested by inserting low resistivity blocks between depths of 30 and 40 km (Features E and D; Fig. 2.1a). Feature F represents the low resistivity layer observed in the upper mantle beneath the eastern half of the profile, and a resistive block was inserted between depths of 40 and 60 km (Fig. 2.1a). A forward calculation of the response curves saw the overall RMS value increase by nearly 10% for features E and F, and nearly 20% for feature D. With subsequent iterations, significant changes are noted in the areas surrounding the fixed blocks, and the RMS values remained higher than the original (Fig 2.1h,j,l). In each case, with the areas unfixed, the models returned to the original conductivity values and had the lowest overall RMS value (Fig. 2.1i,k,m), an indication that these features are robust.

Features G and H were tested to determine the model resolution within the upper mantle (Fig. 2.1a). Although the model returned to the original with area G unfixed, both fixed and unfixed RMS values were lower than the original model and were equal, with little change to the model with the area fixed (Fig. 2.1n,o). This suggests that the data may not be sensitive to this area of the model. With area H fixed, the RMS did not decrease as much as it did for the original model (Fig. 2.1p). Unfixed, the lowest RMS value was attained and the model again returned to the original, indicating that model resolution in the vicinity of feature H is good (Fig. 2.1q).

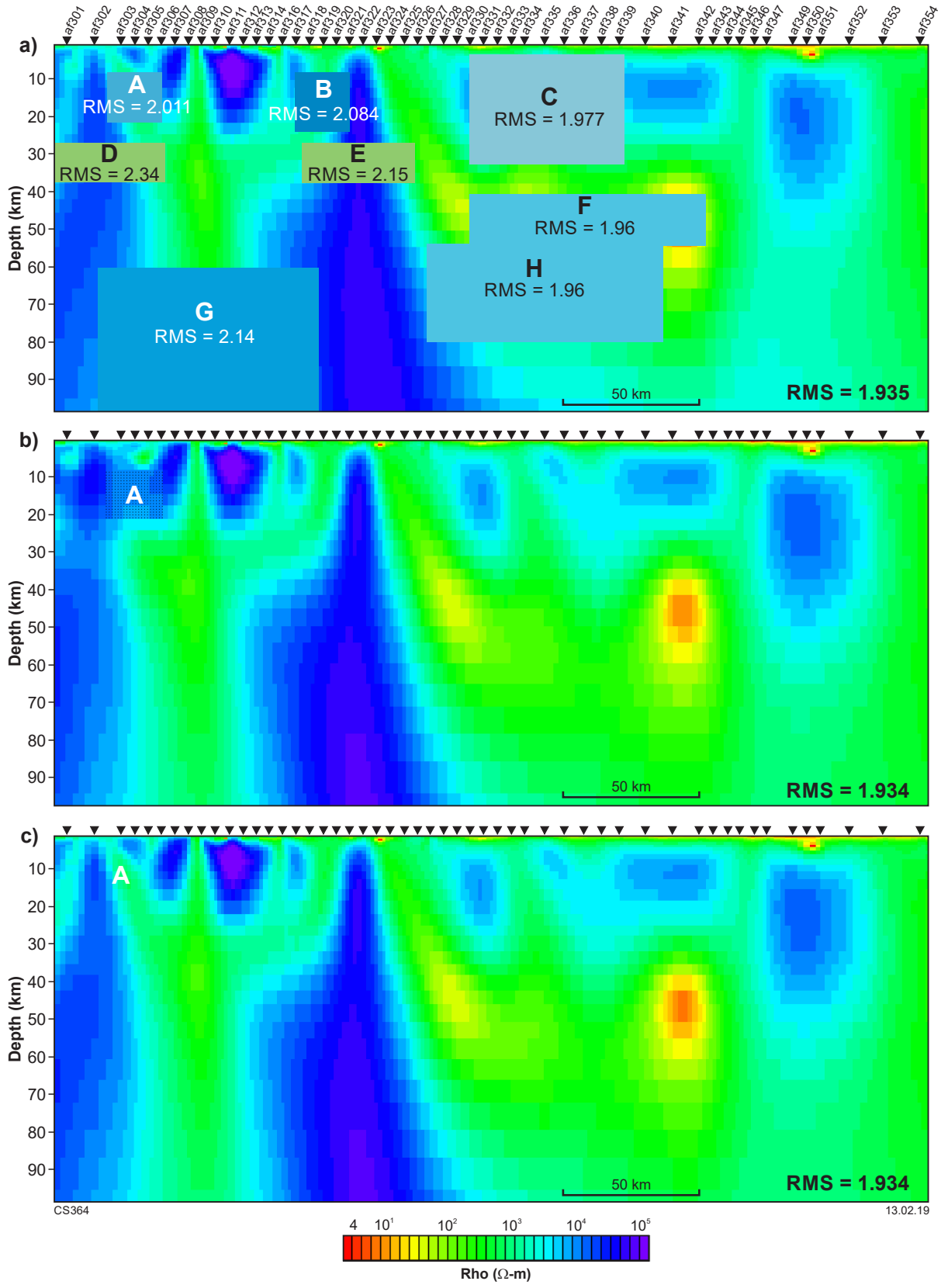

Figure 2.1. **Assessment of the reliability of features with anomalous electrical properties in the preferred resistivity cross-section along the AF3 profile. Warm colours represent areas that are conductive and blue colours represent areas that are resistive: a) shows the lettered features that are altered and the resulting RMS values after a forward inversion; b) new model with feature A 'fixed'; c) new model with feature A 'unfixed'; d) new model with feature B 'fixed'; e) new model with feature B 'unfixed'; f) new model with feature C 'fixed'; g) new model with feature C 'unfixed'; h) new model with feature D 'fixed'; I) new model with feature D 'unfixed'; j) new model with feature E 'fixed'; k) new model with feature E 'unfixed'; l) new model with feature F 'fixed'; m) new model with feature F 'unfixed'; n) new model with feature G 'fixed'; o) new model with feature G 'unfixed'; p) new model with feature H 'fixed'; q) new model with feature H 'unfixed'**

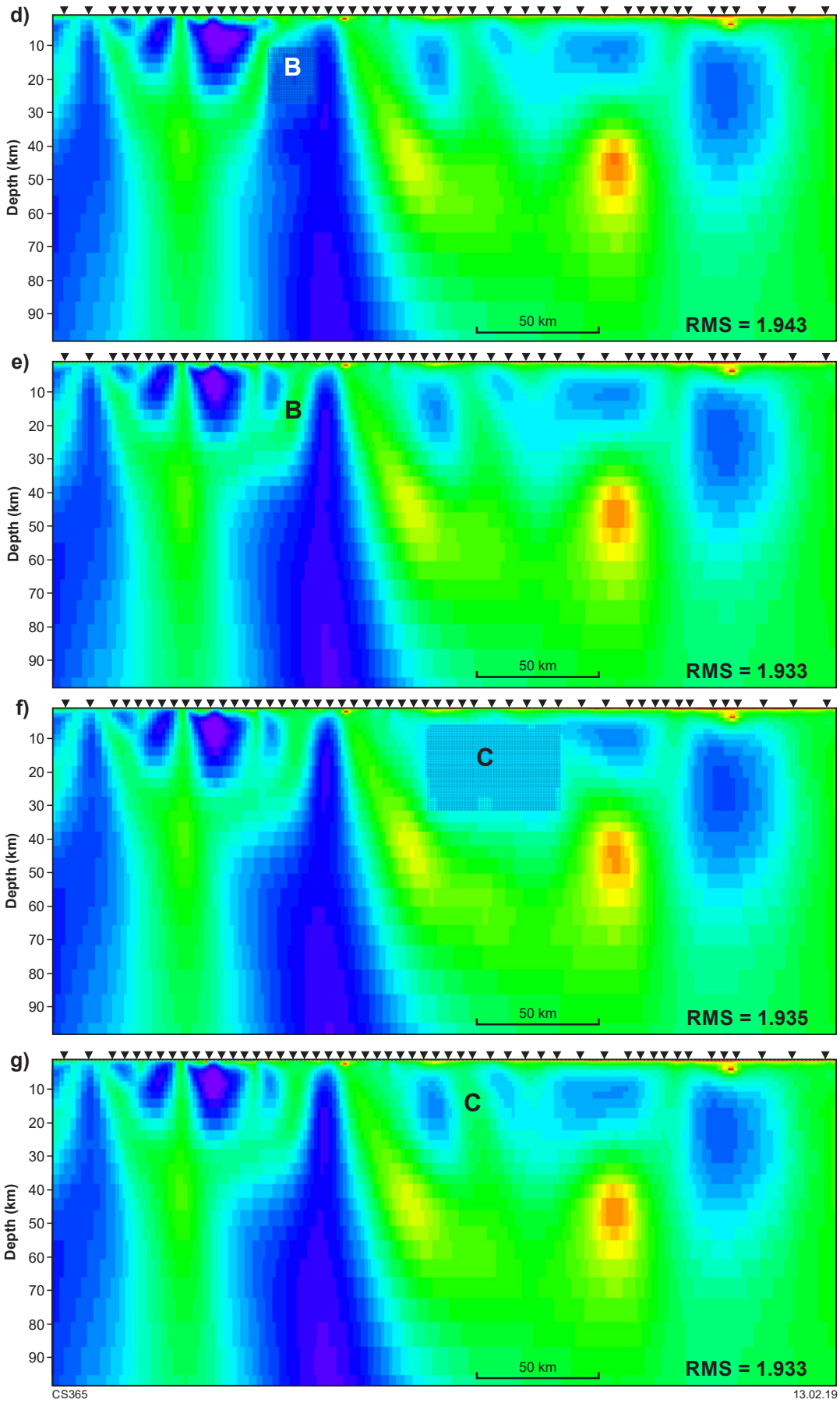

Figure 2.1 continued

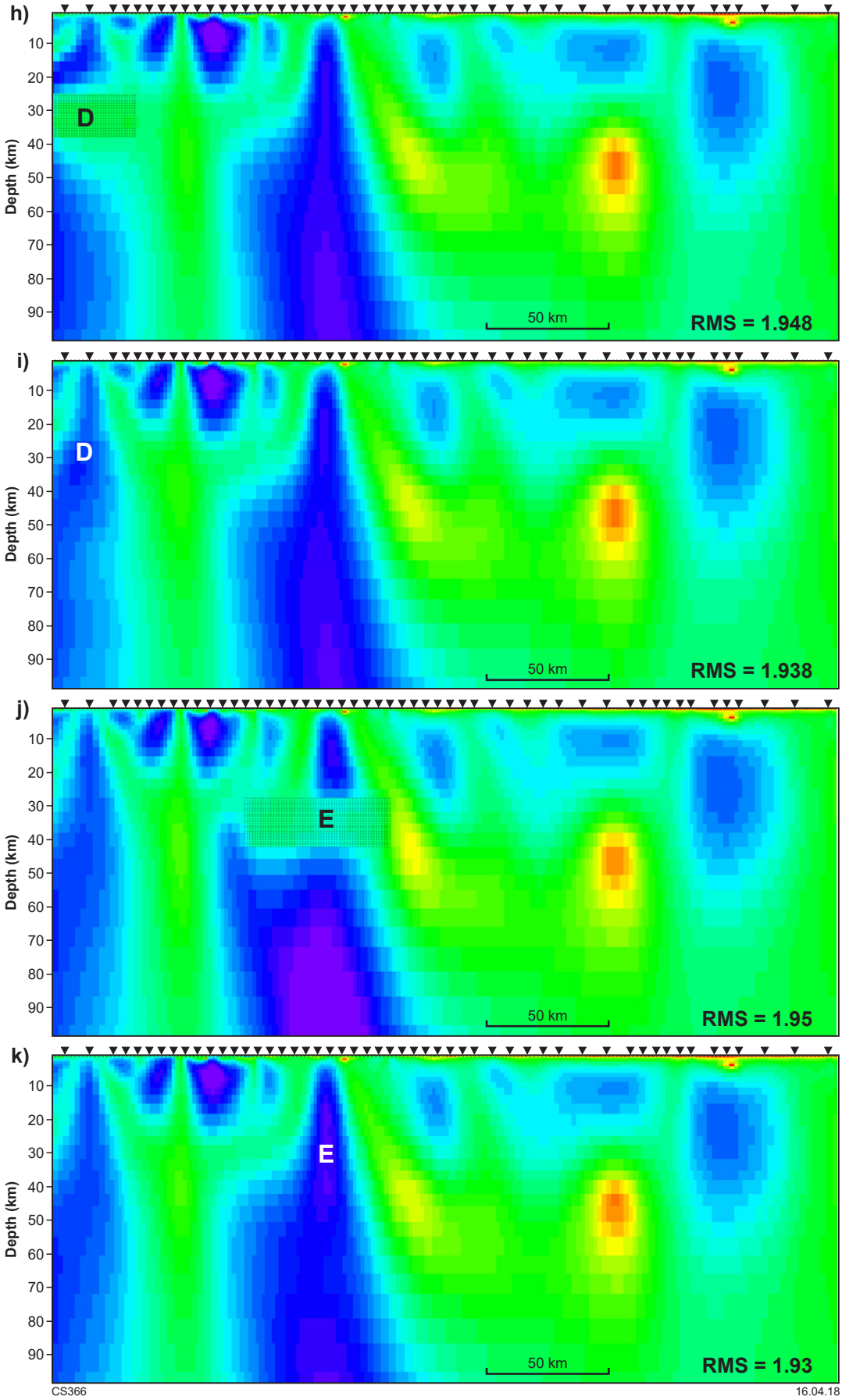

Figure 2.1 continued

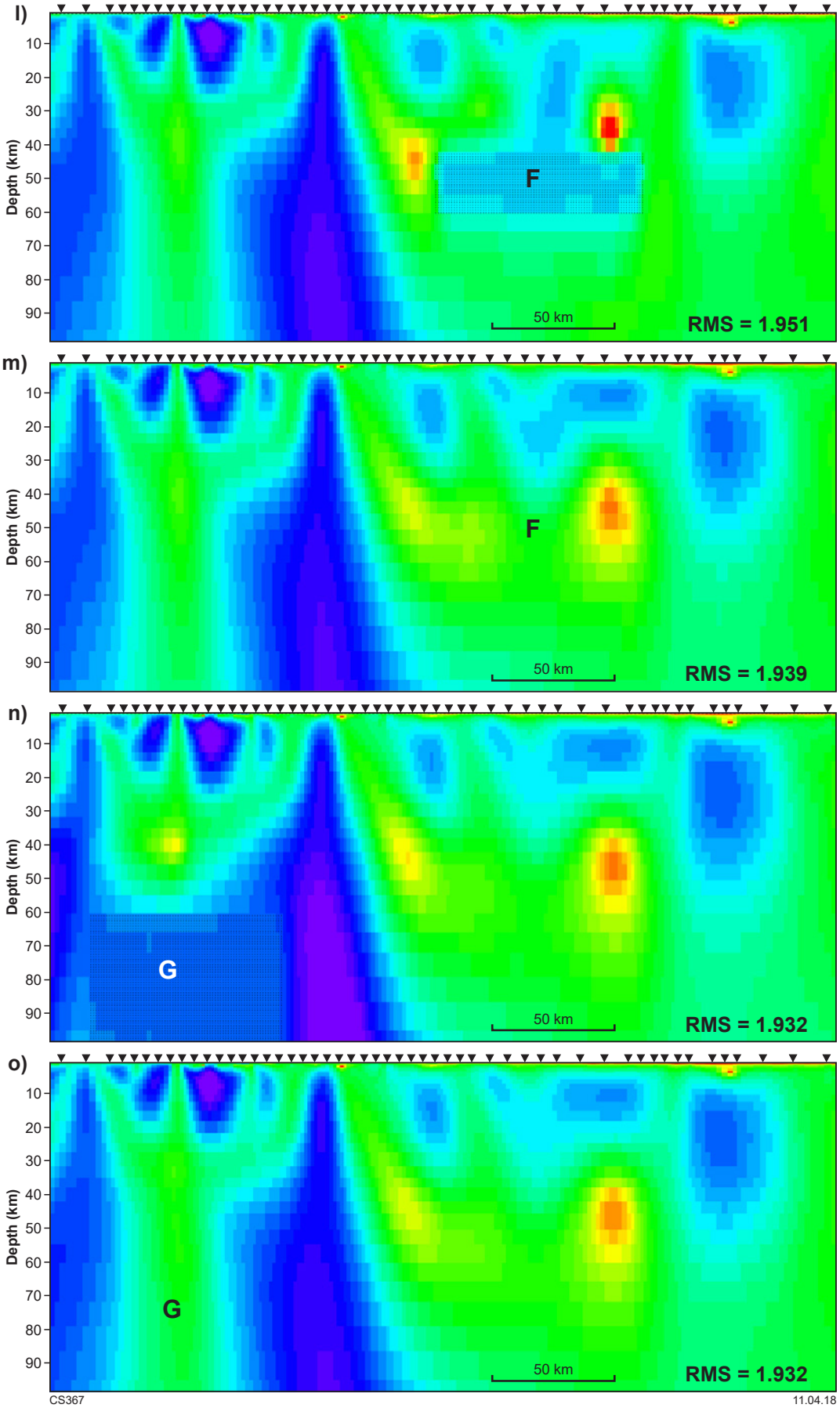

Figure 2.1 continued

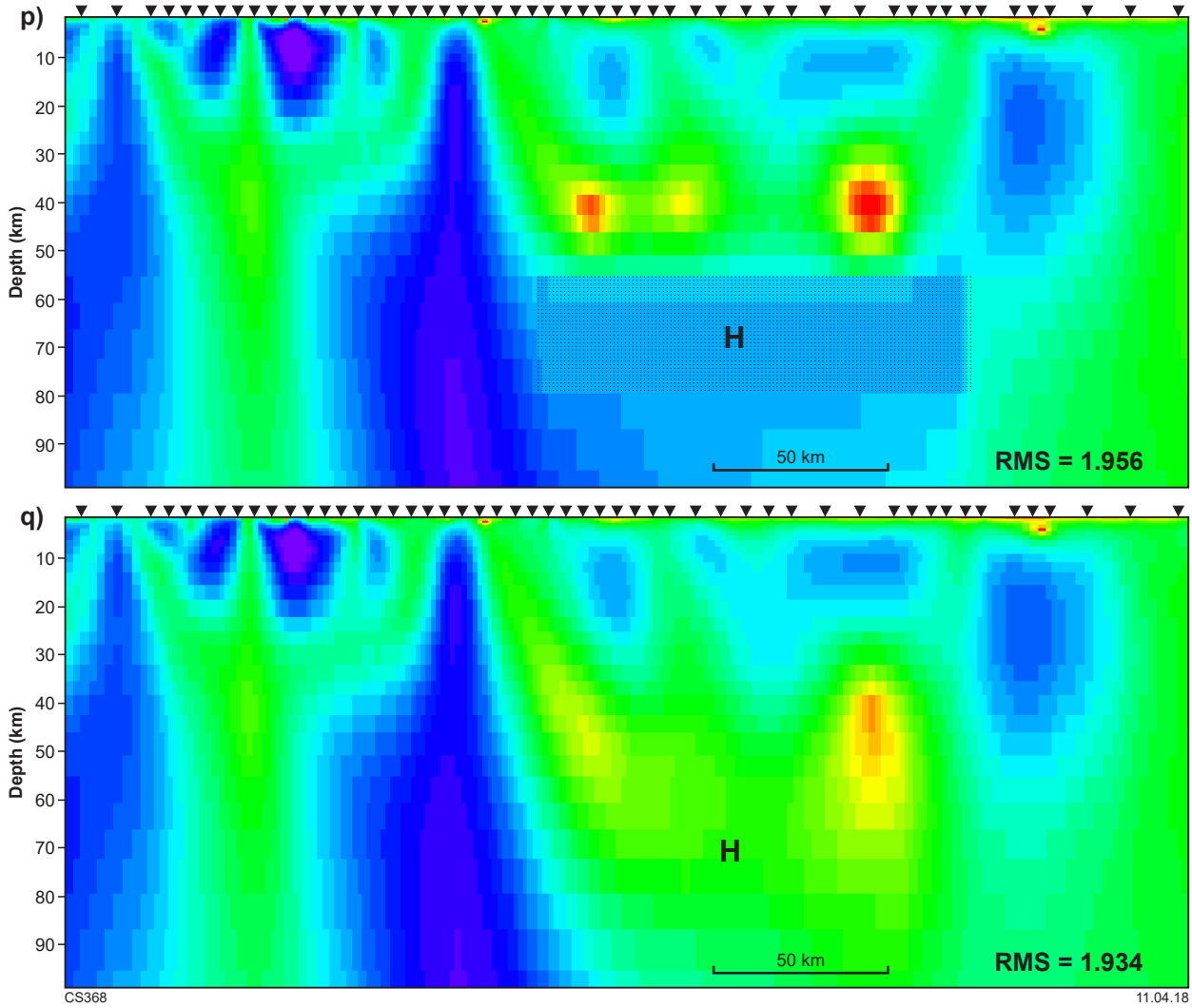

Figure 2.1 **continued**

YFB profile

Eight aspects of the preferred conductivity model from YFB (Fig. 40) were tested. A forward calculation of the altered models resulted in a small (0.8%) increase in RMS value for feature A and large (6.4%) increase for feature B (Fig. 2.2a). For feature A, the model did not show significant changes with the area fixed (Fig. 2.2b). After subsequent inversion, the conductivity structure surrounding feature B changed significantly with the area fixed, and the RMS value, although reasonable, was higher than the original value (Fig. 2.2d). For both features A and B, with the areas unfixed the models returned to the original; however, only the model for feature B had a lower RMS value (Fig. 2.2c,e). This testing suggests that feature B is well resolved and required by the data, but feature A is less robust.

Feature C is an area of resistive lower crust that has been tested by inserting a continuous, lower crustal, conductive layer between depths of 30 and 50 km. The forward calculations saw an increase in RMS of 8.1%. Further iterations result in the lowest RMS value obtained with the area unfixed, and feature C returned to a resistive lower crust suggesting that this is a reliable aspect of the model (Fig. 2.2f,g). Feature D is a conductive layer, the top of which lies at approximately 40 km depth. The depth to this layer was tested by adding a conductive layer at 30 km depth (Fig. 2.2a). Although a forward calculation resulted in a small RMS increase of 1.7%, with the area fixed the RMS value did not change with subsequent inversions (Fig. 2.2h). With the area unfixed, the RMS value was reduced and the model returned to the original (Fig. 2.2i). Feature E is in area where the upper mantle shows low resistivities. A narrow, low conductivity block was inserted at depths between approximately 35 and 70 km beneath the surface expression of the Fraser Shear Zone. The forward calculation resulted in a minor RMS increase of approximately 0.3%. Surprisingly, with the area fixed the lowest RMS value was achieved even though the original conductivity values returned with the area unfixed (Fig. 2.2j). This suggests that the data are not sensitive to a narrow resistive zone at these depths, and that the return of a conductive lower crust is a function of the smoothing effects of model inversions.

In order to test the resolution of the upper mantle, resistive blocks were inserted between depths of 40 and 55 km (Feature F), and between depths of 55 and 90 km (Feature G), beneath the northwest end of the YFB profile. A conductive block was inserted between depths of 60 and 100 km beneath sites yfb03–yfb11 (Feature H; Fig. 2.2a). Forward calculations of the altered models for features F and G resulted in a minor increase in RMS values of 0.6%, with an increase of 7.1% for feature H. Further iterations resulted in similar RMS values with feature F fixed and unfixed (Fig. 2.2l,m); however, the RMS for features G and H remained high with the areas fixed, and lowered to the original value when unfixed (Fig. 2.2n–q). This indicates that the data may not be sensitive to the area directly beneath the lower crustal conductor at the northwest end of the profile, but are sensitive to the deeper structure, and that the lateral changes in upper mantle resistivity structure are robust.

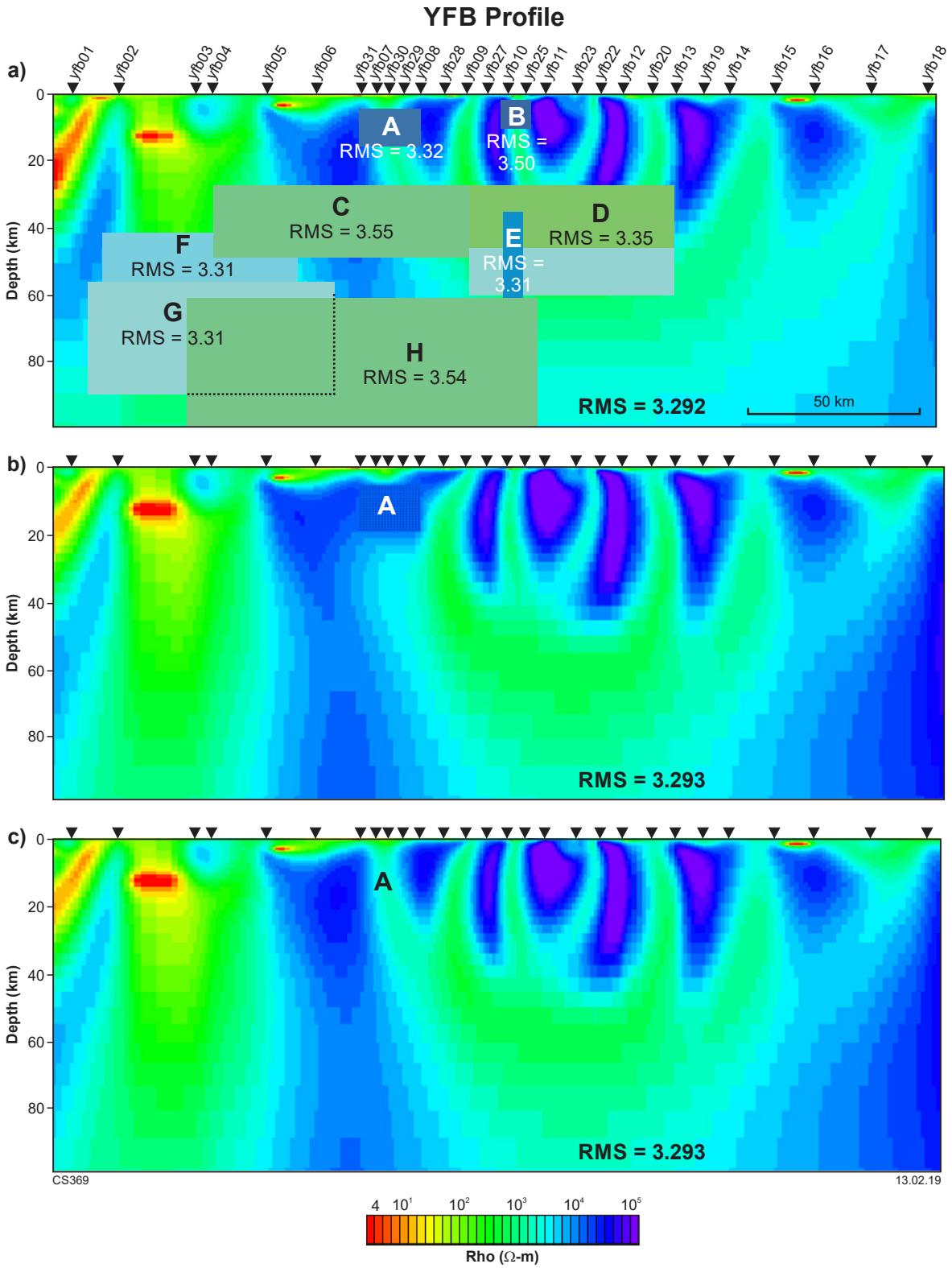

Figure 2.2. **Assessment of the reliability of features with anomalous electrical properties in the preferred resistivity cross-section along the YFB profile. Warm colours represent areas that are conductive and blue colours represent areas that are resistive: a) shows the lettered features that are altered and the resulting RMS values after a forward inversion; b) new model with feature A 'fixed'; c) new model with feature A ' unfixed; d) new model with feature B 'fixed'; e) new model with feature B 'unfixed; f) new model with feature C 'fixed'; g) new model with feature C 'unfixed'; h) new model with feature D 'fixed'; i) new model with feature D 'unfixed'; j) new model with feature E 'fixed'; k) new model with feature E 'unfixed'; l) new model with feature F 'fixed'; m) new model with feature F 'unfixed'; n) new model with feature G 'fixed'; o) new model with feature G 'unfixed'; p) new model with feature H 'fixed'; q) new model with feature H 'unfixed'**

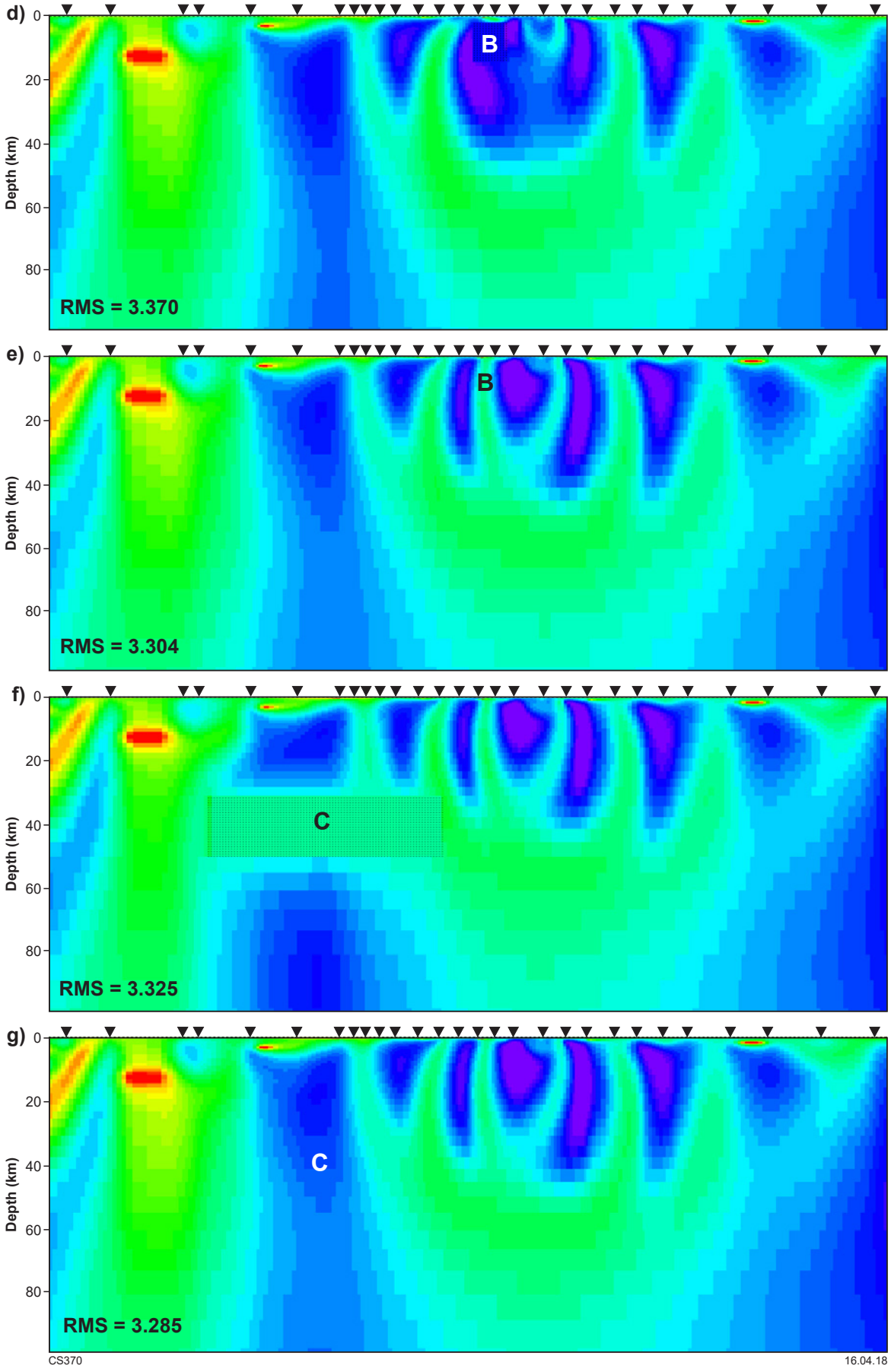

Figure 2.2 continued

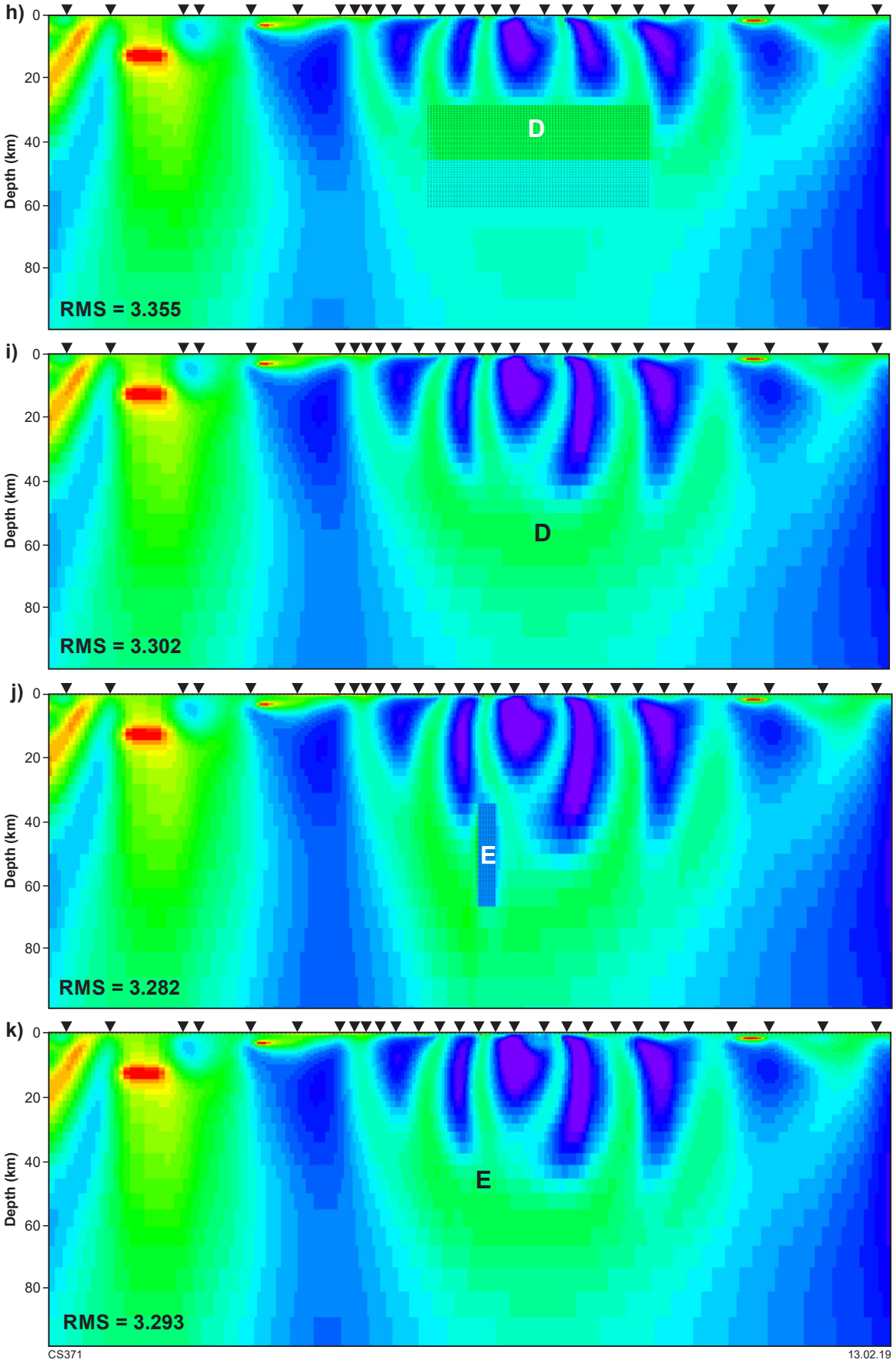

Figure 2.2 continued

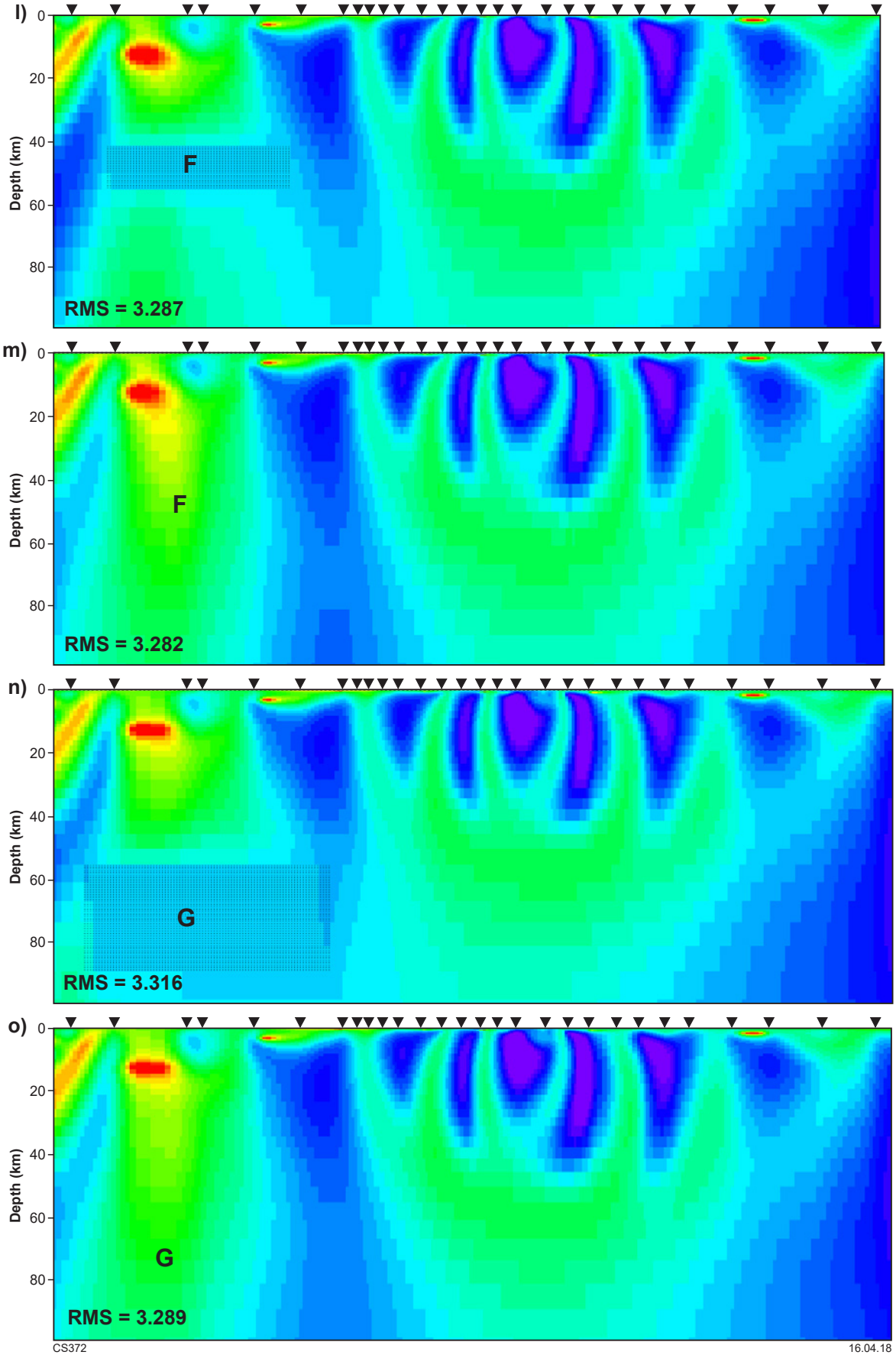

Figure 2.2 continued

CBZ profile

Several features have been tested to ascertain that they are robust and required by the data (Fig. 2.3). Features A, B and C are features in the upper crust. Features D, E, and F test the lateral variations in the lower crust, and features G and H in the upper mantle. Forward models of the altered models saw an increase in the overall RMS value for each feature (Fig. 2.3a). A low resistivity block was inserted where a near-vertical, low resistivity zone was imaged in other profiles beneath the Fraser Shear Zone (Feature A). Features B and C are near-vertical, low resistivity zones cutting through a resistive upper crust that were replaced with resistive blocks. With the areas fixed, the models were not able to obtain an RMS value as low as the original and the cells surrounding the fixed area were significantly changed for features A, B and C (Fig. 2.3b,d,f). Unfixed, the models returned to the original conductivity values and comparably low RMS values (Fig. 2.3c,e,g) indicating that the data are not consistent with the presence of a low resistivity zone beneath the Fraser Shear Zone, but that low resistivities of features B and C are reliable aspects of the preferred model.

Features D and E are areas of resistive lower crust and were altered by inserting a less resistive block forming a continuous, low resistivity layer beneath the profile (Fig. 2.3a,c,e,g). In both cases, the fixed models were unable to obtain the low RMS values and the unfixed models reverted back to the original model and lower RMS value (Fig. 2.3h–k). This indicates that the resistive lower crust beneath these areas is robust. Feature F was altered by inserting a resistive block between depths of 15 and 37 km to test the depth to the top of the low resistivity layer beneath the Fraser Zone. Surprisingly, the lowest RMS value was obtained with the area fixed, even though the model reverted to the original conductivity structure with the area unfixed (Fig. 2.3l,m). Along with the large variability between models of differing strikes, this is a good indication that the depth to the top of this layer is not well resolved.

Features G and H tested upper mantle resistivities by replacing resistive values with less resistive blocks at depths greater than 60 km beneath the northern (Feature G) and the southern ends of the profile (Feature H). In both cases, the lowest RMS value was obtained with the altered areas unfixed, and the models showing the original resistivity values (Fig. 2.3n–q). This suggests that the data are sensitive to depths of at least 100 km beneath the profile.

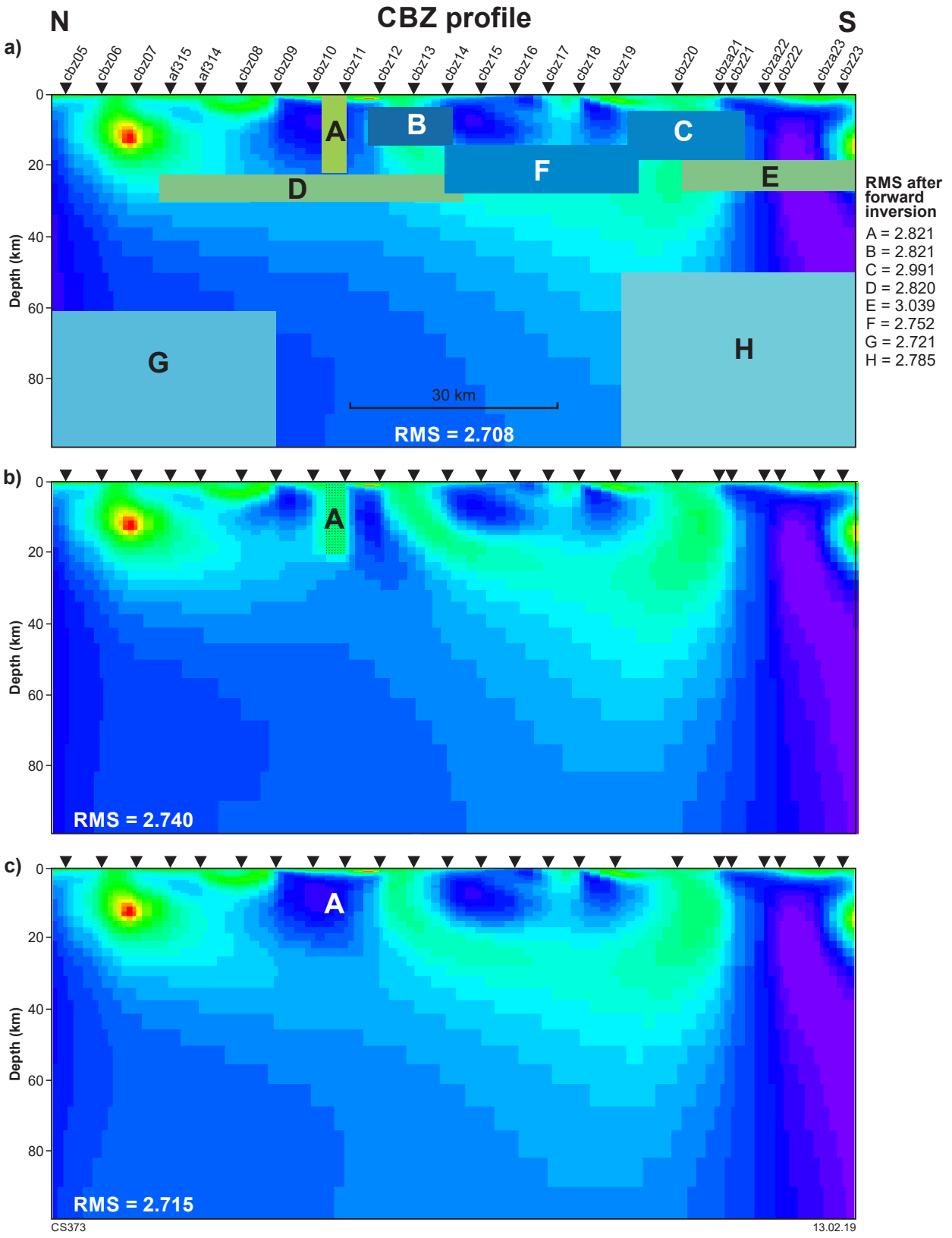

Figure 2.3. Assessment of the reliability of features with anomalous electrical properties in the preferred resistivity cross-section along the CBZ profile. Warm colours represent areas that are conductive and blue colours represent areas that are resistive: a) shows the lettered features that are altered and the resulting RMS values after a forward inversion; b) new model with feature A 'fixed'; c) new model with feature A ' unfixed; d) new model with feature B 'fixed'; e) new model with feature B 'unfixed; f) new model with feature C 'fixed'; g) new model with feature C 'unfixed'; h) new model with feature D 'fixed'; I) new model with feature D ' unfixed'; j) new model with feature E 'fixed'; k) new model with feature E 'unfixed'; l) new model with feature F 'fixed'; m) new model with feature F 'unfixed'; n) new model with feature G 'fixed'; o) new model with feature G 'unfixed'; p) new model with feature H 'fixed'; q) new model with feature H 'unfixed'

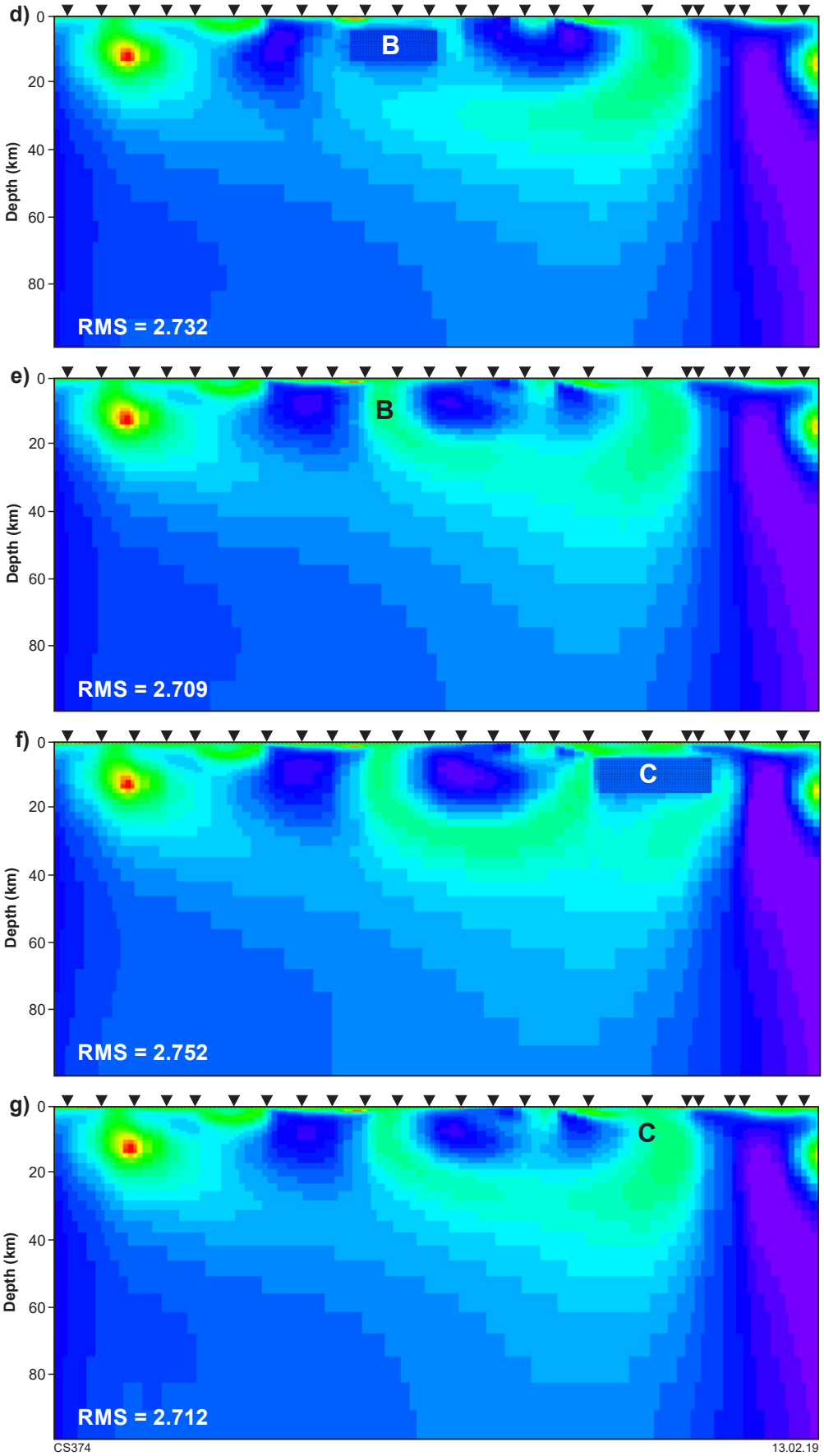

Figure 2.3 continued

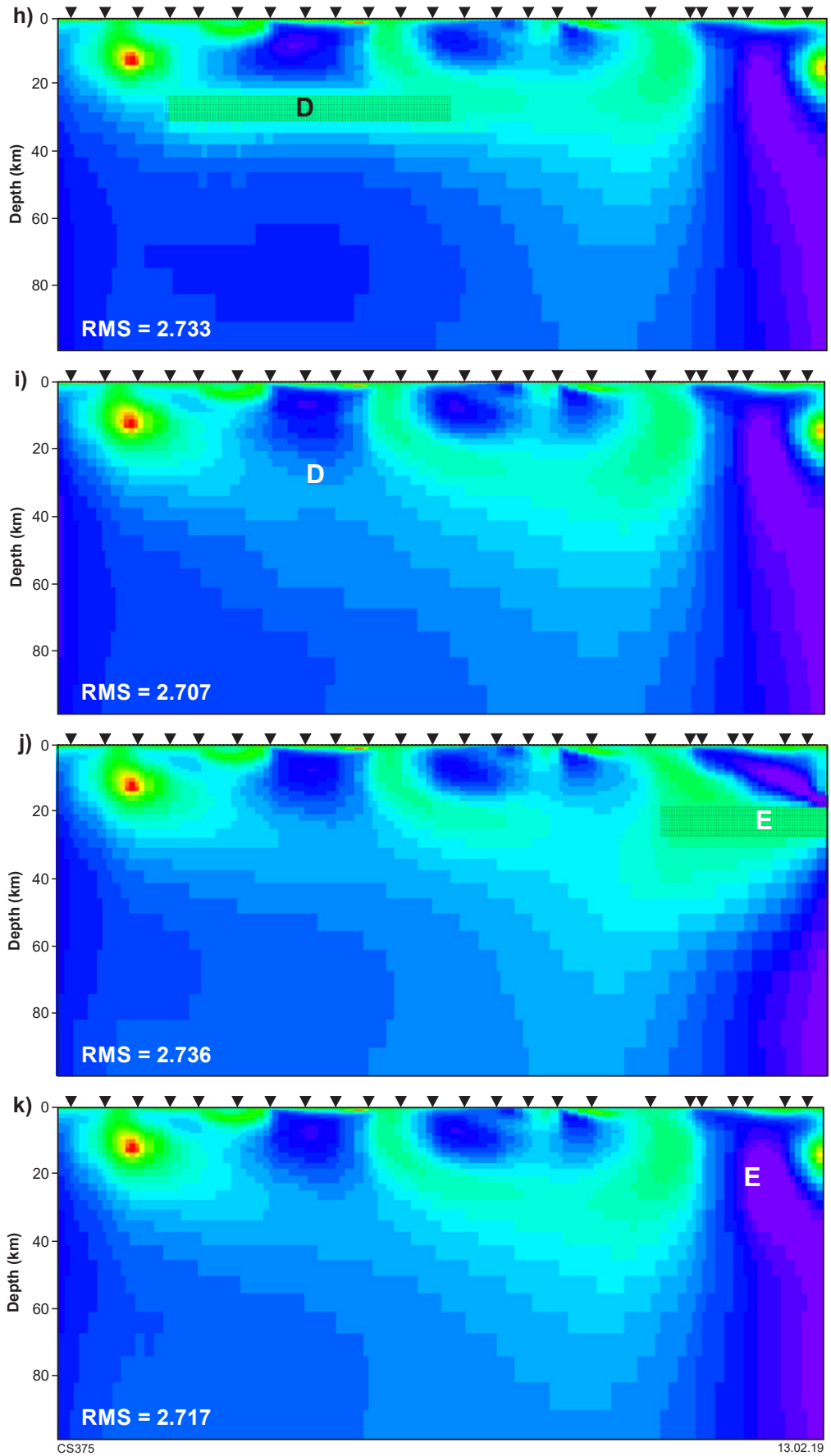

Figure 2.3 continued

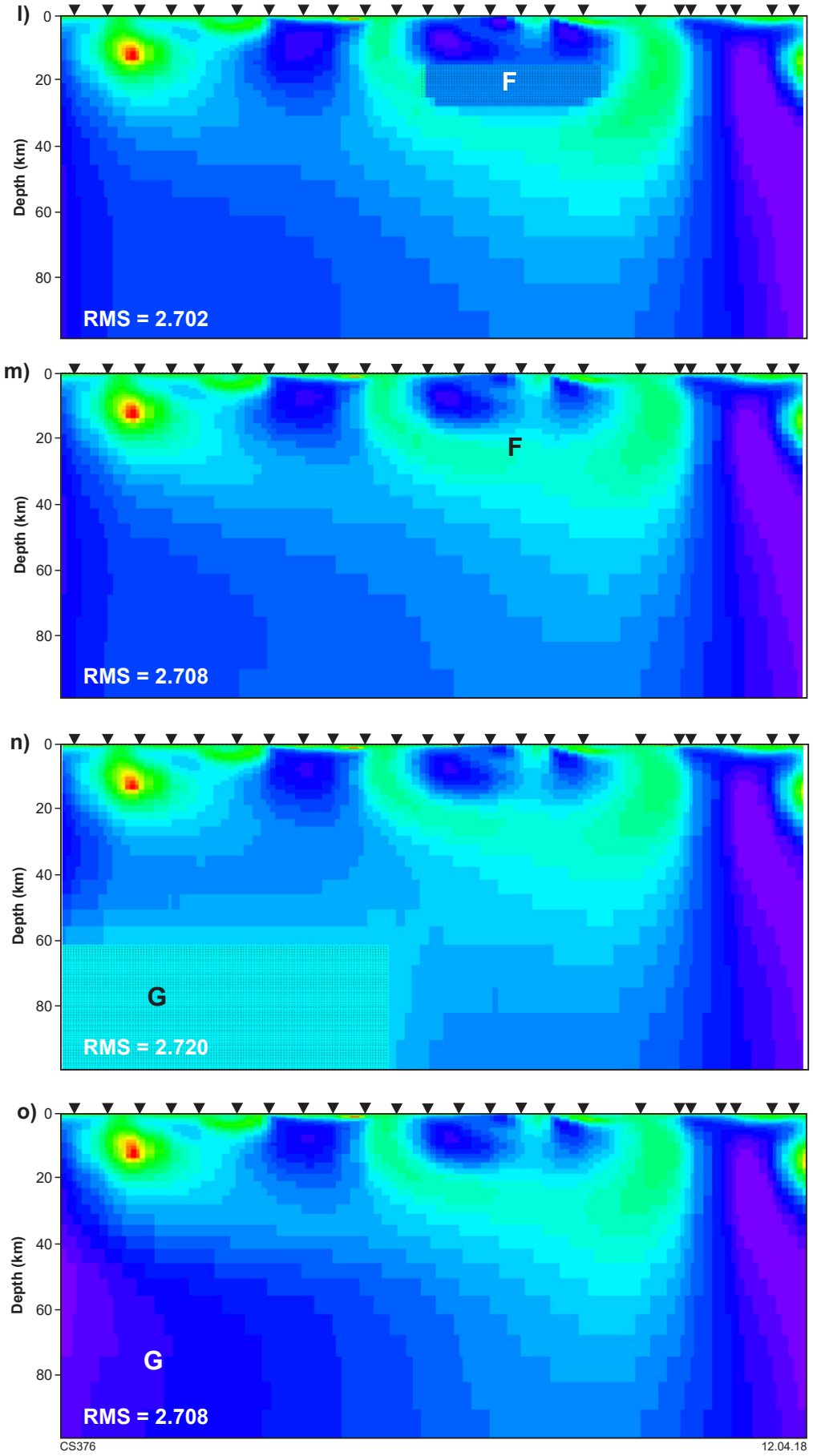

Figure 2.3 **continued**

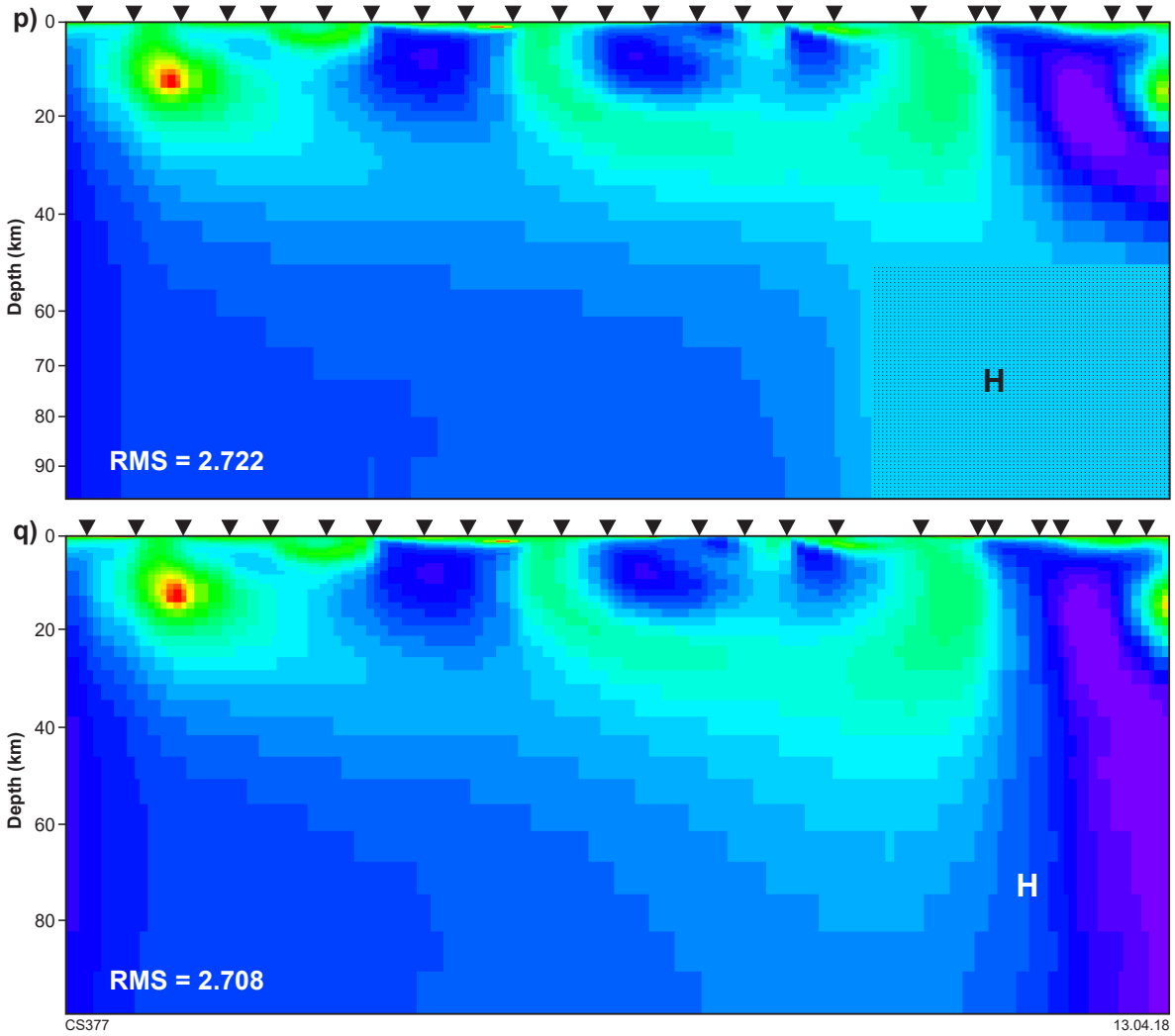

Figure 2.3 continued

FR profile

Feature testing undertaken along the FR profile was performed on some of the near-vertical, low resistivity structures in the upper crust (Features A, B and C), the continuity and thickness of the lower crustal conductor (Features D, E, F and G), and the change in upper mantle resistivity from southwest to northeast (Features H and I; Fig. 2.4a). Three of the near-vertical, low resistivity features were tested by replacing the low resistivities with high resistivity blocks at upper and middle crustal depths. A forward calculation of the altered models resulted in an RMS increase of 2–2.6% for each of the features A, B and C (Fig. 2.4a). For each of the three features, with the areas fixed further iterations resulted in significant changes to the model directly adjacent to or below the fixed area, and the RMS value remained higher than that of the original model (Fig. 2.4b,d,f). In each case, the model returned to the original structure and obtained the lowest RMS value with the areas unfixed (Fig. 2.4c,e,g). This indicates that each of the three features (A, B and C) are reliable aspects of the model.

Features D and E are areas of moderate to low resistivities in the lower crust/uppermost mantle.These were tested by inserting a resistive block between depths of 33 and 55 km beneath sites fr25–fr17 (Feature D), and between depths of 38 and 55 km beneath sites yfb25–yfb26 (Feature E). In both cases, the forward calculation resulted in a minor RMS increase of 0.6% and 0.8%, respectively. Also, in both cases, the lowest RMS value was reached with the areas fixed with little change to the surrounding cells (Fig. 2.4h,j). This suggests that the data do not resolve the structure in these areas well. Feature D lies beneath a low resistivity layer that may be masking the underlying structure. Feature E lies northeast of the Fraser Shear Zone where the profile runs parallel to strike. Features F and G are areas of moderate to high resistivities and were tested by inserting low resistivity blocks between depths of 38 and 55 km beneath sites fr13–yfb25 (Feature F) and between depths of 38 and 55 km beneath sites fr30–fr26 (Feature G; Fig. 2.4a). Forward calculations of the altered models saw an increase in RMS of 4.2% for feature F and 0.8% for feature G. With the area fixed, significant differences are observed in the cells neighbouring Feature F, and the RMS value was not as low as that for the original model (Fig. 2.4l). Unfixed, the models return to the original structure and RMS value (Fig. 2.4m). For feature G, the RMS value is only slightly lower with the area unfixed compared to that with the area fixed (Fig. 2.4n,o). This indicates that the high resistivities observed in the vicinity of Feature F are robust, but that the area near Feature G is likely not well resolved.

A resistive block was inserted to replace higher resistivities at depths between 60 and 100 km beneath the southwestern end of the profile (Feature H), and a moderately resistive block was inserted to replace high resistivities at depths between 60 and 90 km beneath the northeast end of the profile (Feature I; Fig. 2.4a). With the areas fixed, significant differences are observed in the cells neighbouring Features H and I, and the RMS values were not as low as that for the original model (Fig. 2.4p,r). Unfixed, the models return to the original structure and RMS value, an indication that the data are sensitive to the deep structure beneath the profile to at least a depth of 100 km (Fig. 2.4q,s).

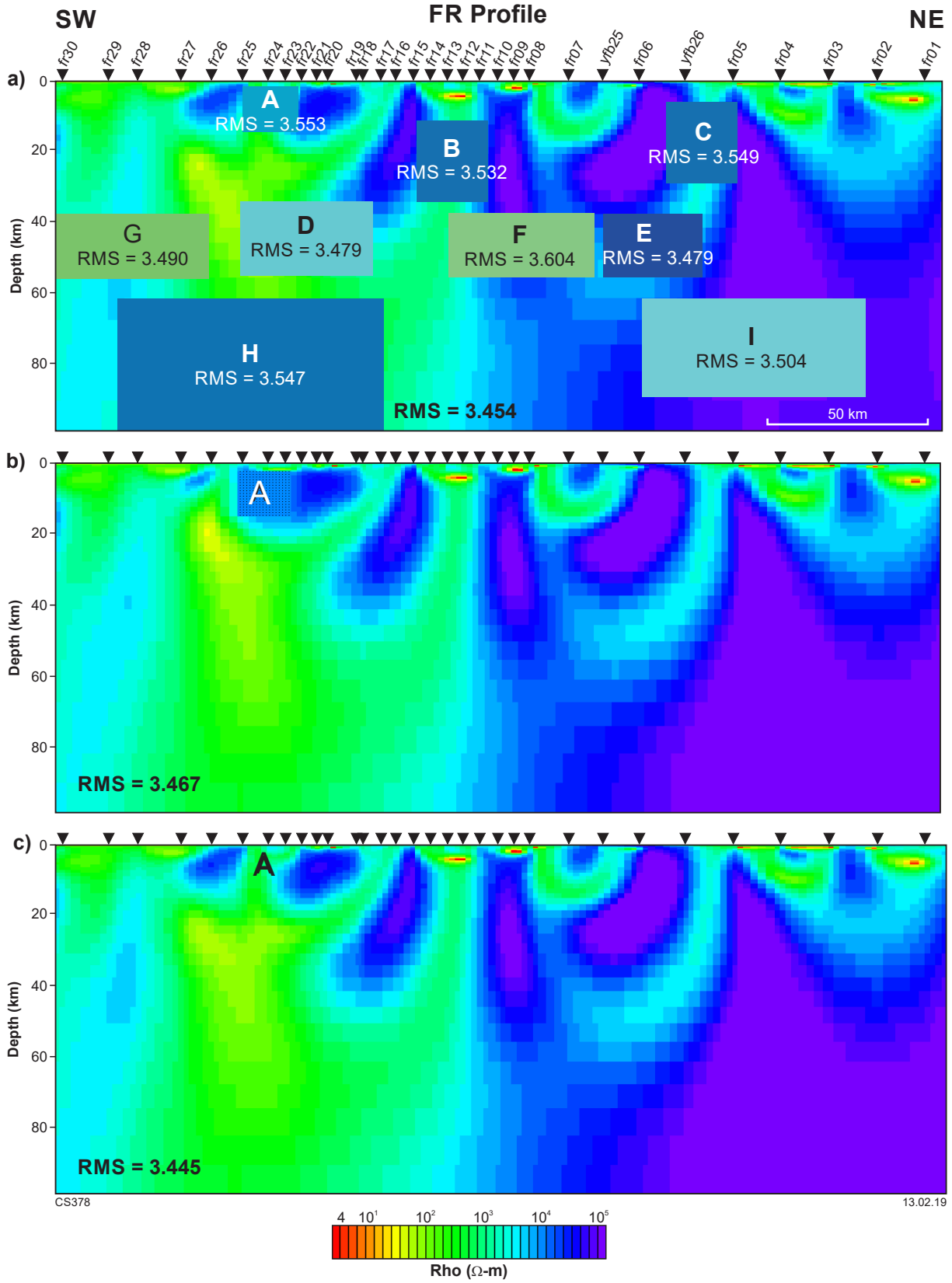

Figure 2.4 Assessment of the reliability of features with anomalous electrical properties in the preferred resistivity cross-section along the FR profile. Warm colours represent areas that are conductive and blue colours represent areas that are resistive: a) shows the lettered features that are altered and the resulting RMS values after a forward inversion; b) new model with feature A 'fixed'; c) new model with feature A ' unfixed; d) new model with feature B 'fixed'; e) new model with feature B 'unfixed; f) new model with feature C 'fixed'; g) new model with feature C 'unfixed'; h) new model with feature D 'fixed'; I) new model with feature D ' unfixed'; j) new model with feature E 'fixed'; k) new model with feature E 'unfixed'; l) new model with feature F 'fixed'; m) new model with feature F 'unfixed'; n) new model with feature G 'fixed'; o) new model with feature G 'unfixed'; p) new model with feature H 'fixed'; q) new model with feature H 'unfixed'; r) new model with feature I 'fixed'; s) new model with feature I 'unfixed'

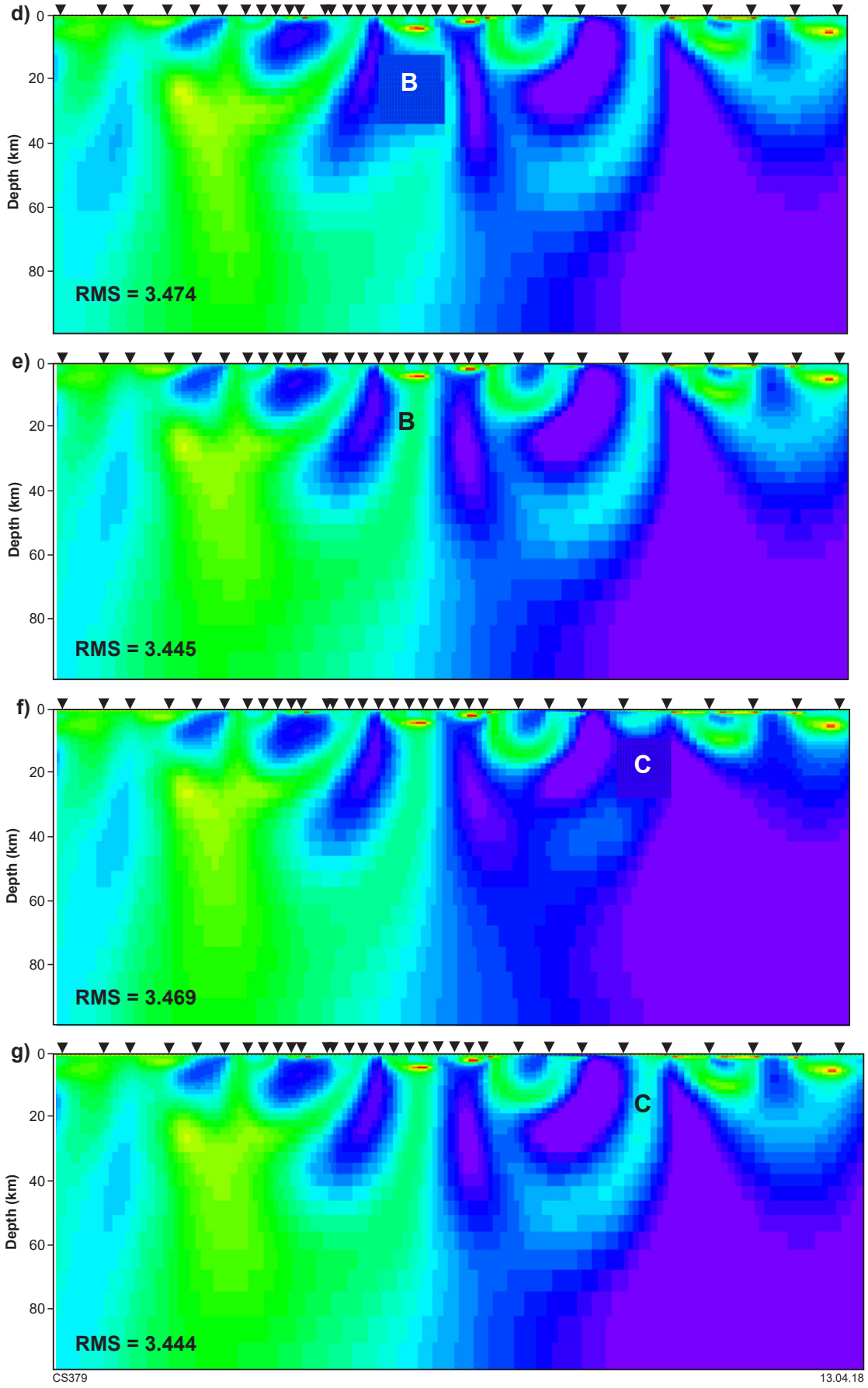

Figure 2.4 **continued**

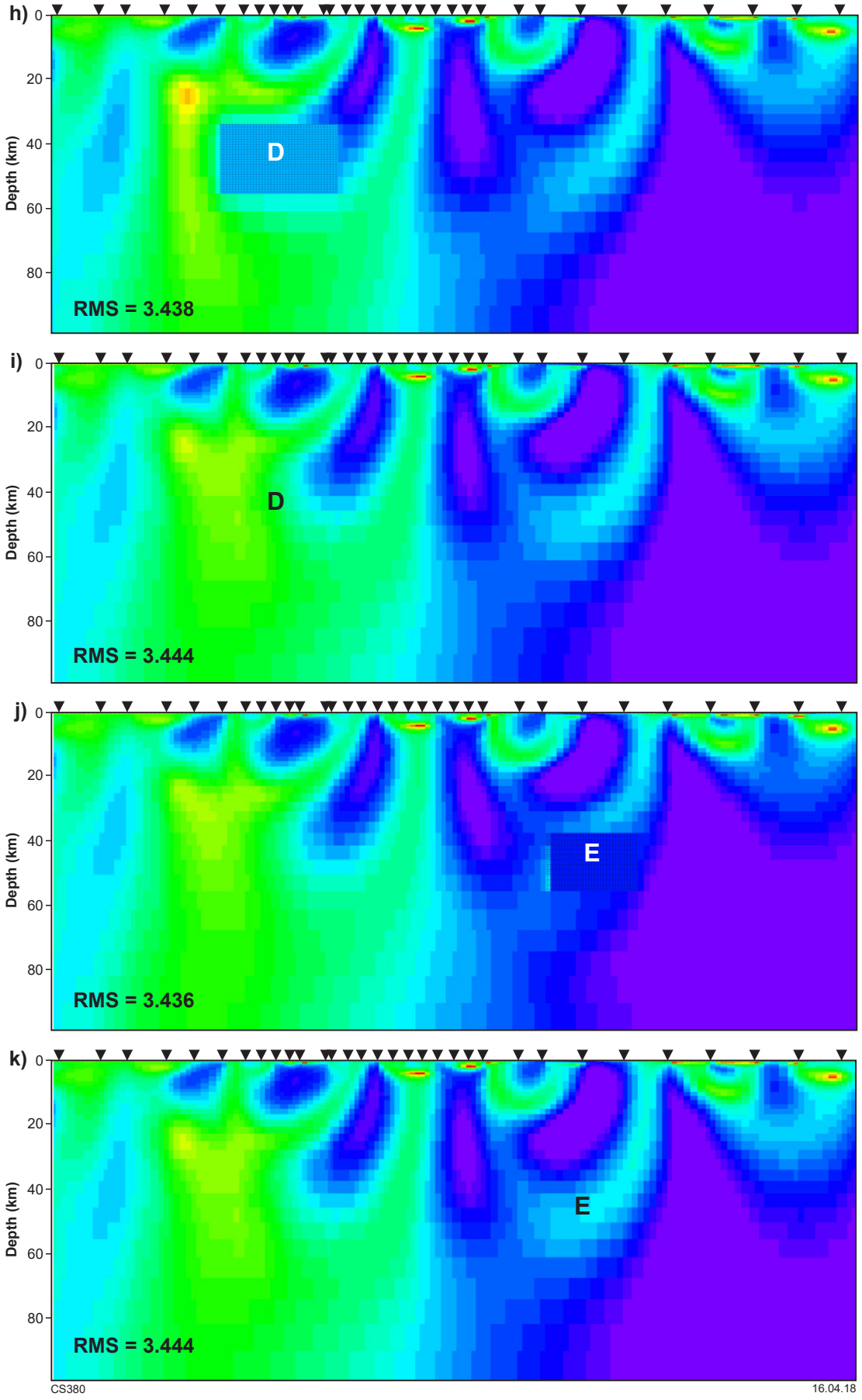

Figure 2.4 continued

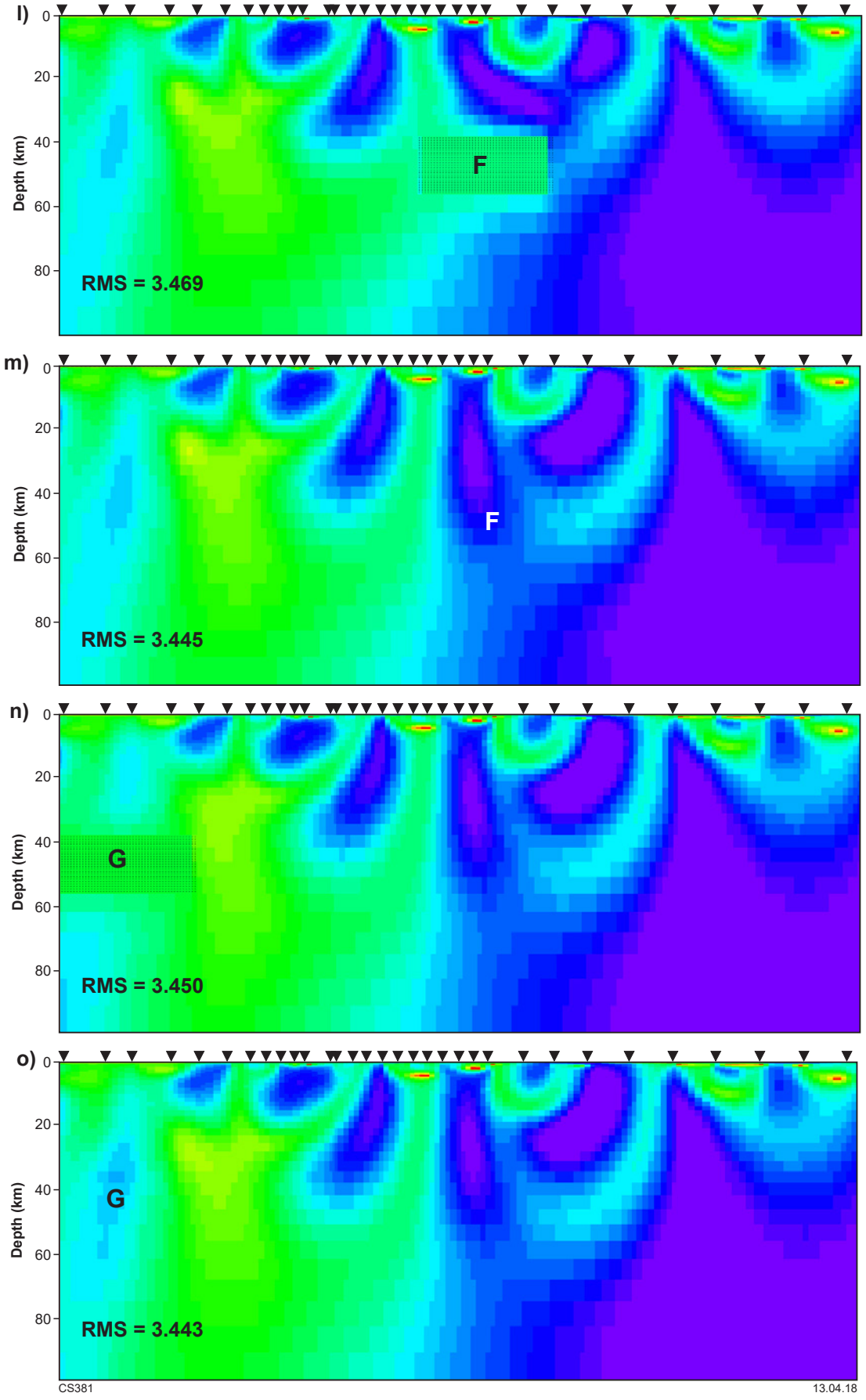

Figure 2.4 **continued**

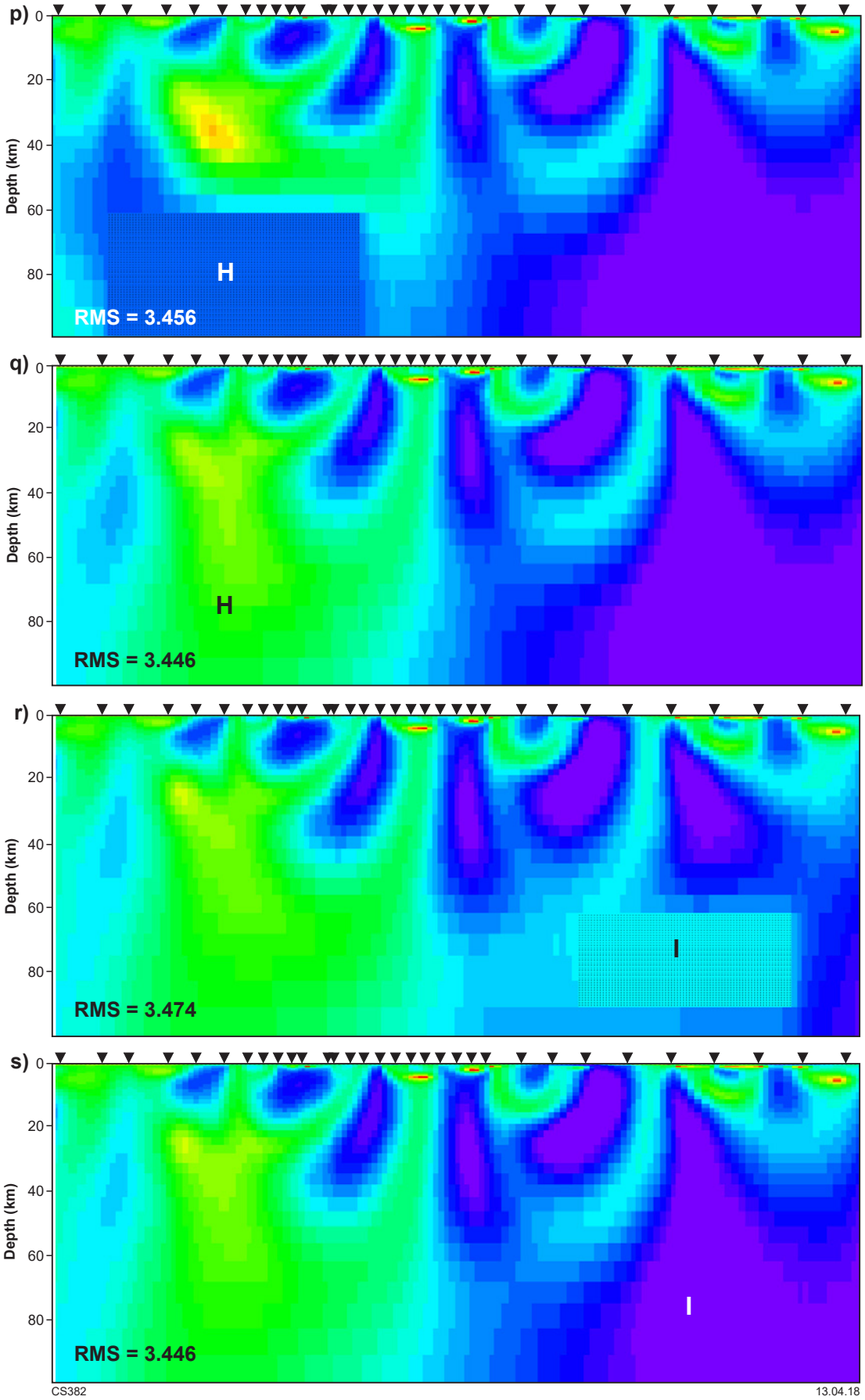

Figure 2.4 continued

This Report presents the results obtained from four regional magnetotelluric transects deployed in the east Albany–Fraser Orogen that have provided 2D and 3D conductivity models of the crust and uppermost lithospheric mantle. Dimensionality and geoelectric strike analysis on these data reveal complex and variable strike directions both laterally and with depth, highlighting the need for 3D modelling. In general, the models reveal a resistive upper crust that is crosscut by several near-vertical, low resistivity zones. In some instances the low resistivity zones can be correlated with the locations of major shear zones or tectonic unit boundaries. A conductive zone in the lower crust below the Northern Foreland and the Biranup Zone coincides with a non-reflective lower crustal zone observed in seismic reflection data, and with a region of thicker crust determined from passive seismic data.

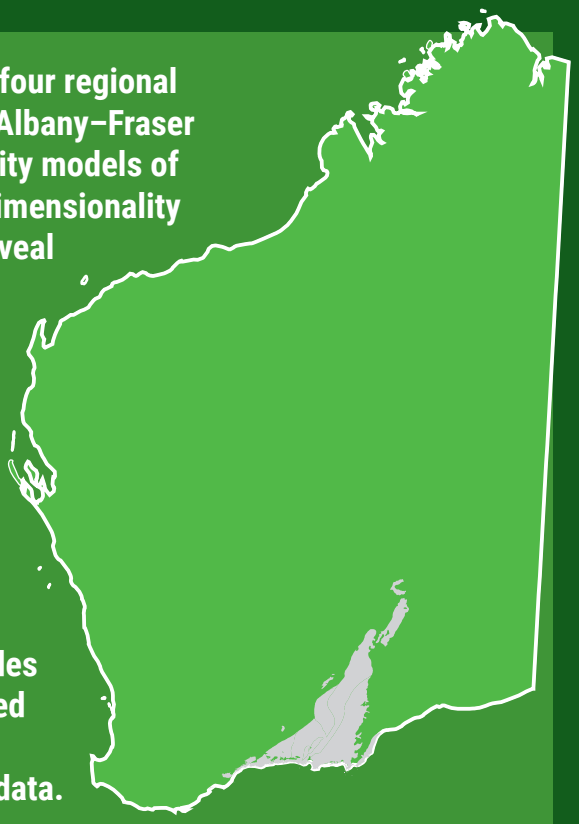

Further details of geological products and maps are available from:

Information Centre
Department of Mines, Industry Regulation and Safety
100 Plain Street
EAST PERTH WA 6004
Phone: (08) 9222 3459 Fax: (08) 9222 3444

www.dmp.wa.gov.au/GSWApublications

SPRATT et al.

A MAGNETOTELLURIC SURVEY ACROSS THE EAST ALBANY–FRASER OROGEN, WESTERN AUSTRALIA

REPORT 189